Joint numerical and experimental study of thermoacoustic instabilities

Maxence Brebion

THÈSE

En vue de l'obtention du

DOCTORAT DE L'UNIVERSITÉ DE TOULOUSE

Délivré par :

Institut National Polytechnique de Toulouse (INP Toulouse)

Discipline ou spécialité :

Dynamique des fluides

Présentée et soutenue par :

M. MAXENCE BREBION

le vendredi 27 janvier 2017

Titre :

JOINT NUMERICAL AND EXPERIMENTAL STUDY OF THERMO-ACOUSTIC INSTABILITIES

Ecole doctorale :

Mécanique, Energétique, Génie civil, Procédés (MEGeP)

Unité de recherche :

Institut de Mécanique des Fluides de Toulouse (I.M.F.T.)

Directeur(s) de Thèse :

M. THIERRY POINSOT

M. LAURENT SELLE

Rapporteurs :

M. THIERRY SCHULLER, ECOLE CENTRALE PARIS

M. WOLFGANG POLIFKE, TECHNISCHE UNIVERSITAT MUNICH

Membre(s) du jury :

M. FRANCK NICOUD, UNIVERSITE DE MONTPELLIER, Président

M. CHRISTOPHE BAILLY, ECOLE CENTRALE DE LYON, Membre

M. LAURENT SELLE, INP TOULOUSE, Membre

M. THIERRY POINSOT, INP TOULOUSE, Membre

Remerciements

This PhD project would not have been possible without the support of many people. Many thanks to my advisers, Thierry Poinsot, who read my numerous revisions and taught me rigorousness and Laurent Selle, who provided me so much nice ideas. Also thanks to my committee members, Thierry Schuller, Wolfgang Polifke, Christophe Bailly and Franck Nicoud, who offered guidance and support.
Thanks to all the members of the Laboratoire de Mecanique des Fluides de Toulouse who also provided me technical support. And finally, thanks to my wife Juliette, my parents, and numerous friends who endured this long process with me.

Abstract

From small scale energy systems such as domestic boilers up to rocket motors, combustion chambers are often prone to combustion instabilities. These instabilities stem from the coupling of unsteady heat release rate and acoustic waves. This coupling is two sided: flame front perturbations generate acoustic waves while acoustic waves impinging on flame holders can disturb flames attached on them. Significant pressure and velocity oscillations can be reached during unstable regimes, that can alter its efficiency or even damage the entire combustion chamber. One major challenge is to understand, predict, and prevent from these combustion instabilities. The objectives of this thesis are twofold: (1) take into account acoustic dissipation and (2) analyze flame/acoustic coupling to obtain Reduced Order Model (ROM) for combustion instabilities.

This work is divided into three parts. First, the concept of ROM that gives the acoustic modes of a combustion chamber is introduced. This modeling strategy is based on the acoustic network theory and may take into account flame/acoustic coupling as well as acoustic dissipation. An efficient numerical algorithm dedicated to solve ROMs was designed on purpose and validated on several academical configurations. Second, an experimental rig was commissioned to study mean and acoustic pressure losses across a diaphragm and two swirl injectors. Results show that these two phenomena are linked and can be simply incorporated into ROMs. Finally, flame/acoustic coupling is investigated by using both direct numerical simulations and experiments: a lean premixed V-shaped laminar flame is anchored on a cylindrical bluff-body and we show that its temperature greatly influences the flame mean shape as well as its dynamics.

Keywords *Combustion instability, Flame transfer function, heat-transfer, acoustic dissipation, pressure loss, network model*

Résumé

Les instabilités thermo-acoustiques se rencontrent fréquemment au sein des chambres de combustion de toute taille, de la petite chaudière au moteur de fusée. Ces instabilités sont causées par le couplage entre ondes acoustiques et dégagement de chaleur instationnaire. En effet, le passage d une onde acoustique au travers d une flamme va moduler son dégagement de chaleur qui, en retour, va générer de nouvelles ondes acoustiques. Lorsqu une chambre de combustion entre en instabilité, d importantes variations de pression sont observées ; ces fluctuations peuvent user prématurément le système ou altérer ses performances.

L étude des instabilités thermo-acoustiques a pour but d améliorer notre compréhension de ces phénomènes complexes afin de les prévenir. L objectif de ce travail est d obtenir et d intégrer au sein de modèles réduits des descriptions précises de la dissipation acoustique - effet stabilisant - et d interaction flamme/acoustique - effet déstabilisant.

Cette étude se décompose en trois axes :
La première partie développe le concept de modèle acoustique réduit qui permet de prédire les modes acoustiques d une chambre de combustion. Pour cela, sont prises en compte les dissipations inhérentes à certaines pièces (diaphragmes, injecteurs, ...) ainsi que le couplage flamme/acoustique. Une fois le modèle établi, il convient d en chercher les solutions à l aide d un solveur numérique spécialement conçu pour cette tache.
Dans une deuxième partie, un banc expérimental est utilisé pour caractériser le lien entre perte de charge et dissipation acoustique. Il est montré de manière théorique et expérimentale que la connaissance des pertes de charge au travers d un élément permet de prédire son comportement acoustique à basse fréquence.
La dernière partie concerne le couplage flamme/acoustique et plus spécifiquement l influence de la température de l accroche-flamme : une flamme pauvre pré-mélangée air/méthane est stabilisée sur un cylindre dont la température peut etre controlée. Ainsi, il est montré que l influence de la température du cylindre sur la flamme - position d équilibre, dynamique et stabilité - est remarquable.

Mots clés *Instabilité de combustion, Fonction de transfert de flamme, transfert de chaleur, dissipation acoustique, perte de charge, modèle réseau acoustique*

Contents

0.1 Context 1
0.2 Objectives of the present work 8

I Introduction to thermo-acoustic instabilities 12

1 Derivation of reduced-order models 13
1.1 Introduction 13
1.2 Reacting Navier-Stokes equations 14
1.3 Acoustic equations 16
1.4 Helmholtz equation 18
1.5 Coupling with Flame and Hydrodynamics 21
1.6 Reduced Order Model (ROM) 23
1.7 Conclusion 28

2 An optimal adaptive methodology for the resolution of the ROM equation 29
2.1 Theoretical context 30
2.2 Algorithm description 32
2.3 Strategies of domain splitting and reshaping 33
2.4 Numerical scheme used for the computation of the generalized argument principle 35
2.5 Numerical results 36
2.6 Parametric study of a laboratory scale combustion chamber 41

II Mechanisms leading to acoustic dissipation 44

3 Acoustic and pressure losses: The PREINTRIG work-bench 45
3.1 Two-port matrix formalism 46
3.2 What can we get from two-port matrices ? 51
3.3 The PREINTRIG workbench 53

4 Pressure losses study 59
4.1 Mesh metric for the prediction of pressure losses 60
4.2 Validation on a canonical test case: pressure losses through a diaphragm 63
4.3 Pressure losses in a swirl injector 66

5 Measurement of acoustic two-port matrices: application to acoustic losses prediction 77
5.1 Measurement of two port matrices 78

5.2 Two-port Matrices . . . 80
5.3 Acoustic losses: a detailed comparison . . . 87
5.4 Conclusion . . . 95

III Influence of flame holder temperature on combustion instabilities 96

6 The INTRIG burner: experimental and numerical descriptions 97
6.1 INTRIG workbench . . . 97
6.2 Flow solver . . . 100
6.3 Heat transfer in the bluff-body . . . 103
6.4 Chemical kinetic mechanisms . . . 106
6.5 Conclusion . . . 114

7 Mechanisms of flame anchoring on cylindrical bluff-bodies 115
7.1 CBB conguration . . . 116
7.2 UBB conguration . . . 118
7.3 Influence of the cylinder emissivity . . . 123
7.4 Bifurcation to upstream stabilizedΦames . . . 125
7.5 Conclusions . . . 127

8 Influence of flame holder temperature on flame acoustic coupling 128
8.1 Measurement of Flame Transfer Function (FTF) . . . 129
8.2 Flame roots mechanisms . . . 137
8.3 Comparison with experimental measurements . . . 145

9 Reduced Order Model of the INTRIG burner 150
9.1 Flame/Acoustic coupling . . . 151
9.2 Boundary conditions and ROM of the INTRIG burner . . . 157
9.3 Acoustic modes prediction in INTRIG . . . 159
9.4 Discussion . . . 163

Appendices 175

A Checking procedure of the roots 176

B Design of a non intrusive lateral loudspeaker system 177
B.1 Geometry description . . . 177
B.2 ROM derivation . . . 178
B.3 Experimental acoustic modes . . . 180
B.4 Discussion . . . 180

C Application of the viscous dissipation QOIΦo compressible flows D 184

Microphone spacing and acoustic forcing in PREINTRIG 185
D.1 Microphone spacing . . . 185
D.2 Acoustic forcing . . . 185

E Suppression of pressure and velocity oscillations **187**

F Continuous and discrete approaches for acoustic propagation in non homogeneous media **189**

F.1 Analytical two-port matrix for a linear temperature prole 189

F.2 Validation of the discrete approach 190

Introduction

0.1 Context

Combustion is the first source of energy generation. Its use ranges from electricity production to rocket propulsion. Today, it still represents about 90 % of the energy used on earth [1]. Despite the growth of renewable energies, combustion is likely to remain the main source of energy in the future decades and is thus still an active subject of research.

Today, the main objective is to reduce pollutant emissions generated by combustion. Except for hydrogen/oxygen flames, which are encountered in some rocket propulsion systems, CO_2 is always obtained as a final product of combustion. Its emission amplifies the green-house effect [2] as it increases the absorption of infra-red radiations. CO_2 emissions can be tempered by reducing the need of combustion, that is to say, reducing the number of devices operated by combustion, or improving the efficiency of combustors. Other pollutants, such as mono-nitrogen oxides NO_x can be avoided by lowering the temperature at which combustion occurs as shown in Fig. 1.

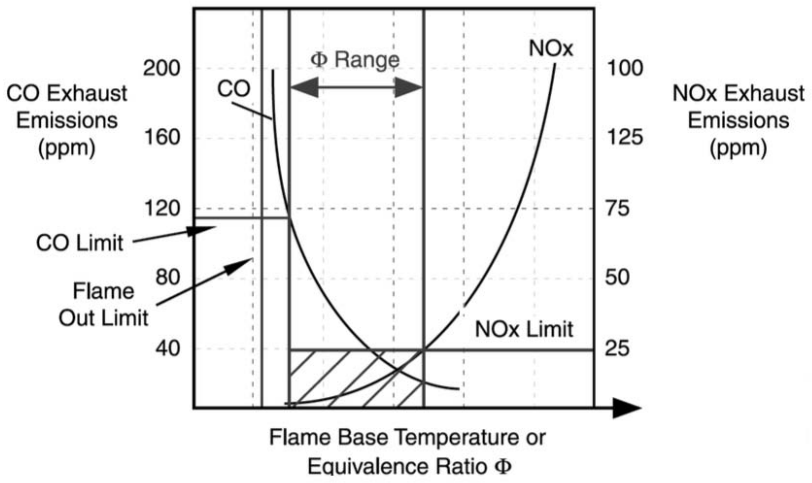

Figure 1: Influence of the Equivalence Ratio (or the temperature) on pollutants emission (NO_x and CO). Reproduced from [3]

NO_x emissions can also be reduced by using lean premixed combustion where the burnt mixture reaches lower temperature than for stoichiometric combustion. In premixed combustion, all reactants are mixed before entering the burner so that the burnt gas temperature never exceeds the adiabatic temperature. Figure 1 shows an example of NO_x and CO emissions, as a function of the Equivalence Ratio (ER) or fresh gas temperature. Contrary to CO, NO_x emissions increase with these parameters and a narrow operating range in which pollutant emissions remain acceptable is obtained.

However, system operating lean premixed mixtures are prone to Combustion Instabilities (CI). One of the mechanism leading to CIs is the coupling between acoustic waves and unsteady heat release. Rayleigh [4, 5] provided a simple criterion to predict the onset of such perturbations, which are called thermo-acoustic instabilities, in reference to the underlying mechanism. This criterion has been later adapted to take into account acoustic radiation and dissipation [6, 7, 8] :

$$\frac{\partial E}{\partial t} + \frac{\partial F}{\partial x_i} = S - D \tag{0.1.1}$$

where E is the acoustic energy, $F = u'p'$ is the flux of acoustic energy, and S: the Rayleigh source term:

$$S = \frac{1}{T} \int_V \frac{\gamma - 1}{\rho_0 c^2} p' q' dV \tag{0.1.2}$$

where p', q' are the acoustic pressure and unsteady heat release fluctuations respectively. The Rayleigh source term appears as a source (or sink) of acoustic energy: acoustic energy increases when the unsteady heat release q' rate and acoustic pressure waves p' are in phase. Finally, the last term D in the RHS of equation 0.1.1 accounts for acoustic energy dissipation.

CIs have been widely documented: Candel et al [9] presented a detailed review on this topic, as well as Lieuwen [10] where different studies are compiled into a book. CIs have also been studied numerically, by the mean of computational fluid dynamics, and interesting methods are presented in the book written by Poinsot and Veynante [11]. The specific case of CI in real engines was discussed in the 2016 Hottel lecture at the Symp. on Comb. in Seoul.

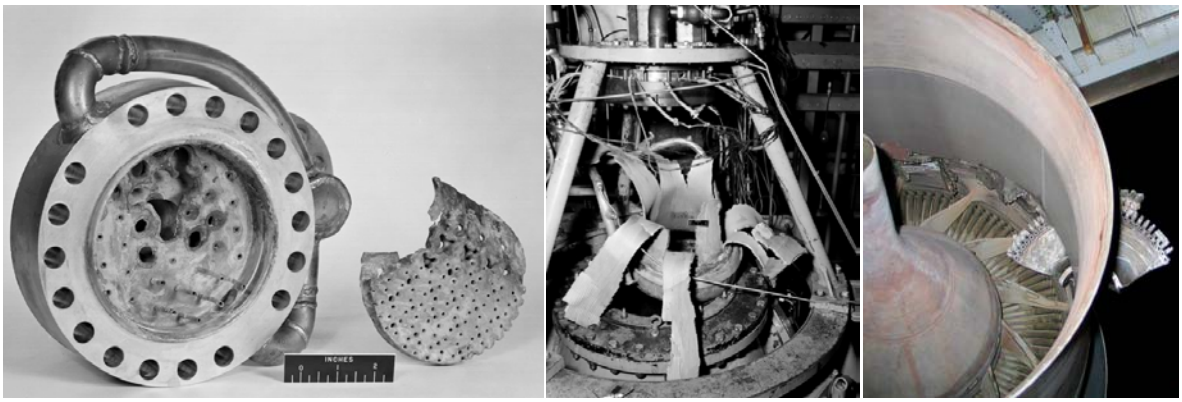

Figure 2: Consequences of thermo-acoustic instabilities. Left: a NASA rocket chamber destroyed during operation (flashback event). Center: Nasa engine damaged on start. Right: Turbo fan engine after a turbine disc is detached from the opposed engine due to vibrations caused by CIs. Reproduced from Mejia et al [12]

Most of the time, combustion chambers are designed in order to avoid the occurrence of CIs: these instabilities may cause excessive vibration or even flashback events. Some examples of engine failures caused by CIs are displayed in Fig. 2. The objectives of thermo-acoustic studies are first to understand the underlying mechanisms leading to high pressure fluctuation, but also to predict these acoustic modes in order to avoid them. In practice, one must model/measure accurately both dissipative effects (D) as well as flame/acoustic coupling (S) to predict thermo-acoustic instabilities.

Acoustic energy losses

Two phenomena are generally contributing to acoustic energy losses. The first contribution is acoustic energy radiation at the boundaries of the system (F in equation 0.1.1). Indeed, in the case of non fully reflective boundary conditions, acoustic energy is transfered outside of the system. This loss in acoustic energy can be measured apart from the other sink terms [13] or modelled by the mean of impedance/reflection coefficients [14, 15].

The second contribution is acoustic energy dissipation (D in equation 0.1.1). Acoustic dissipation occurs in boundary-layers [16] as well as in compact elements such as perforated plates or injectors. The physical mechanism is the generation of vortex eddies, which are convected away from the plate [17, 18]. In the presence of a mean flow, this mechanism remains linear as long as

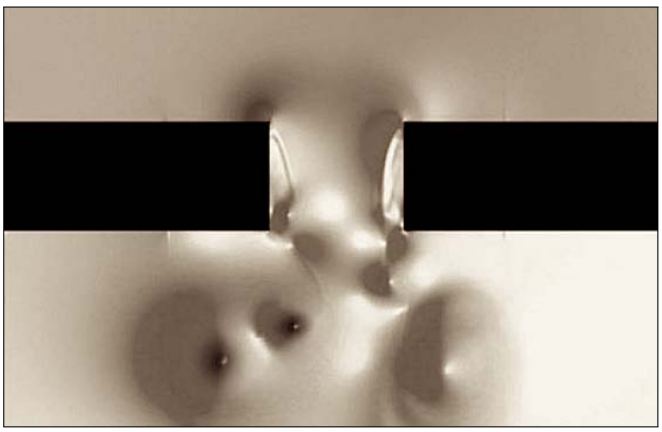

Figure 3: Vortex shedding occuring across a perforated plate in the presence of a mean flow forced by acoustic waves. Reproduced from Tam et al [19].

the amplitude of the acoustic velocity remains lower than the mean flow velocity in the element of interest. An example of vortex shedding occurring at the rim of a perforated plate is shown in Fig. 3. This result has been obtained in a Direct Numerical Simulation (DNS), in the presence of a mean flow, which was forced by acoustic waves.

Acoustic dissipation can be modelled in the case of academical configurations such as diaphragms (as done by Howe [20]) or acoustic dissipation through swirl injectors [21]. Beyond modelling, measurement in both experiments [21] and simulations [22] have been carried out. The idea is to measure a two-port representation of the element which dissipates acoustic energy, by linking acoustic quantities at input and output ports. An instant velocity field of a turbulent flow forced with broadband acoustic waves is displayed in Fig. 4. This flow, obtained in a Large Eddy Simulation (LES), has been post-processed to obtain the acoustic two-port representation of a sudden change of section: acoustic waves are reflected and transmitted across this passage. This procedure permits to retrieve the frequency behavior of the two-port matrix in a single simulation.

Dissipative elements may be added in combustion chambers to damp the existing acoustic modes. For instance, dampers based on Helmholtz [24] or multi-perforated cavities [25] can be designed to absorb acoustic energy in the frequency range where CIs occur. However, few studies quantify the level of acoustic damping, caused by the presence of an acoustic damper. Indeed, Durox et al [26] measured a global dissipation term D directly in their experiment and incorporated it in equation 0.1.1 without any modeling. This is clearly a weak part of many thermo-acoustic models: while may studies focus on the Rayleigh term (The gain in equation 0.1.1) very few models can provide the dissipation (the sink term in equation 0.1.1).

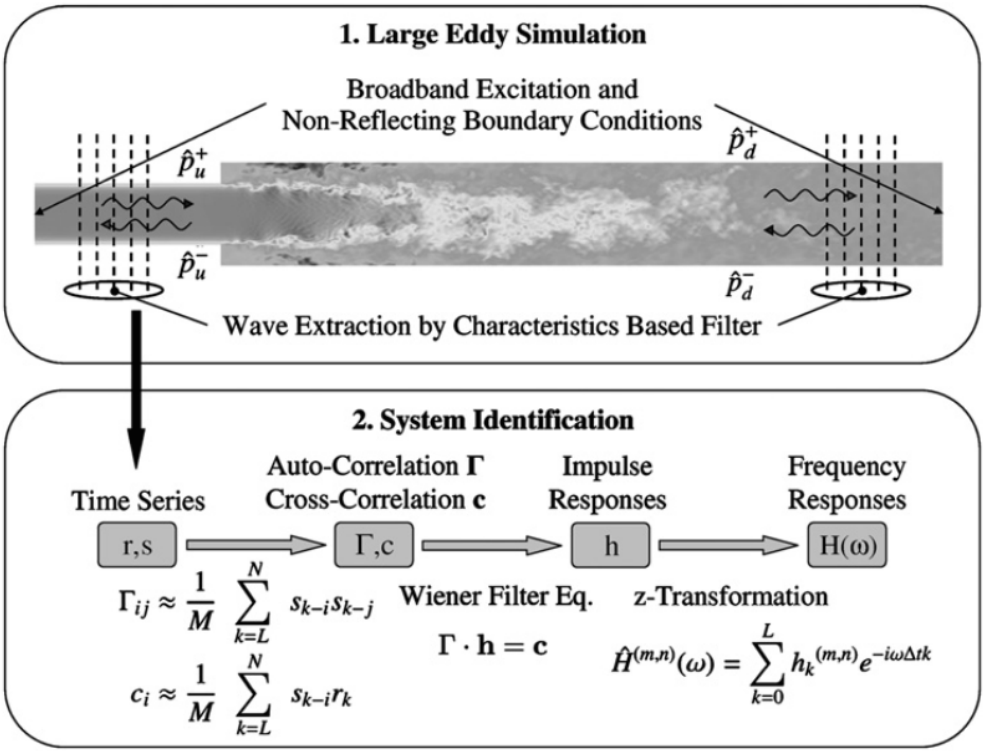

Figure 4: Measurement of an acoustic two-port: the scattering matrix, which links leaving and entering acoustic waves. Top: instant velocity field of a forced turbulent flow experiencing a change of section. Bottom: procedure used to retrieve the scattering matrix from broadband acoustic inputs. Reproduced from Foller et al [23].

Flame/acoustic coupling: influence of the flame holder temperature

The burnt gas temperatures reached in all combustion chambers exceed the maximum temperatures which can be sustained by most materials, especially metals used in engines. Cooling these walls is mandatory for all combustion chamber designers. While cooling is obviously needed to preserve walls, the effects of wall cooling on the flames themselves have received less attention up to now and are usually neglected in many CFD approaches. Flame/wall interaction, for example, is a field of combustion which has not been investigated yet with sufficient attention [27, 28, 29, 30] and is often overlooked. In most cases, authors try to predict the maximum wall heat fluxes induced by the flame but do not investigate the effects of the wall on the flame itself (steady regime as well as dynamics).

Most LES performed for example for real engines [31, 32, 33, 34], assume adiabatic walls. Many models for turbulent combustion also assume adiabatic flows. The famous BML (Bray Moss Libby) approach, for example, which is the workhorse of most theories for turbulent premixed flames [35, 11] assume that a single variable (the progress variable c) is sufficient to describe the flow: this is true only when the flow is adiabatic. Almost all approaches for turbulent combustion using the mixture fraction are valid only if the flow is adiabatic (otherwise there is no equivalence between reduced temperature and species fields). In the same way, many usual methods for chemistry tabulation such as FPV [36], FPI [37] or FGM [38] assume that chemistry depend only on two variables, the mixture fraction z and the progress variable c, which implies that the flames must be adiabatic. Considering that wall heat fluxes in most chambers correspond to approximately 10 to 40 percent of the chamber total power, assuming adiabaticity is clearly

not compatible with the high-precision methods which are sought today [39].

Note that computing correctly the interaction between the flame and the wall usually requires to compute both the flow and the temperature within the walls simultaneously: this requires coupling the LES (or DNS) codes with a heat transfer code within the combustor walls, a task which is not simple [40, 41, 42] because time scales are usually very different (a few milliseconds in the flow and a few minutes in the walls).

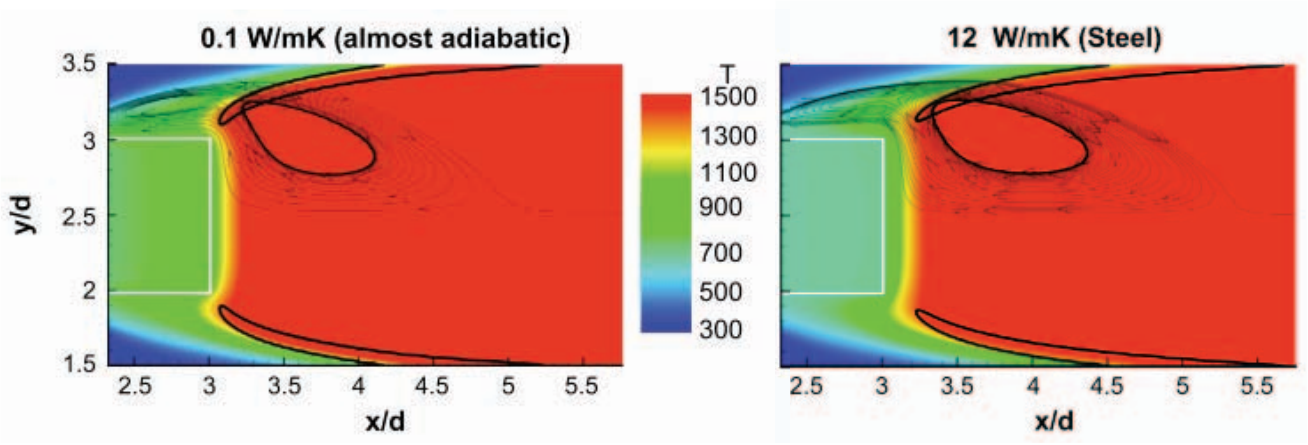

Figure 5: Temperature contours with overlaid streamlines and 10% YHCO black contour line for the case with $\phi = 0.7$ for two different thermal conductivities of the bluff-body (marked by the white square). Adapted from Kedia and Ghoniem [42].

Heat losses to walls obviously play important roles on the mean flame structure (velocity and temperature fields, pollutant levels [32, 43]). A comparison between laminar flames stabilized on quasi-adiabatic and steel flame holders is provided in Fig. 5 for a $\phi = 0.7$ methane/air laminar premixed flame. Post-processing of DNS data shows that in the steel case (Fig. 5, right), the flame is stabilized farther than in the quasi-adiabatic case (Fig. 5, left). Heat losses to walls also affect the flames unsteady behavior and notably, combustion instabilities [44, 41]. This is due to two main mechanisms:

- Mechanism I (sound speed changes): heat losses through the walls change the gas temperature and therefore the sound speed, thereby modifying the chamber stability because the frequencies of the acoustic modes change. Since combustion instabilities require phase criteria to be satisfied to lead to positive growth rate, any change in the acoustic frequencies of a given chamber can push the flame from stable to unstable regime and vice versa.

- Mechanism II (flame response changes): heat losses, especially in the flame holder region, also control the sensitive stabilization region where flames are anchored. A modification of heat transfer in this zone directly affects the unsteady flame response because it changes its position: cold flameholders prevent the flame from finding a stabilization point close to the solid surface. The stabilization region where a flame front can anchor is dominated by viscous mechanisms where chemistry and heat transfer compete to determine a stable anchoring point. These processes are similar to another usual topic in combustion: flame/wall interaction [28, 45, 46] where a flame impacts on a wall. Most flame/wall interaction studies, however, correspond to an unsteady situation where a flame quenches on a cold wall [47, 30, 48] while the stabilization of a flame behind a flame holder is a steady process.

Mechanism I has been studied in a few LES [44, 32] which compared adiabatic and isothermal walls effects on combustion stability. Mechanism II was also investigated numerically by the MIT group [49, 50] and at CERFACS [41, 40] and experimentally at EM2C [51] and IMFT by Mejia et al [52] who showed that the dynamics of the flame root (the place where the flame is anchored) has a direct impact on flame stability. The most direct proof of the combined strengths of Mechanisms I and II is that many flames exhibit different combustion instability characteristics when the flame is ignited (cold walls) and after a few minutes (when the walls become warm) as discussed by Mejia et al [52]. Figure 6 presents a laminar inverted-V flame operated at IMFT which is self-excited. This combustor is built to allow a full control of the flame holder temperature which can be varied from 300 to 400 K using a water cooling system. At $t \leq 40$ s, the burner rim is still cold ($T_c \approx 290$ K), and it reaches higher temperature for t 400 s: $T_h \approx 340$ K. One observes that the flame dynamic is affected by the burner rim temperature.

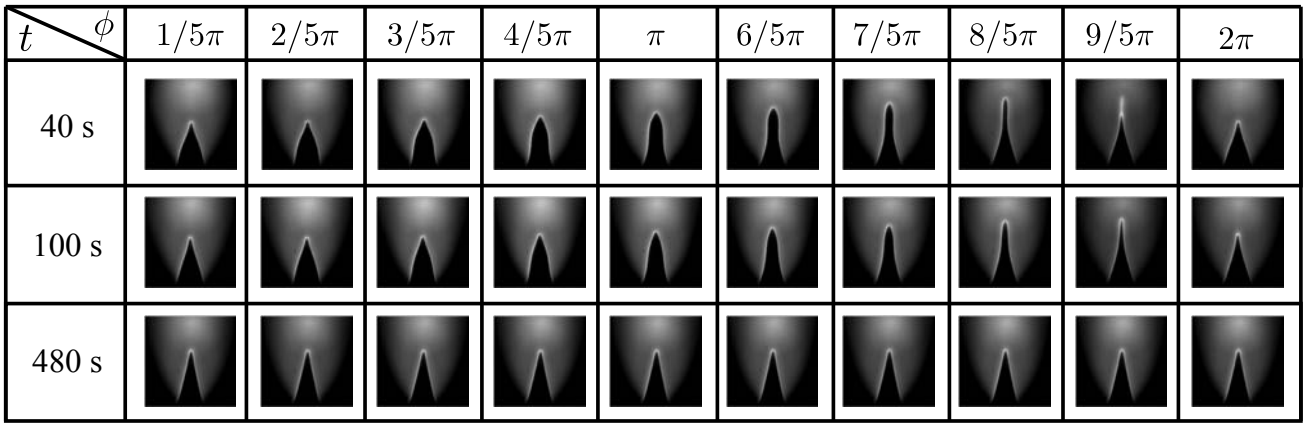

Figure 6: Snapshots at different instant of an unstable cycle of a laminar inverted V-flame stabilized on a flame holder which temperature increases with time. Reproduced from Mejia [12].

Figure 7 shows the evolution of both the RMS pressure fluctuation p_0 and burner rim temperature T_s in both cooled and un-cooled regimes: low temperatures lead to an unstable flame while a hot flame holder (more than 340 K) help to stabilize the flame.

The mechanisms which explain the behavior observed in Figs. 6 and 7 have been elucidated in simple laminar flames [52] and involve mainly a modification of the flame root zone (Mechanism II), leading to different flame dynamics and a flame which switches from stable to unstable modes. How these mechanisms can affect larger, turbulent flames is unclear at this point.

Put it all together: Reduced-Order Model (ROM)

The prediction of thermo-acoustic instabilities can be realized by deriving ROM, built on top of an acoustic network representing the geometry of the burner. ROM are an elegant way to enter the field because they allow to identify the various phenomena controlling CI. They are widely used in industry as well as laboratories. Such networks are based on the assumption that one dimensional acoustic waves propagate in a series of connected elements. A network model consists in the assembly of two-port representation of individual elements [53]. A semi-analytical approach has been employed by Kopitz et al [54] and is shown in Fig. 8.

In this study, CFD is used to measure the scattering of acoustic waves in the flame region while network modelling is used to propagate the acoustic waves in the remaining of the system.

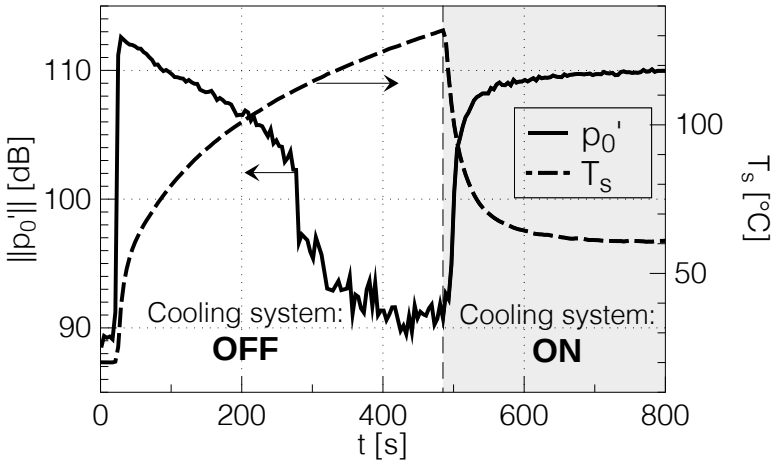

Figure 7: Experiment showing the effect of wall temperature on the combustion instability. At $t = 20$ s, tha flame is ignited, with cooling system OFF. At $t = 480$ s, the cooling system is turned ON. p_0 is the magnitude of pressure fluctuations inside of the chamber while T_s corresponds to the flame holder temperature. Reproduced from Mejia [12].

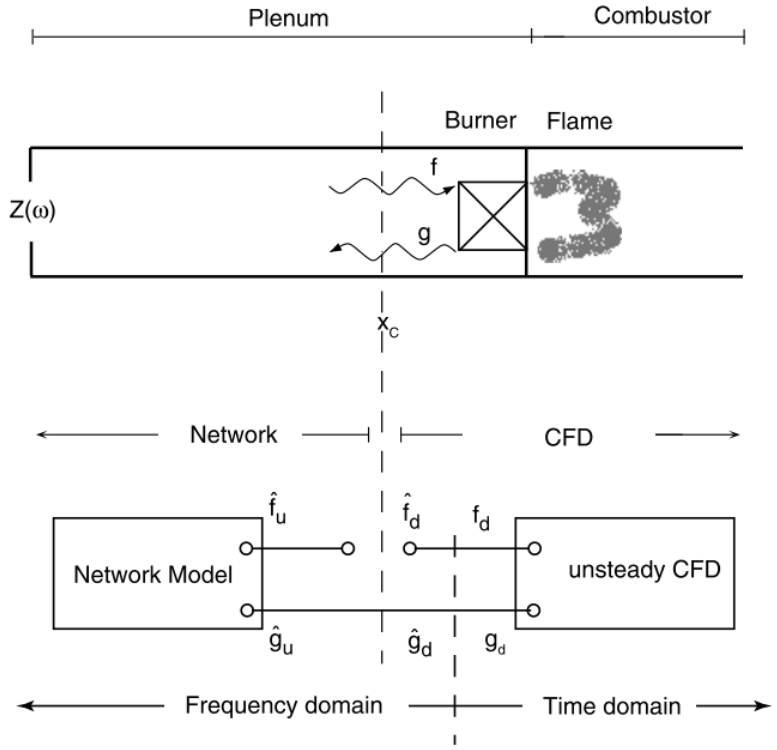

Figure 8: Hybrid CFD/Network approach for the prediction of thermo-acoustic instabilities. The network approach is used for the boundary conditions while the CFD is used for the flame region. Reproduced from Kopitz et al [54].

Such representation permits to modify the chamber design (Lengths, termination impedances) without running a new costly CFD simulation.

Finally, the stability of combustion chambers can be predicted by solving fully analytical ROM at small CPU cost. For instance, Sattelmayer [55] introduced a characteristic equation for a premixed gas turbine combustor. More recently, Parmentier [56] and Bauerheim [57] studied

the linear stability of annular combustion chambers, the latter study including plenum effects. A sketch of the network model corresponding to an azimuthal combustion chamber is reproduced in Fig. 9. Both plenum and chambers are decomposed into n_b sectors, n_b being the number of burners and all these elements are linked in three port junctions. In this study, no acoustic dissipation is taken into account but the flame/acoustic coupling is accounted for by the mean of individual Flame Transfer Functions (FTF) for each burner. ROM have also been used to

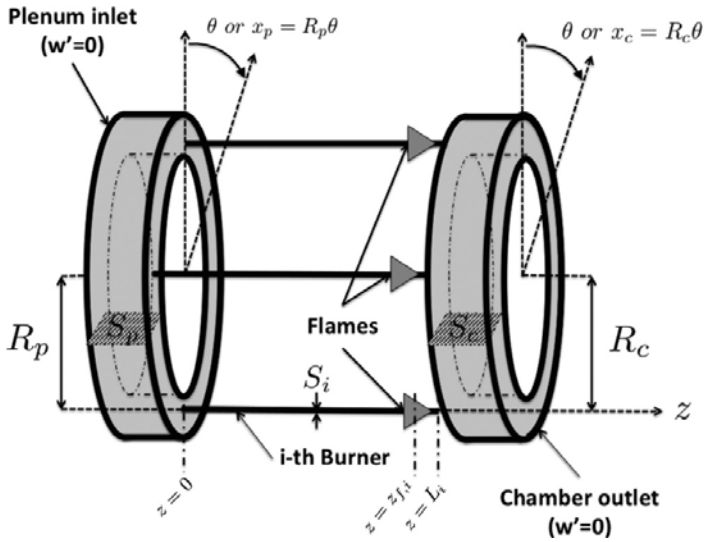

Figure 9: Network representation of an azimuthal combustion chamber split into three parts: the plenum, the burners and the chamber. Reproduced from [57]

compare theoretical and experimental results. For example, Schuller et al [58] proposed a model in which dissipation was taken into account to predict the stability of a laminar premixed flame anchored on a slot burner.

0.2 Objectives of the present work

The general equations to solve for thermo-acoustic studies are presented in Part I: they are rather well known today but impossible to solve analytically in most cases. Chapter 1 will present the different approximations used to solve these equations and focus on one class of solutions: reduced-order models (ROM) [56, 57, 58]. When a ROM approach is used, it leads to a mathematical problem which may be viewed as non critical but rapidly becomes more complicated than expected because it requires to solve for the roots of an equation in the complex plane (of type $F(\omega) = 0$, $\omega \in \mathbb{C}$ where ω is the complex angular frequency of the acoustic modes). During the present work, in collaboration with other researchers of the ERC INTECOCIS grant (intecocis.inp-toulouse.com) project, a specific solver called Rootlocker was developed to address this issue (Chapter 2). The equation to solve is first recalled and various mathematical theorems are presented [59] before describing the basic elements of Rootlocker and its application to the IMFT rig called INTRIG (a burner with a laminar premixed flame stabilized on a cylindrical bluff-body). Two main issues have been identified concerning ROM:

- Taking into account the interaction between acoustic waves and the mean flow field is a first critical topic. Such coupling generally damps acoustic energy and helps to stabilize a thermo-acoustic system. (Part II)

- Studying how heat transfer influences flame dynamics by measuring FTFs for different flame holder will be a second topic. (Part III)

The sources of acoustic losses, which may stabilize a combustion chamber by lowering the growth rate of thermo-acoustic modes are investigated in Part II: independently of the mathematical framework used to solve the equations of Part I, a major difficulty is to quantify acoustic losses. Overall instabilities occur when the gain (measured through Rayleigh type criteria like equation 0.1.1) exceeds the acoustic losses. Most studies focus on the quantification of the gain but very few try to predict acoustic dissipation. These losses occur through acoustic radiation at inlets and outlets, but also through vortex formation [20, 60] in all zones where unsteady vorticity is created by acoustic waves (perforated plates [61] , expansions [23], swirl injectors [21], ...).

Chapter 3 discusses how acoustic dissipation can be evaluated and exhibits the link with pressure losses occuring in the same elements [24]. For instance, the coefficients of modelled two port acoustic matrices for a multi-perforated plate are actually linked to the classical discharge coefficient giving pressure losses for the mean flow in the same elements. In other words, being able to predict accurately acoustic dissipation in a chamber must begin by a computation of mean pressure losses in this chamber (which is the zero-frequency limit of the exercise). Therefore Chapter 4 presents computations and measurements of mean pressure losses in two experiments installed at IMFT: a diaphragm flow and a swirl injector (provided by Safran Helicopter Engines and shown Fig. 9.15, left). This question, even if it is not directly connected to CI, is critical in the LES community. While almost all LES provide excellent results in terms of velocity fields at swirl injectors outlets (within the chamber) [62, 63, 64], almost no author reports values of overall pressure losses. The experience of CERFACS (and others such as CORIA or EM2C) is that predicting pressure losses accurately in swirling flows is a difficulty. This topic was addressed during this PhD work in a collaborative task with CERFACS to define a metric: the kinetic energy dissipation, which must be well resolved for pressure losses to be captured by LES. This metric was used in an automatic mesh refinement tool (MMG3D by INRIA) and chapter 4 shows drastic improvements in LES results for pressure losses as soon as this automatic mesh refinement tool is used.

After the mean flow in the target configurations of Fig. 9.15, left, was computed precisely, it was possible to address the question of acoustic losses. These losses were measured (at IMFT) and computed (by F. Ni at CERFACS) and the methodology to perform measurements is presented in Chapter 5. Two-port matrices were used to define the transfer functions of the elements. These results are compared to simulations and to models (for the diaphragm) and show a path to introduce acoustic dissipation in Helmholtz codes[1] or in ROM approaches.

Finally, part III addresses the question of the influence of wall temperatures on CI. Here the INTRIG rig developed at IMFT [66] is studied, with combustion. The cylinder on which the flame is stabilized was equipped with a water cooling system in order to investigate the effects of flame-holder temperature on the flame steady structure and dynamics. Again, both experiments and simulations were performed. The latter were set-up with a complex chemistry scheme (up to 19 species) for methane/air flames and a coupled heat transfer/flow resolution to compute not only the flow but also the temperature within the cylindrical flame holder. Chapter 6 presents the experimental configuration as well as the numerical set-up. Since the flames are laminar and

[1]This strategy has been published with F. Ni [65]

2D, a full DNS was possible for steady and forced flames.
Chapter 7 describes the steady flames, using both DNS and experimental data. Two different configurations are investigated: a cooled case where the rod temperature is around 300 K and an un-cooled one where it reaches 700 K. It is shown that this latter temperature can be predicted in the DNS only when considering radiative fluxes lost by the rod. As a consequence, a third case of interest is identified in the DNS where the flame would stabilize upstream of the bluff-body when radiative fluxes are neglected[2]. In this case, which was not studied experimentally, the bluff-body would reach very high temperature (close to the adiabatic flame temperature). The flame structures obtained for the three cases are shown to be very different confirming that the temperature play a major role in the structure of the flame.

The next chapter (8) of Part III discusses the influence of the bluff-body temperature on the FTFs of the flame. The three flames introduced in chapter 7 are forced with both harmonic and broad band acoustic fluctuations in order to obtain Flame Transfer Functions. It is shown that the temperature of the flame holder greatly influences the flame response, both in phase and gain. A modeling approach based on the G-equation framework is provided to understand how the flame root dynamics affect the global FTF.

Finally, chapter 9 gathers all the results of the previous chapters. A detailed ROM of the INTRIG burner is designed by taking into account the FTFs obtained in the DNS. The solutions of this ROM are then compared to the acoustic modes observed in the experiment for several geometries: the chamber length is varied from a short configuration, where all flames lead to stable regimes (ideal to measure FTFs) up to a long one, where instabilities have been observed. The agreement between ROM solutions and experimental measurements is very good and a new family of acoustic modes is introduced to explain the modal structure encountered in the burner: the Quasi Intrinsic Thermo-Acoustic (QITA) family of modes.

The outlines of the manuscript are finally gathered in Fig. 10 where the main objectives of the different chapters are recalled.

[2]This case has only been studied in the DNS and corresponds to a transparent bluff-body.

Part I Low order model approach for TA instabilities

1
- Introduction to thermo-acoustic instabilities
- Derivation of Reduced Order Models (ROM)

2
- Numerical algorithm to solve ROMs: RootLocker
- Performance & safety issues

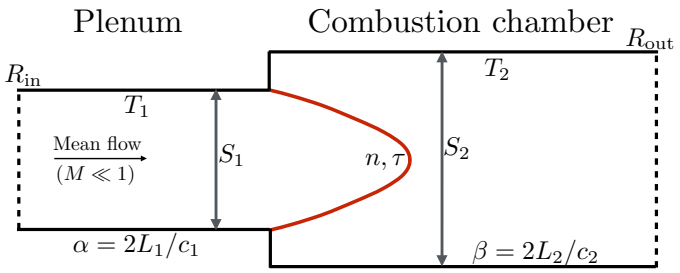

Sketch of a simplified combustion chamber

Part II Mechanisms which damp TA instabilities

3
- Introduction of the PREINTRIG workbench
- Framework for acoustic and mean pressure losses

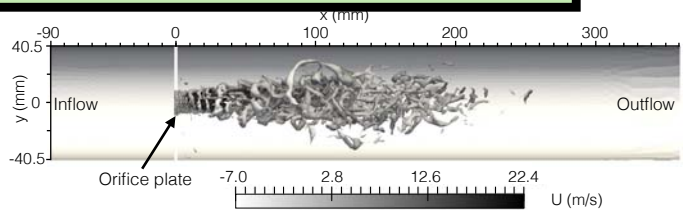

Flow across the diaphragm

4
- LES prediction of pressure losses
- Automated mesh refinement

5
- Measure of acoustic two-port matrices
- XP vs ROM comparison

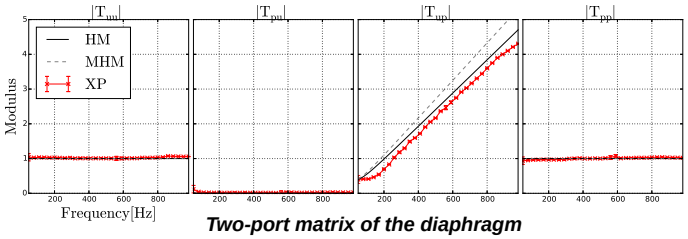

Two-port matrix of the diaphragm

Part III Flame/acoustic coupling: heat transfer influence

6
- Introduction of the INTRIG workbench
- Setup of the associated DNS

7
- Study of flame anchoring mechanism
- Influence of the flame holder temperature

8
- Study of flame Dynamics
- Influence of the flame holder temperature

9
- ROM of the INTRIG burner
- XP vs ROM comparison

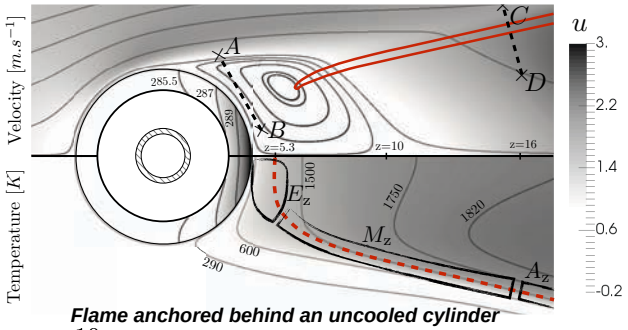

Flame anchored behind an uncooled cylinder

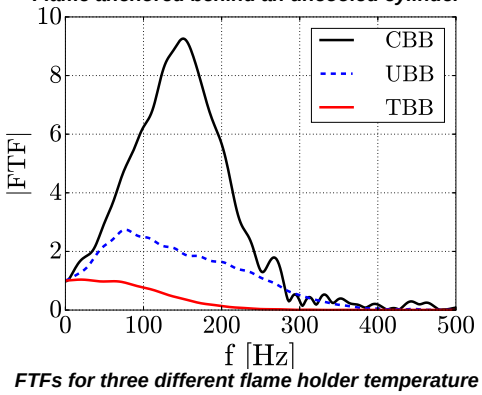

FTFs for three different flame holder temperature

Figure 10: Outlines of the manuscript.

Part I

Introduction to thermo-acoustic instabilities

After recalling the equations associated with thermo-acoustic studies, a methodology dedicated to derive Reduced-Order Models (ROM) is presented (Chapter 1). ROM take the form of analytical equations of the complex variable ω, the angular frequency of the acoustic mode. Such models can be derived for academic configurations as well as for more complex configurations. In Chapter 2, an efficient and robust method (called RootLocker) dedicated to the resolution of the analytical equations is detailed and validated on both polynomial and thermo-acoustic examples. This method is particularly well suited to the resolution of ROM equations.

Chapter 1

Derivation of reduced-order models

The general framework to study thermo-acoustic instabilities is the set of reacting, compressible Navier-Stokes equations, which are recalled in section 1.2. When combined to a realistic chemical kinetic scheme, these equations provide a very precise insight into thermo-acoustic phenomena. These equations cannot be solved directly and must be simplified. The first step consists in deriving the acoustic equations from the reacting, compressible equations (section 1.3). The temporal problem is then recast in the spectral domain to obtain the Helmholtz equation (section 1.4). This equation is linear and easier to solve, especially in regions where only one-dimensional acoustic waves are propagating. ROM can be established by splitting a complex geometry into simpler, one-dimensional components. These components are then linked by the mean of continuity equations, which take the form of acoustic two-port matrices (section 1.5) when acoustic waves are considered. Finally, an example of ROM is derived for the INTRIG burner operating at IMFT which is briefly described here and in more details in Part III.

1.1 Introduction

Distinct approaches exist to predict the stability of a thermo-acoustic system [11, 10]. First, it is possible to use Large Eddy Simulations (LES) or Direct Numerical Simulation (DNS) to check wether the time dependent reactive flow is prone to instability [67, 68, 69]. Although time-consuming, LES and DNS can predict both linear instability growth rate and limit-cycle amplitudes by inherently accounting for non-linear effects.

When a parametric study is of interest, LES and DNS are no more convenient. It is more interesting to use a Helmholtz solver. The Helmholtz equation accounts for sound speed field and flame transfer functions, obtained from simulations or experimental measurement, and acoustic boundary conditions [70, 67]. Such computations remain less expensive than LES or DNS (computational time). Moreover, they output acoustic modes along with their respective complex frequencies. Even so, they rely on a fixed geometry which must be meshed properly.

Finally, the stability of combustion chambers can be predicted by solving corresponding ROM at small CPU cost. For instance, Sattelmayer [55] introduced a characteristic equation for a premixed gas turbine combustor. More recently, Parmentier [56] and Bauerheim [57] both studied the linear stability of annular combustion chambers, the latter study including plenum effects. Courtine et al [71] established a low-order model to predict intrinsic thermo-acoustic instabilities which accounts for realistic flame transfer function. Low-order models have also been used to compare theoretical and experimental results. For example, Schuller et al [58] proposed a model to predict the stability of a laminar premixed flame stabilized on a slot burner. These models

all have in common the final mathematical formulation: they lead to analytical equations : $f(\omega) = 0$, $\omega \in \mathbb{C}$. Contrary to the previous methods, here, one has a complete control over the whole parameter set including geometry description, flow properties or flame transfer functions.

The objective of this chapter is to provide a general methodology to derive ROM. For instance, the configuration depicted in Fig. 1.1 is a typical toy problem in which longitudinal thermo-acoustic instabilities may occur. It is constituted by a plenum, fed by an un-burnt premixed flow, a multi-perforated plate, which aims at both laminarizing the flow and damping the acoustic waves, a flame holder and a combustion chamber. This configuration can be synthesized into a ROM as described in the next sections to illustrate the methodology.

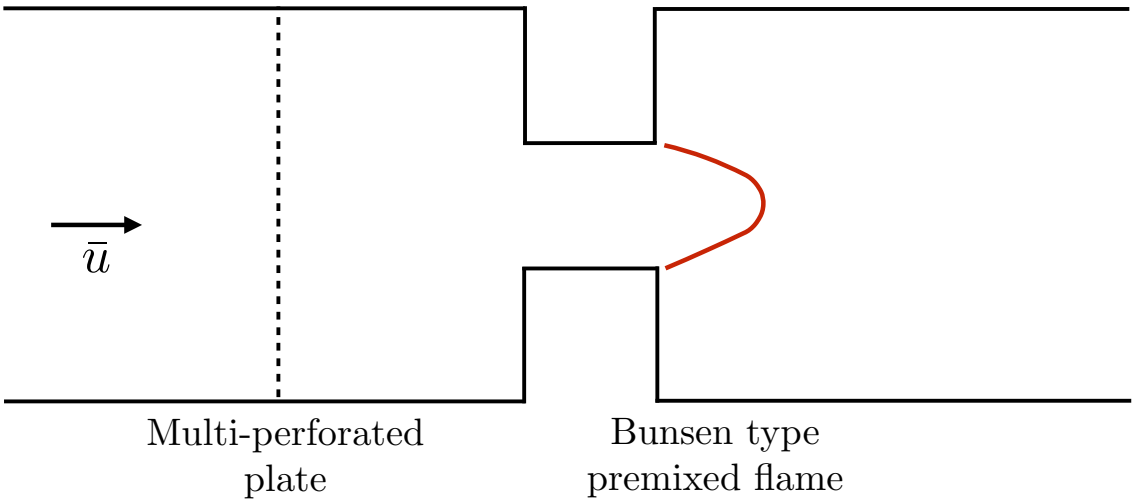

Figure 1.1: Generic geometry of a laminar premixed burner.

1.2 Reacting Navier-Stokes equations

The reacting, compressible Navier-Stokes equations can be established in a conservative form. They state that some relevant quantities: the mass, quantity of momentum, and total energy are globally conserved in the absence of external forces.

1.2.1 Conservation of mass and species

$$\frac{\partial \rho}{\partial t} + \frac{\partial \rho u_i}{\partial x_\mathrm{i}} = 0 \tag{1.2.1}$$

Here, and in the following of the manuscript, the Einstein summation convention is used to ease the reading of partial derivative equations. When a sub-index (here i or j) is twice or more repeated in the same equation, one sums across the n-dimensions considered. The mass conservation equation states that no mass is created nor absorbed in a compressible reacting flow. Any local changes in the density are caused by non zero mass fluxes.

In the context of reacting gaseous flows, one must also provide equations for the mass fractions Y^{k} of the species involved in the chemical kinetic scheme:

$$\frac{\partial \rho Y^{\mathrm{k}}}{\partial t} + \frac{\partial \rho u_i Y^{\mathrm{k}}}{\partial x_{\mathrm{i}}} = -\frac{\partial \rho V_{\mathrm{k,i}} Y^{\mathrm{k}}}{\partial x_{\mathrm{i}}} + \omega_{\mathrm{k}} \tag{1.2.2}$$

The RHS terms are the diffusive fluxes characterized by the diffusion velocity: $V_{\mathrm{k,i}}$ and the chemical consumption/production: ω_{k}. There are various models to describe the diffusion velocities, among them, the Hirschfelder and Curtiss approximation provides quantitative results [72]. The equations of the species $k \in [1 \quad N_{\mathrm{spec}}]$ may be summed to retrieve the mass equation as:

$$\sum_{\mathrm{k=1}}^{\mathrm{N_{spec}}} \nu_{\mathrm{k}} Y_{\mathrm{k}} = 0 \ , \ \sum_{\mathrm{k=1}}^{\mathrm{N_{spec}}} Y_{\mathrm{k}} = 1 \text{ and } \sum_{\mathrm{k=1}}^{\mathrm{N_{spec}}} \omega_{\mathrm{k}} = 0 \tag{1.2.3}$$

1.2.2 Conservation of momentum

$$\frac{\partial \rho u_{\mathrm{i}}}{\partial t} + \frac{\partial \rho u_{\mathrm{i}} u_{\mathrm{j}}}{\partial x_{\mathrm{j}}} = -\frac{\partial p}{\partial x_{\mathrm{i}}} + \frac{\partial \tau_{\mathrm{ij}}}{\partial x_{\mathrm{j}}} \ , \ i \in [1 \quad n_{\mathrm{dim}}] \tag{1.2.4}$$

The momentum equation 1.2.4 links the variation of momentum with pressure and the deviatoric stress tensor. This equation is left unchanged in the case of reacting flows. However, combustion influences the velocity field by altering the density between burnt and un-burnt gases and by modifying the local viscosity, which increases with temperature.

1.2.3 Conservation of energy

The conservation of energy may be expressed into multiple forms. For the sake of clarity, only the conservation equation of the sensible energy e_{s} is presented here:

$$\frac{\partial \rho e_{\mathrm{s}}}{\partial t} + \frac{\partial \rho u_{\mathrm{i}} e_{\mathrm{s}}}{\partial x_{\mathrm{i}}} = \underset{1}{\omega_T} + \underbrace{\frac{\partial}{\partial x_{\mathrm{i}}}\left(\lambda \frac{\partial T}{\partial x_{\mathrm{i}}}\right)}_{2} - \underbrace{\frac{\partial}{\partial x_{\mathrm{i}}}\left(\sum_{k=1}^{N} h_{\mathrm{s,k}} Y_{\mathrm{k}} V_{\mathrm{k,i}}\right)}_{3} + \underbrace{\sigma_{\mathrm{ij}} \frac{\partial u_{\mathrm{i}}}{\partial x_{\mathrm{j}}}}_{4} \tag{1.2.5}$$

The RHS of equation 1.2.5 may be decomposed into four different contributing terms. First, there is the heat release term. The second term represents the thermal diffusion and the third, the variation of sensible enthalpy caused by the molecular diffusion of the different species. Finally, term 4 regroups both the dissipation of kinetic energy , which is a source term of the sensible energy and the power of pressure forces as $\sigma_{\mathrm{ij}} = \tau_{\mathrm{ij}} - p$.

The equation for the temperature field can be established from 1.2.5. It will ease the derivation of the acoustic equation:

$$\rho C_{\mathrm{p}} \frac{DT}{Dt} = \omega'_T + \frac{Dp}{Dt} + \frac{\partial}{\partial x_{\mathrm{i}}}\left(\lambda \frac{\partial T}{\partial x_{\mathrm{i}}}\right) - \frac{\partial}{\partial x_{\mathrm{i}}}\left(\sum_{k=1}^{N} C_{\mathrm{p,k}} Y_{\mathrm{k}} V_{\mathrm{k,i}}\right) + \tau_{\mathrm{ij}} \frac{\partial u_{\mathrm{i}}}{\partial x_{\mathrm{j}}} \tag{1.2.6}$$

Here, the term ω'_T, which is also misleadingly called heat release is different from ω_T: $\omega'_T = \omega_T - \sum_{k=1}^{N} h_{\mathrm{sk}} \omega_k$ with h_{sk} and ω_k, the sensible energy and the mass reaction rate of species k respectively.

1.3 Acoustic equations

Several work have been devoted to provide equation for the propagation of acoustic waves in reacting flows. Among them, the study of Bailly et al [73] clearly differentiates the *direct* noise, which is induced by combustion, and the *indirect* noise, which is caused by acceleration of entropy.

1.3.1 General acoustic equation

The acoustic equations for reacting flows can be derived from the Navier-Stokes equations. It is convenient to derive an equation for the logarithm of the pressure and then, to linearize it. After combining equations 1.2.1, 1.2.4, 1.2.6 and the ideal gas relation $p = \rho r T$, one obtains the following wave equation:

$$\begin{aligned} &\left(\frac{c_0^2}{\gamma}\ \ln(p)\right) - \frac{D}{Dt}\left(\frac{1}{\gamma}\frac{D}{Dt}\ln(p)\right) = \\ &\left(\frac{1}{\rho}\ \ .\tau\right) - \frac{D}{Dt}\ \ \frac{D}{Dt}\ln(r)\ \ - \frac{\partial u_\mathrm{i}}{\partial x_\mathrm{j}}\frac{\partial u_\mathrm{i}}{\partial x_\mathrm{j}} \\ -\frac{D}{Dt}\ \ \omega_T' + \frac{\partial}{\partial x_\mathrm{i}}&\left(\lambda\frac{\partial T}{\partial x_\mathrm{i}}\right) - \frac{\partial}{\partial x_\mathrm{i}}\left(\sum_{k=1}^{N} C_{\mathrm{p,k}} Y_\mathrm{k} V_\mathrm{k,i}\right) + \tau_\mathrm{ij}\frac{\partial u_\mathrm{i}}{\partial x_\mathrm{j}} \end{aligned} \tag{1.3.1}$$

where . is the divergence operator and c_0 is the local sound speed: $c_0^2 = \gamma p/\rho = \gamma \mathrm{r} T$. The LHS of equation 1.3.1 exhibits a propagating behavior. Indeed, by neglecting the convective derivatives of the pressure field and assuming constant sound speed and heat capacities, it reduces to: $c_0^2 \Delta ln(p) - \partial^2 ln(p)/\partial t^2$. Moreover, sink and source terms are present in the RHS. Establishing an exhaustive description of all these terms is out of the scope of this chapter. Even so, three key mechanisms are identified:

- **Flame/Acoustic coupling**
  The coupling between acoustic waves and unsteady heat release rate is the key mechanism leading to thermo-acoustic instabilities. When heat release rate is in phase with acoustic pressure, it produces acoustic energy [4].
  In the following of the manuscript, the flame is supposed to be compact: the length of the region in which the heat release rate ω_T takes non negligible values is small compared to typical acoustic wavelengths. Indeed, most of the longitudinal combustion instabilities occur below $f_{\max} = 1\ kHz$ in common burners. The corresponding wavelength is $\lambda = c_0/f$ $0.5\ m$ with $c_0 \approx 500\ m.s^{-1}$ and a typical scale for a flame is a few centimeters.

- **Natural acoustic energy dissipation**
  Acoustic energy dissipation is observed, even when the mean flow is at rest. The corresponding diffusive mechanisms are the dissipation caused by viscosity, which damps the acoustic waves and laminar dissipation in acoustic boundary layers [74, 16]. These dissipative mechanisms lead to linear damping of the acoustic waves. Similarly to the pressure losses in a constant cross section channel, these losses are proportional to the length of the combustion chambers and plenum walls.

  This linear source term of dissipation increases with frequency and is thus most of the time negligible in combustion chambers subject to low frequency thermo-acoustic instabilities.

- **Hydrodynamics/Acoustic coupling** Finally the last mechanism is about the interaction between acoustic waves and vortex eddies. The later are often encountered when the geometry experiences a sudden change of cross section, such as in diaphragms, backward and upward facing steps and even swirlers. The mechanism leading to acoustic energy dissipation was accurately described by Howe [20] , who predicted a linear damping of the acoustic waves, as long as their amplitude remained small when compared to the mean flow. This mechanism presents some similarities with the singular pressure loss phenomena. These effects will be scrutinized in the second part of the manuscript.

1.3.2 Linearised low-Mach acoustic equation

Equation 1.3.1 is very general, as derived without particular assumptions but it is still too complex to be used for the derivation of ROM. Some assumptions can be introduced to derive a simpler acoustic equation:

Low Mach acoustic assumptions

- **H1** Low-speed mean flow.
  The mean flow is supposed to be at rest: $\bar{u} = 0 \implies M = 0$. This condition is quasi fulfilled in combustion chambers as the mean Mach number often remains below $M \quad 0.1$.
- **H2** Identical molecular weights for all species.
  In air/methane combustion, the flow is mainly composed of nitrogen, which is barely involved in the chemical reactions. As a consequence, this assumption only concerns the remaining species which represent a small part of the total mixture.
- **H3** Constant heat capacity
  The variation of the heat capacity of the mixture with temperature is neglected. It also implies that the ratio of specific heat capacities γ is constant.
- **H4** Viscous and diffusive terms are negligible.
  These terms are negligible when compared to the heat release rate.

Under H1 assumption, all total derivatives can be identified with temporal derivatives. After combining all these assumptions, the following simplified equation is obtained:

$$.(c_0^2 \quad \ln(p)) - \frac{\partial^2}{\partial t^2} \ln p = -\frac{\partial}{\partial t}\left(\frac{1}{\rho C_{\mathrm{p}} T}\omega_{\mathrm{T}}\right) \tag{1.3.2}$$

This equation may now be linearized. Let s first decompose the flow field into mean and fluctuating parts:

$$p = \bar{p} + p' \tag{1.3.3}$$
$$\rho = = \bar{\rho} + \rho' \tag{1.3.4}$$
$$\mathbf{u} = \mathbf{u}' \tag{1.3.5}$$

where it is explicitly assumed that there is no mean flow. One finally obtains the acoustic pressure equation for low-Mach reacting flows:

$$.(c_0^2 \quad p') - \frac{\partial^2}{\partial t^2} p' = -(\gamma - 1)\frac{\partial \omega_{\mathrm{T}}}{\partial t} \tag{1.3.6}$$

The LHS of equation 1.3.6 is similar to the one obtained in non-reacting flows. However, the sound speed field $c_0 = \overline{\gamma r T}$ is non uniform due to the presence of hot burnt gases. A typical ratio of sound speed between burnt and un-burnt mixtures is $c_0^{\mathrm{b}}/c_0^{\mathrm{u}} = \overline{T^{\mathrm{b}}/T^{\mathrm{u}}} \approx 2.5$ with $T^{\mathrm{u}} = 300$ K and $T^{\mathrm{b}} = 1900$ K, the adiabatic flame temperature for methane/air premixed combustion at $\phi = 0.75$.

This equation has been derived under the zero mean flow assumption. On the one hand, this assumption is not very restrictive concerning the free propagation of acoustic wave. For instance, an example detailed in section 1.4.2 shows that the frequency of a longitudinal mode is only modified by the factor $1 - M^2$ in the presence of a mean flow. In most combustion chambers, and especially the ones encountered in this manuscript, mean flows remains below $M \quad 0.1$ so that the impact on the frequencies is below 1%.
On the other hand, the coupling between the mean flow and acoustic waves also produces acoustic dissipation as recalled in section 1.3.1. This effect should be taken into account in thermo-acoustic studies as it alters the stability of a system [75]. A methodology dedicated to take into account the dissipation of acoustic energy caused by the interaction with eddies will be briefly introduced in section 1.5.2 and detailed in the second part of this manuscript. This method allows to introduce acoustic dissipation, even under the zero-Mach assumption.

1.4 Helmholtz equation

Equation 1.3.6 is a linear, partial differential equation for the acoustic pressure field. As stated in the previous section, a combustion chamber may be split into several simpler components in which there is no flame. Flames are modeled using Flame Transfer Functions (FTF) (see section 1.5.1). The homogeneous acoustic equation is now investigated.

1.4.1 Homogeneous Helmholtz equation

The equation for the acoustic pressure field in the non reacting regions reduces to d Alembert s formula:

$$.(c_0^2 \quad p') - \frac{\partial^2}{\partial t^2} p' = 0 \tag{1.4.1}$$

The general method to solve this equation is to first transpose it into the frequency domain and to identify the acoustic modes ω_{k}, p_k by solving the corresponding eigenvalue problem. The temporal evolution of an initial solution p'_0 is then retrieved by decomposing it into the basis formed by the acoustic modes, for which the temporal evolution is known. The acoustic equation written in the frequency domain is known as the homogeneous Helmholtz equation:

$$.(c_0^2 \quad p) + \omega^2 p = 0 \tag{1.4.2}$$

where the solution p is a complex acoustic pressure field defined in the frequency domain:

$$p'_k = \Re \quad p_k e^{-i\omega_{\mathrm{k}} t} \tag{1.4.3}$$

This temporal convention will be kept throughout the manuscript. Results obtained with this temporal evolution can be compared with results obtained with the $\exp(i\omega_{\mathrm{k}} t)$ convention by applying the conjugate operator.

Once the acoustic pressure modes are obtained, it is possible to retrieve the corresponding acoustic velocity modes u_k by using the linearized momentum equation:

$$i\bar{\rho}\omega u_{\mathrm{i}} + \frac{\partial p}{\partial x_{\mathrm{i}}} = 0 \tag{1.4.4}$$

The contribution of unsteady heat release can be taken into account by using the linearized energy equation, combined with the ideal gas relation:

$$\frac{i\omega}{\gamma\bar{p}}p + \frac{\partial u_{\mathrm{i}}}{\partial x_{\mathrm{i}}} = \frac{\gamma-1}{\gamma\bar{p}}\omega_{\mathrm{T}} \tag{1.4.5}$$

Most combustion chambers may be decomposed into one-dimensional components, for which the acoustic equations can be resolved. The solution of both velocity and pressure acoustic one-dimensional fields are harmonic waves:

$$p(z) = a^{+}e^{i\omega/c_0 z} + a^{-}e^{-i\omega/c_0 z} \tag{1.4.6}$$

$$u(z) = \underbrace{a^{+}e^{i\omega/c_0 z}}_{\mathrm{A}} - \underbrace{a^{-}e^{-i\omega/c_0 z}}_{\mathrm{A}} \frac{1}{\rho_0 c} \tag{1.4.7}$$

where a^{+} and a^{-} are the complex Riemann invariants associated with the downstream and upstream acoustic waves respectively. The propagation of acoustic waves in a one dimensional channel can be synthesised into a two-port matrix called the propagation matrix R, which links the complex acoustic waves amplitudes entering the channel to those leaving it:

$$\begin{pmatrix} A^{+} \\ A^{-} \end{pmatrix}_{\mathrm{z=L}} = \underbrace{\begin{pmatrix} e^{i\omega/c_0 L} & 0 \\ 0 & e^{-i\omega/c_0 L} \end{pmatrix}}_{\mathrm{R(L)}} \begin{pmatrix} A^{+} \\ A^{-} \end{pmatrix}_{\mathrm{z=0}} \tag{1.4.8}$$

To determine these unknowns, one must prescribe additional equations for the boundary conditions (inlet or outlet) but also for the interfaces (flame front or acoustic dampers).

1.4.2 Boundary conditions required for the acoustic network equations

The boundary conditions can be characterized by a complex, frequency dependent, reflection coefficient which links the amplitude of entering and reflected acoustic waves.

In the remainder of the manuscript, all reflection coefficients are defined by the ratio of the reflected wave amplitude divided by the incident wave amplitude. This ensures that for passive boundaries, the modulus of the reflection coefficient remains below unity: $R \quad 1$.
For instance, its definition is $R = A^{-}/A^{+}$ for the outlet represented in Fig. 1.2. When the outlet an opened atmosphere, the pressure is roughly imposed so that $p = 0$. As a consequence, $R_{\mathrm{outlet}} = -1$. This result is only a first order approximation of an outlet acoustic boundary condition. Indeed, it does not take into account end tube corrections nor acoustic fluxes. These effects will be addressed in chapter 4. Similarly, the velocity is imposed for a chocked nozzle or even a closed outlet (the mixture leaves the burner by a lateral channel) so that $R_{\mathrm{outlet}} = 1$.

Velocity nodes are also often used for the inlet: $R = A^{+}/A^{-} = 1$. As for the outlet, this constitutes a first order approximation.

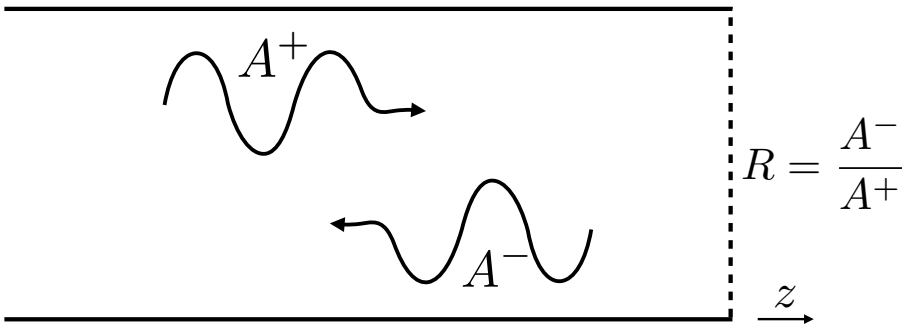

Figure 1.2: Definition of the acoustic reflection coefficient

It is now possible to find the acoustic modes of a simple cavity closed by two boundary conditions. After combining equation 1.4.8 with both inlet and outlet reflection coefficients, one obtains:

$$\frac{A^+_{z=L}}{A^-_{z=0}} \begin{pmatrix} 1 \\ R_{\text{outlet}} \end{pmatrix} = \mathrm{R} \begin{pmatrix} R_{\text{inlet}} \\ 1 \end{pmatrix} \tag{1.4.9}$$

which can only be verified when the vectors from the RHS and LHS are collinear. This can be assessed by using the determinant of the matrix formed by both vectors:

$$\det \left(\mathrm{R} \begin{pmatrix} R_{\text{inlet}} \\ 1 \end{pmatrix}, \begin{pmatrix} 1 \\ R_{\text{outlet}} \end{pmatrix} \right) = 0 \tag{1.4.10}$$

In the case of the 1D channel, equation 1.4.10 reduces to:

$$e^{2i\omega L/c_0} R_{\text{inlet}} R_{\text{outlet}} = 1 \tag{1.4.11}$$

which is an analytic equation of the complex variable $\omega = \omega_r + i\omega_i$. Prior to solving it, one may notice that in the case of non fully reflective boundary conditions: $R_{\text{inlet}} R_{\text{outlet}} \quad 1$ so that $e^{-2\omega_i L/c_0} \quad 1$. Consequently, the imaginary part of the angular frequency ω_i must be negative and the acoustic modes are stable[1].
In the symmetrical case where velocity nodes are imposed at both the inlet and outlet $R_{\text{inlet}} = 1$, $R_{\text{outlet}} = 1$, the following acoustic modes are identified:

$$f_{\mathrm{k}} = k \frac{c_0}{2L} \ , \ k \in \mathbb{N} \tag{1.4.12}$$

For a 1 m long channel fed by air under atmospheric conditions ($c_0 = 350\ m.s^{-1}$), the first acoustic modes are at: 175, 350 and 525 Hz respectively.

The frequency of the first mode can be retrieved by a flight time analysis: a mode is obtained when an acoustic wave propagates from the beginning of the channel to the end and comes back. This takes a time $t = 2L/c_0$ so that $f = 1/t = c_0/(2L)$.
The same analysis can be employed for a channel with an uniform mean flow $\bar{u}$. In the frame of the flow, the acoustic equation derived in the previous section is still valid but the boundary conditions are moving at the speed $-\bar{u}$. The acoustic wave will then take a time $t_1 = L/(c_0 + \bar{u})$ to travel from the beginning of the tube to the end and a time $t_2 = L/(c_0 - \bar{u})$ to go back to the beginning of the tube. The corresponding frequency is:

$$f = \frac{1}{t_1 + t_2} = \frac{1}{\frac{L}{c_0+\bar{u}} + \frac{L}{c_0-\bar{u}}} = \frac{c_0^2 - \bar{u}^2}{2Lc_0} = \frac{c_0}{2L}(1 - M^2) \tag{1.4.13}$$

[1]The temporal evolution of the acoustic mode follows $\exp(-i\omega_r t)\exp(\omega_i t)$

where $M = \bar{u}/c_0$ is the Mach number. The frequency correction for a channel with a non zero mean flow is proportional to M^2 and thus negligible in most combustion chambers. This is true for the real part of the frequency: the growth rate (imaginary part of f) is much more sensitive to M [75].

1.5 Coupling with Flame and Hydrodynamics

As stated in section 1.3.1, flame zones and dissipative regions (multi-perforated plates, diaphragm, ...) occur in compact regions and can be usually described by continuity equations, synthesized into two-port matrices where acoustic wavelengths are large compared to all other characteristic sizes.

1.5.1 Flame Transfer Function (FTF) to model flames

The coupling between flame and acoustic waves is contained in the heat release rate term. Integrating equations 1.4.4 and 1.4.5 leads to the following set of continuity equations [76, 77]:

$$[Su]_{\mathrm{u}}^{\mathrm{d}} = \frac{\gamma-1}{\gamma\bar{p}}\Omega_T \text{ with } \Omega_T = \int_V \omega_{\mathrm{T}} dV \tag{1.5.1}$$

$$[p]_{\mathrm{u}}^{\mathrm{d}} = 0 \tag{1.5.2}$$

where S, is the cross section of the channel. The subscripts d and u refer to upstream and downstream quantities respectively. The acoustic pressure p is constant across the interface while the acoustic volume flux Su experiences a discontinuity caused by the unsteady heat release.

A model for the heat release rate must be provided to close Equation 1.5.1. This can be achieved by using a FTF, which links the heat release rate to the upstream acoustic velocity perturbation:

$$\mathrm{FTF}(\omega) = \frac{\Omega_T/\overline{\Omega}_T}{u/\bar{u}} \tag{1.5.3}$$

where u is measured upstream of the flame holder. The concept of FTF has been introduced by Crocco [78] and is still widely used to study thermo-acoustic instabilities. This transfer function can be measured experimentally (see for instance [79, 52]), numerically [80, 71] or even modeled [81].

For example, the FTF of the Intrig burner is displayed in Fig. 1.3. It has been obtained in DNS by using a Wiener filtering approach [82]. FTF are also functions of the operating conditions: equivalence ratio [83], bulk velocity, heat losses [84, 52] at the walls[2]. The latter effect will be scrutinized in the third part of the manuscript. The gain of the FTF is represented in Fig. 1.3, left. It starts from unity at low frequencies because in the quasi steady regime (zero frequency), a change $u/\bar{u}$ must lead to the same change for $\Omega_T/\overline{\Omega}_T$ as Ω_T is linear in u [85]. It peaks up to 2.5 at $f = 70\ Hz$ and slowly decreases to zero until $f = 400\ Hz$. The phase of the FTF (Fig. 1.3, right) linearly increases up to 400 Hz and then saturates. The linear part of the phase can be approximated by $\phi = \omega\tau$, in which $\tau = 35\ ms$ can be seen as a flame delay.

The FTF (equation 1.5.3) can be introduced into the continuity equation of acoustic velocity (equation 1.5.1):

$$[Su]_{\mathrm{u}}^{\mathrm{d}} = \overline{\Omega}_T \frac{\gamma-1}{\gamma\bar{p}\bar{u}} \mathrm{FTF}(\omega) u_{\mathrm{u}} \tag{1.5.4}$$

[2]FTFs depend also o the amplitude of forcing [6], an effect which will be discussed later.

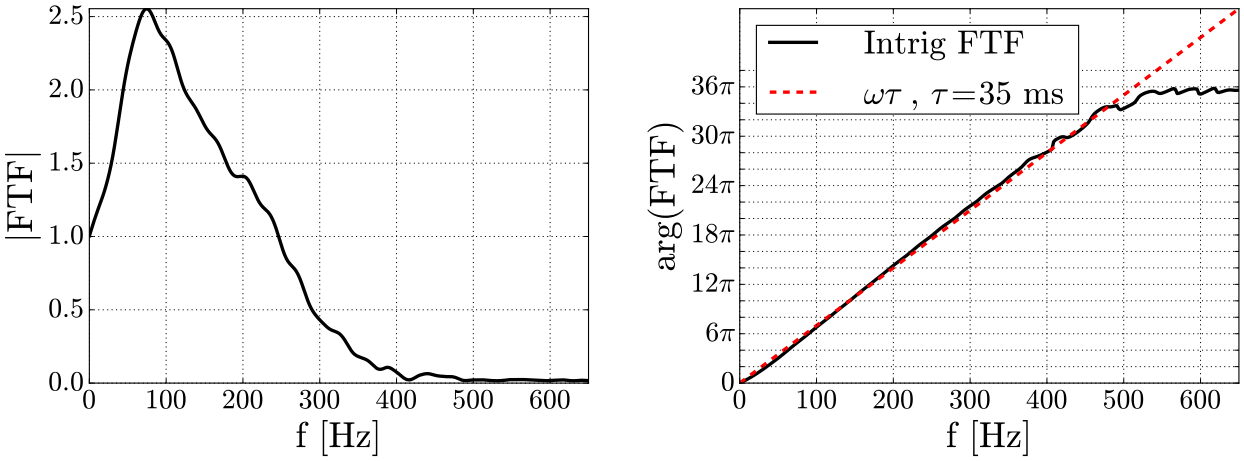

Figure 1.3: FTF of the INTRIG burner obtained by DNS. The operating regime is described in chapter 8. This long flame exhibits large gains for frequencies below 200 Hz and a high flame delays of $\tau = 35\ ms$.

This expression may be simplified after noticing that $\bar{\Omega}_T = \bar{\rho}\bar{u}S_{\text{inlet}}C_{\text{p}}\Delta T$. Consequently, Equation 1.5.4 reduces to:

$$u_{\text{d}}\frac{S_{\text{d}}}{S_{\text{u}}} = u_{\text{u}}\underbrace{\left(1 + \frac{\Delta T}{T}\text{FTF}(\omega)\right)}_{\text{g}(\omega)} \tag{1.5.5}$$

Without the flame contribution ($\text{FTF}(\omega) = 0$), one retrieves the classical continuity equation for the acoustic velocity: the acoustic volume flux is conserved at the interface between burnt and un-burnt gases (see [86, 77] for a complete analysis of this jump condition). Moreover, the explicit reference to the bulk velocity $\bar{u}$, which is supposed to be zero in the low-Mach assumption, disappears from equation 1.5.5. Finally, this continuity equation may be rewritten in the two-port formalism [80, 87]:

$$\begin{pmatrix} A^+ \\ A^- \end{pmatrix}_{\text{d}} = \underbrace{\begin{pmatrix} 1+\Gamma g & 1-\Gamma g \\ 1-\Gamma g & 1+\Gamma g \end{pmatrix}}_{\text{F}(\omega)} \begin{pmatrix} A^+ \\ A^- \end{pmatrix}_{\text{u}} \tag{1.5.6}$$

where Γ is the ratio of the cross sections multiplied by the inverse ratio of the impedances: $\Gamma = (S_{\text{u}}\bar{\rho}_{\text{d}}c_{0,\text{d}})/(S_{\text{d}}\bar{\rho}_{\text{u}}c_{0,\text{u}})$. The matrix $\text{F}(\omega)$ is called the transfer matrix of the flame and accounts for the changes in cross section, impedance and for the flame/acoustic coupling.

1.5.2 Acoustic/vortex eddies two-port representation

The dissipation of acoustic energy caused by the interaction of acoustic waves with vortex eddies can also be described by two-port matrices. These transfer matrices can be obtained theoretically [88, 21] or by numerical [23] or experimental measurements [21]. Some models for perforated plates and diaphragms are recalled in Chapter 3 while an experimental method to measure the transfer matrix of a diaphragm and a swirl injector is described in Chapter 5.

The two port matrix can be defined by its inputs and outputs:

$$\begin{pmatrix} A^+ \\ A^- \end{pmatrix}_{\text{d}} = \text{T}_{\text{wave}}(\omega, \bar{u}) \begin{pmatrix} A^+ \\ A^- \end{pmatrix}_{\text{u}} \tag{1.5.7}$$

where $\mathrm{T}(\omega, \bar{u})$ is the transfer matrix of the compact acoustic element. The dependency to the mean flow velocity $\bar{u}$ is explicitly written in the transfer matrix in order to recall that it couples acoustic waves with vortex eddies.

1.6 Reduced Order Model (ROM)

1.6.1 Derivation of the ROM

ROM are obtained by combining the two-port matrices of sections 1.4, 1.5.1 and 1.5.2 and applying the boundary conditions described in section 1.4.2.
Such models can be established for linear acoustic networks[3]. An example of simplified laminar burner is provided to illustrate the methodology. This burner contains a multi-perforated plate located in the plenum and a flame is attached at the rim of a back-ward facing step. The geometry is described in Fig. 1.4. It can be decomposed into four components, called C_i, $\mathrm{i} \in [1, 4]$, linked by appropriate transfer matrices.

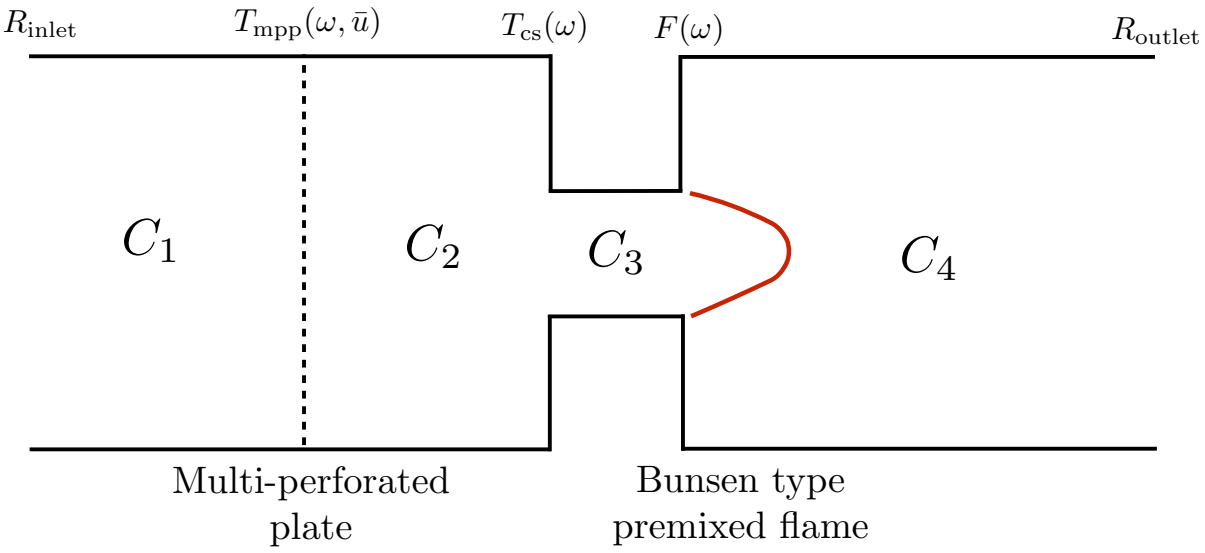

Figure 1.4: Geometry used to illustrate the methodology. It is constituted by four channels, linked by three transfer matrices and closed by two boundary conditions

The procedure applied in section 1.4.2 to construct the characteristic equation of a single channel can be generalized to linear acoustic networks:

$$\det\left(\prod_{\mathrm{i=N}}^{1}(\mathrm{R_i T_i})(\omega)\begin{pmatrix} R_{\mathrm{inlet}} \\ 1 \end{pmatrix}, \begin{pmatrix} 1 \\ R_{\mathrm{outlet}} \end{pmatrix}\right) = 0 \tag{1.6.1}$$

where the first transfer matrix is equal to identity: $\mathrm{T}_1 = \mathrm{Id}$. Equation 1.6.1 is a complex, analytical equation of the angular pulsation $\omega \in \mathbb{C}$. In our example, the product of the rotational and transfer matrices reduces to:

$$\prod_{\mathrm{i=N}}^{1}(\mathrm{R_i T_i})(\omega) = \mathrm{R_4 F}(\omega)\mathrm{R_3 T_{cs}}(\omega)\mathrm{R_2 T_{mpp}}(\omega, \bar{u})\mathrm{R_1} \tag{1.6.2}$$

[3]Here, linear refers to the topology of the acoustic network, on which each interfaces link two channels or less.

The case of non-linear acoustic network with ramifications has been addressed by Parmentier et al [56]. In this study, the ROM of a combustor constituted by an annular combustion chamber fed with multiple injectors is derived. Acoustic boundary conditions are needed at the intakes of the injectors and a periodic boundary condition is applied on the annular chamber. Mathematically, the corresponding characteristic equation reduces to the determinant of the product of two-port matrices.

In a recent study, Bauerheim et al [57] extended this model by adding an annular plenum to the latter configuration. The topology of the acoustic network changed as it now contains loops. In this case, the characteristic equation contained products of four-ports matrices.

Establishing a general theory of acoustic network in the field of thermo-acoustic is out of the scope of this manuscript. However, the reader interested in this topic is refered to the interesting study of Glav et al [53].

1.6.2 Resolution of the ROM equation

The solutions of the ROM are the complex angular frequencies of the acoustic modes. These roots (ω_k) provide two different kinds of information:

- $\Re\omega_k$: The real part of the root provides the angular frequency of the acoustic mode. Once the fundamental frequency of the burner is known, it is possible to design specific dampers, efficient in a narrow frequency band, which help to stabilize the system.

- $\Im\omega_k$: The imaginary part of the angular frequency is linked to the linear stability of the acoustic mode. A negative value means that the mode is exponentially decreasing while a positive value means that the mode is linearly unstable.

However, any information concerning limit cycles cannot be provided by the resolution of the characteristic equation. Indeed, these limit cycles are reached because of the non linearities occurring in the combustion chambers. Among them, the non-linearities observed in the flame response are of primary importance [70].

Starting from the compressible, reacting Navier-Stokes equations, many simplifying assumptions have been proposed to derive equation 1.6.1. However, solving this non-linear analytic equation is not an easy task. Two different methods are often employed:

- **Analytical resolution**
  In order to solve analytically equation 1.6.1, one must introduce other simplifying assumptions such as a low coupling between the flame and the acoustic: $\mathrm{FTF}(\omega) \quad 1$ and study only simplified geometries. Examples of analytical resolution under these additional assumptions are provided in [11] and [56].

- **Numerical resolution**
  Here, a numerical method is employed to solve equation 1.6.1. One major drawback of this method is that the explicit dependency of the solution with the key parameters of the problem is lost. However, this knowledge can be retrieved by performing parametric or even Uncertainty Quantification (UQ) studies, which both help to understand the relation between the acoustic modes of a combustion chamber and the relevant parameters.

The numerical resolution method will be employed in the following of the manuscript. In previous studies, authors have developed various methods to solve ROM numerically. Among them, the most used is the Newton-Raphson (NR) method[4] [89]. This method works fast to find one

[4]When the derivative of the function is not available, this method is replaced by the secant method.

solution of equation 1.6.1 but is not adapted when all solutions must be enclosed and their number is unknown. An example to illustrate this point is provided in section 1.6.3 while a better algorithm is presented in chapter 2 to solve equations like 1.6.1.

1.6.3 Application to the INTRIG burner ROM

In this section, we derive a simplified[5] ROM for the INTRIG burner, which uses a premixed methane/air flame under a laminar regime. This experimental rig will be presented in details in chapter 6. It is constituted by a plenum, a cylindrical flame holder, which is small enough not to reflect the acoustic waves and a combustion chamber. The whole burner has a constant cross section.

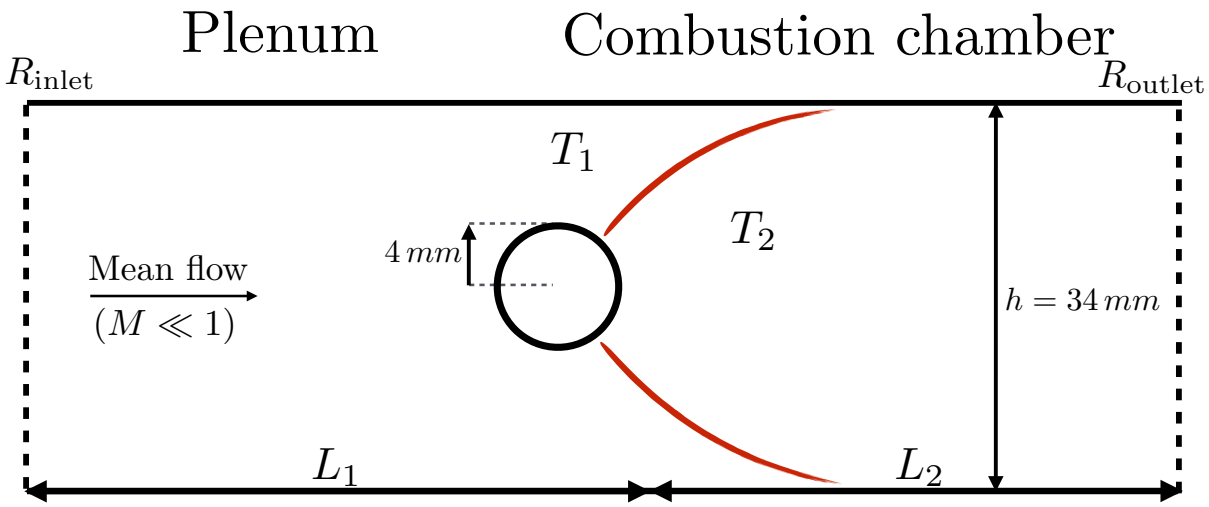

Figure 1.5: Idealized geometry of the Intrig burner. The lengths of both plenum and combustion chamber can be adapted. Here, $L_1 = 0.3\ m$ and $L_2 = 0.16\ m$.

For the sake of simplicity, a simple ROM is derived without sources of acoustic losses and with fully reflective boundary conditions: $R_{\text{inlet}} = 1$ (imposed velocity) and $R_{\text{outlet}} = -1$ (imposed pressure). Moreover, we use the extension of the $n - \tau$ model provided by Crocco [78] for the FTF:

$$\text{FTF}(\omega) = ne^{i\omega\tau} \tag{1.6.3}$$

where n is a constant interaction index[6] set to unity (low frequency limit of FTF) and the delay τ is the characteristic convective time associated with the length of the flame. In the case of the INTRIG burner, it is set to $\tau = 35\ ms$.

After splitting the geometry in two components, of respective temperature and sound speed (T_1, c_1) and (T_2, c_2), one obtains the following ROM:

$$\det\left(\text{R}_2(L_1)F_{T_1,T_2}(n,\tau)\text{R}_1(L_2)\begin{pmatrix}R_{\text{inlet}}\\1\end{pmatrix},\begin{pmatrix}1\\R_{\text{outlet}}\end{pmatrix}\right) = 0 \tag{1.6.4}$$

This scalar analytical equation can be further simplified after substituting the two-port matrices

[5] A more accurate ROM will be established in chapter 9.

[6] The interaction index n corresponds to the N_3 term in [90]

by their expressions:

$$f_0(\omega) = a(\omega) + \Gamma b(\omega) = 0 \tag{1.6.5}$$
$$\text{where} \quad \begin{array}{l} a(\omega) = \left(1 + e^{i\alpha\omega}\right)\left(\left(1 + e^{i\beta\omega}\right)\right. \\ b(\omega) = \left(1 - e^{i\alpha\omega}\right)\left(1 - e^{i\beta\omega}\right)\left(1 + ne^{i\omega\tau}\right) \end{array}$$

with $\alpha = 2L_1/c_1$, $\beta = 2L_2/c_2$ and $\Gamma = \overline{T_1/T_2} = 0.4$. The values of all remaining parameters are recalled in Table 1.1.

$L_1\ [m]$	$c_1\ [m.s^{-1}]$	$L_2\ [m]$	$c_2\ [m.s^{-1}]$	$n\ []$	$\tau\ [ms]$
0.3	348	0.16	877	1	35

Table 1.1: Set of parameters used in equation 1.6.5.

As stated in section 1.6.2, this equation cannot be solved analytically and contains many solutions for frequencies between 0 and 400 Hz (exactly 15 as shown in chapter 2). One easy way to solve it is to use the NR method with a random multi-guess strategy. The difficulty of the exercise with the NR method is the choice of the initial values from which the iterative process starts for each roots. The most naive approach is to use random values to try to cover all possible states and avoid covering only a limited subspace of the complex plane. This can require using many initial guesses. The corresponding algorithm called A_{NR}, is decomposed in three steps and is sightly smarter than using one set of random numbers. Here, two independent sets of initial seeds a_i and b_i are generated to search for the roots of equation 1.6.1:

A_{NR} algorithm

1. Two series a_i and b_i of n_{rnd} complex random guesses are generated.
2. The NR method is applied on both series to output two distinct ensembles of solutions: Sa_i, $i \in [1, N_{\text{a}}]$ and Sb_j, $j \in [1, N_{\text{b}}]$ where N_{a} and N_{b} are the number of distinct solutions found for both series.
3. N_{sol} solutions are extracted by combining the two series of results. Moreover, as the two series are independent, it is possible to estimate the total number of solutions: $N_{\text{est}} = N_{\text{a}}N_{\text{b}}/N_{\text{a,b}}$ where $N_{\text{a,b}}$ is the number solutions found in both series.

The last result can be simply explained in the case where all roots are distinct. Let s suppose that the total number of solution is N and that the probability to find a root z is $P(z) = 1/N$ is equal for each roots. The probability that the root z is contained in the first set of solutions is $P(z \in Sa) = N_a/N$ and $P(z \in Sb) = N_b/N$ for the second set.

In addition, the probability that a root z is present in both sets Sa and Sb is given by

$$\begin{array}{ccc} P(z \in Sa \quad Sb) = P(z \in Sa) & P(z \in Sb) \\ \dfrac{N_{a,b}}{N} = \dfrac{N_a}{N} & \dfrac{N_b}{N} \end{array}$$
$$\Rightarrow N_{\text{est}} = \frac{N_a N_b}{N_{a,b}}$$

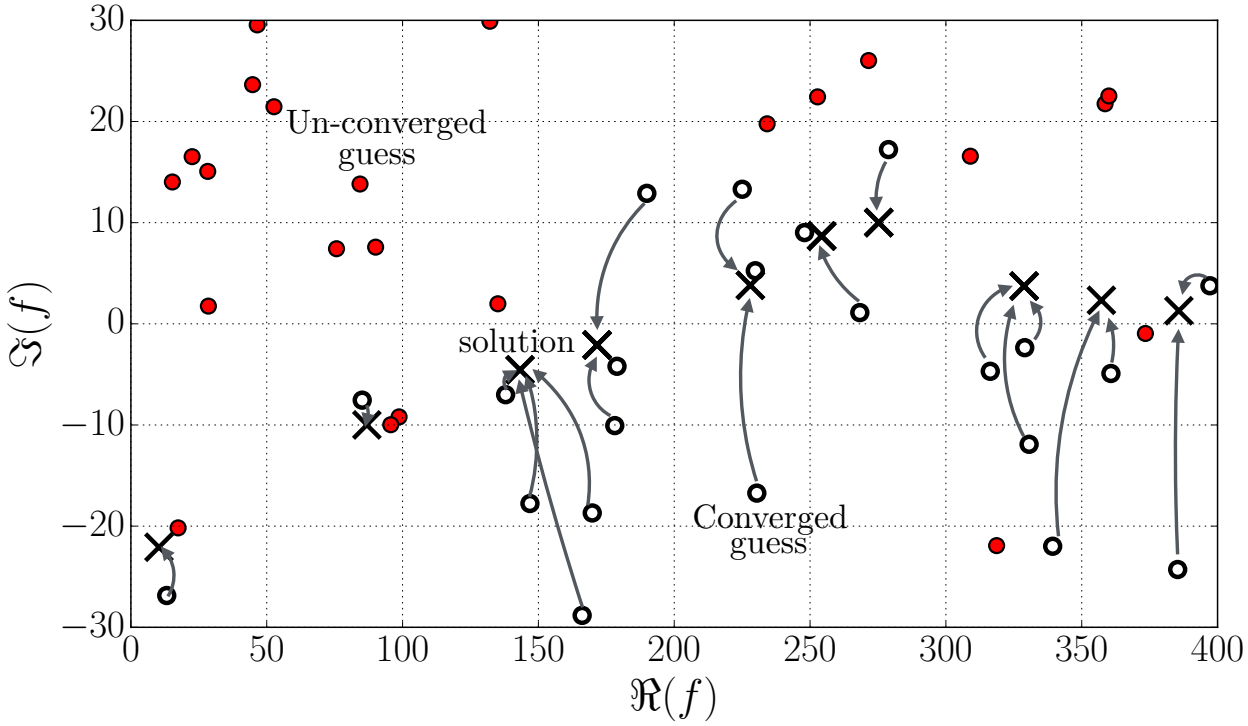

Figure 1.6: Sketch of the A_{NR} algorithm. Multiple NR are started from random guesses and only a few converge

An illustration of the A_{NR} algorithm is provided in Fig. 1.6. Markers with coloured faces represent initial guesses of un-converging NR method. Only ten solutions have been found in this case. The convergence study of the A_{NR} algorithm is shown in tab 1.2: the number of solutions enclosed is displayed as a function of n_{rnd}, the size of the series of guesses. The results presented here have been averaged over 100 samples to get rid of stochastic fluctuations.

n_{rnd}	5	10	20	40	80	120	160	200
N_{sol}	3.9	6.4	10.0	12.7	14.3	14.7	14.8	15.0
RMS	1.2	1.7	1.6	1.3	0.73	0.5	0.4	0.2
n_{est}	89	60	13.5	14.3	14.6	14.9	14.9	15.0
n_{calls}	210	420	810	1700	3400	5100	6700	8300

Table 1.2: Synthesized results of A_{NR} algorithm applied to the INTRIG ROM

The results gathered in tab 1.2 show that there are probably 15 roots of equation 1.6.5 lying in the domain of research $f \in [0, 400] + i[-30, 30]$ but that it takes at least 120 initial guesses and 5100 calls to the calculation of $f(\omega)$ to isolate these roots. A closer look to the data provides quantitative information: first, the estimation of the number of solutions N_{est} converges faster than the number of solutions N_{sol} itself. This guaranties that all solutions are most probably enclosed when both values are equals. Second, the number of enclosed distinct roots converges slowly. At least two series of 120 random guesses are needed to enclose the 15 roots of the problem with a sufficiently small spread (the RMS is below 0.5). This represents a total of 5100 calls (in average) to the function f_0.

The 15 solutions are represented in Fig. 1.7. According to the resolution of the INTRIG ROM, thermo-acoustic instabilities are expected closed to 280 Hz. A detailed physical interpretation

of these solutions is out of the scope of this chapter and will be carried out in chapter 8.

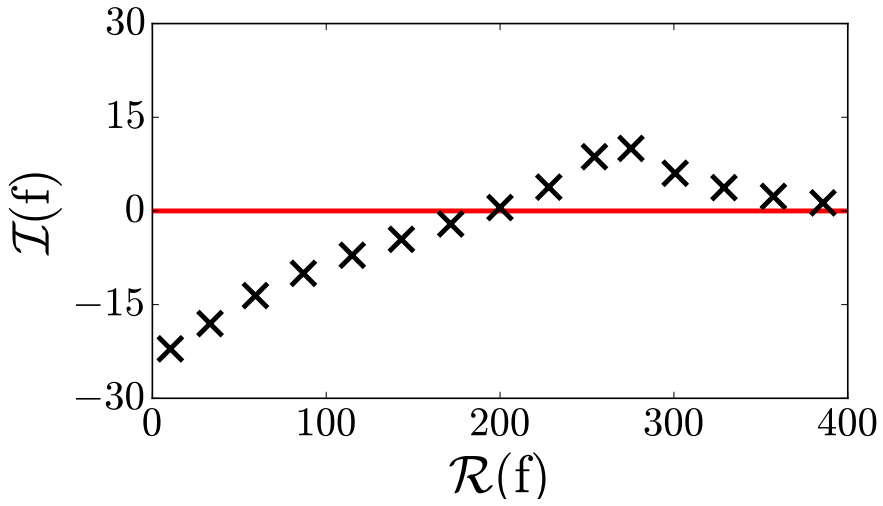

Figure 1.7: Acoustic modes of the INTRIG ROM. Imaginary (damping/growth rate) versus real part (frequency).

1.7 Conclusion

In this chapter, we have detailed the methodology to derive Reduced-Order Models (ROM). Such models are very helpful to predict thermo-acoustic instabilities. Indeed, they allow the user to interact directly with them: no need for long computational time nor meshing. However, such ROM must be fed by accurate models for the coupling of acoustic waves with both the flame and the mean flow field. This coupling can be taken into account by the mean of two-port matrices. Finally, we showed that in most of the cases, these models cannot be solved analytically. The naive numerical algorithm A_{NR}, based on the Newton-Raphson method, exhibited poor convergence properties. Even though this is not a major issue for ROM, it is a problem for 3D Helmholtz solvers like AVSP [70, 91] or Comsol[92] where calling the function $f(\omega)$ means solving a very large linear system, something which can become very expensive. Strategies to optimize this search are therefore critical [93].

A new algorithm (A_{RL}) dedicated to the resolution of the ROM complex equation will be presented in chapter 2. Contrary to the stochastic method introduced here (A_{NR}), its convergence is fast and mathematically proved.

Chapter 2

An optimal adaptive methodology for the resolution of the ROM equation

A new algorithm (A_{RL}), intended to enclose the roots of thermo-acoustic characteristic equations more efficiently is reported in this chapter. It can solve numerically, in a robust and efficient way, the various existing ROM equations. Most of the former thermo-acoustic studies relied on simple algorithms such as the Newton-Raphson method (see chapter 1 and the A_{NR} algorithm), to find the complex-valued frequencies of the acoustic modes one by one, or Nyquist diagram analysis to predict stability. However, the method described here, based on the argument principle, is built specifically to retrieve all the solutions of a ROM. Several solvers based on this principle have already been reported [94, 95, 96] and exhibited robust properties. However, they all suffered from expensive computational costs. Here, the A_{RL} algorithm comes with two major improvements. First, after a short comparison with previous solvers, the best ideas of each are gathered in the A_{NR} solver so that the computational cost is lowered. Second, a new method is employed to enclose multiple zeros (whatever the order of multiplicity) at a negligible cost. Finally, the implementation of the A_{RL} algorithm exhibits very good performance in term of computational time when compared to other algorithms found in the literature.

Introduction

In chapter 1, we derived a simple ROM for the INTRIG burner and showed that algorithms only based on Newton-Raphson (NR) methods may be used to find some solutions of equation 1.6.5 (Hopefully, all of them). However, the whole set of solutions must be computed to assess the stability of the thermo-acoustic system.

It can be seen that equation 1.6.5 is highly non-linear since it involves multiple exponentials terms. Moreover, f_0 derives from a certain class of functions of the complex variable z or ω that are called *meromorphic functions*, for which the numbers and values of the poles and zeros can be obtained with contour integrals. In the following, we will restrict our target to the case of *holomorphic functions*, a restriction of meromorphic functions for which there is no pole in the entire domain of interest. This assumption holds for all the ROM equations presented in this manuscript. However, in the case of a function containing some poles, the domain of research can be adapted to exclude them as done in [97]. This restriction also implies that all models or fit used in ROM such as flame transfer functions or transfer matrices coefficients are also holomorphic.

The objective of this study is to find the roots of a given analytic function $f \quad \mathbb{C} \to \mathbb{C}$ in a

bounded domain of the complex plane. To solve this problem, an efficient and robust algorithm has been designed and implemented with success. The backbone of the algorithm stems from a generalized version of *Cauchy's argument principle*, as first described by Delves and Lyness [94, 59]. This theorem is used recursively throughout an adaptive multilevel subdivision strategy, the challenge being to find a satisfactory compromise between robustness and computational efficiency.

Algorithms based on the principle argument have been detailed and implemented more recently by Dellnitz [95]. Johnson et al [96, 97] proposed two implementations which used validated integral computations. However, theses methods, albeit mathematically rigorous, happen to be computationally intensive. Other families of algorithm that do not rely explicitly on *Cauchy's argument principle* have been developed. Suzuki et al [98] proposed a method which relies on the Numerical Integration Error Method derivation. Ko et al [99] first designed a method to compute the topological degree of a mapping in $\mathbb{R}^2$ and then applied these results to analytic functions in $\mathbb{C}$. Kopitz et al [54] resolved thermo-acoustic ROM by using the Nyquist criterion, which stems from Cauchy s argument principle. Finally, Semenov[100] described a method which only work with non multiple zeros. The A_{RL} algorithm combines some of the advantages of the previous solvers, in addition to some new extensions dedicated to enhance its robustness and rapidity.

In section 2.1, we recall the theoretical background associated with analytic functions, and state the generalized *Cauchy's argument principle*. The algorithm is detailed in section 2.2. Sections 2.3 and 2.4 elaborate on the particular implementation of the algorithm. Section 2.5 displays results and comparison with other solvers in terms of accuracy, robustness and efficiency on both standard performance benchmarks and thermo-acoustic ROM. Finally, a parametric study concerning the INTRIG burner is realized (section 2.6).

2.1 Theoretical context

The resolution of a characteristic equation in a compact subset $\mathbf{U}$ of the complex plane like equation 1.6.5 is equivalent to the following problem:

$$z \in \mathbf{U} \quad f(z) = 0 \tag{2.1.1}$$

2.1.1 Cauchy's argument principle

The argument principle, based on an integration over a closed contour $\partial\mathbf{U}$, allows to retrieve the number of roots of a holomorphic function contained within $\partial\mathbf{U}$. Let $f \quad z \in \mathbf{U} \to f(z) \in \mathbb{C}$ be a holomorphic, non constant function and $\mathbf{U} \in \mathbb{C}$ is defined by its closed contour $\partial\mathbf{U}$. As f is analytical within $\mathbf{U}$, it is equal to its Taylor series [1]:

$$f(z) = \sum_{k=0}^{\infty} a_k z^k \,,\; z \in \mathbf{U} \tag{2.1.2}$$

which can be recast into a product form:

$$f(z) = g(z) \prod_{i=1}^{n} (z - z_i)^{p_i} \tag{2.1.3}$$

[1] This equality is the definition of an analytic function and holds for most usual functions.

where z_i, $i \in [1, n]$ are the zeros of f contained in $\mathbf{U}$, p_i 0 their multiplicity and g $z \in \mathbf{U} \rightarrow g(z) \in \mathbb{C}$ is an holomorphic function containing no zeros in $\mathbf{U}$ nor in $\partial\mathbf{U}$. The ratio between f and its derivative f' is equal to:

$$\frac{f'(z)}{f(z)} = \sum_{i=1}^{n} \frac{p_i}{z - z_i} + \frac{g'(z)}{g(z)} \tag{2.1.4}$$

which can be integrated over the closed contour $\partial\mathbf{U}$:

$$\frac{1}{2\pi i} \oint_{\partial\mathbf{U}} \frac{f'(z)}{f(z)} dz = \sum_{i=1}^{n} \frac{1}{2\pi i} \oint_{\partial\mathbf{U}} \frac{p_i}{z - z_i} dz + \frac{1}{2\pi i} \oint_{\partial\mathbf{U}} \frac{g'(z)}{g(z)} dz \tag{2.1.5}$$

This expression can be simplified by using both Cauchy s integral theorem (equation 2.1.7) and formula (equation 2.1.7) which are valid for holomorphic functions within $\mathbf{U}$:

$$\frac{1}{2\pi i} \oint_{\partial\mathbf{U}} h(z) dz = 0 \tag{2.1.6}$$

$$\frac{1}{2\pi i} \oint_{\partial\mathbf{U}} \frac{h(z)}{z - a} dz = h(a)\delta(a, \mathbf{U}) \tag{2.1.7}$$

where $\delta(a, \mathbf{U}) = 1$ if a lies inside $\mathbf{U}$, 0 else. The second term of the RHS of equation 2.1.5 is equal to 0 as $g'(z)/g(z)$ is still holomorphic in $\mathbf{U}$. The first term of the RHS is equal to $N_{\text{sol}} = \sum_{i=1}^{n} p_i$. Finally, one obtains the Cauchy s argument principle:

$$I_0(\partial\mathbf{U}) = \frac{1}{2\pi i} \oint_{\partial\mathbf{U}} \frac{f'(z)}{f(z)} dz = N_{\text{sol}} \tag{2.1.8}$$

where N_{sol} is the number of zeros of f contained in $\mathbf{U}$.

If the tested function is only meromorphic, so that is has poles, one gets $I_0(\partial\mathbf{U}) = N_{\text{sol}} - N_{\text{poles}}$ and it is thus not possible to retrieve the number of zeros contained in $\mathbf{U}$.

2.1.2 Extension of the argument principle

Results provided by equation 2.1.8 can help to enclose the roots of holomorphic functions: knowing the number of zeros of f is the first step of an algorithm dedicated to find all the solutions of equation 2.1.1. It is however possible to go further with the generalized argument principle [94, 59]:

$$I_k(\partial\mathbf{U}) = \frac{1}{2i\pi} \oint_{\partial\mathbf{U}} z^k \frac{f'(z)}{f(z)} \mathrm{d}z = s_{\mathrm{k}} \tag{2.1.9}$$

$$s_{\mathrm{k}} = \sum_{i=1}^{n} p_i z_i^k \tag{2.1.10}$$

where z_i, p_i are the zeros of f and their respective multiplicity. With $k = 0$, one retrieves the number of zeros contained in $\mathbf{U}$. The sum of all these roots is obtained for $k = 1$. In the case of a domain $\mathbf{U}$ containing only one root z_1, the latter can be directly extracted as $z_1 = I_1(\partial\mathbf{U})$. In the general case, once the number of zeros contained within $\partial\mathbf{U}$ is known, it is possible to construct an equivalent polynomial $Q_{\mathrm{N}}(z)$ of order $N = N_{\text{sol}}$ which coefficients q_k are directly linked with the power sums s_{k} so that the zeros of Q_{N} correspond to the zeros of f contained in $\mathbf{U}$ [94]. The method used to obtain such a polynomial is detailed in section 2.1.3.

2.1.3 Construction of the equivalent polynomial

Newton s Identities provide the link between the power sums s_k and the corresponding equivalent polynomial Q_N [101] :

$$Q_N(z) = \sum_{j=0}^{N} (-1)^j e_j z^{N-j} \tag{2.1.11}$$

$$\text{with } e_0 = 1\,,\; e_{k\ 0} = \frac{1}{k}\sum_{j=1}^{k} (-1)^{j+1} e_{k-j} s_j$$

The polynomial Q_N is constructed to share the same roots as f in $\mathbf{U}$. Analytical methods exist to solve this polynomial up to the fourth order ($N = 4$). In the $N = 3$ case, the following equivalent polynomial is obtained:

$$Q_3(z) = z^3 - s_1 z^2 + \frac{s_1^2 - s_2}{2} z - \frac{1}{6}(2s_3 - 3s_1 s_2 + s_1^3) \tag{2.1.12}$$

2.2 Algorithm description

The A_{RL} algorithm dedicated to compute all the solutions of equation 2.1.1 within a closed subset $\mathbf{U}$ $\mathbb{C}$ is now detailed. An example is then provided to illustrate its behaviour.

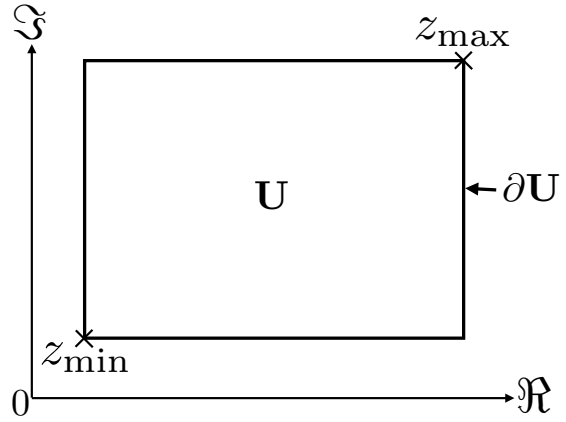

Figure 2.1: Initial mesh $\mathbf{U}$ $\mathbb{C}$ defined by Z_{min}, Z_{max}.

The domain $\mathbf{U}$, which has a rectangular shape, is defined by:

$$\begin{aligned} \mathbf{U} = \{z \in \mathbb{C} \,|\, \{&\Re(Z_{min}) \quad \Re(z) \quad \Re(Z_{max})\,, \\ &\Im(Z_{min}) \quad \Im(z) \quad \Im(Z_{max})\} \end{aligned} \tag{2.2.1}$$

This domain, shown in Fig. 2.1, is called the initial mesh and its contour is called $\partial\mathbf{U}_{mesh}$. The A_{RL} algorithm is applied recursively to compute all the solutions of equation 2.1.1: the number of root is identified with the Cauchy s argument and the problem is locally recast into an equivalent polynomial resolution.

A_{RL} algorithm

1. Generalized Cauchy s argument principle (equation 2.1.9) is used to compute both the number of roots N ($k = 0$) which are contained in the current mesh and the corresponding power sums ($k > 0$). If a root is located too close to the boundary $\partial\mathbf{U}_{\mathrm{mesh}}$, all the adjacent meshes are reshaped. This procedure is detailed in section 2.3. Once the number of root is known, the problem is reformulated in term of an equivalent polynomial, which maximal order is limited to $N_{\max}$.

2. **If** $N = 0$
   There are no roots in this mesh, nothing to be done.

   If $1 \quad N \quad N_{\max}$
   The solutions are obtained in three steps:

   (a) The equivalent polynomial Q_{N} is constructed according to Eq. 2.1.11.

   (b) The equivalent polynomial Q_{N} is solved with an appropriate analytical method. The roots of Q_{N} are only approximations of the roots of f as its coefficients are provided by non exact, numerical integration.

   (c) Starting from the roots of the equivalent polynomial, the NR algorithm is applied to compute the zeros of f with a better accuracy. All zeros are finally strictly checked with an integral computation : this procedure is described in the appendix A.

   If $N > N_{\max}$
   The existence of a single root of multiplicity N is first checked (see section 2.3). If not found, the mesh is split in two sub-meshes and the procedure described in step 1 is applied on both of them.

3. If the refinement reaches a user-defined size $\mathbf{L} = |Z_{\max}(\mathbf{U}_{\mathrm{mesh}}) - Z_{\min}(\mathbf{U}_{\mathrm{mesh}})| < \epsilon$ and there are still more than $N_{\max}$ roots within this mesh, the refinement is stopped and a single root (of multiplicity N) is extracted and set to $(Z_{\min}(\mathbf{U}_{\mathrm{mesh}}) + Z_{\max}(\mathbf{U}_{\mathrm{mesh}}))/2$.

To illustrate this algorithm, an example is described in Fig. 2.2. Here, the maximum equivalent polynomial order is set to $N_{\max} = 2$ for the sake of clarity. During the first step, four solutions are found in the initial mesh M_1. As $4 > N_{\max}$, the latter is split in two sub-meshes: M_3 on the left and M_2 on the right. Only one root is found in M_2 and is enclosed by first, the resolution of the first order equivalent polynomial and then by an additional use of the NR method. Meanwhile, M_3 still contains $3 > N_{\max}$ roots and must be split. At step 3, a root lies exactly on the boundary so that the computations of the number of solutions failed in both lower and upper sub-meshes. As a consequence, both of them are reshaped. Finally, two solutions are extracted from the upper mesh M_4 by solving the equivalent polynomial and one is extracted from the lower mesh M_5.

2.3 Strategies of domain splitting and reshaping

When $N > N_{\max}$ in a given mesh, a two-step checking procedure is performed to decide whether a single root of multiplicity N is located in it or not. Assuming a zero z_{N} of multiplicity N in equation 2.1.10 leads to

$$s_2 - \frac{s_1^2}{N} = N z_{\mathrm{N}}^2 - \frac{(N z_{\mathrm{N}})^2}{N} = 0 \tag{2.3.1}$$

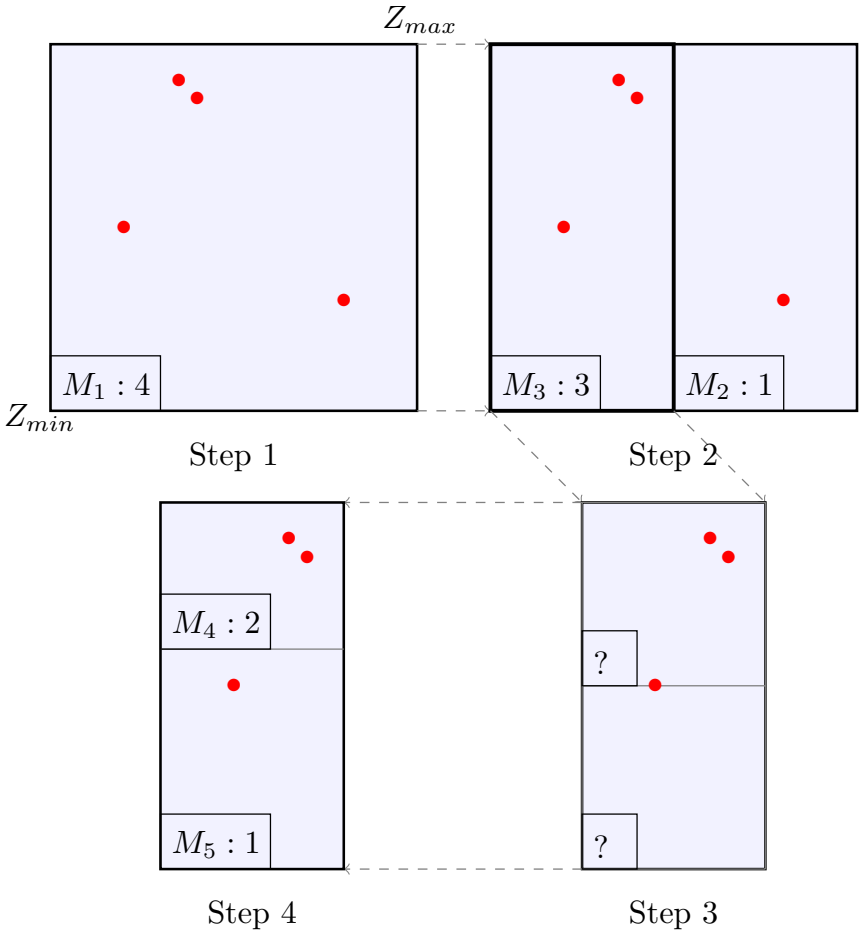

Figure 2.2: Illustration of the algorithm used to find the solutions of equation $f(z) = 0$. Step 1: initial domain of research. Step 2: creation of the sub-meshes. Step 3: problem of convergence for both lower and upper sub-meshes. Step 4 : sub-meshes are reshaped.

As s_1 and s_2 are not computed exactly, the following condition is tested to detect the existence of a multiple root:

$$d = |\frac{s_2}{N} - \left(\frac{s_1}{N}\right)^2|^{\frac{1}{2}} < 0.001 L_{\text{mesh}} \tag{2.3.2}$$

As long as s_1 and s_2 are known with a sufficient precision, equation 2.3.2 should be verified for a single root of multiplicity N. However, this criterion is not sufficient to ensure the existence of the single root as it may be fulfilled with distinct roots too. For instance, the three single roots of equation $z^3 - 1 = 0$: $\{1\,,\, e^{i2\pi/3}\,,\, e^{i4\pi/3}\}$, lead to $s_1 = 0$ and $s_2 = 0$ so that $d = 0 < 0.001 L_{\text{mesh}}$.

In the second step, an approximation of the root is provided by $z_{\text{N}} = s_1/N$. The NR method applied to the function $f^{1/N}$, starting from this guess. In case of convergence, the existence of the single root is proved with contour integration.

If the two-step checking procedure fails, the mesh is split as it contains too many distinct roots. Various mesh shapes have been used in previous studies: rectangles [96, 99], triangles [97] or even circles [94], for which there is overlapping. The rectangular shape was preferred in this study (Fig. 2.2). Meshes can be split along the real or the imaginary axis. Here, a simple solution is retained: the mesh is cut in its larger dimension as done in [96]. Once split into two sub-meshes, some roots may lie too close to

the shared boundary. Such situations are identified by performing a new contour integration:

$$I_\infty(\partial\mathbf{U}) = \frac{1}{2\pi i}\oint_{\partial\mathbf{U}} \frac{f'(z)}{f(z)}\,\mathrm{d}z \tag{2.3.3}$$

which numerically diverges if a root of whatever multiplicity is located within the boundary. In the vicinity of the root z_i of multiplitiy p_i, equation 2.1.4 shows that f'/f is equivalent to:

$$\frac{f'}{f}(z) \approx \frac{p_i}{|z - z_i|} \tag{2.3.4}$$

which is not integrable on paths containing z_i [2]. Except for the initial domain, specified by the user, these roots are always located on the common boundary of the two meshes issued from the last split. If divergence occurs in the initial mesh, a domain sightly larger is used instead and only the roots contained in the initial domain are kept. If the divergence occurs in a sub-mesh, the shared boundary is translated and a new computation is performed. An example is given in Fig. 2.2 between steps 3 and 4.

2.4 Numerical scheme used for the computation of the generalized argument principle

The computation of the generalized argument principle requires $4N_{\max}$ integrations for each mesh. Each integral requires a line integration in the complex plane:

$$\Gamma_k = \frac{1}{2i\pi}\int_{z_1}^{z_2} g_k(z)\mathrm{d}z\,,\ 0 \quad k \quad N_{\max} \tag{2.4.1}$$
$$g_k(z) = z^k \frac{f'(z)}{f(z)}$$

All Γ_k integrals on the same path $\mathbf{P} = [z_1 \to z_2]$ are computed simultaneously to avoid redundant calls to f and its derivative. Three integration schemes have been implemented in this study. The first one, called the Modified Romberg scheme (MR), is an adaptive scheme based on a fourth order approximation of the derivative f'. The two others are the well known Romberg scheme (R) and Adaptive Simpson scheme (AS), which both require automated differentiation for f'. All these schemes must return a result with a controlled accuracy $\Gamma_{\mathrm{err}} < 1/8$ in order to estimate properly $I_0(\partial\mathbf{U})$. In practice, a criteria of $\Gamma_{\mathrm{err}} = 0.01$ was preferred as the integration error is only estimated.

2.4.1 Modified Romberg scheme (MR)

To avoid the use of automatic differentiation, the MR scheme, derived from the Romberg adaptive [102, 95] scheme was implemented and tested. The composite Simpson s rule is first applied with $n = 2$ initial subintervals to compute $\Gamma^{\mathrm{MR}}_{k,2}$. The same rule is then applied recursively with twice more subintervals at each iteration to compute $\Gamma^{\mathrm{MR}}_{k,2^i}$. At each step $i > 1$, the integration error is approximated by $\Gamma_{\mathrm{err}} = |\Gamma^{\mathrm{MR}}_{k,2^i} - \Gamma^{\mathrm{MR}}_{k,2^i\ 1}|$ and the computation stops when it is sufficiently low. All the g_k computed during step i are reused at step $i+1$ so that the function f is called as few as possible.

In order to compute $g_k(z) = z^k \frac{f'(z)}{f(z)}$, a fourth-order finite difference centred stencil is used to evaluate $f'(z)$ so that additional calls to f are needed to compute the derivatives at the extremities of the path $\mathbf{P}$. However, this overhead only add two additional calls to f during each iteration as shown in figure 2.3.

[2] This complex integral can be recast into $\int_{-1}^{1} |t|^{-1} dt$ which do not converge

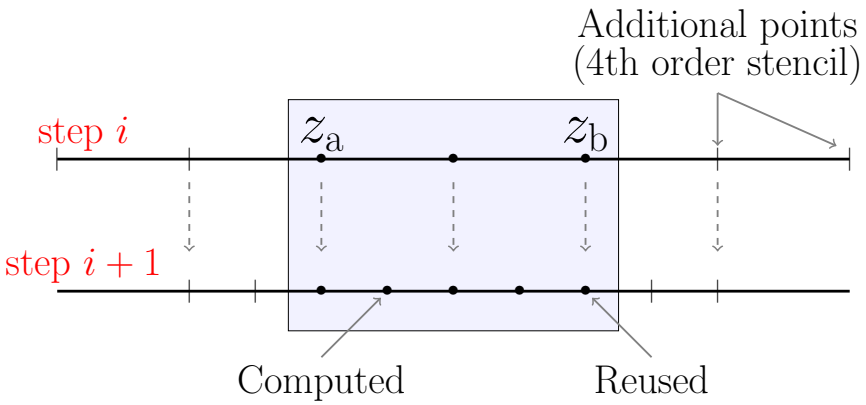

Figure 2.3: Illustration of the MR scheme of integration. During step $i+1$, values computed from step i are reused. Additional values are computed to compute the derivative with a fourth order finite difference centred stencil.

2.4.2 Romberg scheme with automated differentiation (R)

The R scheme [102] has been implemented and tested. By using automated differentiation, the $g_k(z_i)$ are exactly computed so that truncation errors are avoided. Contrary to the MR scheme which was limited to fourth order accuracy, the R scheme s order of accuracy is increasing with the number of iterations. This scheme provides better performance than the MR scheme when the function f is simple. However, it may become slower when the extra computational time necessary to compute the derivative of f increases.

2.4.3 Adaptive Simpson Scheme with automated differentiation (AS)

Finally, the AS scheme [96] was also tested. In this scheme, the fourth order Simpson rule of integration is applied in any subdivision $\mathbf{P}_{\mathrm{ab}}$ of the original path. These subdivisions are split in two parts: $\{\mathbf{P}_{\mathrm{ac}}, \mathbf{P}_{\mathrm{cb}}\}$, only when more precision is needed according to the following relation [103]:

$$|\Gamma_0^{\mathrm{AS}}(\mathbf{P}_{\mathrm{ac}}) + \Gamma_0^{\mathrm{AS}}(\mathbf{P}_{\mathrm{cb}}) - \Gamma_0^{\mathrm{AS}}(\mathbf{P}_{\mathrm{ab}})| > 15\frac{\Gamma_{\mathrm{err}}}{2^{\mathrm{Nsplit}}} \tag{2.4.2}$$

where $1/2^{\mathrm{Nsplit}}$ refers to the relative length of the newly created subdivision compared to the original path. An illustration of this adaptive integration scheme is depicted in Fig. 2.4.

For performance purposes, the convergence criteria is only checked for $k = 0$ as only the computation of the number of roots in a mesh must be carried out in a safe manner. Finally, a global fifth-order of accuracy is obtained by combining the last two results obtained for each subdivisions. This scheme exhibits very good performance when compared to MR and R schemes as less calls to f are needed to provide the same precision. Indeed, far from the zeros of f, the g_k functions are rather smooth so that a uniform refinement as proposed in both R and MR schemes is not well suited. A quantitative comparison of all schemes is given in section 2.5.

2.5 Numerical results

The implementation of the A_{RL} algorithm has been realized in Java, into a program called RootLocker. The ANTLR library [104] is used to translate the equation $f(z) = 0$ proposed by the user into Java code which is then dynamically compiled and loaded by the Java virtual machine. This technique has

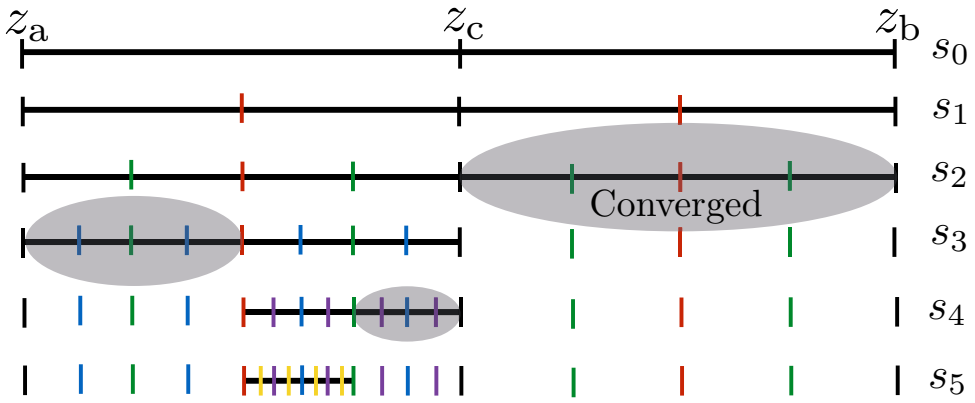

Figure 2.4: Illustration of the AS scheme of integration. All subdivisions are converged after step s_5 so that function f has been called 21 times

several advantages. It first simplifies the implementation of the forward mode automatic differentiation [105] by using the source code transformation technique. Moreover, it allows faster computation by using only native Java code to describe the function f and its derivative. Finally, this procedure is transparent for the user, who only needs to describe the function f.

In the following part of this section, a few examples illustrating the improvement realized in terms of accuracy and performance compared to previous solvers are detailed. Example 1 is taken from [96], example 2 is adapted from [99] and example 3 is taken from [97]. The last example focus on a thermo-acoustic model proposed in [57]. Examples 1, 2 and 3 were all carried out with $N_{\max} = 3$ while the influence of this parameter is studied in example 4. In all cases, two performance measurements are provided. First, the total number of calls to the function f is monitored. However, these data are not always available in all the reference papers for the first three examples and thus, cannot be compared. As a consequence, both the number of meshes and the computational time measured on a macbook air 2013 are provided (these data are available in the aforementioned references).

2.5.1 Academic cases

The first two examples concern complex polynomial equations.
Example 1:

$$f_1(z) = z^{11} - a \quad , \quad a = \frac{1}{2} + i\frac{\sqrt{3}}{2} \tag{2.5.1}$$

This polynomial has exactly 11 zeros which are uniformely distributed on the unit circle as shown in Fig. 2.5. The computation was conducted in the initial domain $\mathbf{U} = [Z_{\min} = -3 - 3i, Z_{\max} = 3 + 3i]$ and required 1270 calls to f_1 to compute the roots with seven decimals with the AS scheme. This corresponds to a computational time of $t = 5\ ms$ to be compared with the 40 seconds obtained in [96]. All other schemes of integration provided exactly the same roots, but with a longer computational time.

An other computation was realised with $a = 1$. In this case, one root is located on the real axis thus two sub-meshes needed reshaping (see Fig. 2.5, right). Despite this difficulty, only 1461 calls to $f1$ were needed to compute all the roots (corresponding to a time $t = 6$ ms). Finally, the criterion defined in equation 2.3.2 was verified in the initial mesh for both values of a. Checking that this was not caused by the presence of a single root of multiplicity $N = 11$ only required two additional calls to $f1$ as the NR algorithm diverged rapidly out of the domain.

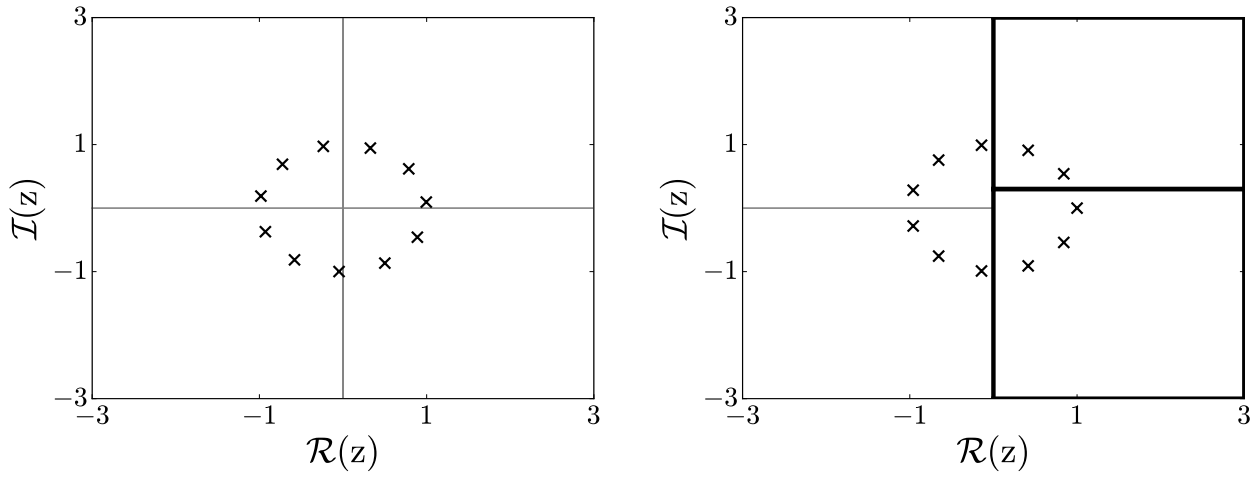

Figure 2.5: Location of the roots of f_1 for $a = 1/2 + i\sqrt{3}/2$ (left) and $a = 1$ (right). Meshes are represented in thin grey lines except for reshaped ones, which are represented in thick black lines.

Example 2:

$$f_2(z) = (z^2 + z + 1)^2(z - 1)^4(z^3 + z^2 + z + 1)^3(z - 2)(z - 4)^4 \tag{2.5.2}$$

This polynomial has exactly 22 roots (see Fig. 2.7), all located in the domain of research defined by $\mathbf{U} = [Z_{\min} = -5 - 5i, Z_{\max} = 5 + 5i]$. This example exhibits fourth order roots which cannot be computed directly with $N_{\max} = 3$. For this reason, they are enclosed thanks to the criteria defined in equation 2.3.2. Finally, 4564 calls to f_2 were needed with the AS scheme. This corresponds to a computational time of $t = 26\ ms$ which may be compared with the 22.7 seconds obtained in [99].

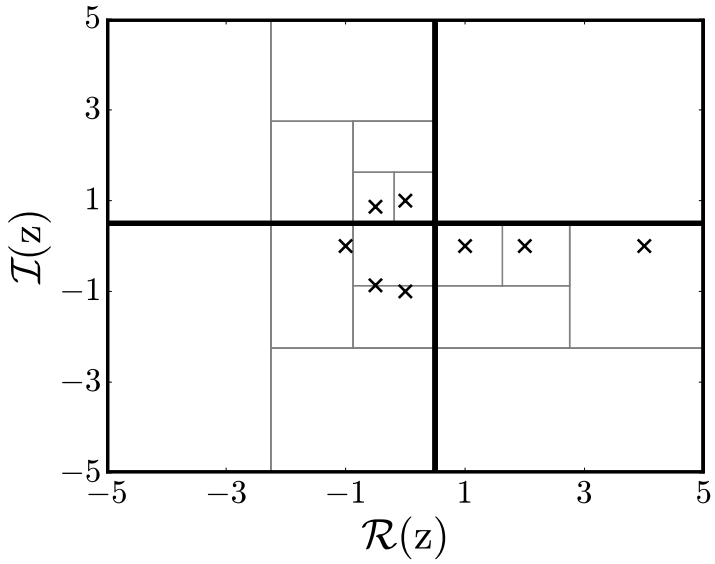

Figure 2.6: Visualisation of the zeros of f_2. Meshes are represented by thin grey lines, except for reshaped ones, which are represented in thick black lines.

2.5.2 Thermoacoustic cases

The two following examples are associated with thermo-acoustic problems formulated by Dellnitz et al [95] and Bauerheim [57].

Example 3:

$$f_3(z) = z^2 + Az + Be^{-Tz} + C \tag{2.5.3}$$

This case concerns the acoustic stability study of a reactive flow in an annular combustion chamber (see [95] for more details), the following set of values is used : $A = -0.19435$, $B = 1000.41$, $C = 522463.0$ and $T = 0.005$. 24 zeros are enclosed in the domain defined by $\mathbf{U} = [Z_{\min} = -5000 - 15000i, Z_{\max} = 5000 + 15000i]$. This computation required 11828 calls to f_3 (AS scheme). This corresponds to approximately 62 ms which can be compared with the 3 seconds obtained in [97] and 83 integrals computations (24 were dedicated to validate the guesses). As a comparison, solving f_3 without the generalized argument principle ($N_{\max} = 0$) required 17588 calls to f_3 and 111 integrals computations.

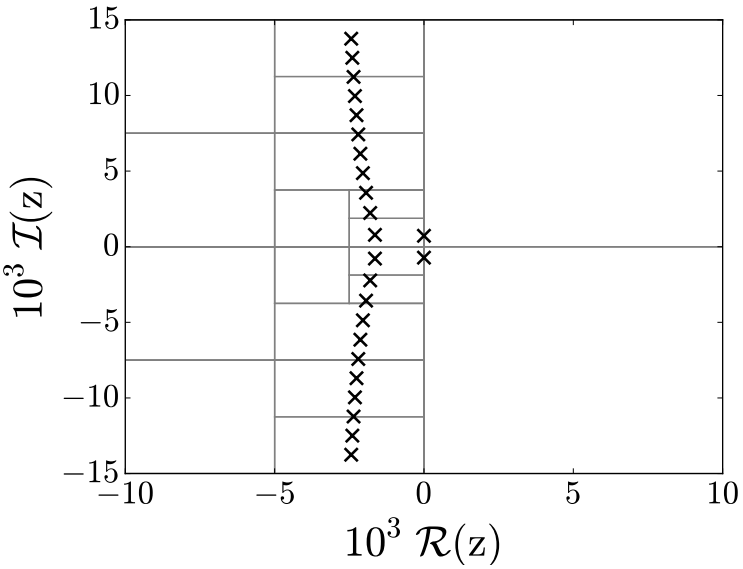

Figure 2.7: Visualisation of the zeros of f_3. Meshes are represented by thin grey lines

Example 4:

The function used in example 4 is proposed by Bauerheim et al [57] and dedicated to predict the thermo-acoustic modes of annular combustion chambers:

$$f_4(z) = \det\left(\prod_{i=4}^{1} \mathrm{R_i}(z)\mathrm{T_i}(z) - \mathrm{Id}\right) \tag{2.5.4}$$

where $\mathrm{R_i}$ designates a four by four rotation matrix and $\mathrm{T_i}$, a four by four transfer matrix which accounts for the flame/acoustic coupling. This model enlightens the ability of RootLocker to deal with realistic characteristic equations. All parameters are described in [57], table 1, except τ, the flame delay, which is set to 5 ms and $n = 1.57$, the interaction index. In symmetrical configurations, when all burners are identical and uniformely distributed around the annular chamber, some acoustic modes are of second multiplicity. Symmetry may be broken by sightly modifying the interaction between the burners and the acoustic [106]. Second order acoustical modes are then split into separate modes. However, the roots of equation 2.5.4 may still stay very close to each other if the asymmetry remains small. In such situations, enclosing several roots from a single mesh without splitting it is very useful.

The domain of interest is defined by $\mathbf{U} = [Z_{\min} = 4-20i\ ,\ Z_{\max} = 70+22i]$ where z $[Hz]$ is the complex valued frequency. In the symmetrical case, one unstable solution is enclosed at $z_1 = 28.17118 + 4.70674i$ and stable solution is found equal to $z_2 = 57.11084 - 0.32660i$ (multiplicity of two). Computational time and number of calls to f_4 are reproduced in table 2.1. The meshes needed to enclose the roots are displayed in Fig. 2.8 for $N_{\max} \in \{0, 1, 2, 3\}$.

Scheme \ $N_{\max}$	0	1	2	3
MR	161996 (5.1s)	132121 (4.1s)	19489 (0.59s)	11153 (0.33s)
R	158015 (7.8s)	157459 (6.8s)	667 (0.03s)	387 (0.02s)
AS	8437 (0.42s)	7972 (0.40s)	406 (0.021s)	241 (0.012s)

Table 2.1: Number of calls to f_4 and associated computational time in the symmetrical case.

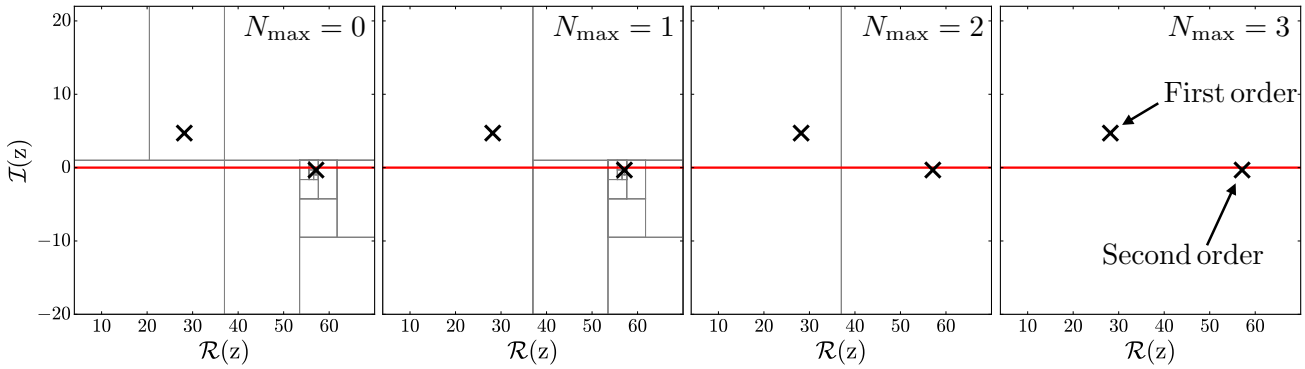

Figure 2.8: Visualisation of the zeros of f_4 in the symmetrical case with the AS scheme. From left to right: $N_{\max} \in \{0, 1, 2, 3\}$.

When $N_{\max} = 0$, contour integrals only provide the number of zeros contained in the meshes. When a mesh contains only one root, it is extracted thanks to the NR algorithm started from the center of the mesh. In the present case, the NR algorithm did not converge and the mesh has been refined two additional times (see Fig. 2.8, $N_{\max} = 0$). When $N_{\max} = 1$, the contour integrals provide a guess to the NR algorithm by solving the one order equivalent polynomial. This guess helps the NR algorithm to converge as the single root was extracted without mesh refinement. However, roots of multiple order are not extracted directly and the concerned meshes are refined until the minimal size is reached. When $N_{\max}$ 2, the complete algorithm is applied with equivalent polynomials of order 2 and 3 respectively as shown in Fig. 2.8.

One can notice that the best results are obtained in the case $N_{\max} = 3$ as fewer meshes are needed to enclose all the roots. When $N_{\max} < 2$, using the R scheme takes a longer time than unsing the MR scheme for an equivalent number of calls to f_4 as it implies the computation of derivatives with automated differentiation. However, when $N_{\max}$ 2, the R scheme performances reach those of the AS scheme. As calls to f_4 are quite expensive, both R and AS schemes exhibit the same amount of calls per second which is roughly equal to 20000 s^{-1} showing that the overhead caused by the algorithm is negligible.

The asymmetrical case is obtained with the following set of interaction indexes: $\{n_1 = 1.55\ ,\ n_2 = 1.6\ ,\ n_3 = 1.54\ ,\ n_4 = 1.59\}$ so that $\bar{n} = 1.57$, all the other parameters being kept unchanged. The following single roots are enclosed: $\{28.17117 + 4.70662i\ ,\ 57.10970 - 0.33192i\ ,\ 57.11195 - 0.32127i\}$. Computational time and number of calls of f_4 are reproduced in table 2.2.

When $N_{\max}$ 2, the numbers of calls to f_4 from both symmetrical and asymmetrical cases are similar. Indeed, enclosing two single solutions instead of a multiple one only implies an additional call to the NR method in this case. The factor 2 between the computational times is justified by the increased complexity of f_4 computations in the asymmetrical case as four different matrices must be assembled instead of one. However, when $N_{\max} < 2$, fewer calls to f_4 are needed to enclose all roots as meshes are not split down to the precision limit as it was the case in the symmetrical case.

The combination AS, $N_{\max} = 3$ always provided the fastest results. For instance, a speed up of

Scheme \ $N_{\max}$	0	1	2	3
MR	132580 (7.1s)	98236 (5.3s)	19673 (1.08s)	11338 (0.69s)
R	75467 (6.7s)	74519 (6.7s)	715 (0.072s)	435 (0.040s)
AS	5392 (0.54s)	4789 (0.51s)	428 (0.045s)	257 (0.026s)

Table 2.2: Number of calls to f_4 and associated computational time in the asymmetrical case.

500 is observed when compared with the worst combination: MR, $N_{\max} = 0$. The presented algorithm can be further improved by increasing $N_{\max}$ up to the number of solutions encountered in the initial domain: $N_{\max} = N$. This can be achieved by solving numerically the equivalent polynomial of order N with an efficient method such as the Jenkins Traub algorithm [107]. However, this procedure is limited by the accuracy of the polynomial coefficients, determined by contour integrals computations which are bounded to discretization errors.

2.6 Parametric study of a laboratory scale combustion chamber

In this section, we use again the example of the INTRIG ROM derived in chapter 1. After taking exactly the same parameters, 15 single roots are finally enclosed to the precision 10^{-5}. This computation costs 640 (+440 for verifications) calls to the function f_0 defined in equation 1.6.5, which is much less than the number of calls needed for the stochastic A_{NR} algorithm presented in chapter 1 (more than 5000 calls for the same precision). These roots are reproduced in Fig. 2.9 and are identical to the ones obtained in chapter 1.

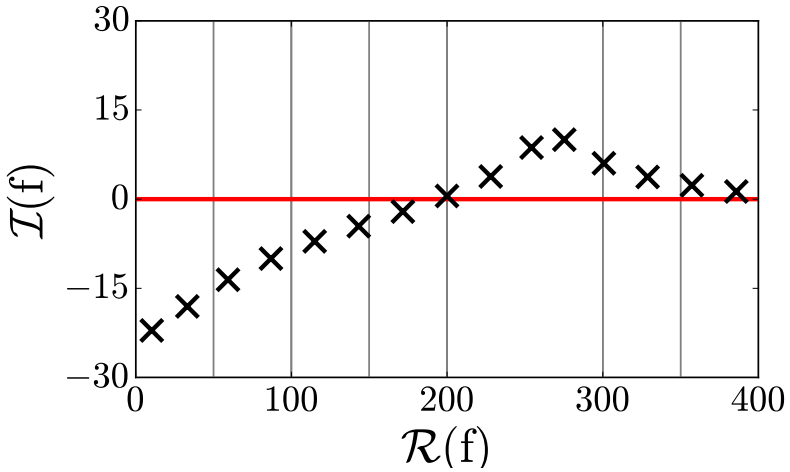

Figure 2.9: Solutions for the INTRIG ROM with un-realistic FTF. The meshes are denoted by thin gray lines

It is now interesting to focus on parametric studies, as they provide information on the acoustic modes of the INTRIG setup. Two kinds of parametric studies can be performed on top of the rootlocker algorithm:

parametric studies

- **Safe parametric mode**:
  In this mode, the A_{RL} algorithm is called for each value of the varied parameter. This ensures that all the solutions are enclosed properly but the cost is proportional to the number of values taken by the parameter.

- **Fast parametric mode**:
  In this mode, the A_{RL} algorithm is only called for the first value of the parameter. The NR method is then called for each successive value, by taking the previous results as initial guesses. This has the major advantage of reducing the cost of the parametric study as all integral computations are removed. However, this method may first fail to capture correctly a mode which crosses an other on the complex plane. Second, it cannot detect new solutions that can appear at the boundary of the domain of research.

In the case of the INTRIG ROM, the A_{RL} algorithm performs very fast so that the safe parametric mode is preferred. The first parametric study concerns the flame delay τ which had been arbitrarily set to 35 ms in chapter 1. This parameter often controls the onset of thermo-acoustic instabilities [79]. It is now varied from 0, which corresponds to a one-dimensional flame approximation up to 50 ms. This study can be performed experimentally by modifying both the equivalence ratio, to variate to flame delay, and the bulk velocity, to maintain the flame shape.

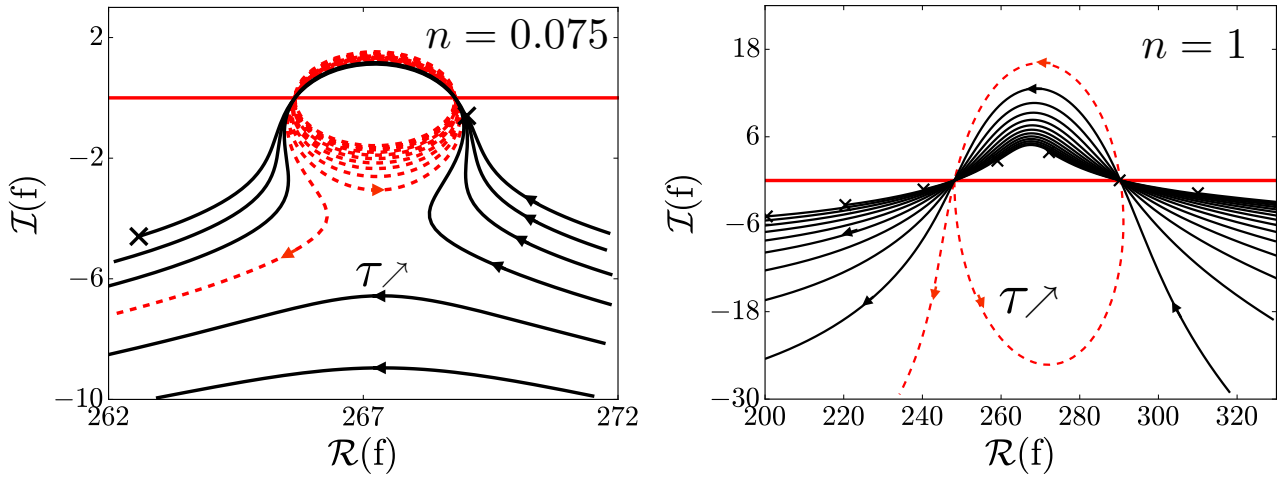

Figure 2.10: Parametric study for the flame delay τ. Studies have been performed with two different interaction index: left $n = 0.075$; right $n = 1$.

In order to study the influence of this parameter, two values for the interaction index are used: $n = 0.075$ and $n = 1$[3]. With the small interaction index, two different kinds of modes are observed. First, there is an acoustic mode which is present even without flame delay (semi-line in Fig. 2.10, left). This mode switches between stable and unstable regimes until $\tau = 40$ ms, when it finally remains stable. This results is coherent with the theoretical stability analysis which can be performed in the low interaction index limit[11]. The other family (thick lines in Fig. 2.10, left) is constituted by the modes which do not exist without flame delay ($\tau = 0$). Some of these modes remain stable, whatever the value of the flame delay. Others are coupled with the first family mode: they exhibit unstable behaviour.

With the interaction index set to unity, the two families of acoustic modes are still observed, but the coupling between them is stronger: the first mode (semi-line in Fig. 2.10, right) stops alternating

[3]Even though values of n larger than unity are sometimes observed, $n = 1$ is a reasonable upper value for parametric studies.

between stable and unstable regimes after only one cycle. For important interaction indices ($n \quad 1$), the stability of the system is not affected by the flame delay anymore: there is always at least one unstable mode close to $f = 270\ Hz$.

The second parametric study concerns the interaction index of the $n - \tau$ model: n, which is varied from zero to unity. The corresponding complex frequencies are displayed in Fig. 2.11. One may notice that only one mode is present when the coupling between the flame and the acoustic waves is removed ($n = 0$). As the interaction index increases, other modes, which are initially under-damped, enter the domain of research and some become unstable. A physical discussion concerning this classification, based on block diagram analysis, is provided in chapter 9.

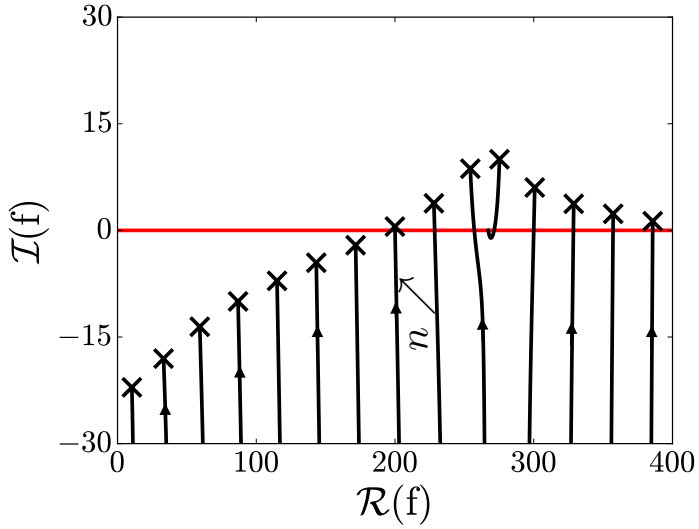

Figure 2.11: Parametric study for the interaction indices $n \in [0, 1]$ in the INTRIG ROM. The lines show the trajectories of the modes when n goes from 0 to 1.

Conclusion

The A_{RL} algorithm dedicated to find all the solutions of a ROM has been detailed and validated. Its Java implementation, called RootLocker, is more efficient than previous solvers based on the principle of the argument. All roots, multiple or distinct, are enclosed with the accuracy prescribed by the user. Among all the variants of the algorithm, the AS scheme of integration, based on the adaptive Simpson scheme, combined with third order ($N_{\max} = 3$) equivalent polynomial resolution, gives the best results in term of computational time (below 0.1 s in all examples) and calls to the function f. This short computational time makes it possible to perform fast but still safe parametric studies. Furthermore, the A_{RL} algorithm used here for the resolution of thermo-acoustic equations is also suitable for other kind of problems implying the resolution of holomorphic equations. Indeed, this method is particularly adapted to solve low-dimension non linear eigen-value problems, or characteristic equations obtained in wave dynamic studies such as hydrodynamics, optics or structure mechanics.

All the resolutions of ROM presented in the following chapters of the manuscript were carried out with the RootLocker tool, which is built upon an intuitive graphical user interface. For instance, it is used in chapter 5, in order to find the acoustic modes of a cavity containing a diaphragm in the presence of a mean flow. The simple ROM of the INTRIG burner presented here as an example permitted to retrieve unstable modes closed to 270 Hz which were observed in the experiments. To go further and provide more quantitative results, a more realistic ROM of the INTRIG burner will be introduced and solved in chapter 8.

Part II

Mechanisms leading to acoustic dissipation

This part is dedicated to provide quantitative data concerning acoustic wave scattering for elements typically encountered in modern combustion chambers such as diaphragm, multi-perforated plates or even swirl injectors. These data are needed as input of ROM or Helmoltz solvers to predict the thermo-acoustic stability with a better accuracy. This part is decomposed into three chapters. In chapter 3, A link is established between acoustic and pressure losses which occur in compact elements. These effects are monitored in an experimental rig called PREINTRIG designed at IMFT. Pressure loss is then specifically investigated in chapter 4 to answer to the following problem: *Is it possible to accurately predict the pressure losses in Large Eddy Simulations (LES) ?* Finally, the acoustic loss mechanisms are scrutinized in chapter 5 by the mean of two-port matrix measurement. These matrices are then used in a ROM of the PREINTRIG rig and a detailed comparison of the predicted and measured damping of the first acoustic modes is performed.

Chapter 3

Acoustic and pressure losses: The PREINTRIG work-bench

In this chapter, a detailed description of the existing models of two-port matrices for multi-perforated plate is provided. Starting from this example, the link between acoustic and pressure losses is established. Finally, the non reacting PREINTRIG workbench is introduced. This experimental apparatus is dedicated to the study of both acoustic and pressure losses for elements typically encountered in combustion chambers such as perforated plates or swirl injectors.

Introduction

Designing a complete combustion chamber is a challenging task. The main objective is to ensure that the combustion process is complete. Second, since the chamber walls cannot sustain high temperature, they must be cooled. This can be achieved by inserting a multi-perforated housing separating the chamber from a cold air flow [108]. This multi-perforated casing also induces acoustic damping, which diminishes the occurrence of self-oscillating acoustic modes in the combustion chamber. In the case of the multi-perforated plates, the mechanism leading to acoustic damping is the generation of vortex eddies, which are convected away of the plate [17, 18, 24]. In the presence of a mean flow, this mechanism remains linear as long as the amplitude of the acoustic velocity remains lower than the mean flow velocity in the apertures.

The same mechanism: coupling of acoustic waves with vortical eddies, is also observed in dump planes [23], diaphragms (which are treated as mono-perforated plates) [20] or even swirl injectors [21, 109]. These losses can be modelled by using equation 1.3.1 but this requires a precise knowledge of all terms appearing on the RHS. The scattering of acoustic waves across such elements can be described by the mean of acoustic two-port matrices as explained in section 1.5.2. Such matrices can be modelled [20] by the mean of the Rayleigh conductivity (see section 3.1.2), which links the acoustic pressure discontinuity through the element of interest with the fluctuating acoustic flux. Two port matrices can also been measured experimentally [21] with the multi-microphone technique (presented in chapter 5) or numerically [22, 110] with the system identification approach (presented in the case of FTF measurements in chapter 8).

Both mean and acoustic pressure losses are encountered in such compact elements and these phenomena present similarities. Indeed, both mean kinetic energy and acoustic energy are dissipated across compact elements with sudden area restrictions [10]. These similarities are investigated in section 3.2.2 in the case of a diaphragm but the result is more general: the mean pressure loss is associated to the low frequency limit of the acoustic loss.

Other sources of acoustic damping exists in combustion chambers and can be separated in two distinct categories. First, sound is convected and/or radiated at both inlet and outlet [10, 24]: acoustic

energy is not dissipated but tranported outside of the combustion chamber. A detailed characterization of the boundary condition is sufficient to take into account this cause of damping and examples are provided in both chapter 6 (non reacting PREINTRIG workbench) and chapter 9 (reacting INTRIG workbench). Second, damping is observed in mechanical and thermal boundary layers [74]. These losses can be taken into account by post-processing results provided by Helmholtz codes or ROMs.

3.1 Two-port matrix formalism

3.1.1 Definitions

The two-port matrix formalism can be used to describe mathematically an *Acoustically Compact Element (ACE)* such as a dump plane, a diaphragm or even a swirl injector, which is surrounded by ducts as shown in Fig. 3.1. Several definitions exist in the litterature and are briefly introduced in this section. Among them, the transfer matrix T, introduced by Munjal [111], links upstream acoustic quantities (u_u, p_u) with downstream ones (u_d, p_d):

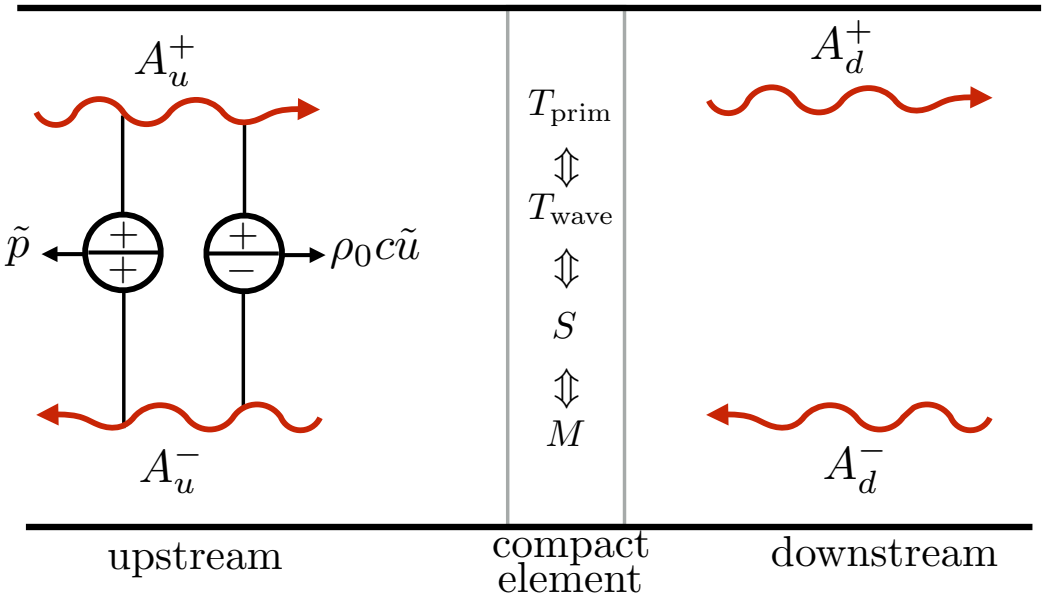

Figure 3.1: Sketch of the compact element and the associated acoustic waves. Several matrix representations are available to describe the scattering of acoustic waves across the ACE.

$$\underbrace{\begin{pmatrix} T_{uu} & T_{pu} \\ T_{up} & T_{pp} \end{pmatrix}}_{\mathrm{T_{prim}}} \begin{pmatrix} \rho_0 c\, u_u \\ p_u \end{pmatrix} = \begin{pmatrix} \rho_0 c\, u_d \\ p_d \end{pmatrix} \tag{3.1.1}$$

An example of diaphragm transfer matrix is shown in Fig. 3.2. It has been measured in the PREINTRIG rig (see section 3.3). The experimental method is detailed in chapter 5 while the two models (HM and MHM) are introduced in section 3.1.2.

The transfer matrix T_{prim} relies on the acoustic primitive variables u and p and should not be confused with the Riemann coefficient based [21] transfer matrix T_{wave} defined in equation 1.5.7. Using T_{wave} is convenient to build network models as shown in chapter 1. However, the two-port matrix T_{prim} is more convenient for use in CFD codes [60]. The link between these two-ports is provided in

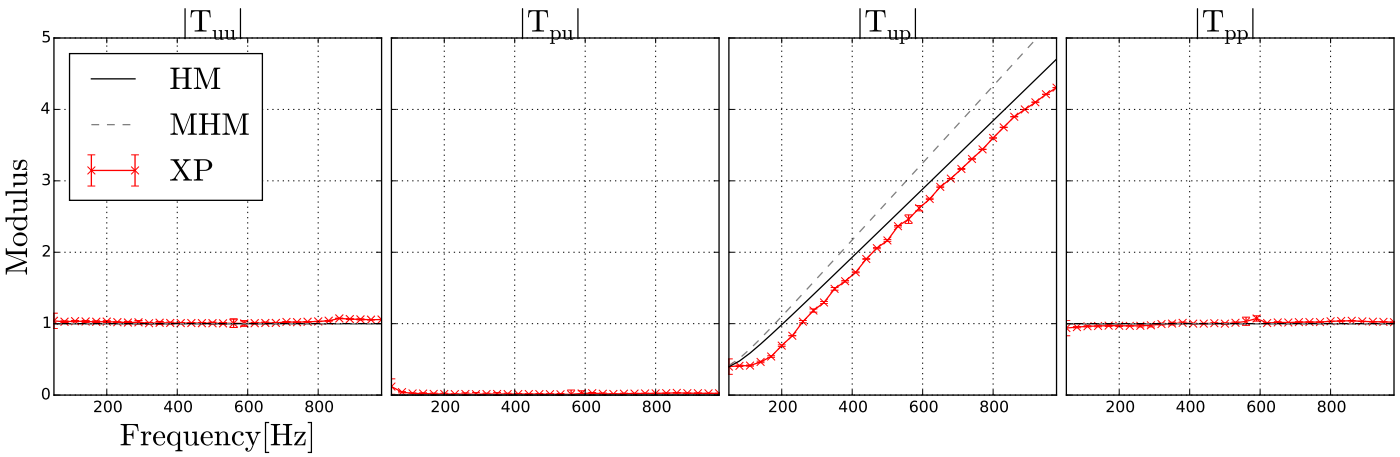

Figure 3.2: Example of primitive transfer matrix (gain of the four terms only) measured in the PREINTRIG workbench for a diaphragm. The measurement technique is detailed in chapter 6 while the models HM and MHM will be introduced in section 3.1.2.

equation 3.1.2 which expresses the terms of T_{wave} as a function of the terms of T_{prim}:

$$\underbrace{\frac{1}{2}\begin{pmatrix} T_{uu}+T_{pu}+T_{up}+T_{pp} & T_{pu}-T_{uu}-T_{up}+T_{pp} \\ -T_{uu}-T_{pu}+T_{up}+T_{pp} & T_{uu}-T_{pu}-T_{up}+T_{pp} \end{pmatrix}}_{\mathrm{T_{wave}}} \begin{pmatrix} A_u^+ \\ A_u^- \end{pmatrix} = \begin{pmatrix} A_d^+ \\ A_d^- \end{pmatrix} \tag{3.1.2}$$

where $A_d^+, A_d^-, A_u^+, A_u^-$ are the complex amplitudes associated with the acoustic waves upstream and downstream of the acoustic element as recalled in Fig. 3.1

It is sometimes more convient to use the scattering matrix formalism introduced by Davies [112], which links acoustic waves coming into the port (A_u^+, A_d^-) to the waves leaving it (A_d^+, A_u^-) by the mean of transmission and reflection coefficients:

$$\underbrace{\begin{pmatrix} t_u & r_d \\ r_u & t_d \end{pmatrix}}_{\mathrm{S}} \begin{pmatrix} A_u^+ \\ A_d^- \end{pmatrix} = \begin{pmatrix} A_d^+ \\ A_u^- \end{pmatrix} \tag{3.1.3}$$

Scattering matrices, as built on top of transmission and reflection coefficients, are more suitable for the physical interpretation of complex phenomena. Both transfer and scattering matrix formalisms are equivalents as it is possible to switch from one to another by using matrix transformation. For instance, one can rewrite the transfer matrix in term of scattering matrix coefficients:

$$\begin{pmatrix} T_{uu} & T_{pu} \\ T_{up} & T_{pp} \end{pmatrix} = \frac{1}{2}\begin{pmatrix} t_u + \frac{(1-r_d)(1+r_u)}{t_d} & t_u - \frac{(1+r_d)(1+r_u)}{t_d} \\ t_u - \frac{(1-r_d)(1-r_u)}{t_d} & t_u + \frac{(1+r_d)(1-r_u)}{t_d} \end{pmatrix} \tag{3.1.4}$$

This transformation will be used in chapter 5 to obtain transfer matrices from measured scattering matrices.

Finally, the mobility matrix M links the acoustic velocities at both sides of the two-port element with the acoustic pressure perturbations. This formulation has been introduced by Pierce [113] and will not be used in this manuscript. All the two-port representations are synthesized in table 3.1.

3.1.2 Models for perforated plates

All models presented in this section are related to the work of Howe [20] (see [60] for a detailed review of existing models). According to Howe, the acoustic-vortex interaction created when acoustic waves

Name	Context	Defining equation
Transfer matrix (p,u)	Modelling, CFD	$T_{\text{prim}} \begin{pmatrix} \rho_0 c\, u_u \\ p_u \end{pmatrix} = \begin{pmatrix} \rho_0 c\, u_d \\ p_d \end{pmatrix}$
Transfer matrix (waves)	Acoustic network, ROMs	$T_{\text{waves}} \begin{pmatrix} A_u^+ \\ A_u^- \end{pmatrix} = \begin{pmatrix} A_d^+ \\ A_d^- \end{pmatrix}$
Scattering matrix	Physical insights, ROMs	$S \begin{pmatrix} A_u^+ \\ A_d^- \end{pmatrix} = \begin{pmatrix} A_d^+ \\ A_u^- \end{pmatrix}$
Mobility matrix	Helmholtz codes	$M \begin{pmatrix} p_u \\ p_d \end{pmatrix} = \begin{pmatrix} \rho_0 c\, u_u \\ \rho_0 c\, u_d \end{pmatrix}$

Table 3.1: Various representations of two-port matrices used in the literature. This table is adapted from [21].

create vorticity at the aperture borders is the key mechanism responsible for sound absorption in small apertures. Linear behaviour is expected for small acoustic perturbations. Otherwise, the acoustic flow generates itself a vortex field and losses become non-linear as reported in [60]. Sketches for the perforated plate and the mean flow topology are provided in figure 3.3.

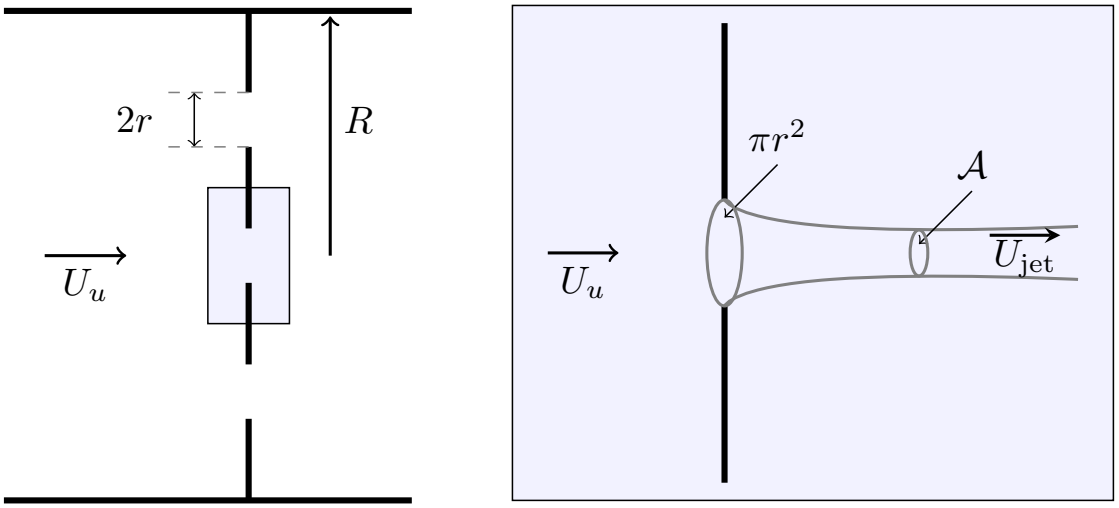

Figure 3.3: Left: Scheme of the perforated plate : r is the radius of an aperture. Right: View of a single aperture and the velocity jet downstream. $\mathcal{A}$ is the effective surface of the jet and πr^2, the surface of the aperture.

3.1.2.1 Rayleigh conductivity

The Rayleigh conductivity has been identified as an important quantity for modelling ACEs which contain apertures [20, 114]. Similarly to the electric conductivity defined as the ratio between current and voltage drop across an electric component, it completely characterises an ACE provided the acoustic flow-rate q is conserved:

$$K_r = \frac{i\omega\rho_0 q}{\Delta p} \quad , \quad q = \pi r^2 u_{aper} \tag{3.1.5}$$

where $\Delta p = p_d - p_u$ is the acoustic pressure loss. Contrary to the electric conductivity, the Rayleigh conductivity contains the term $i\omega$ in its definition: the loss in acoustic energy induced by the aperture is linked to the imaginary part $\Im(1/K_r)$. In the case of a diaphragm (studied experimentally in chapter 5), the acoustic velocity in the apertures is deduced by using the conservation of the fluctuating volume flow-rate:

$$u_{aper} = u_u \left(\frac{R}{r}\right)^2 \tag{3.1.6}$$

Combining equations 3.1.6 and 3.1.5 finally gives :

$$K_r = \frac{i\omega\pi\rho_0 R^2 u_u}{p_d - p_u} \tag{3.1.7}$$

which only relies on acoustic quantities taken upstream and downstream of the multi-perforated plate. Finally,equation 3.1.7 directly links the Rayleigh conductivity with the transfer matrix of the acoustic element :

$$\underbrace{\begin{pmatrix} T_{uu} & T_{pu} \\ T_{up} & T_{pp} \end{pmatrix}}_{\mathrm{T_{prim}}} = \begin{pmatrix} 1 & 0 \\ 2\zeta & 1 \end{pmatrix} \quad , \quad \zeta = \frac{i\omega\pi R^2}{2cK_r} \tag{3.1.8}$$

In the limit of an infinite Rayleigh conductivity, $|\zeta| \to 0$ and the transfer matrix tends to unity which is the expected behaviour. Moreover, when $|\zeta| \to \infty$, equation 3.1.8 is only defined provided that $u_u = 0 = u_d$. This case is equivalent to a zero-velocity boundary condition imposed at the location of the ACE.

3.1.2.2 Howe's model

Howe s model [20] is dedicated to predict the Rayleigh conductivity of an infinitely thin aperture in a high Reynolds mean flow as a function of the Strouhal number:

$$\mathrm{St} = \frac{\omega r}{U_{\mathrm{jet}}} \tag{3.1.9}$$

where U_{jet} is the bulk velocity of the jet. Because of the vena contracta effect, the surface of the jet is smaller than the one of the aperture: the contraction coefficient is $C_{C,HM} = \mathcal{A}/(\pi r^2) = 1/2$ so that the surface of the jet is $\mathcal{A} = \pi/2R^2$. Scarpato et al [25] recommended to use a vortex convection velocity equal to half of the jet bulk velocity. However, best results are obtain by keeping the jet velocity itself (choice of Mendez et al [60]) as shown in Fig. 3.2 in the low frequency limit. The conservation of the volume flow-rate through the aperture leads to:

$$U_{\mathrm{jet}} = \frac{1}{C_{C,HM}} U_u \left(\frac{R}{r}\right)^2 \tag{3.1.10}$$

where U_u is the bulk velocity upstream of the plate. Finally, Howe obtained the following analytical expression for the Rayleigh conductivity of an infinitely thin perforated plate by solving the divergence of the momentum equation for an inviscid, incompressible flow:

$$K_{r,HM} = 2r(T^*_{up} - i\delta) \tag{3.1.11}$$

$$T^*_{up} - i\delta = 1 + \frac{(\pi/2) I_1(\mathrm{St}) \exp(-\mathrm{St}) - iK_1(\mathrm{St}) \sinh(\mathrm{St})}{\mathrm{St}[(\pi/2) I_1(\mathrm{St}) \exp(-\mathrm{St}) + iK_1(\mathrm{St}) \cosh(\mathrm{St})]} \tag{3.1.12}$$

where I_1 , K_1 are the modified Bessel function of the first and second kinds respectively. This model (denoted as HM in the following of the manuscript) derived for a single aperture is still valid for a multi-perforated plate as long as the jets do not interact with their neighbours: $d >> r$. Jing and Sun [115]

proposed a modification of the previous model (denoted as MHM) to take into account the thickness h of the plate:

$$K_{r,MHM} = 2r\left(\frac{1}{T^*_{up} - i\delta} + \frac{2h}{\pi r}\right)^{-1} \tag{3.1.13}$$

This modification is function of the ratio between the depth h and the radius r of the perforation. Taking into account the plate thickness only alters the real part of $1/K_{r,MHM}$ and thus, does not modify the absorbing properties of the media as shown in section 3.2.1.

3.1.2.3 Uniform models

Uniform models have been proposed by Mendez in [60]. These models, which stem from the resolution of the temporal Bernoulli s equation, are approximation of Howe s equations. Moreover, they are easier to use in the context of CFD or Helmholtz solvers as the evaluation of Bessel s functions are avoided.

$$K_{r,UM_{1,2}} = \frac{\pi r}{2}\frac{\mathrm{St}}{i + l_{1,2}\,\mathrm{St}/(2r)} \tag{3.1.14}$$

The effective length l accounts for both the end correction effects in infinitely flanged configuration [15] (UM_1): $l_1 = \pi r/2$ and the thickness of the plate h (UM_2) :$l_2 = l_1 + h$ (see [60], [116]). Both UM_1 and UM_2 models give the same asymptotic results as HM and MHM models respectively for $\mathrm{St} \to 0$ and $\mathrm{St} \to \infty$ as shown in figure 3.4.

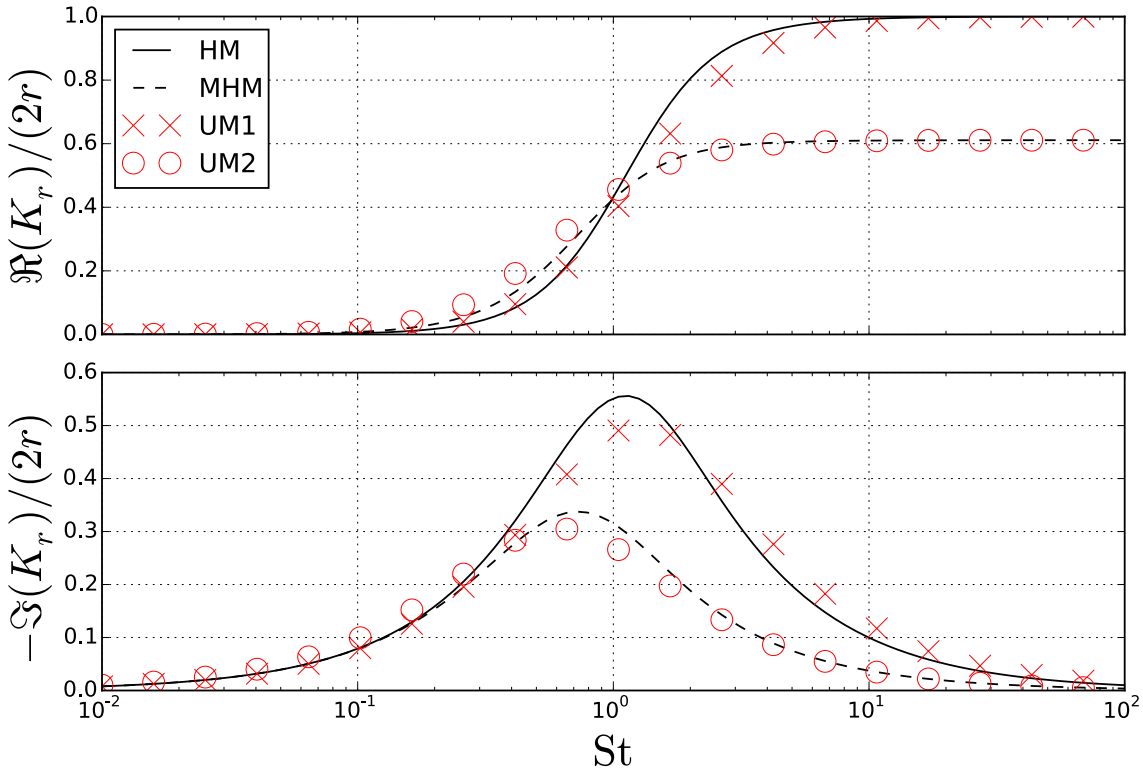

Figure 3.4: Comparison between models HM,MHM,UM1 and UM2 with $r/h = 1$. The Rayleigh conductivity is plotted against the Strouhal number. Models HM and UM1, which do not take into account the plate thickness give similar results. Models MHM and UM2, which take into account the plate thickness also give similar results.

The models presented here will be compared to measurements (from both experiments ans simulations) of transfer matrices in chapter 5.

3.2 What can we get from two-port matrices ?

In this section, we start from acoustic two-port matrices and establish the link with acoustic damping (section 3.2.1) and mean pressure losses (section 3.2.2). General results but also application in the case of perforated plates are provided.

3.2.1 Link with acoustic damping

The knowledge of an acoustic two-port is not sufficient to predict the total acoustic damping which can occur in a system. Indeed, the damping also rely on the boundary conditions. The simplest way to recover the damping of the total system $\{ACE + BCs\}$ is to solve equation 1.6.1. However, two-port matrices contain the seed of acoustic energy dissipation. A first method consists in looking at the eigenvalues of the matrix $\mathcal{I} - S \times S$ as shown in [117]. According to the signs of the two eigenvalues, the ACE may generate (active behaviour) or dissipate acoustic energy.

An other argument can be used for the primitive transfer matrix. As far as an element is acoustically compact, the acoustic flow-rate q is conserved. Moreover, in the absence of acoustic velocity fluctuations, the acoustic pressure must also be constant. These two assumptions introduce several simplifications in the transfer matrix (primitive form):

$$T_{\text{prim}} = \begin{pmatrix} 1 & 0 \\ 2\zeta & 1 \end{pmatrix} \tag{3.2.1}$$

where ζ is a complex function of the frequency. This transfer matrix shape is also retrieved for the multi-perforated plate model as shown in section 3.1.2 and in experiments (see Fig. 3.2). A budget of the acoustic energy can be performed upstream and downstream of the ACE:

$$\frac{\partial E_u}{\partial t} = \Phi_{\text{in}} - \Re\frac{1}{2}(pu^*)_- \tag{3.2.2}$$

$$\frac{\partial E_d}{\partial t} = \Re\frac{1}{2}(pu^*)_+ - \Phi_{\text{out}} \tag{3.2.3}$$

where $\Phi_{\text{in}} = \Re(pu^*)_{\text{in}}/2$ denotes the acoustic energy flux entering the upstream section and $\Phi_{\text{out}} = \Re(pu^*)_{\text{out}}/2$, the flux leaving the downstream section. Both of these fluxes may be characterized by taking into account the boundary conditions and are thus not linked to the dissipative behavior of the ACE. Moreover, the terms (pu) are the fluxes entering/leaving the ACE. Both equations 3.2.2 and 3.2.3 can be summed to retrieve the acoustic energy equation of the complete system:

$$\frac{\partial E}{\partial t} = \underbrace{(\Phi_{\text{in}} - \Phi_{\text{out}})}_{\text{Boundary fluxes}} + \underbrace{\Re\frac{1}{2}[(pu^*)_+ - (pu^*)_-]}_{\text{Two-port dissipation}} \tag{3.2.4}$$

The second term appearing in the RHS of equation 3.2.4 account for the dissipation which may occur in the ACE. According to equation 3.2.1, we know that:

$$u_+ = u_- \tag{3.2.5}$$

$$p_+ = p_- + 2\zeta u_- \tag{3.2.6}$$

The dissipative term stems from the combination of equations 3.2.5 and 3.2.5:

$$Re\frac{1}{2}[(pu^*)_+ - (pu^*)_-] = \Re(\zeta)|u|^2 \tag{3.2.7}$$

Equation 3.2.7 shows that when $\Re(\zeta) \neq 0$, acoustic pressure waves are generated in phase (or opposite phase) with the acoustic velocity so that acoustic power is added/removed. More precisely, $\Re(\zeta) < 0$ means that acoustic energy is dissipated. In addition, the dissipation only occurs when acoustic velocities is non null at the location of the ACE. In the case of a perforated plate (UM1 model), this term reduces to:

$$\Re(\zeta_{\text{UM1}}) = -2\frac{U_u}{c}\left(\frac{R}{r}\right)^4 \tag{3.2.8}$$

Equation 3.2.8 shows that the absorbing properties of a perforated plate are independent of the frequency. However, they are linearly linked to the bulk velocity. In the absence of a mean flow, no losses are expected. The fact that ζ is not a function of the frequency does not mean that perforated plates damp acoustic modes at every frequency. Indeed, when a velocity node is located close to the plate, the dissipation cancel as shown in equation 3.2.7.

3.2.2 Link between transfer matrix and pressure losses

The mean pressure loss of an ACE can be deduced from the low frequency limit of transfer matrices. As observed in equation 3.2.1, the non diagonal term $T_{up} = 2\zeta$ of the transfer matrix T_{prim} links the acoustic pressure drop with the acoustic velocity:

$$\Delta p = \rho_0 c T_{up} u_u \tag{3.2.9}$$

Before retrieving the steady state equation from equation 3.2.9, one must provide a model for the U_u (bulk velocity upstream of the element) dependency of T_{up}. For the infinitely thin perforated plate case, both HM and $UM1$ models are equivalent in the low frequency limit: $K_{r,(HM,UM1)}/(2r) = St^2/3 - i\pi St/4$ which leads to:

$$T_{up} = -4\left(\frac{R}{r}\right)^4 \frac{U_u}{c} \tag{3.2.10}$$

Equation 3.2.10 shows that T_{up} is a linear function of the upstream mean velocity U_u. As a consequence, the following non-dimensioned function $T^*_{up} = (c/U_u)T_{up,\omega=0}$ is independent of U_u and it is now possible to retrieve the steady state behaviour from equation 3.2.9. The method consists in finding the global equation for which the first order linearization leads to equation 3.2.9:

$$\Delta(p+p) = \frac{1}{2}\rho_0 T_{up}(U_u+u)^2 \implies \begin{array}{l} \Delta p = \frac{1}{2}\rho_0 T_{up}(U_u)^2 \ \text{(0 order)} \\ \Delta p = \rho_0 T_{up} U_u u \quad \text{(1st order)} \end{array} \tag{3.2.11}$$

In the general case, equation 3.2.11 shows that the mean pressure loss across an ACE is linked to the low frequency limit of the non-diagonal term which appears in the transfer matrix T_{prim}: $\Delta P = 1/2\rho_0 T_{up,\omega=0} U_u$. The pressure loss can be studied by the mean of a reduced coefficient ξ, which relates the ratio between pressure drop and kinetic energy:

$$\xi = \frac{\Delta P}{\frac{1}{2}\rho_0 U_u^2} \tag{3.2.12}$$

In the case of the perforated plate, combining equations 3.2.11, 3.2.10 and 3.2.12 provides an expression for the pressure loss coefficient:

$$\xi_{\text{UM1}} = -4\left(\frac{R}{r}\right)^4 \tag{3.2.13}$$

Equation 3.2.13 can be compared to a model dedicated to predict the pressure losses across a perforated plate. In a recent study, Malavasi et al [118] provided a detailed review of the existing models for the pressure loss across perforated plates. Among them, the model from Miller et al [119] states that:

$$\xi_{\mathrm{M}} = -\frac{C_0(1 - C_C\beta^2)^2}{C_C^2\beta^4} \tag{3.2.14}$$

where $\beta = r/R$ is the ratio of the inner and outer radius, C_0 is a parameter which relies on the thickness of the plate and C_C is the contraction coefficient of the jet. In the case of an infinitely thin plate and in the limit of very small apertures ($\beta \quad 1$), as prescribed for the Howe model HM, Malavasi provides values for the two coefficients: $C_0 = 1$ and $C_C = 0.6$. However, a different value have been used to derive the Howe model: $C_{C,HM} = 0.5$. Finally, equation 3.2.14 reduces to:

$$\xi_{\mathrm{M}'} = -\frac{1}{C_{C,HM}^2}\left(\frac{R}{r}\right)^4 = -4\left(\frac{R}{r}\right)^4 \tag{3.2.15}$$

which is equivalent to equation 3.2.13. The models detailed in this section (for both acoustic and mean pressure losses) will be then confronted to both numerical and experimental measurements on the PREINTRIG workbench. The setup of the PREINTRIG workbench, which is operated at IMFT, is detailed in section 3.3. Results concerning the mean pressure losses are then provided in the next chapter (4) while results concerning the acoustic scattering are gathered in chapter 5.

3.3 The PREINTRIG workbench

The PREINTRIG work bench has been designed to study both mean pressure losses and acoustic scattering through elements commonly encountered in modern combustion chambers as shown in Fig. 3.5.

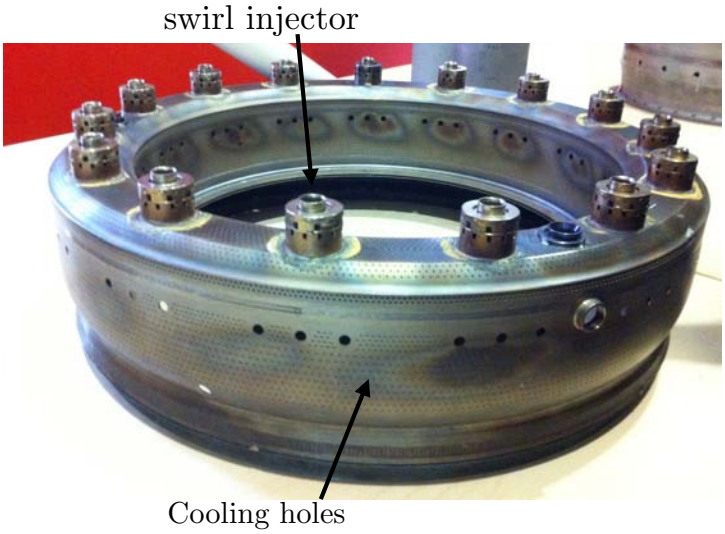

Figure 3.5: Annular combustion chamber of a an helicopter engine (Courtesy of Turbomecca). It contains 15 swirl injectors and small perforations are located on the walls for cooling purpose.

3.3.1 Introduction of the PREINTRIG rig

The PREINTRIG workbench is shown in fig 3.6. The experimental rig contains up to three cylindrical ducts of different lengths and an ACE (perforated plate or swirl injector) can be installed between them.

The three PVC ducts share the same cross section. Their inner radius is $R = 41\ mm$ and lengths with the connection are respectively 0.26, 0.34 and 0.56 m. When acoustic measurements are to be performed, the number of ducts used and their order can be varied as well as the outlet state (closed or open) as shown in Fig. 3.6. This permits to vary the structure of the acoustic waves propagating in the rig. When pressure losses are investigated, the ducts downstream of the compact element can be removed to ease the measurements (PIV, hot-wire anemometry) as described in section 3.3.3.

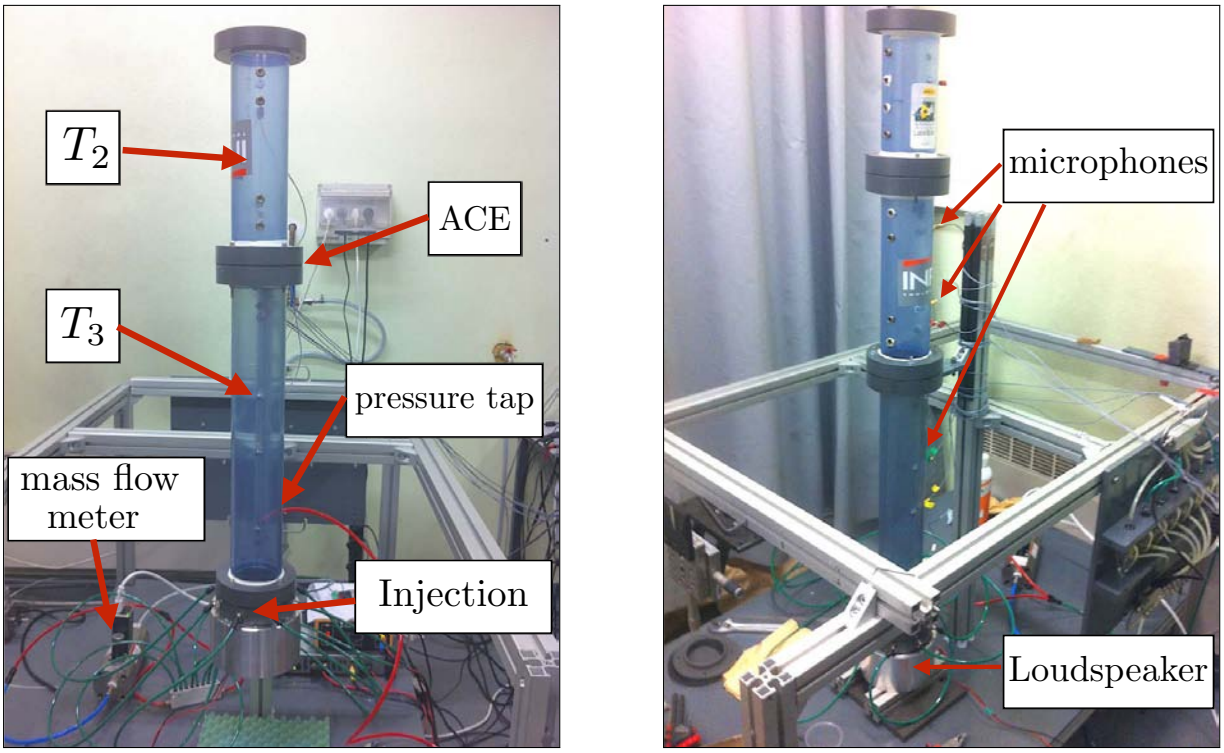

Figure 3.6: Pictures of the experimental workbench in the acoustic measurement configuration. On the left picture, only two ducts are used while on the right picture, three are mounted.

A mean flow is imposed by a mass-flow meter fed by a 7 bar air supply channel. The air flow is then split into 8 individual circular injectors disposed right after the loudspeaker at the bottom of the rig, as shown in Fig. 3.6, left. The flow passes trough duct T_3, crosses the ACE (diaphragm or swirl injector) and finally exits the rig by the outlet. When a closed outlet boundary conditions is required ($u = 0$, as shown in chapter 1), a small hole just upstream of the top is left open to let the air flow outside.

Experiments have been conducted at various flow-rates characterized by their bulk velocities: $U_u \in [0\,,\,1]\,m.s^{-1}$. These bulk velocities have been checked with an accuracy of 2% by using hot-wire based velocity profile measurements: the upstream velocity profile has been measured and integrated in cylindrical coordinates to retrieve the volumetric flow rate as shown in 3.7 for the highest velocity. A fit function is then used as an inlet boundary condition for simulations:

$$\bar{u}(y) = \beta_n \left(1 - \left(\frac{y}{R}\right)^n\right) \tag{3.3.1}$$

with β_n a normalization constant which ensures the conservation of the volume flow rate $q = m/\rho$:

$$\int_{y=0}^{R} 2\pi y \bar{u}(y) dy = \frac{m}{\rho} \tag{3.3.2}$$

which leads to:

$$\beta = \frac{m}{\pi R^2 \rho} \frac{n+2}{n} \tag{3.3.3}$$

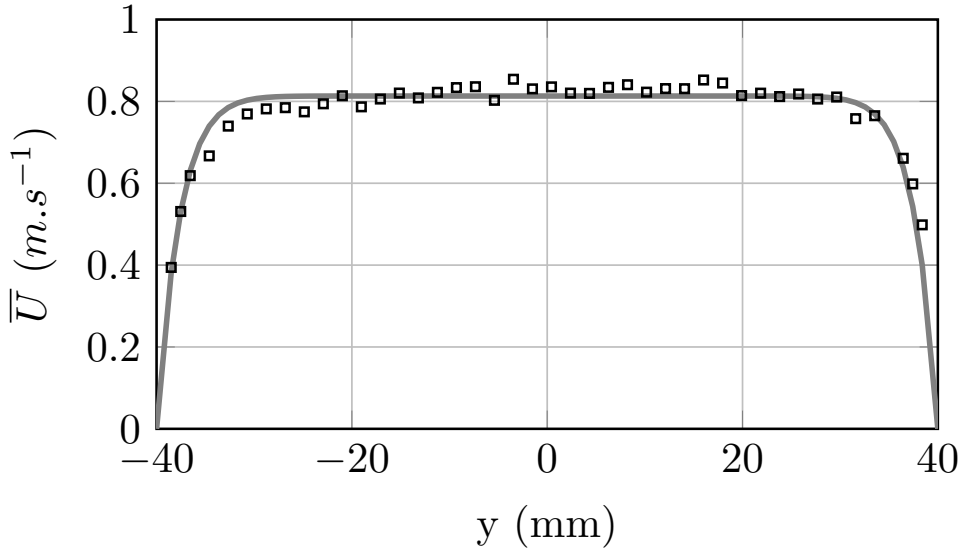

Figure 3.7: Mean axial velocity profile inside the plenum at x = −90 mm from hot-wire measurement: U_u = 0.67 $m.s^{-1}$ which corresponds to m = 4.29 $g.s^{-1}$ (squares) and fit function used to compute the flow-rate (solid line)

3.3.2 Presentation of the ACEs

The first ACE is the diaphragm shown in fig (3.8, left). It has a diameter of $2r$ = 18 mm and a thickness of h = 2 mm. The swirl injector (fig 3.8, middle) has been provided by TurboMecca. It is referred as the S1 swirl injector and has two counter-rotating passages for air. The fuel injection passage, not used in this study, has been blocked by a plug. An other geometry has been studied. It is constituted of the S1 swirl injector on which a cylindrical rod has been mounted on the top of the plug (Fig. 3.8, right) and is called the S2 swirl injector. The outlet radius is common for both injectors as well as for the diaphragm: r = 9 mm.

The low porosity (below 5%) of all these elements guaranties a high Reynolds number within the perforations. The compact hypothesis, which is necessary to ease the study of acoustic scattering is now investigated for the three elements of interest. The diaphragm may be seen as a compact element as the ratio between its effective thickness h and the acoustic wavelength stay below 1 % for all the frequencies[1] reported in chapter 5.
The effective thickness of the swirl injector is defined by the following relation [120]:

$$l_{\text{eff}} = \int_{x_u}^{x_d} \frac{A_u}{A(x)} \, \mathrm{d}x \tag{3.3.4}$$

It is approximately equal to l_{eff} = 0.2 m. For frequencies above 350 Hz, with ambient air conditions, the acoustic wavelengths are lower than $\lambda = c/f \approx 1$ m: the swirl injector may not be seen as an ACE for $f > 350$ Hz. Experimental measurements provided in chapter 5 tend to validate this assumptions (for instance, see Fig. 5.6 and the associated comments).

[1] from 0 up to 1 kHz, the ratio $c/(hf)$ never exceeds 0.6%

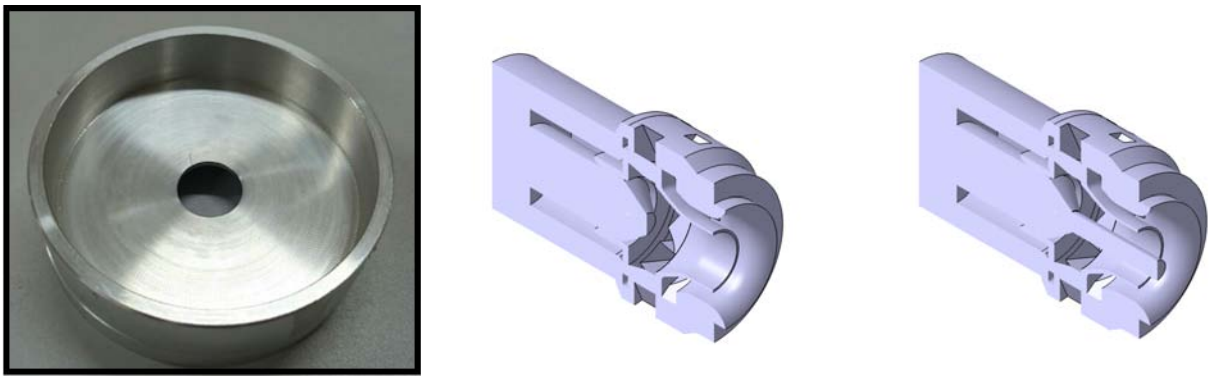

Figure 3.8: sketches of the ACE studied. From left to right, the diaphragm, the swirl injector without rod (S1) and with rod (S2). For the sake of clarity, S1 and S2 elements are cut to reveal the two separated networks of air injection but also the cylindrical rod in the S2 configuration

3.3.3 Specific setup for the pressure loss study

The measuring instruments required to study the mean pressure loss across ACEs at IMFT is detailed in this section.

3.3.3.1 Differential pressure measurement

Pressure losses through the ACE are measured with an electronic micro-manometer with an uncertainty smaller than 0.25% in the range $\Delta P \in [0:2]\, kPa$. The differential probe records the pressure upstream of the ACE, as shown in Fig. 3.6, left (pressure tap) and outside of the rig. The pressure drop along ducts T_3 is negligible so that the exact location of the pressure probe does not influence the pressure loss. Pressure loss as a function of the mass-flow rate is shown in chapter 4 and is compared to values obtained in a CFD code for the diaphragm and the swirl injector S1.

3.3.3.2 Particle Image Velocity (PIV)

PIV measurements have been carried out for the swirl injectors S1 and S2. The velocity field was measured downstream of the injector, along a longitudinal (xOy) plane (Fig. 3.9). A double cavity Nd:YAG laser (Quantel Big Sky) operating at 532 nm fires two laser beams, with a delay varying between 4 and 11 μs according to the operating conditions. The beam is expanded through a set of fused silica lenses (spherical and diverging). Because of the important out-of-plane velocity component, the laser sheet was intentionally thickened to approximately 1 mm. Olive oil particles (typical size of 1-2 μm) were seeded through the various flow injections systems (by means of venturi seeders). Mie scattering is collected on a 4 Hz PCO-Sensicam, operating with a resolution of 1280×600 pixels for the longitudinal plane. A f/16 182 mm telecentric lens (TC4M64, Opto-engineering) is used to reduce parallax displacements occurring with classical lenses. PIV images are processed with a cross-correlation multi-pass algorithm (Davis 8.2.3), resulting in a final window of $16 \times 16\,\text{pix}^2$ and a 50% overlap. 1320 images are collected over a region of $20 \times 32\,\text{mm}^2$ with a vector resolution of 0.4mm.

PIV measurements are performed at three mass flow rates m = 2.15, 3.22, 4.29 g.s^{-1} with an ambient temperature and pressure of T = 298 K and P = 101150 Pa, respectively. This roughly corresponds to upstream bulk velocities of U_u = 0.34, 0.51, 0.68 $m.s^{-1}$ respectively. The theoretical swirl number is S = 0.76 (estimated at the exit of the injector from the definition given by Merkle [121]).

In chapter 4, Large Eddy Simulations (LES) have been carried out to predict the total pressure loss of the swirl injector S1. These results have been validated by comparing the velocity profile downstream of the injector obtained in the LES with PIV data and are shown in chapter 4.

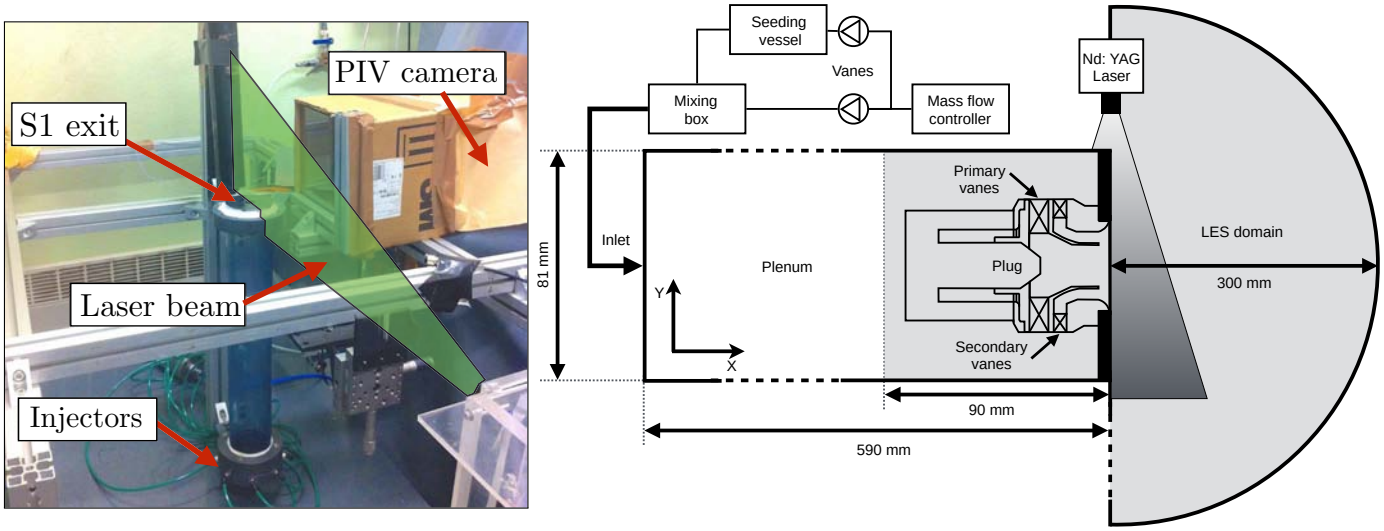

Figure 3.9: Picture of the experimental setup (left) and schematic view (right) for PIV measurement. The longitudinal (xOy) PIV plane is highlighted. The shaded area corresponds to the CFD domain (see chapter 4).

3.3.4 Specific setup for acoustic scattering study

We now focus on the measurement instrument dedicated to reconstruct acoustic two-port matrices.

3.3.4.1 Loudspeaker and microphones

Actuators and sensors are required to generate and monitor the acoustic waves upstream and downstream of the ACEs. Six slots are located on the sides of each ducts inside which microphones of type Bruel & Kjaer 1/4 Type 4954B can be plugged. Considering the three different ducts and the possibility to let the outlet opened or closed, four different configurations have been retained (see 3.10).

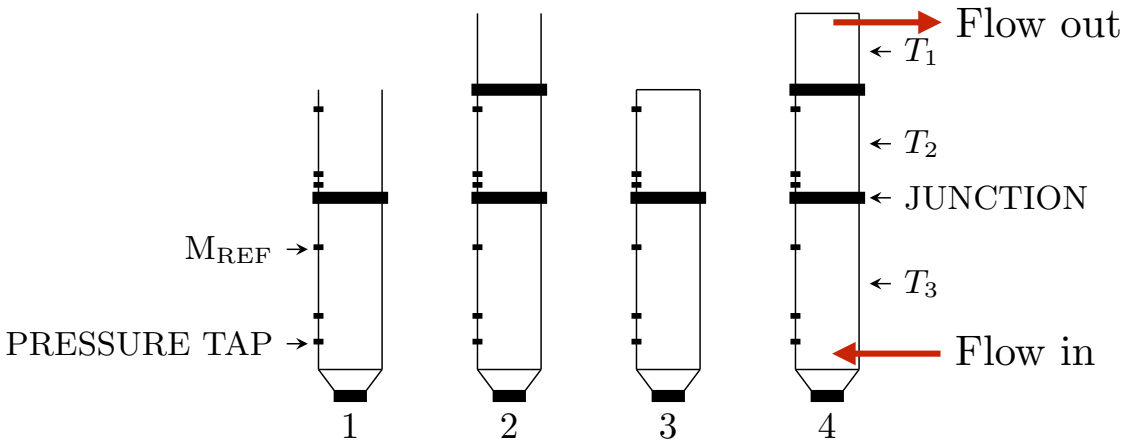

Figure 3.10: Description of the four configurations used in this study. For example, the second configuration is composed of the 3 ducts while the ACE is located in the junction between ducts T_3 and T_2 and the outlet is left opened. This configuration is denoted as **ls_t3_element_t2_t1_opened** in the following.

A loudspeaker of type Focal ISN 100 is fixed in a PVC casing at the bottom of the rig. As the

loudspeaker is mounted flush, acoustic waves can easily propagate in the ducts: the system { loudspeaker + casing } transmits the sound with very few attenuation in the frequency range of interest $f \in [0, 1]$ kHz. This feature is of primordial importance to measure acoustic two-port matrices in turbulent flows, where the acoustic signal must be important in both upstream and downstream ducts.

3.3.4.2 Acquisition of time series

The acquisition system is based on the Labview software and its associated multichannel acquisition board. The six temporal acoustic pressure signals are recorded simultaneously while feeding a sinusoidal excitation to the loudspeaker amplifier. All measurements are performed with harmonic excitations, for a frequency ranging between 50 and 1000 Hz. For each frequency and configuration, samples of 2 s were recorded at a sampling rate of 10 kHz. This represents at least 100 periods of acoustic forcing.

Conclusions

The concept of acoustic two-port matrices have been detailed in this chapter in order to model Acoustically Compact Elements (ACEs). Such matrices detail how the acoustic waves are linearly scattered across the ACE. Two interesting properties of two-port matrices have then been introduced:

- The two-port matrix representation contains informations about acoustic energy dissipation.
- The mean pressure loss coefficient $\xi = \Delta P/(1/2\rho U^2)$ can be deduced from the low-frequency limit of the transfer matrix:

$$\xi = \lim_{\omega \to 0} T^*_{up} = \lim_{\omega \to 0} \frac{c}{U_U} T_{up} \tag{3.3.5}$$

Finally, the PREINTRIG workbench has been designed to first verify these assumptions but also to provide quantitative data concerning pressure and acoustic losses. This rig is fully equipped to measure two-port matrices, pressure losses but also asymmetrical velocity field for CFD validation purposes.

A numerical method, based on automated mesh refinement, is presented in chapter 4 in order to correctly predict the pressure losses in LES. Acoustic energy dissipation is then investigated: A ROM is constructed on top of acoustic two-port matrices (measured in both experiments and LES) and damping rates are compared with experimental measurements.

Chapter 4

Pressure losses study

In the previous chapter, the link between mean pressure losses and two-port matrices has been established. The acoustic losses, which causes acoustic damping in ROM must be accurately taken into account to predict the stability of combustion chambers. As a consequence, a fundamental problem is tackled here: prior to accurately predicting acoustic two-port matrices in simulations, it is necessary to capture correctly the mean pressure drop (simply denoted as *pressure loss* or *pressure drop* in the remaining of the chapter).

This chapter focuses on the prediction of pressure losses occuring across ACEs (diaphragm and swirl injector) using a joint experimental and numerical study based on Large Eddy Simulation (LES). An automated procedure, based on mesh refinement using the MMG3D tool of INRIA, has been developed to accurately predict them. In order to refine the LES mesh and correctly predict the experimental pressure losses in this complex geometry, a new monitor function is introduced, which is based on the mean dissipation of kinetic energy Φ. After a first validation on a diaphragm flow, results obtained for a swirl injector with two counter-rotating passages show that a h-refinement algorithm based on this quantity coupled to the remeshing library MMG3D [122] can effectively produce the desirable local mesh refinement to match the target losses, measured experimentally. The refinement also improves the computed velocity and turbulence profiles at the swirl injector outlet, compared to PIV results.

Introduction

The design of swirl injectors used in combustion chambers is often based on multiple passages and relies on complex geometrical shapes. The swirl injector controls a large part of the chamber performances: flame stabilization, mixing between fuel and air, flame stability, ignition capabilities, etc [123] and its optimization is a crucial part of an engine design. Large-Eddy Simulation (LES) has become a reference method for the simulation of swirling flows in the last ten years [124, 125, 126]. Nevertheless, the prediction of pressure losses in swirl burners using LES remains a challenge for most industrial solvers: errors on pressure losses in swirled systems computed with LES can be surprisingly high as discussed below. This chapter shows that the accuracy of pressure losses prediction is mainly controlled by the mesh quality and density in the swirl injector passages. Uniform mesh refinement is not an affordable option, so that adaptive mesh refinement appears as an appropriate tool. In turn, a local mesh refinement approach requires a sensor which robustly flags all areas relevant to pressure loss, but does not expend valuable mesh resources in irrelevant areas.

Only few studies have addressed prediction of losses in combustors with complex geometry [127, 128], whereas the sensitivity of LES to mesh quality is a well-known issue for non-reacting flows [129] as well as for reacting flows [130, 125]. Three different approaches are commonly used in Adaptive Mesh Refinement (AMR) strategies in CFD: r-refinement methods where cells of a given mesh are redistributed, p-refinement methods where the order of discretization is locally increased and h-refinement approaches

where cells are subdivided isotropically or anisotropically [131]. In this latter case, a new mesh with a modified density distribution is generated [132, 133]. Whereas r- and p-refinement are most useful for dynamic mesh refinement as they do not change the mesh topology, h-refinement and remeshing are very appropriate for static mesh adaptation as they allow to add cells. While h-refinement is the most costly approach, it is the only one which can produce a high-quality mesh that is independent of the initial mesh.

AMR methods have been developed for Reynolds Average Navier-Stokes (RANS) methods for a long time [134, 135] but they remain a challenge in LES: being able to generate LES meshes on the basis of well-established metrics instead of relying on the intuition of the LES user is probably the overarching question for future LES. The present paper focuses on this problem for one specific case: non-reacting flows in swirl injectors. LES have been applied with tremendous success to swirled injectors used in combustion chambers for both non-reacting [136, 137] and reacting flows [138, 126, 139, 108]. Velocity profiles at various positions downstream of the swirled injectors usually match experimental velocity profiles very well, with and without reaction. What is seldom studied, however, is the capability of the LES solvers to predict pressure losses through these systems. These losses are a first order parameter in the design of swirled injectors in combustion: excessive pressure losses directly impact the engine efficiency so that predicting pressure losses accurately is as important as predicting velocity profiles. Unfortunately, recent studies show that while most LES capture velocity profiles accurately downstream of the swirl injector, they fail to predict pressure losses through the swirl injector itself with precision, usually overestimating them by 20 to 50 %.

Pressure losses in a swirling system are mainly induced by sudden expansion within the swirl injector passages, where strong flow directional perturbations occur [127]. Of course, increasing the total number of points inside the swirl injector helps to improve the accuracy of the prediction of pressure losses, but refining uniformly in the swirl injector is not affordable. A more effective method based on h-refinement is to develop a sensor which adds points inside the swirl injector only where they are needed. The objective of the present work is to propose an adaptive h-refinement method to increase the accuracy of the prediction of pressure losses while keeping the total number of mesh points to a minimum. The approach employs remeshing which is driven by a sensor that is based on mean flow data. The sensor considers as Quantity of Interest (QOI) the dissipation of kinetic energy as shown in Section 4.1. This QOI is averaged during the simulation and provided as field function to the MMG3D library [122] which carries out the remeshing operations. A new solution is then computed on the refined mesh, and the process is repeated once or twice during a full simulation. This is sufficient to reach an accuracy of a few percent on pressure losses while preserving or improving the quality of all velocity profiles and retaining an appropriate number of cells.

This chapter is organized as follows: Section 4.1 shows why the kinetic energy dissipation is the right mesh metric to predict pressure losses and presents the mesh adaptation procedure where the LES solver is coupled to the mesh refinement code MMG3D. The remeshing methodology is then validated on the diaphragm in Section 4.2 while section 4.3 presents the results concerning the swirl injector S1.

4.1 Mesh metric for the prediction of pressure losses

As underlined by Mitran [140], the criterion governing grid refinement in CFD should represent the physics of the problem. Due to the unsteady chaotic nature of turbulence, knowing where to refine the mesh in an LES is a complicated question which may depend on the objectives of the simulation: the best mesh to predict far field noise sources is probably not the best mesh to capture pressure losses. Metrics for CFD have been proposed for RANS meshes for a long time [141, 132] and are still studied today [142, 143]. Metrics for LES or DNS have also been derived recently. This can be done either as a dynamic approach, i.e. performed at run time, so that the mesh is adapted to the instantaneous solution (see [144, 145, 146]), but can also be done statically, i.e. performed using mean flow characteristics once

or twice during the whole simulation [128], as proposed here.

The first step to build a proper QOI adapted to the accurate prediction of pressure losses occurring across ACEs such as swirl injectors is to identify which physical mechanisms generate these losses. This can be obtained by considering conservation equations for kinetic energy $E_c = 1/2{u_i}^2$ and for entropy s. The equation for kinetic energy E_c can be written in incompressible flows as:

$$\underset{\pm}{\underset{1}{\frac{\partial E_c}{\partial t}}} + \underbrace{\frac{\partial}{\partial x_j}\left(u_j\left(E_c + P\right)\right)}_{2} = \underbrace{\frac{\partial\left(\tau_{ij}u_i\right)}{\partial x_j}}_{3} + \underbrace{\tau_{ij}\frac{\partial u_i}{\partial x_j}}_{4} \tag{4.1.1}$$

where terms (1), (2), (3) and (4) correspond respectively to the temporal variation of the kinetic energy, the mechanical energy flux, the viscous diffusion and the viscous dissipation.The entropy equation expressed with the same notations is:

$$\frac{\partial \rho s}{\partial t} + \frac{\partial \rho u_j s}{\partial x_j} = \frac{1}{T}\left(\tau_{ij}\frac{\partial u_i}{\partial x_j} + \frac{\partial}{\partial x_j}\left(\lambda\frac{\partial T}{\partial x_j}\right)\right) \tag{4.1.2}$$

Equations 4.1.1 and 4.1.2 reveal the importance of the viscous dissipation Φ:

$$\Phi = \tau_{ij}\frac{\partial u_i}{\partial x_j} = \frac{\mu}{2}\left(\frac{\partial u_i}{\partial x_j} + \frac{\partial u_j}{\partial x_i}\right)^2 > 0 \tag{4.1.3}$$

This term is present in the entropy equation and measures the losses due to fluid friction irreversibilities [147, 148, 149]. Of course, this is not a surprising result and the dissipation Φ plays a major role in all turbulence theories where it controls the dissipation to the small scales. The aerodynamic community [150, 151, 152, 147, 149] and the applied mathematicians [153, 154], have also been using entropy as a quality indicator for a long time. Φ also appears in the kinetic energy equation and rewriting this equation to introduce the total pressure $P_t = P + E_c$ shows that the dissipation Φ is the quantity which controls the dissipation of total pressure and therefore pressure losses:

$$\frac{\partial E_c}{\partial t} + \frac{\partial}{\partial x_j}\left(u_j P_t\right) = \frac{\partial\left(\tau_{ij}u_i\right)}{\partial x_j} + \Phi \tag{4.1.4}$$

For a steady flow, the integration of Eq. 4.1.4 over the whole computational domain of volume Δ bounded by a surface Σ, with the Ostrogradsky s theorem gives:

$$\int_\Sigma P_t u_i n_i d\sigma = \int_\Delta \frac{\partial\left(\tau_{ij}u_i\right)}{\partial x_j} dV + \int_\Delta \Phi dV \tag{4.1.5}$$

Finally, for a case with non-moving walls, the first right-hand side term of Eq. 4.1.6, which corresponds to the power of external viscous forces, cancels. The pressure losses are then directly expressed by the integral of the volumetric dissipation rate:

$$Q_v \Delta P_t = \int_\Delta \Phi dV \tag{4.1.6}$$

where Q_V is the volume flow rate and ΔP_t is the pressure loss between inlet and outlet sections. Eq. 4.1.6 confirms that errors on pressure losses ΔP_t in a simulation are due to the fact that the total dissipation $_\Delta \Phi dV$ is not computed with sufficient accuracy. The fact that the dissipation field Φ controls the irreversible losses in the entropy equation as well as the pressure losses in the kinetic energy equations suggests that a proper QOI to use in a metric aiming at adapting meshes to improve pressure losses prediction is the field of Φ.

Finally, an additional complexity introduced by LES is that the equations used in LES are not Eq. 4.1.1. Some differences must be accounted for to construct the QOI to use in an LES:

- Many LES use compressible formulations where additional phenomena (dilatation dissipation for example [155]) contribute to losses. However, one can demonstrate that the QOI Φ still controls the pressure drop across the ACE so that this criterion can be used in compressible LES codes such as AVBP. More details about the application of the QOI to compressible flows are provided in appendix C.

- In the present mesh adaptation strategy, Eq. 4.1.1 will be averaged over time to produce a steady field. Therefore the proper QOI is not the instantaneous field Φ but its time averaged field $\overline{\Phi}$.

- Finally, LES does not resolve all spatial scales: the LES field corresponds to a filtered velocity u_i and not the local velocity u_i [156, 157]. The filtering operation introduced by LES leads to an expression for dissipation which contains two parts: the first one is produced by the fluctuations resolved on the LES grid and can be written $\phi = \mu \left(\frac{\partial \tilde{u}_i}{\partial x_j} + \frac{\partial \tilde{u}_j}{\partial x_i} \right)^2$. The second contribution to dissipation corresponds to the unresolved part and can be written $\varphi = \mu_t \left(\frac{\partial \tilde{u}_i}{\partial x_j} + \frac{\partial \tilde{u}_j}{\partial x_i} \right)^2$ where μ_t is the local turbulent viscosity. Therefore a proper expression for the QOI is the time averaged of the sum of these two contributions: $\overline{\Phi} = \overline{\phi + \varphi}$:

$$\overline{\Phi} = \overline{(\mu + \mu_t) \left(\frac{\partial u_i}{\partial x_j} + \frac{\partial u_j}{\partial x_i} \right)^2} \tag{4.1.7}$$

  This is the QOI used in the following sections. It is expected to provide a metric leading to mesh refinement in zones where $\overline{\Phi}$ will be large so that the precision of pressure losses, which are controlled by this field, will improve. Interestingly, results show that the prediction of the velocity fields is also more accurate and suggest that this metric improves the quality of all results and not just of pressure losses.

In practice, the implementation of the metric in the LES code AVBP is performed as follows (Fig. 4.1). From the dissipation field $\overline{\Phi}$, a dimensionless variable Φ is first defined as:

$$\Phi = \begin{cases} < \\ 1 - \left(\dfrac{\overline{\Phi} - \overline{\Phi}_{\min}}{\overline{\Phi}_{\max} - \overline{\Phi}_{\min}} \right)^{\alpha} \\ > \end{cases}, \quad \Phi \in [0:1] \tag{4.1.8}$$

where the parameter α scales the value of Φ in order to ensure continuous variation of QOI and to obtain smoother stretching of the cells size in the new mesh. Then the maximum factor to divide the volume of the tetrahedral cells is imposed by the variable ϵ in the metric:

$$\text{metric} = \Phi \ (1 - \epsilon) + \epsilon \tag{4.1.9}$$

Typical values used for these two terms are $\epsilon = 0.3$ and $\alpha = 10$. The MMG3D library [122] then interpolates the mesh size to use from the prescribed metric on the current mesh. Finally, the MMG3D library is used to generate an entirely new mesh. The mesh refinement strategy is shown on Fig. 4.1. No restriction on the number of tetrahedra is specified but a minimal cell volume is fixed. The AVBP code uses a compressible formulation with explicit time-stepping and is hence subject to a CFL condition based on the fastest acoustic wave. To maintain an appropriate time-step Δt, the local mesh size must not be too small. Only isotropic subdivisions of the tetrahedra are considered to preserve the mesh quality [158]. While anisotropic remeshing can be very appropriate in producing high-aspect ratio cells aligned with strong gradients in steady flow [133], the present computations are unsteady and the extreme element angles found in anisotropic tetrahedral meshes would adversely affect accuracy. All simulations in sections 4.2 and 4.3 are performed using the compressible cell-vertex Navier-Stokes solver AVBP [159, 160]. The third-order scheme TTGC [161] is used on a fully tetrahedral mesh. In order to remove spurious numerical oscillations, an artificial viscosity operator of 2nd and 4th order

is also applied according to a local sensor [161]. At the inlet and outlet boundaries, the classical Local One-Dimensional Inviscid (LODI) Navier-Stokes Characteristic Boundary Conditions (NSCBC) are used [162]. An eddy-viscosity approach is considered for the SubGrid-Scale (SGS) stress, based on the SIGMA model [163]. No-slip adiabatic conditions are applied at all walls.

4.2 Validation on a canonical test case: pressure losses through a diaphragm

The AVBP-MMG3D strategy is first validated for the canonical test case of a diaphragm in a straight duct (Fig. 4.2) introduced in section 3.3.2. The evaluation of the pressure losses through a diaphragm is a usual task in the industry to measure flow rates. Due to the simplicity of the geometry, many pressure loss correlations derived from experiment are available in the literature [118, 164, 165]. In order to compare LES and experimental data, a series of experimental measurement were performed on a diaphragm to make sure that pressure losses were evaluated correctly. The experimental pressure drop curve measured in the PREINTRIG workbench is displayed in Fig. 4.3. Two models are compared

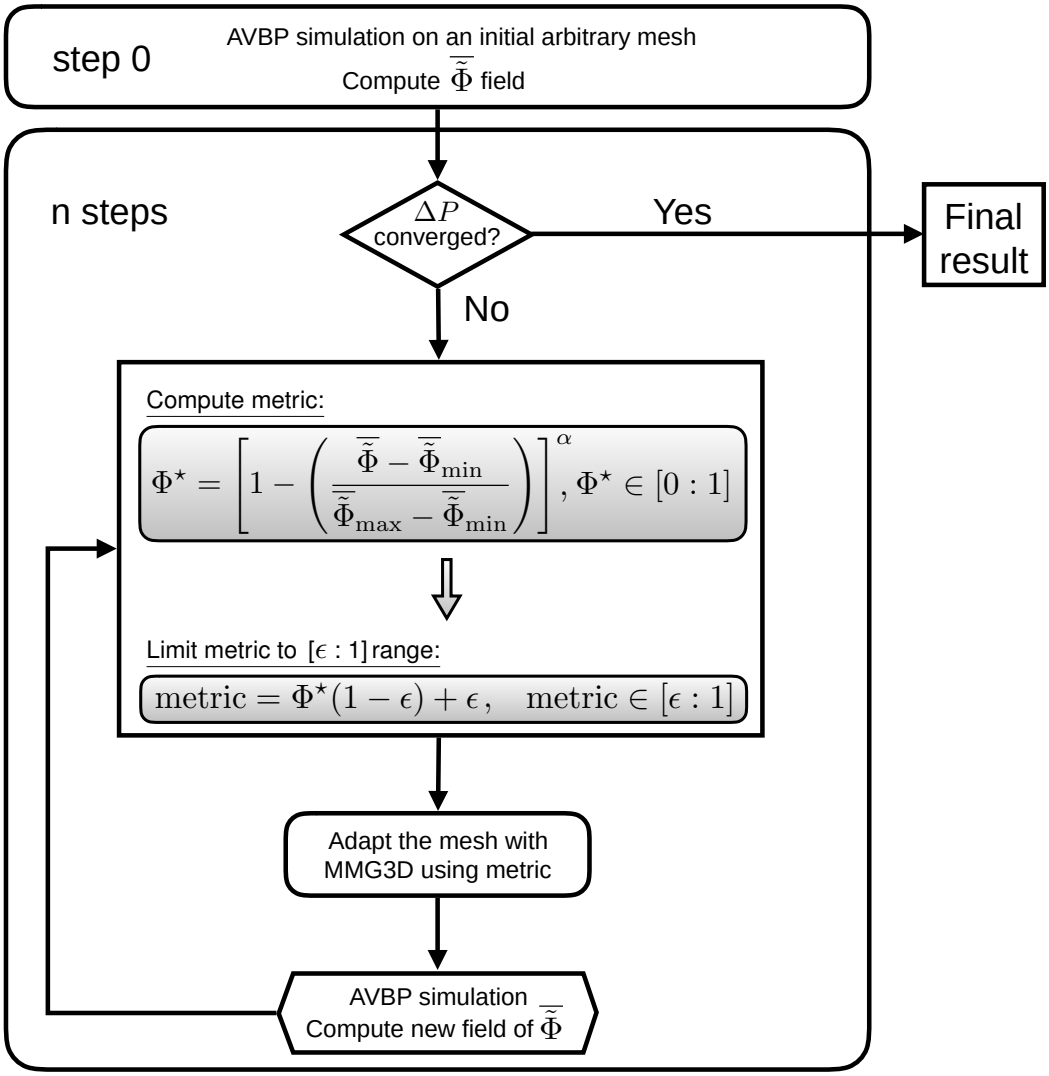

Figure 4.1: Mesh adaptation procedure.

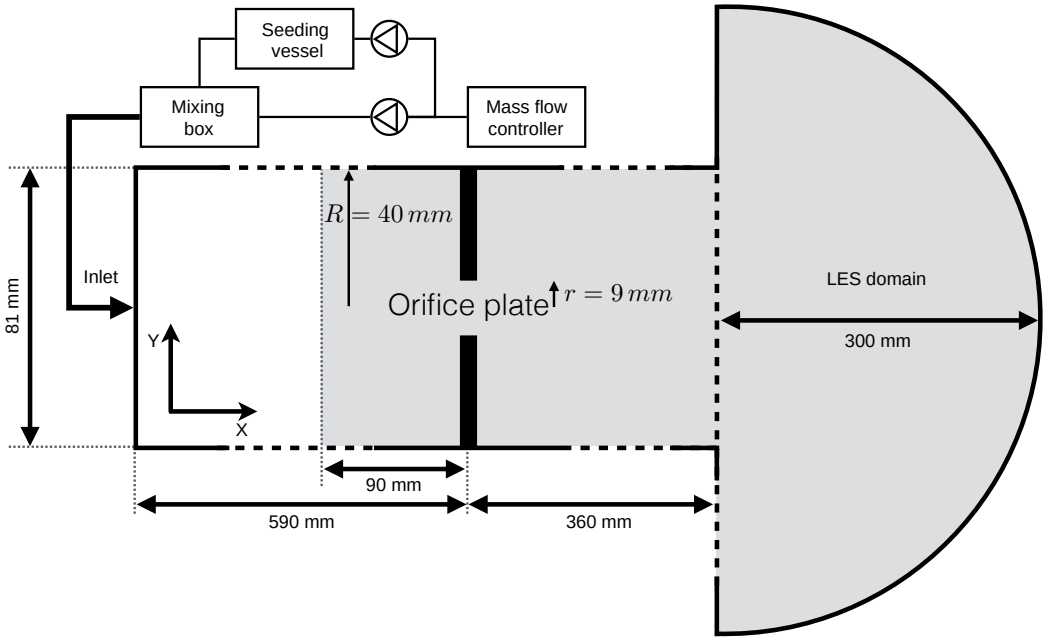

Figure 4.2: Schematic view of the experimental setup of the diaphragm. The shaded area correspond to the LES domain.

to the experimental measurements. The Idel Cik correlation [164] for diaphragm and Reynolds number $Re < 10^5$ is the model which best agrees with the experimental measurement for all mass flow rates. The Idel Cik correlation predicts a pressure loss coefficient ξ_{IC} = 920 However, the Miller [118] model recalled

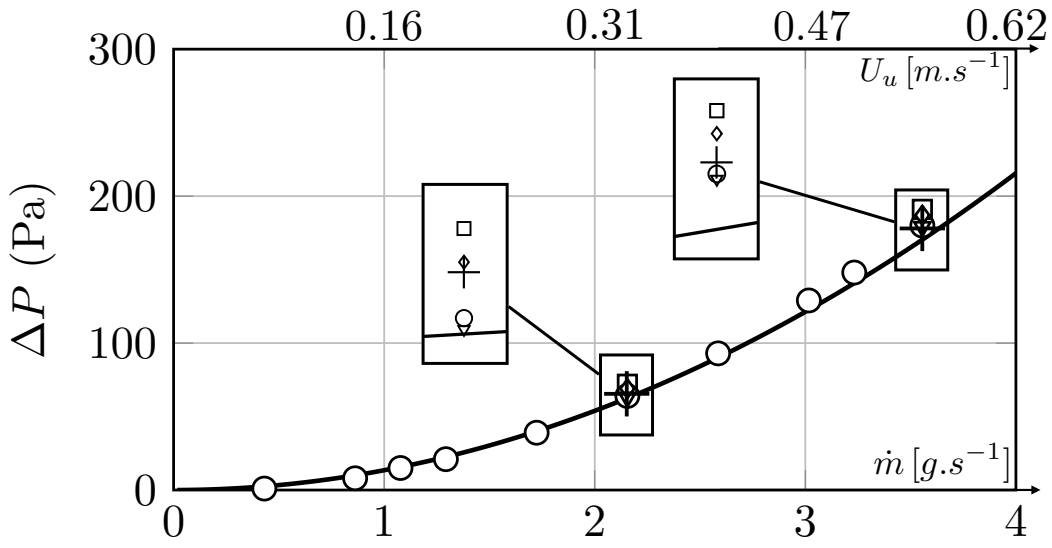

Figure 4.3: Experimental pressure loss evolution across the diaphragm for different mass flow rates. Comparison of the measured values (circles) with the Idel Cik model [164] (solid line), the Miller model [118] (crosses) and the LES results for the coarse (squares), the adapted 1 (diamonds) and the adapted 2 (triangles) meshes.

in equation 3.2.14 is very close to the measurement at the higher mass flow rate tested. Indeed, this

model is dedicated to study higher Reynolds number flows. Finally, the approximation (equation 3.2.15) established in section 3.2.2, where a link between acoustic and mean pressure losses was established, exhibit bad results: $\Delta P_{3.2.13}$ = 320 Pa which overestimate the measured value ΔP_{XP} = 180 Pa when m = 3.55 $g.s^{-1}$ and U_u = 0.55 $m.s^{-1}$. This happens because the vena-contracta effect is sightly over-estimated in the Howe model (C_C = 0.5 instead of C_C = 0.6 in [118]) but also because the porosity $\beta = r/R$ = 0.222 is not negligible so that a correction must be added. The pressure loss coefficient ξ defined in equation 3.2.12 is provided in table 4.1 for the experiment as well as other models. This coefficient is roughly independent of the flow-rate in the three models and relies on geometric parameters.

model	ξ
Idel Cik	920
Miller (equation 3.2.14)	970
UM1 (equation 3.2.15)	1750
XP	976

Table 4.1: Non-dimensioned pressure loss coefficients ξ

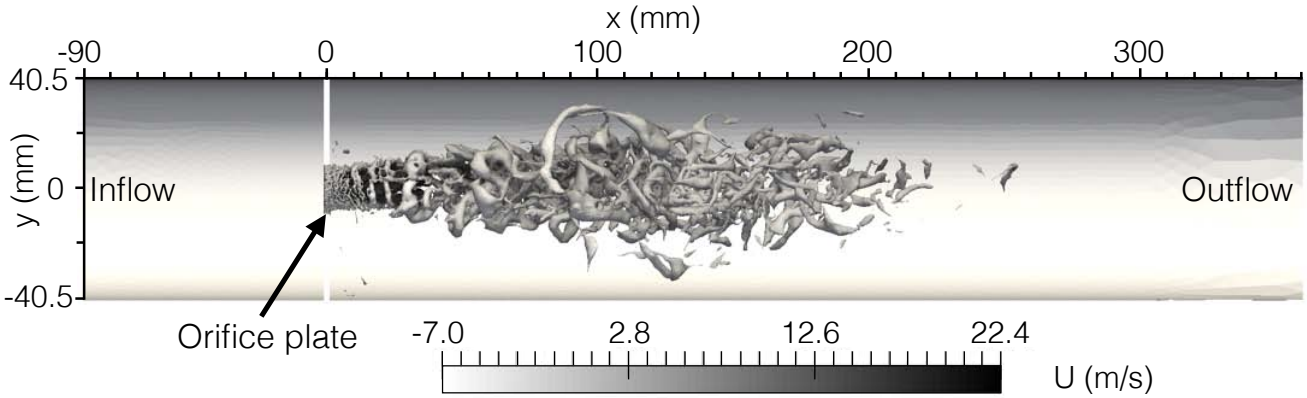

Figure 4.4: LES of the diaphram at m = 3.55 g.s^{-1}. The instantaneous flow is represent using Q-criterion $Q = 1.62(U_j/D_j)^2$ colored by axial velocity, on mesh AD 2.

The mesh refinement procedure is tested first for a mass flow rate of m = 3.55 g.s^{-1} where the pipe flow upstream of the perforated plate characterized by a bulk velocity U_b = 0.55 m.s^{-1} and a Reynolds number $Re_D = U_b D/\nu$ = 3000. The ambient pressure and temperature of the experiment are P = 101150 Pa and T = 292 K. The computational domain is shown on Fig. 4.2. The inlet plenum is truncated at x = −90 mm in the LES. A semi-hemisphere, defined by a radius of (r = 0.3 m) is added at the duct outlet in order to mimic the atmosphere in the experiment and dissipate free-jet flow fluctuations. Downstream of the diaphram, centered at x = 0 mm (the upstream inlet edge is at x = −1 mm), a jet-plume flow develops as expected. This is shown using Q-criterion (as defined by Hunt *et al.* [166]) on Fig. 4.4.

In this test case, the target pressure loss is obtained in two adaptation steps and three LES only. Table 4.2 summarizes the parameters and the cost. From an initial coarse mesh (Fig. 4.5), a first adapted mesh AD 1 is obtained. The central picture in Fig. 4.5 shows that the mesh refinement follows the distribution of viscous dissipation $\overline{\Phi}$ obtained on the coarse mesh. This first refinement step leads to an overestimation of the pressure drop compared to the experiment of only 3.8% while it was 6.1% on the coarse mesh. Finally, an acceptable discretization is obtained in the second step and the mesh AD 2 . The error on the predicted losses is less than 1%. Figure 4.6 shows radial profiles of the axial mean

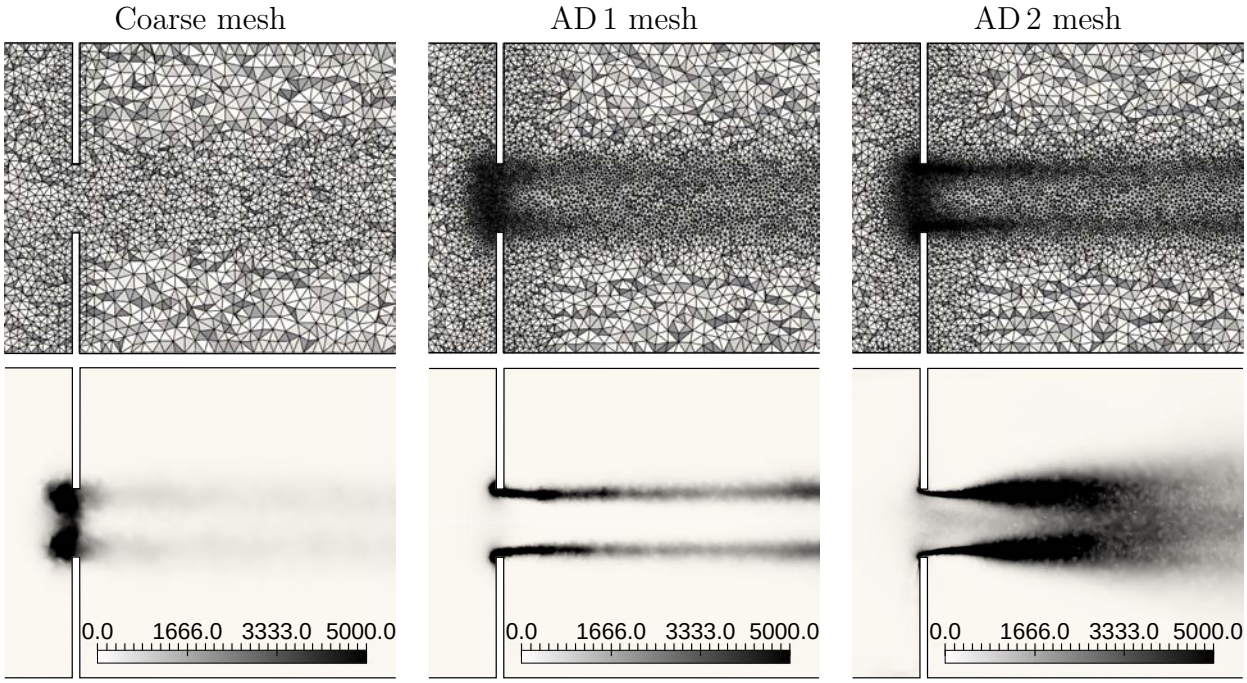

Figure 4.5: Diaphram test case at $m = 3.55$ g.s^{-1}: zoom on the mesh on the diaphragm for each LES (top images) and mean kinetic energy dissipation $\overline{\Phi}$ (bottom images) in W.m^{-3}.

velocity across the orifice at the leading edge ($x = -1$ mm), the center ($x = 0$ mm) and the trailing edge ($x = 1$ mm), respectively. Only the last mesh AD 2 , allows the apparition of the vena-contracta effect, with a flow separation zone across the diaphragm. Indeed, no reverse flow appears downstream the leading edge of the diaphragm at $x = 0$ mm and $x = 1$ mm with the coarse and AD 1 mesh.

Moreover, a remarkable change is observed for the mean kinetic energy dissipation field between mesh AD 1 and AD 2 on Fig. 4.5. The solution on mesh AD 1 would suggest that a persistent shear layer has been captured well at the orifice and is then swept downstream. AD 2 refinement leads to a mesh which is refined much closer to the perforated plate: this allows the growth of Kelvin-Helmholtz instabilities and a rapid transition to a fully developed turbulent jet-plume. This is in agreement with the spectral power density obtained from the axial velocity signal recorded at $x = 2d$ and $r = 0.5d$ for the three meshes (Fig. 4.7). Only the axial velocity spectrum of mesh AD 2 is fully broadband and exhibits a typical $k = -5/3$ slope over one decade. Mesh AD 1 allows the development of instabilities, characterized by a narrow band with a maximum for $f = 700\ Hz$, but no inertial zone is found in the spectrum. The result for the coarse mesh suggests that the flow remains fully laminar.

The adaptation approach was repeated at a mass flow rate of $m = 2.15$ g.s^{-1} to further check its validity (cf. Fig. 4.3). The experimental target is also reached in two mesh refinement steps with a final error of 1.6%.

4.3 Pressure losses in a swirl injector

Two swirl injectors have been introduced in chapter 3. Only the swirl injector S1 is investigated here for the sake of clarity but similar results have been obtained with the swirl injector S2. A schematic view of the S1 injector is displayed in Fig. 3.9.

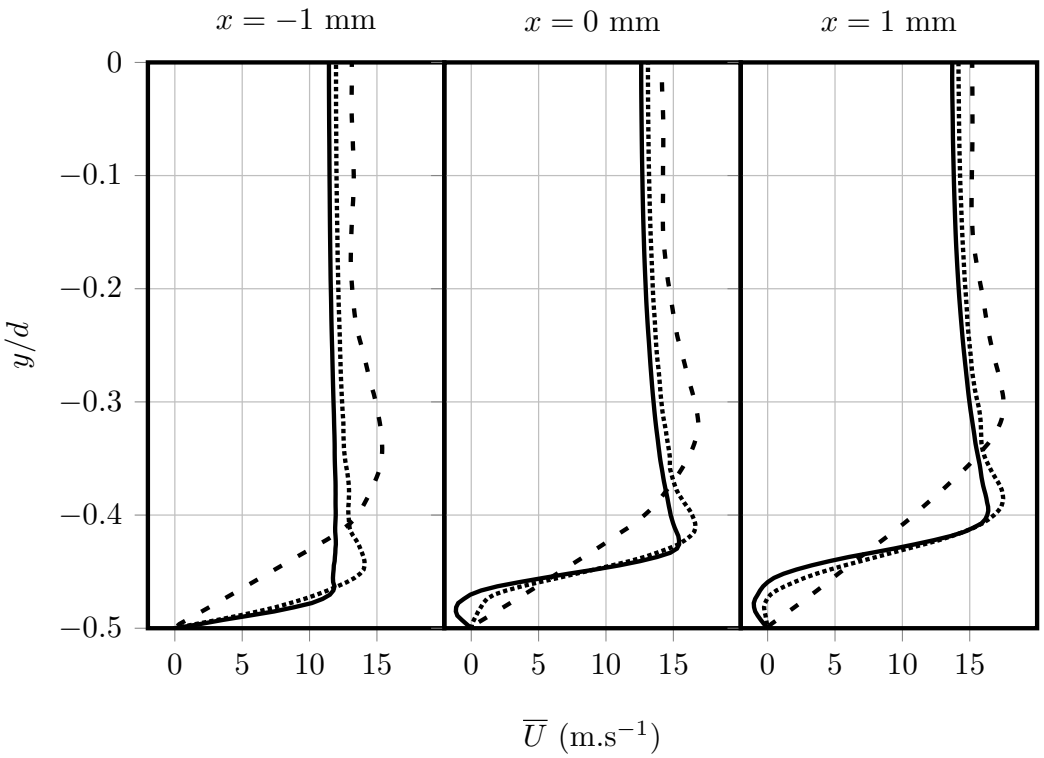

Figure 4.6: Radial distribution of axial mean velocity across the orifice at m = 3.55 g.s^{-1}. Coarse mesh (dashed line); mesh AD 1 (dotted line) and mesh AD 2 (solid line).

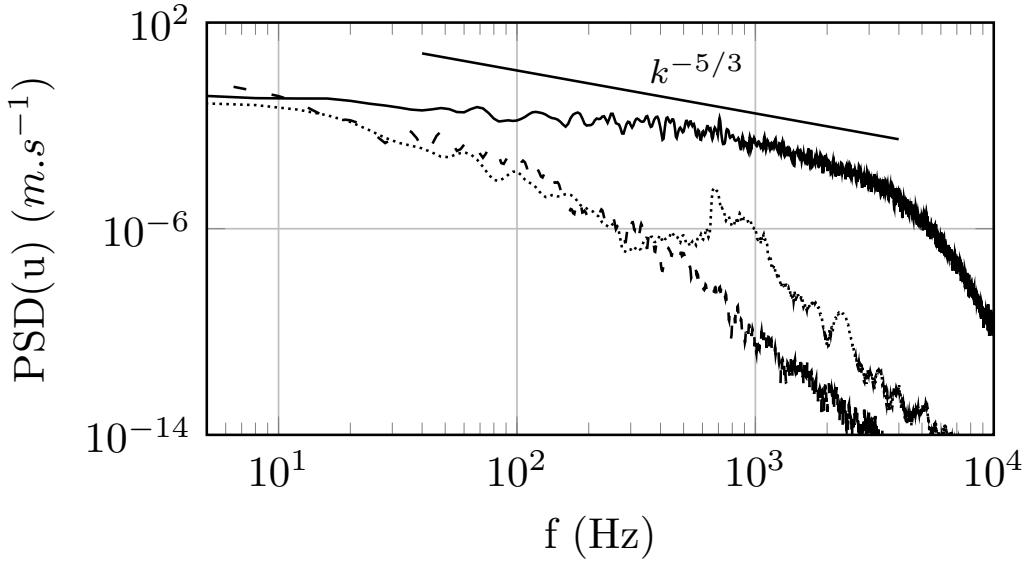

Figure 4.7: Diaphragm test case at m = 3.55 g.s^{-1}: power spectral density of the axial velocity in the jet-plume shear layer at $x = 2d$ and $r = 0.5d$. Coarse mesh (dashed line); mesh AD 1 (dotted line) and mesh AD 2 (solid line).

4.3.1 Description of the swirl injector S1

The air entering the swirl injector is divided into two passages: the primary flow passes through the inner region of the passages with eight tangential vanes. The secondary flow passes through the outer

Table 4.2: Summary of the mesh adaptation LES on the perforated plate at $m = 3.55$ g.s^{-1}.

	Coarse	AD 1	AD 2
α		100	50
ϵ		0.3	0.4
T_{init} (s)	1.5	0.3	0.3
T_{stat} (s)	0.5	0.5	0.5
time step (10^{-6} s)	1.4	0.41	0.13
number of cells (10^6)	0.71	1.55	2.75
number of CPU hours	3h06mn	5h30mn	19h
number of cores	256	720	1152
ΔP error	6.1%	3.8%	–0.5%

passages with the same number of vanes but with counter-rotating swirl direction. No fuel is injected for these tests: in order to replace the fuel injection system, a plug is inserted in the primary flow along the centerline of the swirl injector producing a recess of 14 mm with respect to the exit plane. The experimental apparatus used to measure pressure losses and have been previously described in chapter 3. The pressure loss plotted as a function of the mass flow rates are displayed in Fig. 4.8.

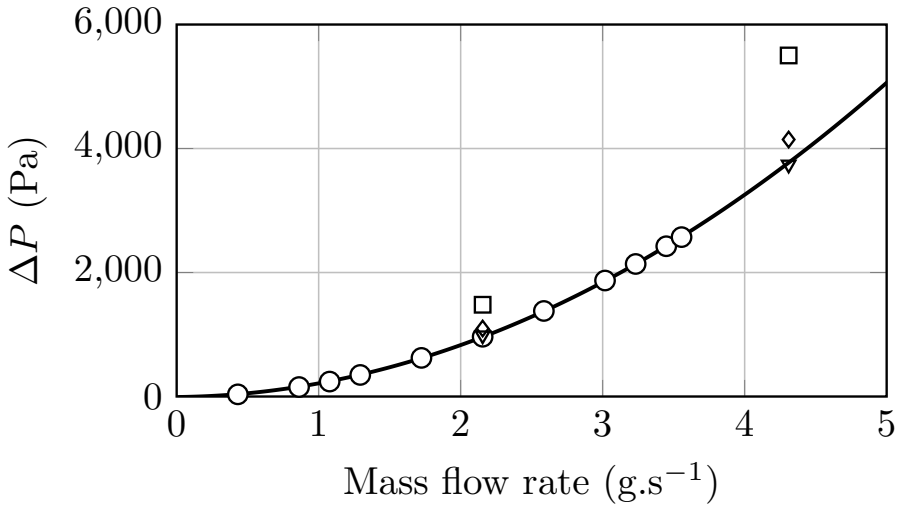

Figure 4.8: Pressure loss evolution through the swirl injector: experimental data (circles), fit function (solid line), LES results for the coarse (squares), the adapted 1 (diamonds) and the adapted 2 (triangles) meshes.

4.3.2 Flow parameters

The pressure losses of the swirl injector system are measured over a range of mass flow rates 0.43 g.s^{-1} m 3.55 g.s^{-1}. PIV measurements are performed at three mass flow rates m = 2.15, 3.22, 4.29 g.s^{-1} with an ambient temperature and pressure of $T = 298$ K and $P = 101150$ Pa, respectively. First, LES are performed at $m = 4.29$ g.s^{-1}. The bulk velocity at the nozzle exit is defined as $U_b = m/(\rho A) = 13.9$ m.s^{-1}. The theoretical swirl number is $S = 0.76$ (estimated from the definition given by Merkle [121]) and a

Reynolds number based on the bulk velocity and the swirl injector exit diameter is $Re = U_b D/\mu \quad 14{\times}10^3$. The inlet plenum is truncated to $x = -90$ mm in the LES where the velocity profile have been measured in the experiment (see chapter 3, section 3.3.1).

4.3.3 Pressure losses

Figure 4.9 shows the time evolution of the instantaneous pressure loss measured in the LES, for one reference case where the flow rate is $4.29\,\mathrm{g.s^{-1}}$. The pressure loss evolves during the coarse mesh computation until its average becomes steady with the value overestimated by 46%, compared to the experiment. As observed by many LES users in recent years [128, 127], the pressure losses error obtained on a first arbitrary mesh can be very large and a 46% error is not acceptable. The application of the refinement method corrects this problem: pressure losses change abruptly when the mesh is refined for the first time to AD 1 and a second one to AD 2. The error on the pressure losses drops to 10% for AD 1 and finally to less than 1% for AD 2. To investigate mesh convergence, an additional adaptation step AD 3 was performed. The pressure losses predicted on this mesh are again in agreement with the experiment (less than 1% of error). These results and the values for the parameters α and ϵ, used to build the mesh refinement metric (cf. Fig. 4.1) are summarized in table 4.4. Finally, the pressure loss coefficient obtained in both LES and experiment $\xi_{\mathrm{swirl}} \approx 13900$ is much higher than the one for the diaphragm ($\xi_{\mathrm{dia}} \approx 920$).

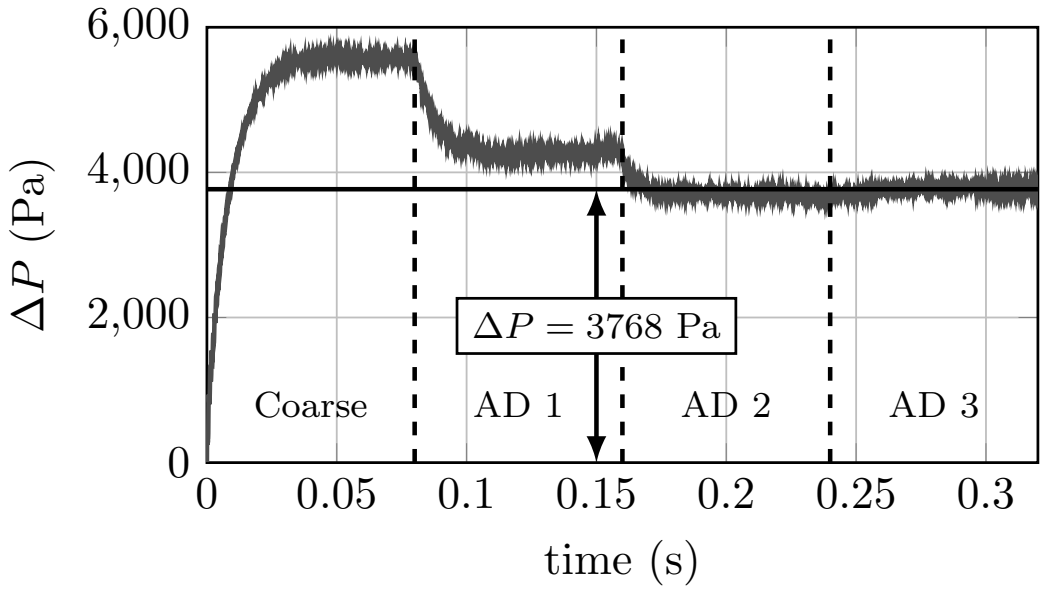

Figure 4.9: $m = 4.29$ g.s^{-1} case: Evolution of the pressure loss computed with LES as a function of time and comparison with the target experimental value (straight solid line). The pressure signal is recorded in the upstream plenum at the wall ($x = -50$ mm and $r = 40.5$ mm). The mesh is refined by the AVBP-MMG3D three times during the whole procedure.

An important parameter of the LES is the evaluation of the flow characteristic time $\tau_F = D/U_b = 1.3$ ms. The simulation time based on this value need to be chosen sufficiently long for the flow to reach steady state as well as the averaged time needed to gather samples in the LES[1]. Fig. 4.9 shows that the flow adapts to all changes of mesh within 30 τ_F. All statistics used in the rest of the paper were gathered over a period of 40 ms corresponding to 30 flow-through times.

[1]In the experiment, all measurements were performed over 110 s, corresponding to very long times compared to τ_F.

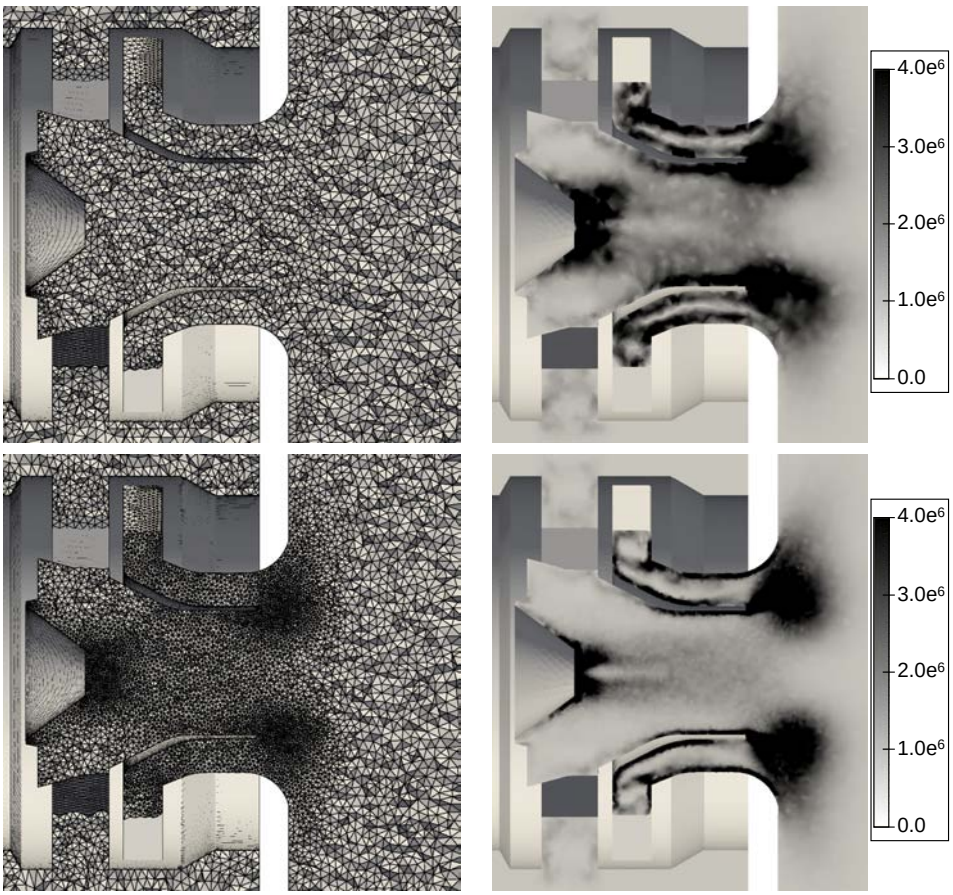

Figure 4.10: m = 4.29 g.s^{-1} case: meshes (left) and fields of $\overline{\Phi}$ in W.m^{-3} (right) for the coarse and AD 1, meshes in the central plane of the swirl injector, from top to bottom, respectively.

The four meshes (coarse, AD 1, AD 2 and AD 3) are displayed in Fig. 4.10. As expected, mesh refinement is performed in regions where the total mean dissipation $\overline{\Phi}$ is large, allowing to resolve the field of $\overline{\Phi}$ with precision, thereby increasing the precision of the pressure loss evaluation. The convergence of the process can be clearly observed: meshes and results on AD 2 and AD 3 are almost similar.

The automatic refinement procedure AVBP+MMG3D was also applied to an other flow rate at m = 2.15 g.s^{-1}. Fig. 4.8 displays the values of the experimental pressure loss vs flow rate compared to the values obtained by the LES for each refinement step. All values of pressure losses correspond to the average pressure loss measured over at least 30 flow-through times (Fig. 4.9 shows that this time is sufficient for the pressure loss to converge). The procedure appears to be robust for all cases tested here: the refinement procedure leads systematically to small errors compared to the experiment. Note that the procedure is unmodified for all cases: this is a fully automatic method determining a sufficiently resolved mesh in terms of pressure losses, independent of the LES user. Moreover, in most cases, two refinement steps are sufficient to reach the target so that the simulation costs remain comparable to a normal simulation where the user would try to refine the grid using intuition. Obviously, it is also much cheaper than a brute-force strategy where the whole mesh would be refined homogeneously: here, the homogeneous mesh having the same refinement everywhere as mesh AD 2 has in the swirl injector region would require 1.4 billion points. The next section shows that the mesh refinement procedure allows also to better predict the velocity field in the chamber itself.

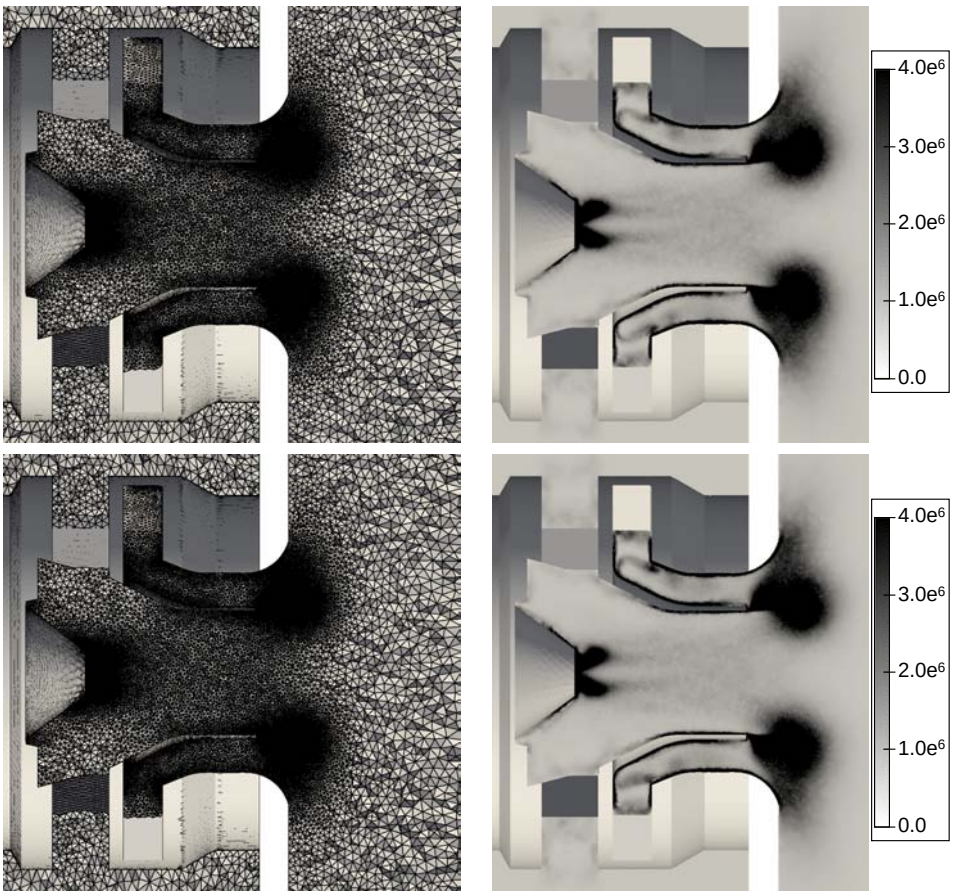

Figure 4.11: $m = 4.29$ g.s^{-1} case: meshes (left) and fields of $\overline{\Phi}$ in W.m^{-3} (right) for the AD 2 and AD 3 meshes in the central plane of the swirl injector, from top to bottom, respectively.

4.3.4 Velocity fields for the $m = 4.29$ g.s^{-1} case

The previous section has shown that the AVBP+MMG3D tool was able to produce an acceptable mesh for the pressure loss because it allowed a proper resolution of the time-averaged dissipation field. It is to be expected that with a correct resolution of the mixing phenomena, not only pressure losses but also velocity fields will be predicted more accurately. To assess this aspect, PIV measurements were performed in the experimental setup (section 3.3.1) for the $m = 4.29$ g.s^{-1} case and compared to the LES velocity fields on the coarse, AD 1 and AD 2 meshes (AD 3 gave results which are very similar to AD 2). The accuracy of the PIV data was carefully checked by investigating the effects of the measurement windows. Results (table 4.3) exhibit less than 9% of error on the mass flow rates recovered from PIV compared to the target imposed by the mass flow controller at the plenum inlet in the experiement. Fig. 4.12 shows the mean axial velocity field in the vicinity of the swirl injector over the quarter of the field which was accessible by the PIV optical window. A strong flow reversal due to vortex breakdown dominates downstream of the exhaust of the primary swirl injector, which is as expected for flows with a swirl number $S > 0.6$. This very compact reverse flow zone is associated with high turbulence levels [167].

Even if the mean PIV data reveal a smooth averaged field, a visualization of the instantaneous structures obtained by LES for the same regime (Fig. 4.13) shows that the flow is highly turbulent with multiple structures developing in the breakdown zone.

Fig. 4.14 shows that the precision of the LES, in terms of velocity fields, also increases with mesh

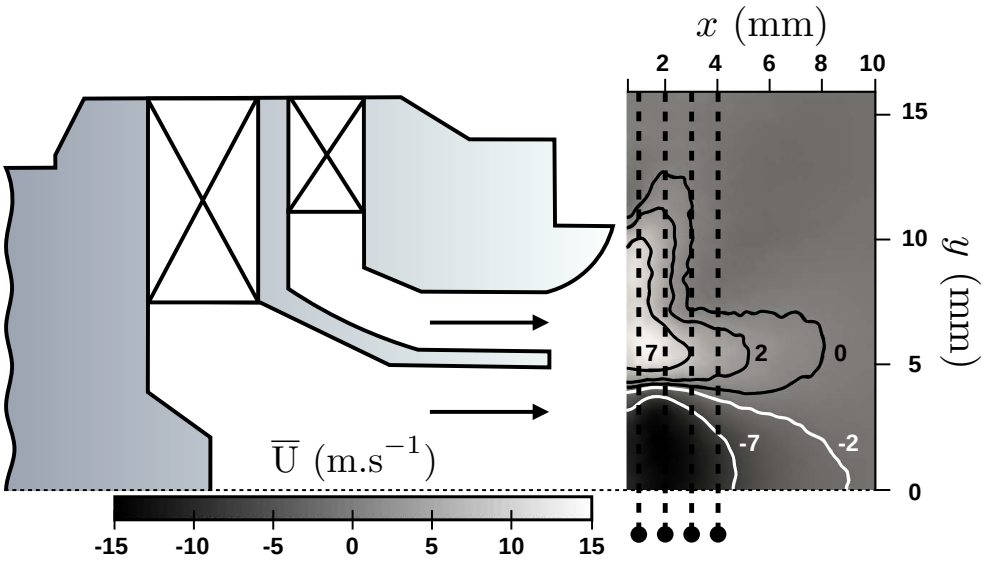

Figure 4.12: Mean velocity from PIV measurement and schematic representation of the swirl injector. White lines denotes negative mean velocity contours at −7 m.s^{-1} and −2 m.s^{-1}. Positives and zero mean velocity contours of 7 m.s^{-1}, 2 m.s^{-1} and 0 m.s^{-1} are shown with black line. Dashed-lines identify the position of the measurement cross-sections downstream of the exit plane at $x = 1, 2, 3, 4$ mm.

refinement levels defined by the AVBP+MMG3D procedure. For the mean axial velocity profile at $x = 1$ mm, the differences between simulation and PIV results in the shear regions may be explained by a limitation of the PIV spatial resolution [168, 169]. The LES results for the radial profiles of axial velocity on the AD 2 and AD 3 meshes give similar fields, again confirming grid convergence for the adaptation for this feature. A similar conclusion can be drawn for the radial profiles of turbulence intensities given in Fig. 4.15. This confirms that capturing the flow features that govern pressure losses through the swirl injector passages is sufficient for a good prediction of velocity fields further downstream in the chamber. This is not an obvious result: most of the mechanisms controlling pressure losses occur within the swirl injector passages where separation on the vanes change the effective sections and directly affect pressure losses. On the other hand, velocity and temperature profiles in the chamber are controlled by the local resolution in the chamber itself and not in the swirl injector. It is interesting to observe that an improved resolution within the swirl injector also increases the quality of the velocity profile far downstream of the swirl injector passages. This suggests that the mesh refinement metric for the pressure losses based on the kinetic energy dissipation provides most if not all of the refinement needed to predict the flow with accuracy.

Table 4.3: Error on the experimental mass flow rates recovered from PIV result.

Target mass flow rates (g.s^{-1})	PIV mass flow rates (g.s^{-1})	error (%)
4.29	3.99	7.0
3.22	2.95	8.4
2.15	2.04	5.1

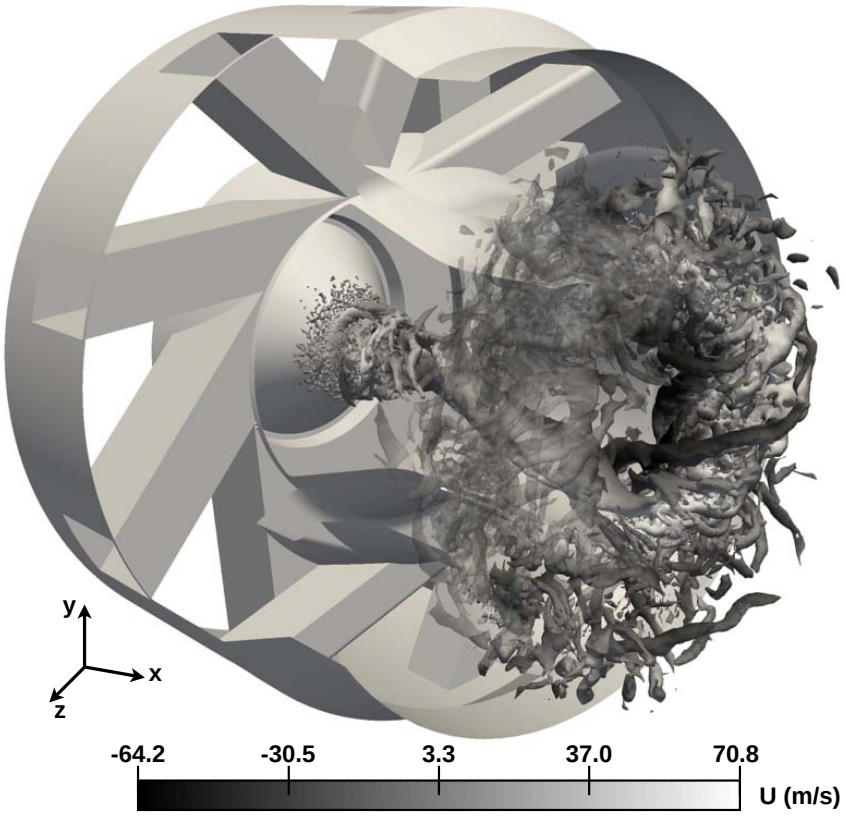

Figure 4.13: LES of the swirl injector on AD 2 mesh: Q-criterion $Q = 1.67 \times 10^4 (U_b/D)^2$ colored by axial velocity for the $m = 4.29$ g/s swirl injector case.

Table 4.4: Summary of the mesh adaptation LES on the swirl injector

	Coarse	AD 1	AD 2	AD 3
α		30	30	30
ϵ		0.3	0.3	0.7
T_{stat} (s)	0.04	0.04	0.04	0.04
time step (10^{-7} s)	1.0	1.0	0.35	0.23
number of cells (10^6)	1.4	3.1	10.8	14.7
number of CPU hours	6h22mn	11h44mn	20h20mn	33h40mn
number of cores	240	240	1140	1728
ΔP error	46%	10%	−0.7%	0.8%

4.3.5 Evaluation of costs

The previous sections have shown that the AVBP+MMG3D procedure provides accurate predictions of pressure losses as well as of velocity and turbulence profiles. A natural question is to determine the cost of this procedure: going from a coarse mesh to refined meshes increases the number of nodes and therefore the overall cost of the simulation. Table 4.4 summarizes the number of cells and the

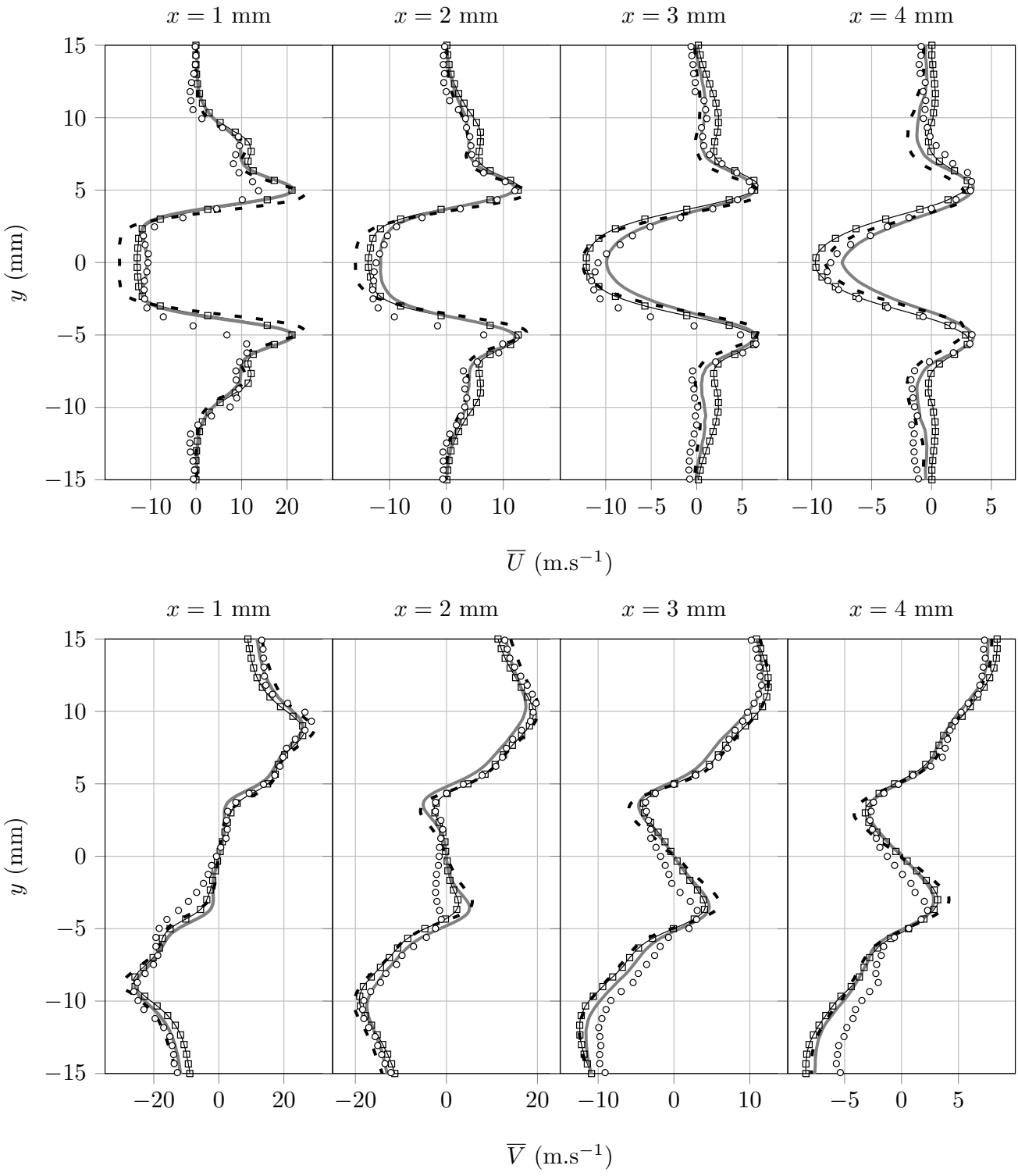

Figure 4.14: Comparison of the radial distribution of mean axial (top) and tangential (bottom) velocity at four axial locations (from left to right $x = 1, 2, 3, 4$ mm). Coarse mesh (dashed lines); mesh adapted 1 (squares); mesh adapted 2 (solid lines) and experiments PIV (circles).

CPU cost (number of hours to compute one flow-through time[2]) on all grids used for the $m = 4.29$

[2]All CPU costs are given on a single processor. Most runs were performed on 500 to 1000 processors but the parallel efficiency is almost unity for these cases so that the total CPU cost is a good measure of the mesh

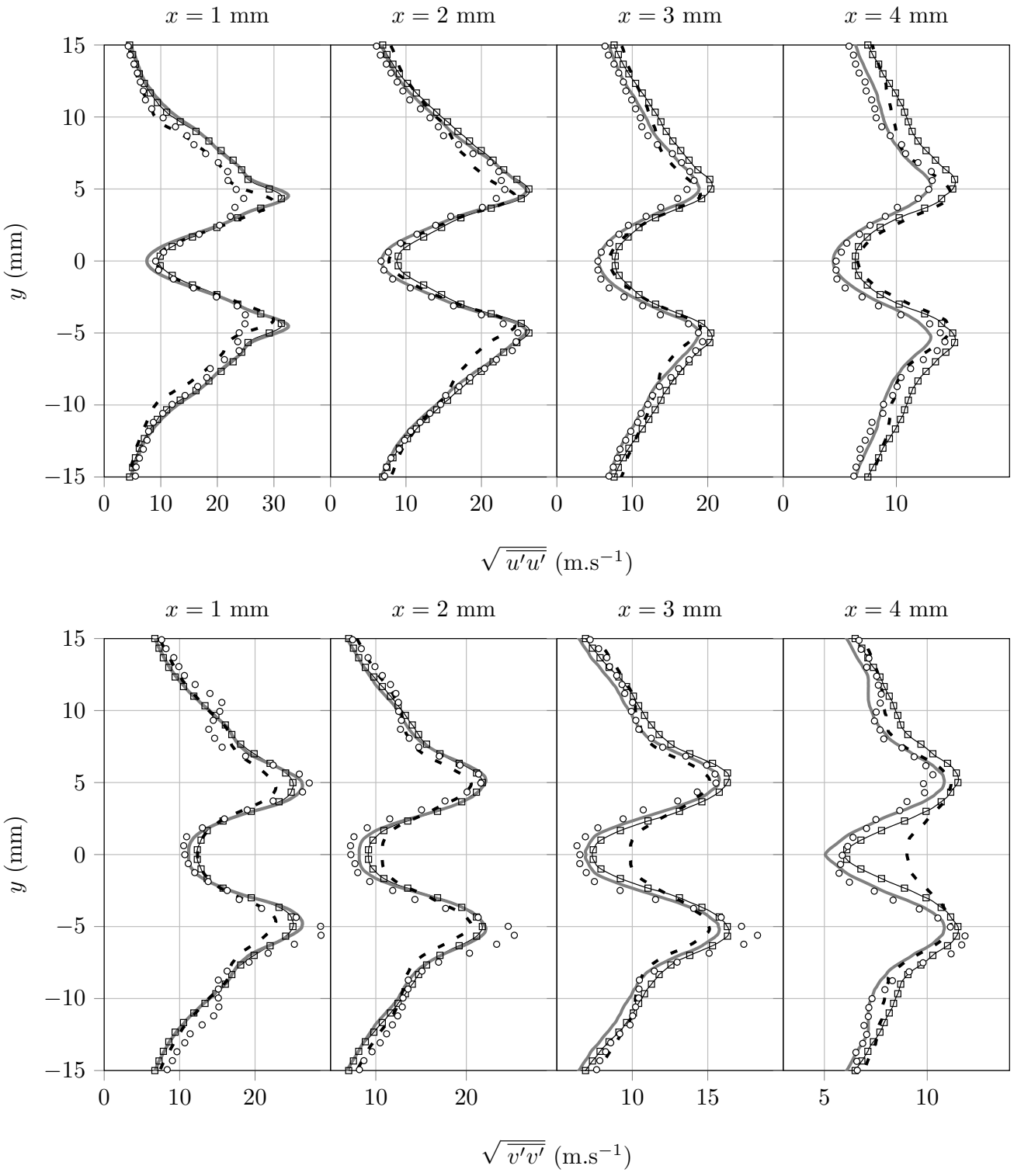

Figure 4.15: Comparison of the radial distribution of turbulence intensities in axial (top) and tangential (bottom) direction at four axial locations (from left to right $x = 1, 2, 3, 4$ mm). Coarse mesh (dashed lines); mesh adapted 1 (squares); mesh adapted 2 (solid lines) and experiments PIV (circles).

efficiency.

g/s case. Obviously the cost per flow through time increases when the mesh is refined. The increase is not proportional to the number of cells as the total time needed on each grid to achieve statistical convergence decreases because the initial flow is interpolated from the converged-average state on the previous mesh and hence is close to its own converged-average state. As a result, the cost of the refined mesh cases remains affordable to improve the capture of physical phenomena relevant to pressure losses.

Another relevant question is whether the proposed AVBP+MMG3D refinement algorithm is more efficient than a purely intuitive mesh refinement method, as typically performed manually by the user based on strong gradients in pressure or velocities. Looking at the various meshes created by the AVBP+MMG3D method (Fig. 4.10) shows that the method adds points in places which are not obvious to guess: they correspond to regions where $\overline{\Phi}$ is large and these regions, and their extent, do not correlate with easily identified flow-features. For example, not all shear layers are refined to the same extent, but only those that are highly relevant for pressure losses. As a result, an important aspect of the present refinement procedure is to offer a systematic and robust, user-independent method to optimize meshes for swirl injector computations. It is acknowledged that while certain users who have very good knowledge of a particular configuration may obtain a similarly efficient refinement based on their specific experience, a systematic computation methodology as AVBP+MMG3D allows to retain this efficiency for a large variety of flows.

Conclusion

A mesh refinement algorithm has been proposed that improves the prediction of pressure losses in Large Eddy Simulations of turbulent flow in swirl injectors at reasonable computational cost. The method is based on an existing compressible LES code (AVBP) and mesh refinement program (MMG3D). Mesh refinement is done only a few times (1 to 3) during a complete simulation and it uses only mean flow information. It is performed outside the LES solver and needs no intrusive modification of the solver itself. The metric that defines the local mesh size is the time-averaged value of the kinetic energy dissipation $\overline{\Phi}$. When this field is sufficiently well resolved, both pressure losses and velocity fields are correctly predicted.

The method is validated on two cases: (1) the flow through a diaphragm and (2) the flow through an industrial swirl injector used for helicopter engines. However, the method is not specific to these flows but may be applied to other flows. Results confirm its power in these two cases and suggest that it can be used for other LES solvers where it would bring a systematic, user-independent method to define meshes for LES tools.

We have shown that it is possible to accurately predict mean pressure losses in LES as all errors remained below 1%. It is then possible to return to the original problem: *How to predict acoustic damping across the same elements ?* In the following chapter, acoustic two-port matrices have been measured both in experiments and in LES, on meshes which have been adapted for the mean pressure loss. We will demonstrate that using such matrices in ROM can be sufficient to predict acoustic energy damping in academical configurations.

Chapter 5

Measurement of acoustic two-port matrices: application to acoustic losses prediction

This chapter focuses on the acoustic dissipation in Acoustically Compact Elements (ACEs). As shown in the previous chapters, there is a link between this dissipation at low frequency and the steady pressure drop: the limit of the T_{up} term in the primitive transfer matrix is linked to the pressure loss coefficient ξ (see equation 3.3.5, which will be validated in this chapter). As a consequence, a method has been provided in chapter4 in order to accurately predict the steady pressure drop in LES by using automated mesh refinement. The meshes used to predict the pressure drop are used here to measure acoustic two-port matrices in LES, which will be compared to experimental measurements.

Such acoustic two-ports are then introduced in a Reduced Order Model (ROM) of the PREINTRIG workbench and acoustic modes identified with the RootLocker solver (see chapter 2) are compared to a measure of the damping in the experiment.

Introduction

Acoustic dampers are used in combustion chambers in order to absorb sound. Indeed, including acoustic dampers such as perforated liners can prevent the onset of thermo-acoustic instabilities. Early works intended to model some simples ACEs such as perforated plates [20, 115] and provided analytical expressions for the primitive transfer matrix as shown in section 3.1.2.

At the same time, measurements were performed on experimental workbench by using the two-microphone technique originally developed by Seybert et al [170]. In this method, acoustic pressure measurements are performed at two different locations and acoustic wave amplitudes are retrieved by assuming one dimensional propagation. Later on, this method was improved by increasing the number of inputs: the multi-microphone technique [171, 21] combines the time traces of more than two microphones to lower the influence of additional perturbation such as turbulence.

Similarly, CFD data can be used to retrieve acoustic two-ports [82, 22, 172, 23, 173]. In this case, a new method, based on the inversion of the Wiener-Hopf equations [82] permits to obtained in only one or two simulations the complete two-port of an ACEs, that is to say for all frequencies of interest. However, this method implies to use a broad-band signal of excitation and it is thus very complicated to assess the linearity of the response[1].

This chapter is constituted as follows. The method dedicated to measure acoustic two-port in both experiments and simulations is detailed in section 5.1. The two-port matrices are then presented

[1]The two-port matrix formalism is valid as long as the system studied is linear.

in section 5.2: a comparison with existing models is provided with the diaphragm while interaction between hydrodynamical and acoustic modes is investigated in the case of the swirl injector. Finally, acoustic losses are scrutinized in section 5.3 where the damping measured in the experiment in the case of the diaphragm is compared to a dedicated ROM resolution, which is built upon both measured and modelled two-port matrices.

5.1 Measurement of two port matrices

In this section, a method used to retrieve the acoustic two-port matrix of an ACE from both experimental and numerical measurements is described. Taking a look at equation 3.1.1, it is clear that the two-port matrix of an ACE can be retrieved by using a set of at least two independent states [170] where both acoustic pressure and velocity are recorded upstream and downstream of the element. As long as experiments are concerned, direct measurements of acoustic velocity fields are not easy as they imply the use of fragile hot wires which are more intrusive than microphones located at the walls of the workbench. Concerning simulations, acoustic velocities are not more convenient to use: they are subject to acoustic boundary layers close to the walls.

It is easier to first reconstruct the scattering matrix by using the Riemann invariants (A^+,A^-) associated with the one-dimensional planar acoustic waves. These quantities may be retrieved by using a multi-microphones technique [174, 171, 175]. The two following steps are then applied to retrieve a scattering matrix:

- First, the Riemann invariants upstream and downstream of the ACE are reconstructed for each frequency.
- Then, the scattering matrix is obtained by using a set of at least two linearly independent states.

5.1.1 Acoustic wave decomposition

Under the assumption of harmonic signals, let a_j and ϕ_j, $j \in [\![1, J]\!]$ designate the respective amplitudes and phases of each acoustic pressure signals and J, the number of available microphones. The acoustic pressure at position z_j writes:

$$p'(z_j, t) = \Re(p(z_j)e^{i\omega t}) = \Re(a_j e^{i\phi_j + i\omega t}) \tag{5.1.1}$$

where p is the complex amplitude of the acoustic pressure. The determination of amplitude and phase of each temporal signals is performed by a non-linear sinusoidal regression. The Levenberg-Marquardt algorithm is used to minimize the following expression:

$$\Delta G_j = \int_{t_{\text{initial}}}^{t_{end}} |\mathrm{s_{j,estim}} - \mathrm{p'_j(t)}|^2 \, \mathrm{d}t \tag{5.1.2}$$

where $s_{j,\text{estim}} = a_{j,\text{estim}} \cos(\omega t + \phi_{j,\text{estim}})$. The one-dimensional acoustic decomposition introduced in chapter 1 is employed:

$$p(z_j) = a_j e^{i\phi_j} = A^+ e^{-ik\ z_j} + A^- e^{ik\ z_j} \tag{5.1.3}$$

$$\rho_0 c\, u(z_j) = A^+ e^{-ik\ z_j} - A^- e^{ik\ z_j} \tag{5.1.4}$$

where ρ_0 is the mean density and c the speed of sound while the origin $z = 0$ is taken at the center of the ACE. After estimating a_j and ϕ_j at different locations z_j, a system of J equations is formed to

determine the Riemann invariants A^+ and A^-:

$$\underbrace{\begin{pmatrix} e^{-ik\ z_1} & e^{ik\ z_1} \\ e^{-ik\ z_J} & e^{ik\ z_J} \end{pmatrix}}_{\mathrm{F}} \underbrace{\begin{pmatrix} A^+ \\ A^- \end{pmatrix}}_{\mathrm{x}} = \underbrace{\begin{pmatrix} a_1 e^{i\phi_1} \\ a_J e^{i\phi_J} \end{pmatrix}}_{\mathrm{b}} \tag{5.1.5}$$

Contrary to the two-microphone method described in [170], which are ill-conditioned for certain frequencies [176], the multi-microphones method rely on the inversion of an over-determined system of equations. The latter system is solved by using the least square method:

$$x = (F^\dagger F)^{-1} F^\dagger b \quad , \quad \epsilon = |Fx - b|/|b| \tag{5.1.6}$$

where $F^\dagger$ is the hermitian matrix of F. Using $J > 2$ microphones has multiple advantages [21, 171], such as reducing the impact of errors induced by turbulence or providing an estimation of the uncertainty ϵ. This method is also less sensitive to uncertainties associated with the locations of the sensors. In the experiment, the microphones are located at the side of the rig, as shown in Fig. 3.10 and are not equally spaced as explained in appendix D.

Finally, Mach effects may be taken into account by modifying the up and down-travelling wave numbers [177, 175] $k^+ = \frac{\omega/c}{1+M}$ and $k^- = \frac{\omega/c}{1-M}$. However, only cases where $M < 0.01$ will be investigated in the present chapter so that these corrections are neglected.

5.1.2 From the acoustic waves to scattering matrix

The acoustic waves complex amplitudes notations (following the notations introduced in chapter 1) obtained upstream and downstream of the acoustic element are summarized in figure 5.1.

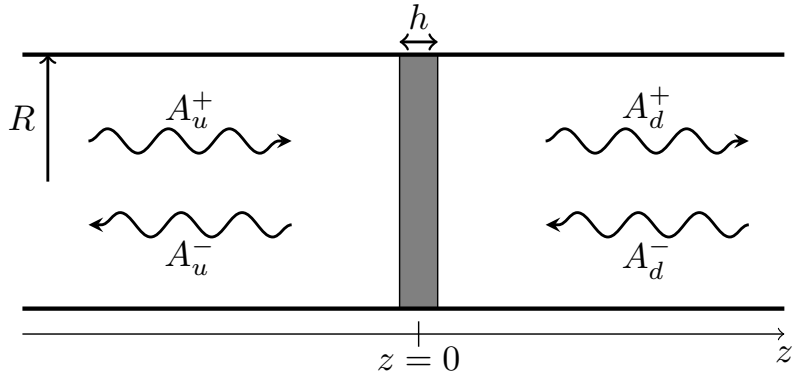

Figure 5.1: Description of the acoustic waves. The origin of the z axis is located at the center of the ACE (thickness h). The waves amplitudes $A_{u,d}^{+,-}$ are valid at $z = 0$.

Following the work of Holmberg [175], the scattering matrix (equation 3.1.3) is reconstructed. Let N denotes the number of linearly independent datasets available. The following system of equations is

solved to obtain the scattering matrix:

$$\underbrace{\begin{pmatrix} A^+_{u,1} & A^-_{d,1} & 0 & 0 \\ 0 & 0 & A^+_{u,1} & A^-_{d,1} \\ A^+_{u,i} & A^-_{d,i} & 0 & 0 \\ 0 & 0 & A^+_{u,i} & A^-_{d,i} \\ A^+_{u,N} & A^-_{d,N} & 0 & 0 \\ 0 & 0 & A^+_{u,N} & A^-_{d,N} \end{pmatrix}}_{\mathrm{G}} \underbrace{\begin{pmatrix} t_u \\ r_d \\ r_u \\ t_d \end{pmatrix}}_{\mathrm{s}} = \underbrace{\begin{pmatrix} A^+_{d,1} \\ A^-_{u,1} \\ A^+_{d,i} \\ A^-_{u,i} \\ A^+_{d,N} \\ A^-_{u,N} \end{pmatrix}}_{\mathrm{a}} \tag{5.1.7}$$

The complex system of equation 5.1.7 is over-determined when $N > 2$. By applying a least square method, one gets an estimation of s and its associated relative error:

$$s = (G^\dagger G)^{-1} G^\dagger a \quad , \quad err_{\text{relative}} = ||Gs - a||/||a|| \tag{5.1.8}$$

The $N = 2$ case has already been described by Fischer et al [21]. However, using more than two linearly independent states allows to estimate the uncertainty associated with each matrix [178]. In the following of the chapter, all experimental matrices have been obtained with at least four different states which were represented in Fig. 3.10 while two-port matrices extracted from simulations were obtained with two states.

5.2 Two-port Matrices

In this section, we present two-port matrices obtained in both experiments and LES for the diaphragm case and two-port matrices from experiments only for the swirl injectors cases S1 and S2.

5.2.1 Diaphragm case

The diaphragm introduced in section 3.3.2 is fit in the junction between ducts 2 and 3 (see Fig. 3.6). The scattering matrices of the diaphragm are shown against HM and MHM models[2] in Figs. 5.2.

Experimental results are displayed with error bars (see equation 5.1.8) from 20 up to 1000 Hz while LES results are provided for 6 discrete frequencies. LES have been carried out by Franchine Ni at CERFACS. The setup of the LES is described in [65].

First, experimental and numerical data are in excellent agreement: both gains and phases are well reproduced. This proves that LES data can be used to retrieve acoustic two-port matrices. Second, as the ratio between the radius and the thickness of the diaphragm is small, both models HM and MHM provide similar results. However, small differences exist for low frequencies ($f < 200$ Hz) where the phases of the measured reflection coefficients do not properly match the models.

Concerning experimental data, the four configurations used to retrieve the two-port matrices provide accurate results (errors remains below a few percent). Strong vibrations have been observed in the experimental rig in the 500-600 Hz frequency range. These may explain the important uncertainties observed in this region.

Finally, one may observe that both transmission $t_u\, t_d$ and reflection $r_u\, r_d$ coefficients are equal. This stems from the conservation of the acoustic flow-rate q across the ACE: the two-port is completely

[2]The two uniform models described in chapter 3 have not been added to the graphs because they provide results very similar to the corresponding Howe models.

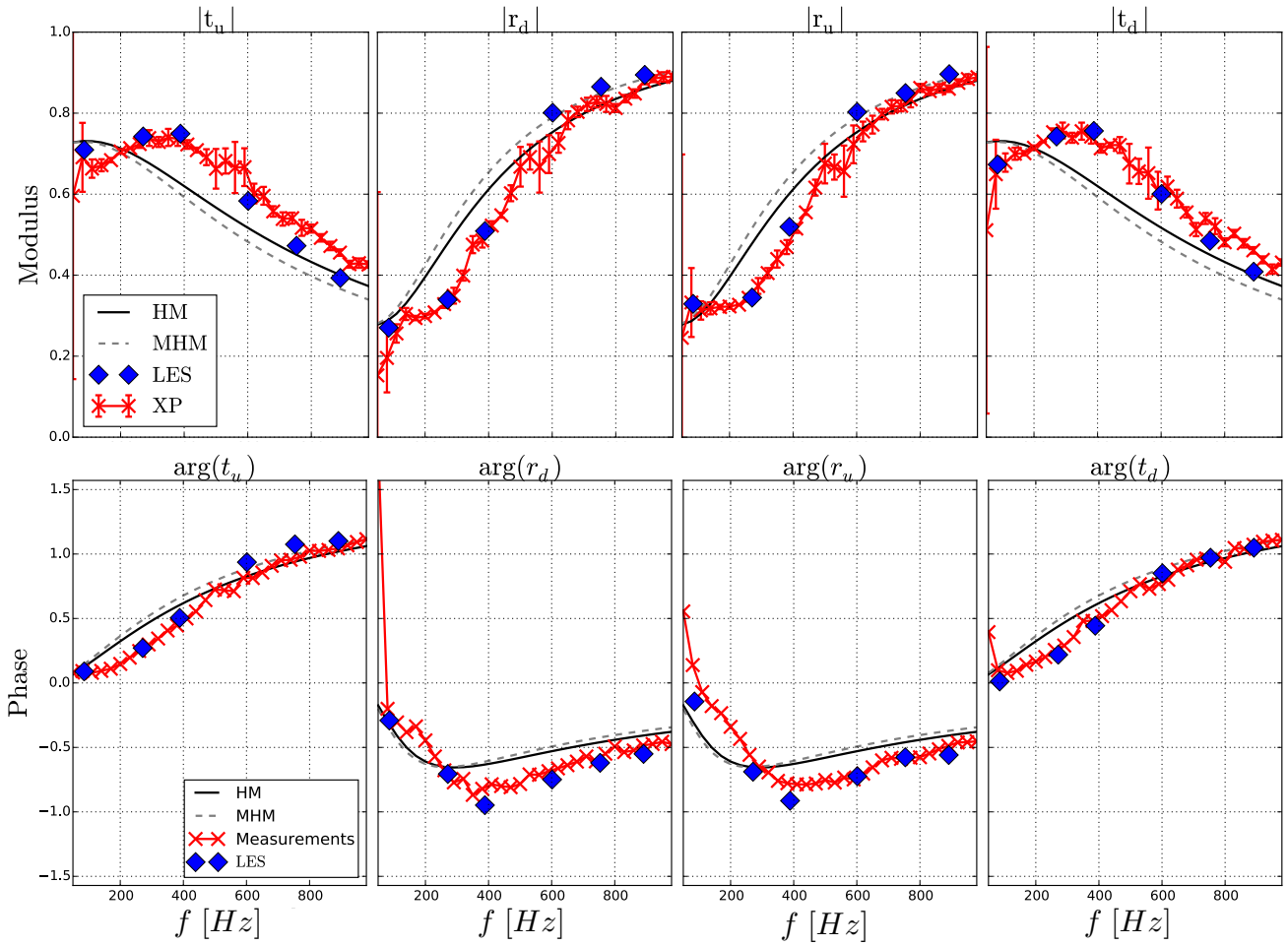

Figure 5.2: Scattering matrix of the diaphragm at $U_u = 0.344\,ms^{-1}$. Top: modulus, bottom: phases.

characterized by the Rayleigh conductivity as shown in equation 3.1.8 for the primitive transfer matrix. The corresponding scattering matrix can be deduced:

$$S = \frac{1}{1-\xi}\begin{pmatrix} 1 & -\xi \\ -\xi & 1 \end{pmatrix} \tag{5.2.1}$$

and is symmetrical with both transmission coefficients equal to each-other. Acoustic primitive transfer matrices can be deduced from scattering matrix by using equation 3.1.4. The corresponding two-ports at the same flow-rate ($U_u = 0.344\ m.s^{-1}$) are displayed in Fig. 5.3.

One can notice that diagonal terms T_{uu} and T_{pp} are equal to one which is the expected behavior for an ACE placed in a constant section channel as stated in equation 3.1.8. The T_{up} term is more interesting as it is the only one which varies with frequency as shown theoretically in section 3.1.2.1 by equation 3.1.8: $T_{up} = 2\zeta$. Its phase is in good agreement with both HM and MHM models, especially for frequencies above 400 Hz. However, its modulus is sightly over-estimated by both models.

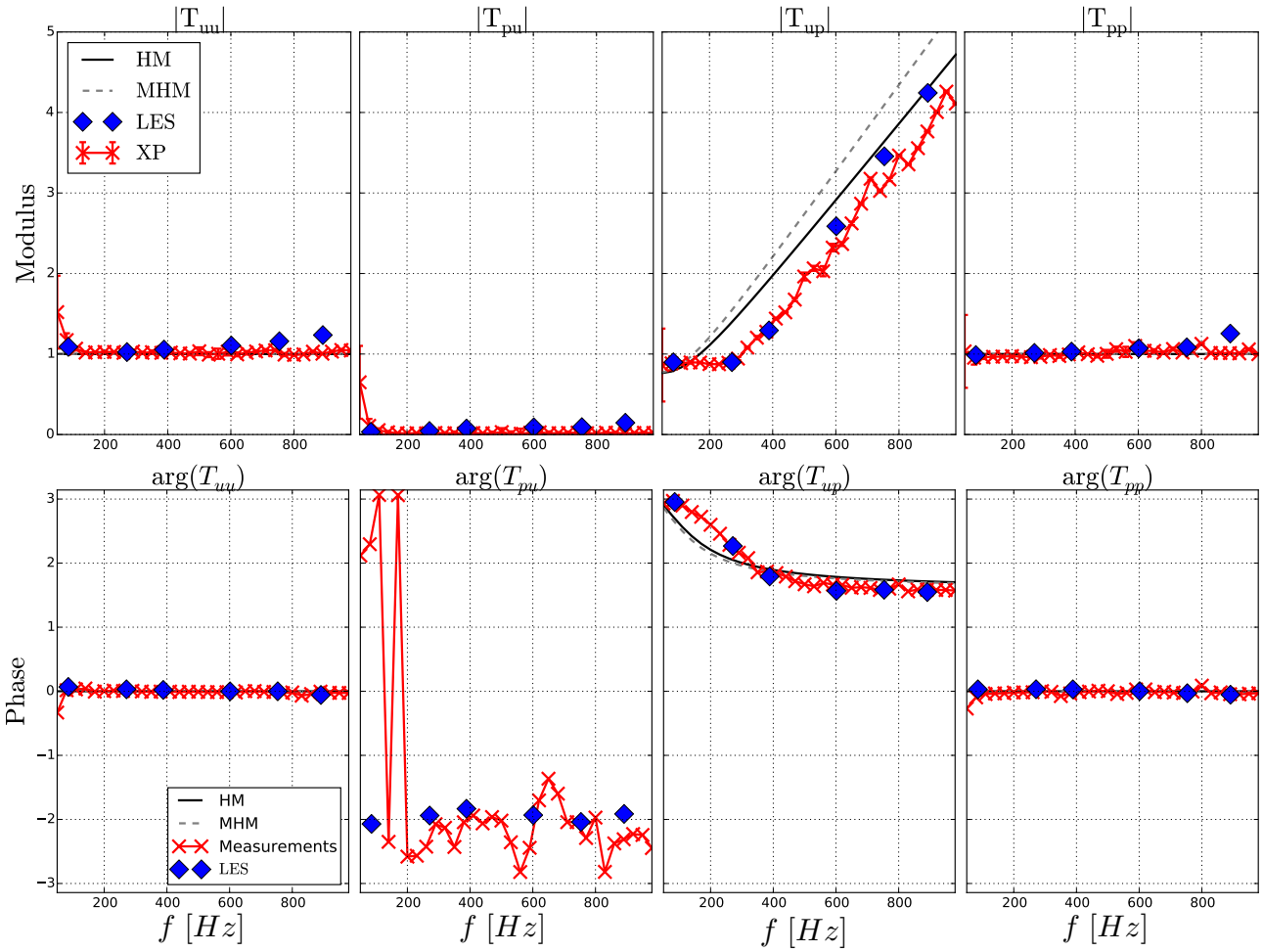

Figure 5.3: Transfer matrix of the diaphragm at $U_u = 0.344\,ms^{-1}$. Top: modulus, bottom: phases.

The influence of the mean flow is then investigated experimentally through the T_{up} term for three different flow-rates: $U_u = 0.172, 0.344, 0.516\ m.s^{-1}$ and the results are gathered in Fig. 5.4. Moreover, experimental measurements of mean pressure losses shown in chapter 4 have also been recast as transfer coefficient and displayed in Fig. 5.4. The link between transfer and pressure loss coefficient was established in equation 3.2.6 and is recalled here for the sake of clarity:

$$T_{\Delta \text{P}} = \frac{U_u}{c}\xi_{\text{XP}} \tag{5.2.2}$$

where $T_{\Delta \text{P}}$ corresponds to the equivalent transfer coefficient associated with a mean pressure drop. Two important features are observed:

- In the low frequency limit, the T_{up} term goes to a constant value which is in good agreement with the mean pressure drop experimental measurement detailed in section 4.2. These results are also coherent with the uniform model (approximation of the Howe model HM) which predicts a linear dependency to the bulk upstream velocity U_u.

- In the high frequency limit, the three flow-rates provide similar results: the slope is independent of the mean flow-rate and the gain shift between the three curves remains small. This behavior is predicted by the uniform model $UM1$ but also by both HM and MHM models.

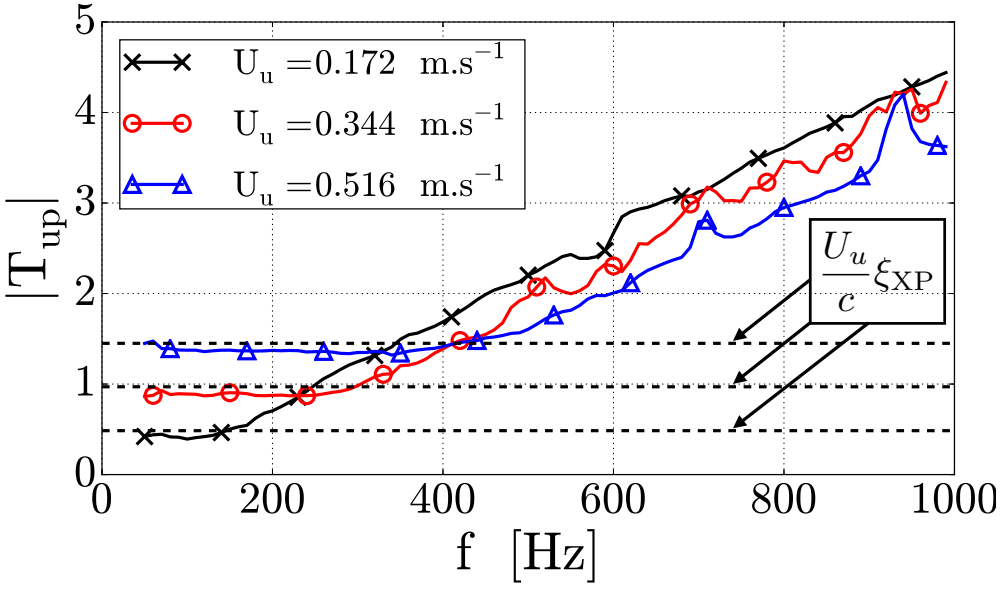

Figure 5.4: Gain of the T_{up} term measured experimentally for three different flow-rates. The horizontal dashed lines corresponds to the experimental measurement of pressure losses obtained in chapter 4 and recast into transfer coefficient

In this section, we showed that acoustic two-ports measured in both experiments and simulations exhibited excellent agreement. Moreover, the results obtained are coherent with existing models and the uncertainties remains very low below 5% for all frequencies. As a consequence, the following study of an industrial swirl injector is conducted only in experiments.

5.2.2 Swirl injectors

The study of the swirl injectors is more demanding. The flow is much more turbulent and the workbench becomes noisy. As a consequence, the acoustic forcing level must be increased to maintain a correct signal to noise ratio. For instance, the S1 injector generates noise at a frequency which scales with the mass flow rate as shown in Fig. 5.5, left.

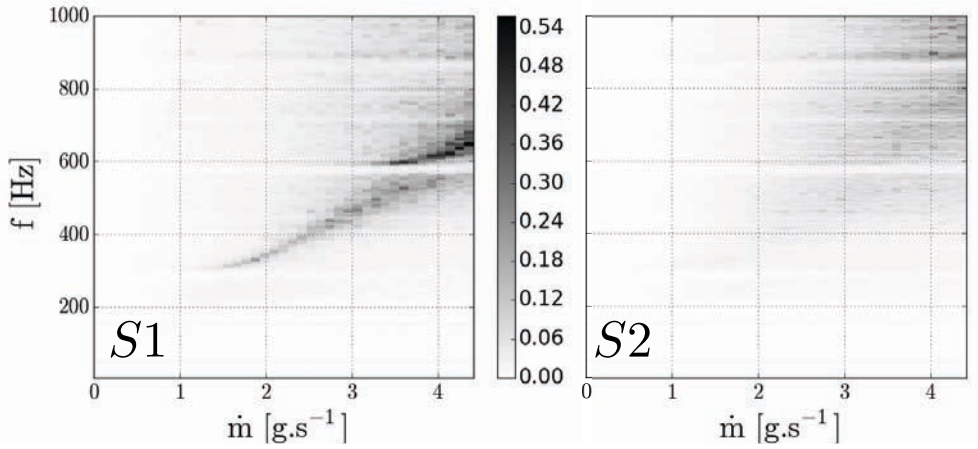

Figure 5.5: Amplitude of acoustic fluctuations as a function of flowrate and frequency for the injectors S1 (left) and S2 (right). The addition of a cylindrical rod in the S2 injector diminishes the noise when compared to the S1 injector.

It has been observed experimentally that placing a small object at the center of the outlet plan of the swirl injector S1 lowered the sound self generated by the system. This discovery led to the design of

the swirl injector S2 on which a cylindrical rod has been inserted as shown in Fig. 3.8, right. The mass flow / frequency map of this new injectors is displayed in Fig. 5.5, right: much less noise is generated.

5.2.2.1 Injector S1

The swirl injector S1, shown in figure 3.8 is placed in the junction between ducts 2 and 3 as sketched in figure 3.6 and the corresponding scattering matrices obtained at three different flow-rates: $U_u[m.s^{-1}] \in [0\,,\,0.172\,,\,0.344]$ are shown in figures 5.6, 5.7 and 5.8 respectively.

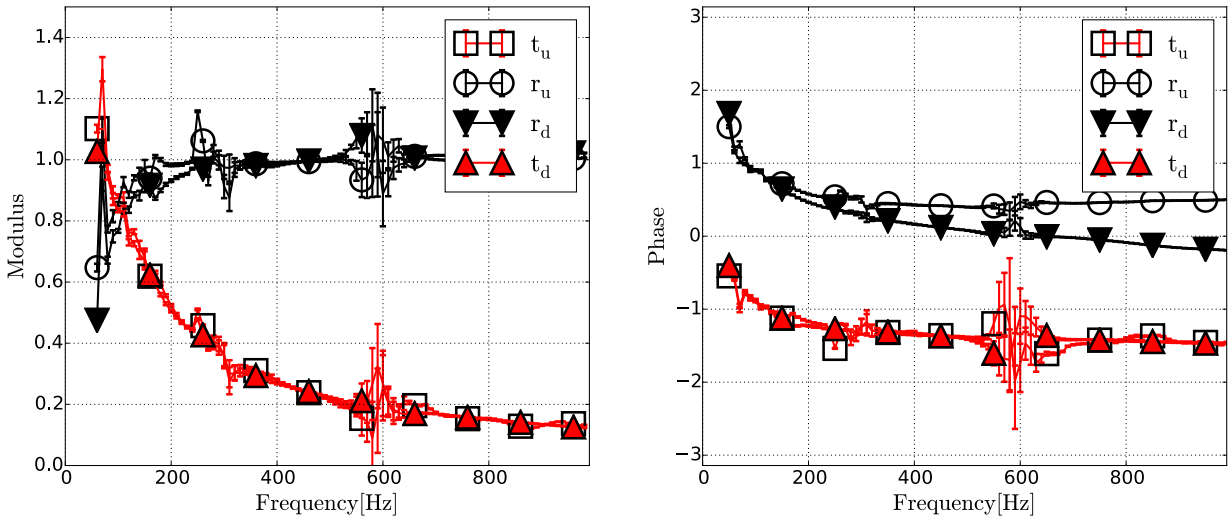

Figure 5.6: Amplitude and phase of the scattering matrix of the swirl injector (S1) at rest. (U_u = 0 m.s^{-1})

As expected for the passive system constituted by the swirl injector at rest, all reflection and transmission coefficients are below unity except for frequencies below 50 Hz. Moreover, transmission and reflection coefficients from upstream and downstream are identical in term of magnitude but a small difference is observed in the phase of r_u and r_d as the frequency is increasing. This prove that the swirl injector is not fully compact, as predicted in equation 3.3.4. The uncertainties remain small except in the $500 - 600\ Hz$ frequency range where the rig itself suffered from mechanical vibrations. This region of important uncertainties is also observed for the diaphragm.

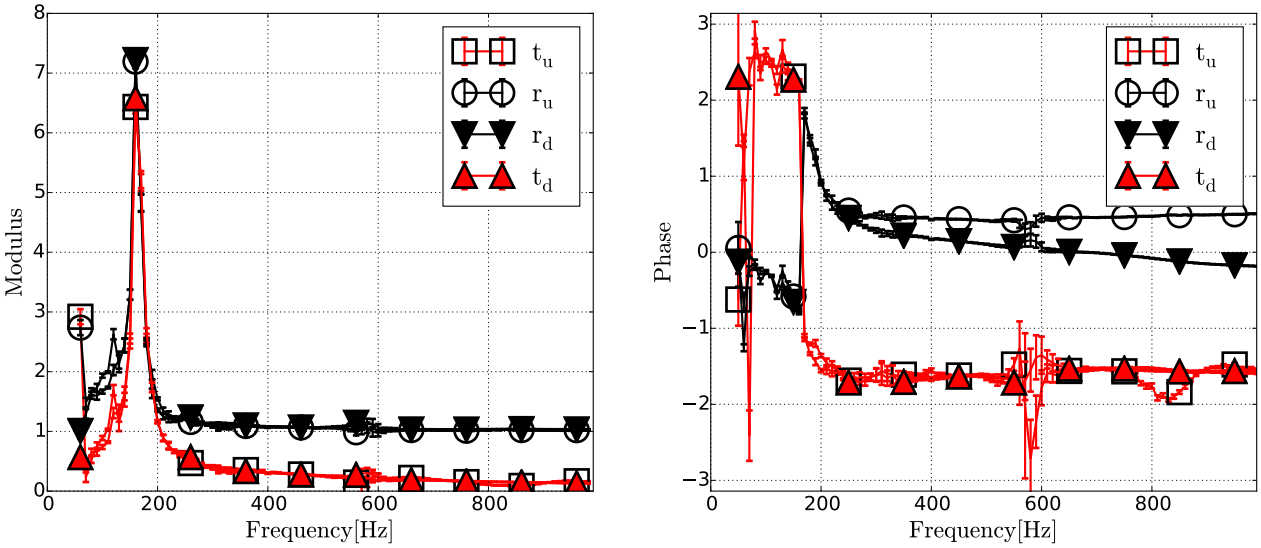

Figure 5.7: Amplitude and phase of the scattering matrix of the swirl injector (S1) at intermediate flow rate. (U_u = 0.172 m.s^{-1})

Concerning the intermediate flow-rate ($U_u = 0.172\,\mathrm{m.s^{-1}}$), a sharp peak in transmission and reflection coefficients is observed at 165 Hz. For frequencies above 200 Hz, these coefficients are similar to the one measured at rest. Uncertainties in the region of the peak are small enough to ensure that it is a physical effect and not an artefact. Phases are also affected in the peak region: They are shifted by $\Delta\phi \approx \pi$ when compared to the values measured in the case at rest.

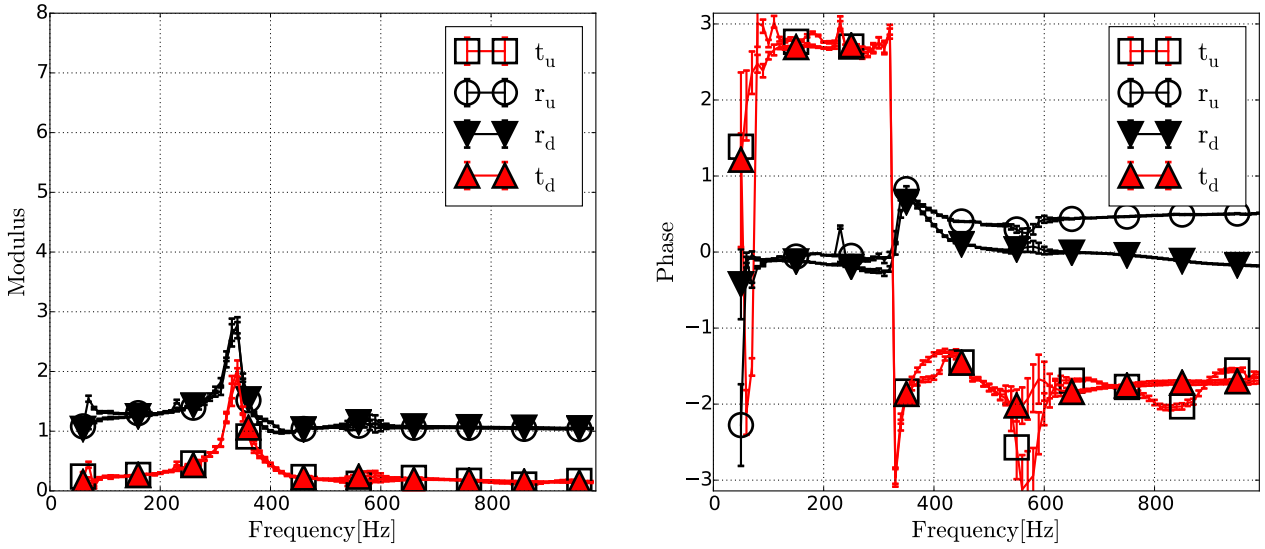

Figure 5.8: Amplitude and phase of the scattering matrix of the swirl injector (S1) at higher flow rate. ($U_u = 0.344\,\mathrm{m.s^{-1}}$)

Finally, for the highest flow-rate ($U_u = 0.344\,m.s^{-1}$), the peak is still present but shifted up to 335 Hz which is twice the frequency observed with the previous flow-rate (165 Hz). Moreover, peaks of reflection and transmission coefficients have different amplitudes, approximately 3 and 2 respectively and these amplitudes are also lower than the one obtained at the previous flow-rate (≈ 7).

The presence of these peaks is counter-intuitive. Indeed, they lead to acoustic energy amplification, which was not expected for a passive system. This point is investigated in section 5.2.2.3.

5.2.2.2 Injector S2: inhibiting instabilities

The injector S2 is mainly constituted of the same swirl injector, with an extra rod added on top of the plug, in the precessing vortex core. Although not modifying in a significant manner the pressure losses (the difference is below 5% the the flow-rates considered here.), the presence of the rod diminishes the acoustic noise that is generated by the swirl injector as shown in Fig. 5.5. It is thus important to determine whether differences are observed in the scattering matrix of the S1 and S2 elements or not. The modulus of the corresponding scattering matrices are displayed in fig 5.9 for the three same flow-rates ($U_u = 0$, 0.172, 0.344 $m.s^{-1}$).

In order to compare the injectors S1 and S2, the same excitation signals have been used to force the acoustic waves. First, the scattering matrices of the two injectors are identical in the absence of mean flow (see Figs. 5.9, left and 5.6). Second, when a mean flow $U_u \neq 0$ is imposed, peaks in transmission (t_u, t_d) and reflection (r_u, r_d) coefficients are still observed for the injector S2 (see Fig. 5.9, center and right) However, the amplitudes of the peaks are diminished when compared to the injector S1: for the intermediate flow-rate ($U_u = 0.172\,m.s^{-1}$), it decreases from 7 (Fig. 5.7) down to 2 (Fig. 5.9, center).

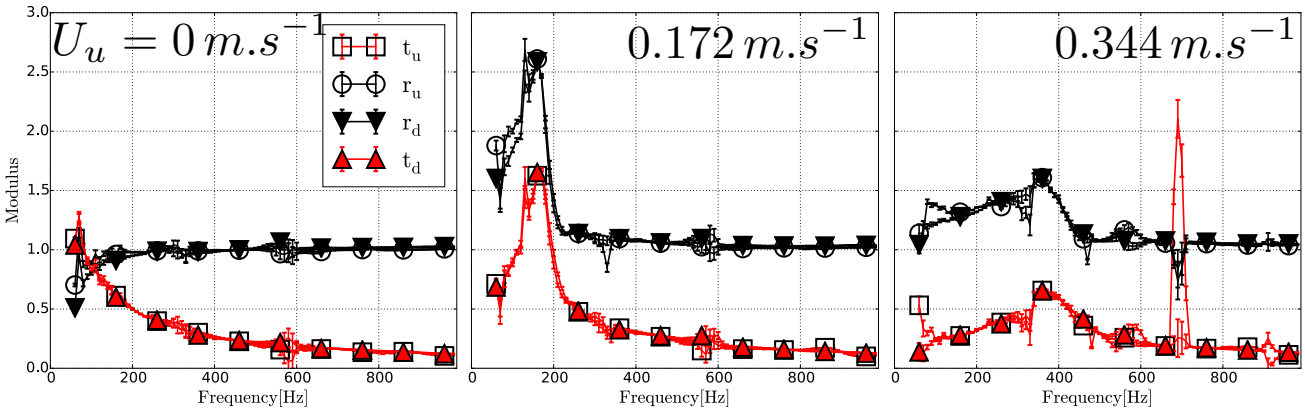

Figure 5.9: Amplitude of the scattering matrix for the S2 configuration. From left to right, the three studied flow-rates: U_u = 0, 0.172, 0.344 $m.s^{-1}$

5.2.2.3 Discussion

As both scattering matrices of injectors S1 and S2 are identical in the absence of mean flow, the rod does not modify significantly the transmission and reflection coefficients of the swirl injector. Furthermore, peaks in transmission and reflection coefficients are observed at frequencies scaling with the imposed flow-rate. A Strouhal number may be used to characterize the peak frequencies at different flow-rates:

$$St = \frac{fD}{u_s} \tag{5.2.3}$$

where $D = 2r$ is taken as the diameter of the outlet rim of the injector and U_s, the corresponding bulk velocity (taken at the outlet of the swirl injector). This bulk velocity is obtained by closing a volume-flow budget between the plenum and the outlet of the swirl injector:

$$St = 2\left(\frac{R}{r}\right)^2 \frac{fr}{U_u} \tag{5.2.4}$$

where R is the radius of the plenum and r, the radius of the swirl injector outlet (see section 3.3.2 for the complete description of the swirl injectors). For the injector S1, Strouhal numbers of 0.85 and 0.86 have been obtained for the two higher flow-rates U_u = 0.172 and 0.344 $m.s^{-1}$ respectively. Furthermore, strouhal numbers are more difficult to define with a sufficient precision for the injector S2 as the peaks are too damped, but are also roughly equal to 0.85. The constant Strouhal number is typical of hydrodynamic instabilities which may occur in the center recirculation zone in the wake of the swirl injector [179]. This suggests that acoustic waves interact with the hydrodynamic instability.

The acoustic wave reconstruction method only detects coherent acoustic signals. Therefore, acoustic waves generated by hydrodynamic instabilities must be locked in phase with the external forcing. The existence of a coupling between forced acoustic and hydrodynamic instabilities may also explain the transmission and reflection values greater than one in the peak s regions [175]. In the following, we provide a possible scenario which can explain this behaviour.

The hydrodynamic instability results in an acoustic source term through convective to acoustic mode conversion. This instability may be locked in phase with the forced acoustic waves for Strouhal numbers close to 0.85, but its strength is quasi not affected by the amplitude of the incoming acoustic wave. It is possible to decompose the observed S_O scattering matrix into passive and active source contributions:

$$\begin{pmatrix} A_d^+ \\ A_u^- \end{pmatrix} = S_O \begin{pmatrix} A_u^+ \\ A_d^- \end{pmatrix} = \underset{\text{Passive}}{S} \begin{pmatrix} A_u^+ \\ A_d^- \end{pmatrix} + \underset{\text{Active}}{g(St)} \begin{pmatrix} \alpha \\ \beta \end{pmatrix} \tag{5.2.5}$$

where S stands for the passive scattering matrix of the system. The second term of the RHS of equation 5.2.5 is an active source term. The function g peaks to unity around $St = 0.85$ and decreases rapidly to zero elsewhere. α and β are the complex amplitudes of the acoustic source terms emitted in upstream and downstream direction. The relation between the observed scattering matrix (S_O) and the source term may be retrieved by rewriting the latter as a function of the incoming acoustic waves:

$$\begin{pmatrix} \alpha \\ \beta \end{pmatrix} = \begin{pmatrix} \frac{\alpha}{2A_u} & \frac{\alpha}{2A_d} \\ \frac{\beta}{2A_u} & \frac{\beta}{2A_d} \end{pmatrix} \begin{pmatrix} A_u^+ \\ A_d^- \end{pmatrix} \tag{5.2.6}$$

By combining equations 5.2.5 and 5.2.6, it is possible to express the observed scattering matrix S_O as a combination between the passive scattering matrix and the source term:

$$S_o = \begin{pmatrix} t_u + \frac{\alpha}{2A_u} & r_d + \frac{\alpha}{2A_d} \\ r_u + \frac{\beta}{2A_u} & t_d + \frac{\beta}{2A_d} \end{pmatrix} \tag{5.2.7}$$

As exhibited in equation 5.2.7, both observed transmission and reflection coefficients may be greater than one although their passive contributions (t_u, r_d, r_u, t_d) remain bounded below unity. Such situations may occur when the amplitude of excitation is lower than the source term strengths α and β. Despite the non uniqueness of the decomposition performed in equation 5.2.6, this explain the existence of transmission and reflection coefficients greater than unity.

In order to validate this model, it would be necessary to measure the observed scattering matrix at a different level of forcing excitation or to use system identification (SI) methods as recently described by Sovardi [180].

5.3 Acoustic losses: a detailed comparison

The objective of this section is to prove that the acoustic modes of academic systems containing one or more ACEs can be predicted by Reduced Order Models (ROM) built on top of acoustic two-port matrices. As the two-port matrices of the swirl injectors S1 and S2 were subject to acoustic/hydrodynamic instabilities, it has been decided to focus only on the diaphragm case.

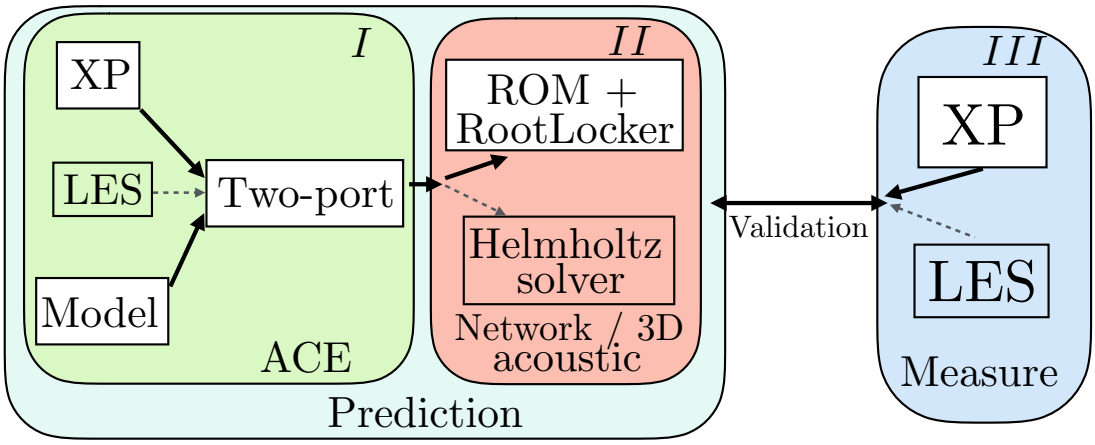

Figure 5.10: Work-flow of the comparison between predicted and measured acoustic damping. The paths denoted by the solid black arrows correspond to the work presented in the manuscript. The paths denoted by the gray dashed arrows have been investigated in [65]

The work-flow of this section is synthesized in Fig. 5.10 where we follow the paths denoted by black solid arrows: first, two-port matrices (modelled or measured in the experiment) are obtained (I, see

section 5.2) and then introduced in a ROM (II, see equation 5.3.1), which solutions contain both the tone ($\Re f$) and the damping rate ($\Im f$). In the same time, measurements of damping rates are performed in the experimental rig PREINTRIG by using an harmonic response method described in [181]. (III, see section 5.3.4). These results are then compared in section 5.3.4 and a good agreement is observed.

The other dashed paths introduced in Fig. 5.10 have been reported by Franchine Ni [65]. LES can be used to measure two-port matrices (see Fig. 5.2) as well as damping rates. The two-port matrices are then integrated in a 3D Helmholtz solver instead of a ROM.

5.3.1 ROM of the PREINTRIG rig in the P-ROM configuration

As detailed in section 3.2.1, the damping of an acoustic mode is a function of the entire network description and not only the ACE. For instance, an acoustic mode with a velocity node at the location of a diaphragm will not be damped. Conversely, acoustic modes can be computed numerically from the knowledge of scattering matrices and boundary conditions [175] in simple configurations by solving a ROM.

The flush mounted loudspeaker configuration used to measure the acoustic two-port is not suitable for the measurement of natural acoustic modes. Indeed, a quantitative comparison with a ROM would require an accurate modelling of the loudspeaker impedance, which is not available. An other configuration is used instead: the forcing system is moved to the side of the main duct and connected by a small aperture. The corresponding configuration is displayed in Fig. 5.11.

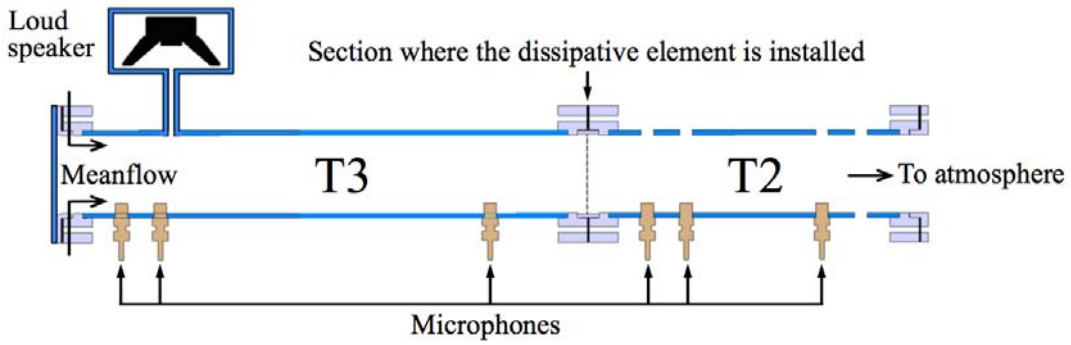

Figure 5.11: sketch of the PREINTRIG rig configuration used for acoustic modes measurement.

As the loudspeaker is displaced at the side of the main duct, a precise knowledge of its impedance is no more needed. The occurrence of unwanted acoustic modes, which arise from the coupling between the loudspeaker system and the main duct can be avoided by using a small connection between the loudspeaker casing and the main system {T3 + T2}. A detailed proof of this assumption is provided in appendix B in which experimental measurements are compared to a ROM of the complete system. This configuration is denoted as P-ROM in the following of the manuscript.

A sketch of the P-ROM configuration in which the diaphragm is inserted is displayed in Fig. 5.12. The acoustic end corrections $\delta_{\text{in}}, \delta_{\text{out}}$ will be determined experimentally in section 5.3.3.

The corresponding ROM is retrieved by following the method described in chapter1:

$$\det\left(\mathrm{R}_{\mathrm{L2}+\delta_{\text{in}}} T(\omega) \mathrm{R}_{\mathrm{L2}} \begin{pmatrix} R_{\text{inlet}} \\ 1 \end{pmatrix}, \begin{pmatrix} 1 \\ R_{\text{outlet}} \end{pmatrix}\right) = 0 \tag{5.3.1}$$

where $T(\omega)$ is the transfer matrix of the diaphragm which can be either measured or modeled. For the sake of clarity, fully reflective boundary conditions are applied at both inlet and outlet: $R_{\text{inlet}} = 1$ and $R_{\text{outlet}} = -1$.

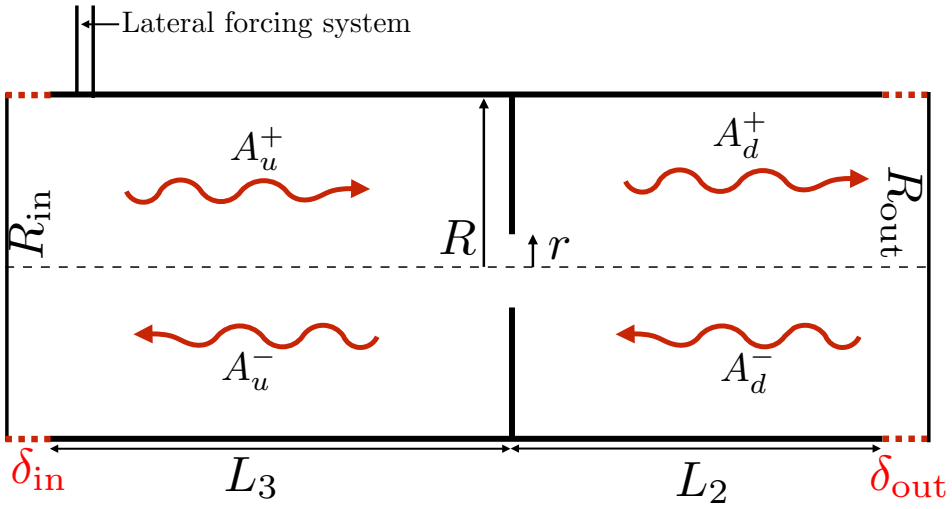

Figure 5.12: Sketch of the PREINTRIG rig in the P-ROM configuration: The forcing system {Loudspeaker + casing} is displaced at the side of the rig.

5.3.2 Experimental damping measurement

Acoustic modes are retrieved by forcing the test rig at different frequencies using a loudspeaker located at the side of the rig (see Fig. 5.11). The acoustic waves complex amplitudes A^+, A^- are measured in upstream and downstream ducts by using the multi-microphone technique described in section 5.1.1. Focusing at the acoustic waves amplitudes permits to directly observe the acoustic modes from inside of the workbench: a peak in acoustic wave amplitude corresponds to an acoustic mode.

A model which takes into account damping and assumes that the system behaves like an oscillator driven by an external forcing is used to fit the experimental data around a mode and permits to retrieve both its tone and damping rate [182]. This method has been described in detail by Mejia et al [181] to characterize the damping/growth rate of a laminar burner and we only focus here on its application. The model used for the acoustic wave amplitude around a mode writes:

$$|A\ \ (\omega = 2\pi f)|^2 = \frac{g}{(\omega_0^2 - \omega^2)^2 + 4(\nu\omega)^2}\ ,\ f \in \mathbb{R}^+ \tag{5.3.2}$$

where $\omega_0/(2\pi)$ is the real part of the complex frequency of the acoustic mode and ν, its damping rate. It is important to note that the gain g is not relevant to characterize the acoustic modes and will not be assessed in the following of the study. Indeed, this parameter is proportional to the forcing level, which is chosen small enough in order to avoid the occurrence of non-linear dissipation.

An example of curve fitting performed on experimental data is shown in Fig. 5.13. One can notice that the model perfectly fits the data.

Measurements of acoustic modes have been conducted for two different setups:

- The single duct configuration has been examined (Duct Configuration). In this case, the diaphragm has been replaced by an element with the same inner radius as both upstream and downstream ducts, leading to a constant cross section along the test rig. In this case, no dissipation is expected.

- the diaphragm configuration has then been studied at two different flow-rates: one case at rest, when no dissipation is expected across the diaphragm[3] and the other at an intermediate flow-rate: $U_u = 0.344\ m.s^{-1}$.

[3]In the absence of the mean flow, only non-linear dissipation is expected.

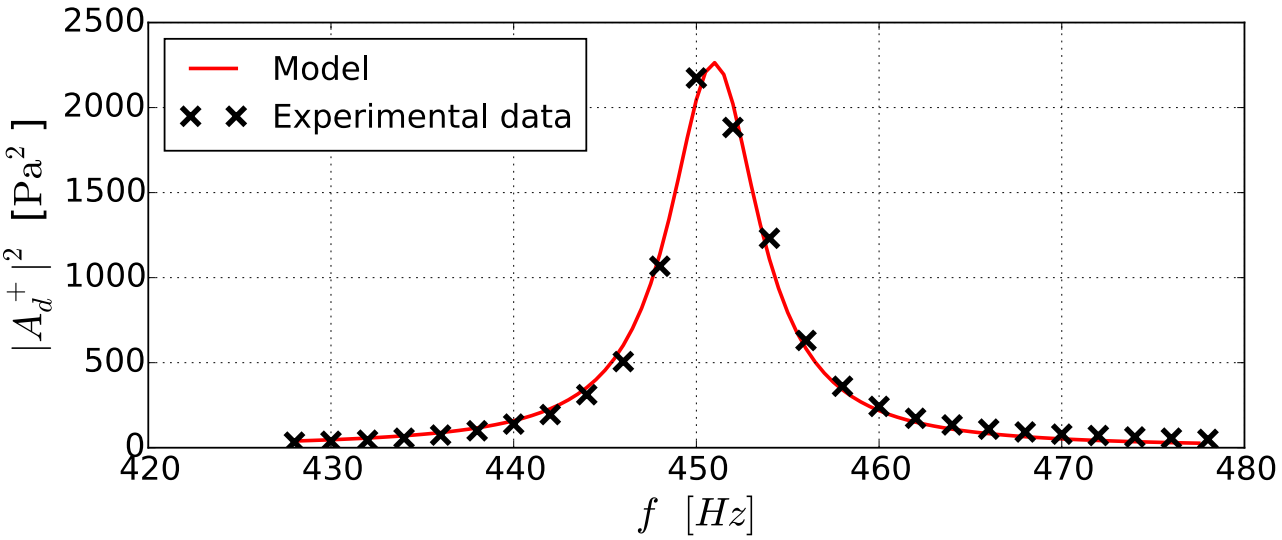

Figure 5.13: $|A_d^+|^2$ as a function of frequency for the diaphragm configuration. The model is displayed in red solid line. The optimal values are: $f_0 = \omega_0/(2\pi) = 451\ Hz$ and $\nu = 18.7$ [Hz].

5.3.3 Evaluation of the acoustic end corrections with the duct configuration

It is first important to characterize the acoustic boundary conditions at the inlet and the outlet of the rig. This is done here without diaphragm to concentrate on end effects. The inlet is constituted of eight radial injectors equally spaced on its contour at 1 cm of a closed bottom, while the outlet is left opened. Both boundaries may be accurately modelled by taking into account acoustic end corrections. Such corrections are obtained in two steps:

- Characterization of the rig with a closed outlet where the difference between theory and experiment is caused by the inlet end correction δ_{in}.
- Characterization of the rig with an open outlet. The difference between theory and experiment is due to both inlet and outlet end corrections (δ_{out}) and these effects may be separated.

In the first case (closed inlet, closed outlet, zero mean flow), experimental modes are compared to the theoretical ones (adapted from equation 1.4.12):

$$f_{k,\text{cc}} = \frac{c_0}{2(L+\delta_{\text{in}})}k\ ,\ k \in \mathbb{N} \tag{5.3.3}$$

where $L = L_3 + L_2 = 0.9\ m$ denotes the total length of the rig constituted by the two ducts T_3 and T_2. The inlet end correction δ_{in} is obtained by minimizing the distance between theoretical and experimental acoustic modes as shown in Fig. 5.14. It is estimated to $\delta_{\text{in}} = 12\ mm$ and remains small when compared to the duct radius $R = 40.5\ mm$.

An open outlet is then used for the following studies: this boundary condition is easier to use and characterize at non zero flow-rates. In this case, the quarter wave family of acoustic modes is expected in the duct configuration with a closed inlet ($u = 0$) and an opened outlet ($p = 0$). The same technique used to obtain the inlet end correction is used to determine the correction associated with the open outlet:

$$f_{k,\text{total}} = \frac{c}{4(L+\delta_{\text{in}}+\delta_{\text{out}})}(1+2k)\ ,\ k \in \mathbb{N} \tag{5.3.4}$$

where δ_{out} refers to outlet end correction. The comparison between theoretical and experimental frequencies is shown in Fig. 5.15. The value found for the outlet end correction, $\delta_{\text{out}} = 25\ mm$ can be

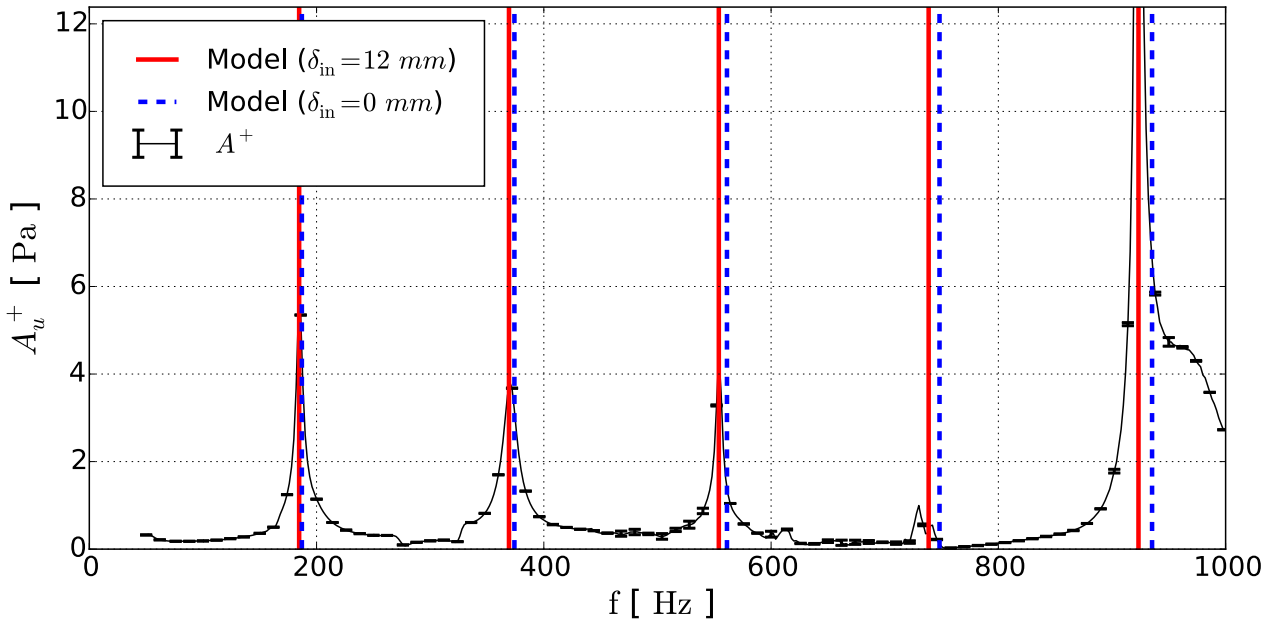

Figure 5.14: A_u^+ as a function of frequency for the closed end configuration. Vertical lines correspond to the modes of equation 5.3.3, taking into account or not inlet end correction.

scaled by the radius of the duct: $\delta_{out} = 0.62r$. Such a ratio is in good agreement with existing studies of unflanged, opened end acoustic correction below the cut-off frequency [15, 14].

Finally, the two end corrections are supposed to be independent of the mean flow. These values are kept constant for the diaphragm case as they only rely on the boundaries.

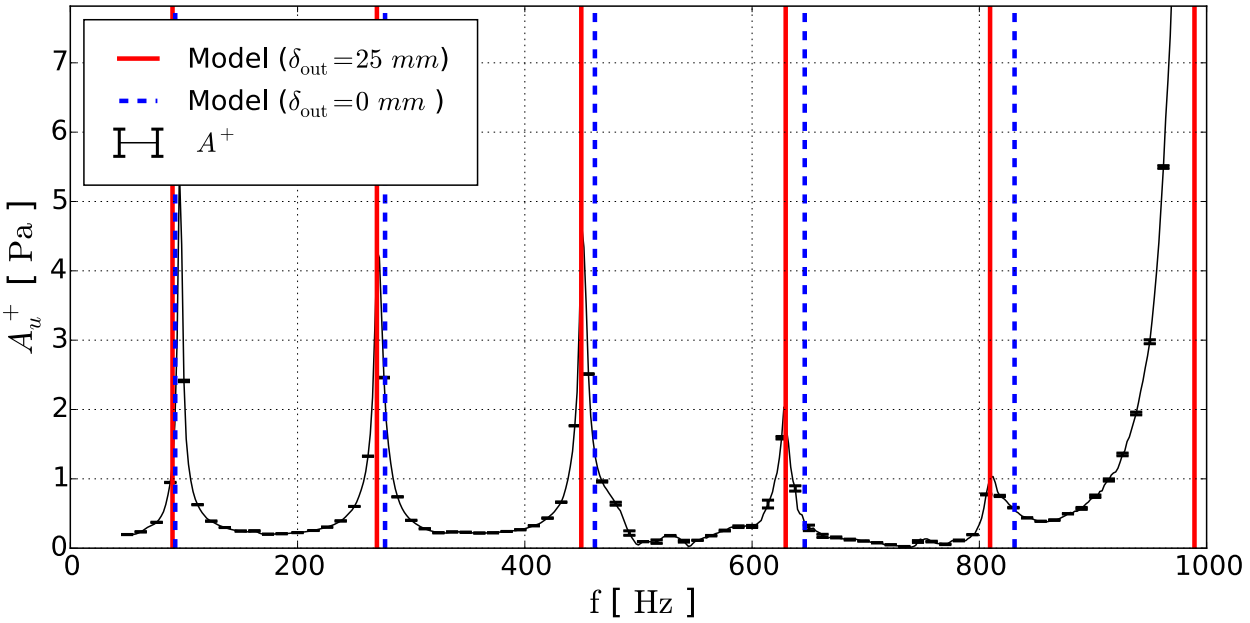

Figure 5.15: A_u^+ as a function of frequency for the opened end configuration. Vertical lines correspond to the modes of equation 5.3.4, with or without outlet end correction. Figures 5.15 and 5.14 exhibit sharp peaks, compatible with very small dissipation as expected for this case.

5.3.4 Damping comparison in the diaphragm case

It is now possible to focus on the diaphragm configuration, where acoustic dissipation caused by the coupling with hydrodynamics is expected (see section 3.2.2). Transfer matrices from experiments and model (UM1) are introduced in the ROM equation 5.3.1 which solutions are obtained with the numerical solver RootLocker (see chapter 2). The latter are then compared with the acoustic modes obtained in the experiments.

We begin by a comparison in the absence of a mean flow. In this case, the diaphragm does not dissipate acoustic energy and the losses are only due to radiation at the boundaries. The comparison between experimental (upstream measurement) and predicted acoustic modes frequencies is shown in Fig. 5.16. As already mentioned for the duct configuration, uncertainties remain below one percent for all frequencies. Most peaks are well predicted. However, the fifth analytical mode at 736 Hz predicted by the ROM is not observed in experimental data. Conversely, the missing mode is retrieved in the

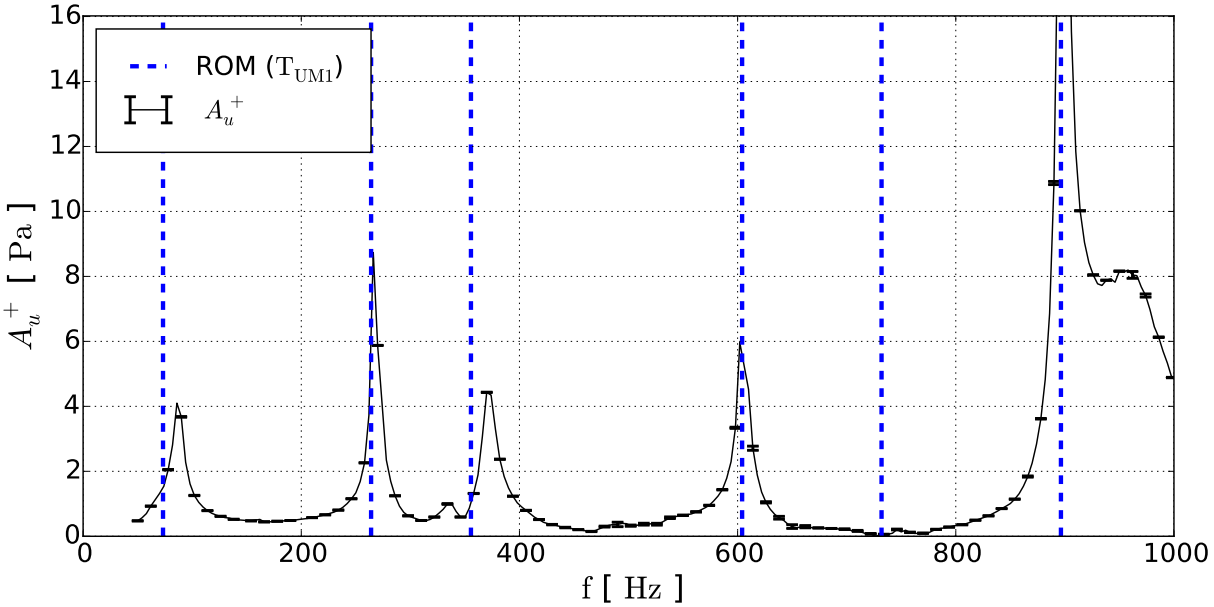

Figure 5.16: A_u^+ (upstream) as a function of frequency for the diaphragm configuration. Dashed lines correspond to analytical modes obtained with the UM1 model in the infinity Strouhal limit.

section located downstream of the diaphragm as shown in fig 5.17. Although present, this mode seems to be over damped.

Frequencies and damping rates obtained experimentally from equation 5.3.2 are displayed in table 5.1. These values have been extracted upstream and downstream of the diaphragm. The frequencies are captured with a precision below 1 Hz although the experimental frequency step was set to 4 Hz. Damping rates measured upstream and downstream are consistent which validate the method. Finally, results for the fifth acoustic mode are only displayed for the downstream section as it was not observed upstream of the diaphragm.

The damping rates of the experimental acoustic modes are not constant. These losses could be predicted at the price of taking into account the coupling with the loudspeaker system, linear losses caused by laminar dissipation of acoustic energy in boundary layer [183], or even non linear vortex shedding [20] which is out of the scope of this study. Once the acoustic modes have been characterized at rest, further studies may be conducted for non zero flow-rates.

A comparison between experimental and predicted acoustic modes obtained for $U_u = 0.344\ m.s^{-1}$ is displayed in Fig. 5.18.

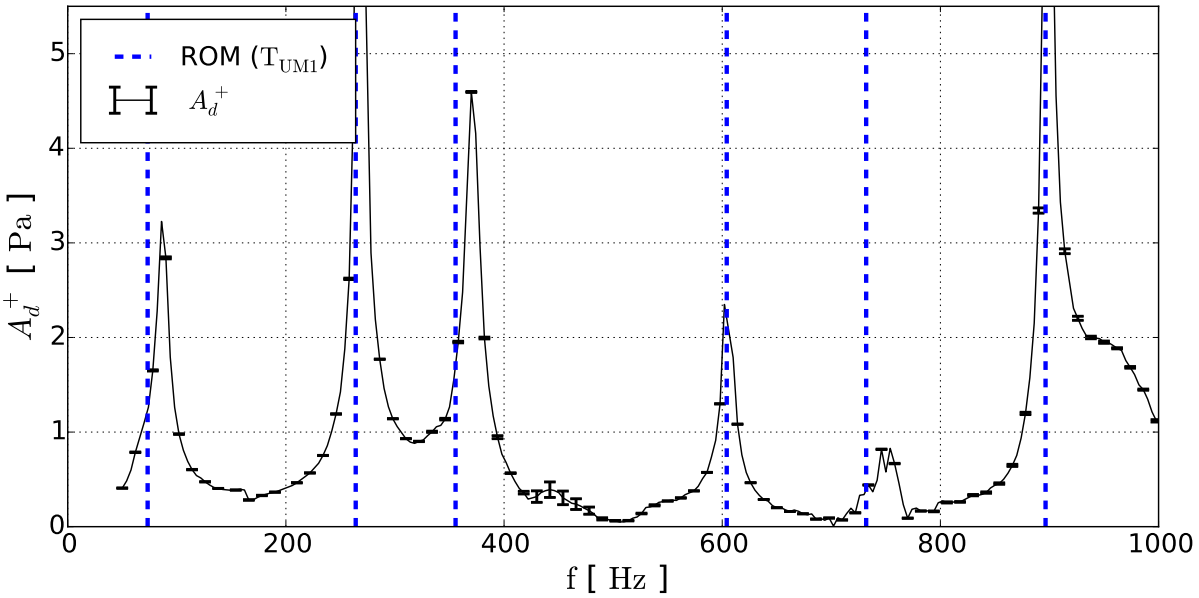

Figure 5.17: A_d^+ (downstream) as a function of frequency for the diaphragm configuration. Dashed lined corresponds to analytical modes obtained with the UM1 model in the infinity Strouhal limit.

Parameters	M1	M2	M3	M4	M5	M6
f_u	87.7	266.9	371.5	605.2	x	898.7
f_d	87.4	267.2	371.0	605.2	751.6	898.5
ν_u	31.9	13.8	34.3	19.4	x	22.7
ν_d	30.1	12.6	35.1	18.6	(58.2)	22.3

Table 5.1: The frequency and damping obtained experimentally from equation 5.3.2 for upstream and downstream sections. Values between parenthesis must be taken with cautious as the curve fitting procedure gave poor correlation results.

Acoustic mode prediction has been performed by solving ROMs built upon modeled and measured transfer matrices. The UM1 analytical model, which is equivalent to the Howe model and do not take into account the diaphragm thickness is first compared with the experimental results: some of the acoustic modes are well recovered and other not. For instance, there is an error of 30 Hz for the mode M3 at 380 Hz. Second, a global synthetic model is used to fit the transfer matrix coefficients for frequencies ranging between 50 and 1000 Hz. In practice, only the parameter ξ is fitted:

$$\xi = ip_1(f + p_2 + e^{ip_5}\frac{p_3}{f + p_4}) \tag{5.3.5}$$

and the corresponding values are $p_1 = 0.0028$, $p_2 = -229.0$,$p_3 = 44800$, $p_4 = 62.6$, $p_5 = 0.89$. This method provides more accurate results than the UM1 model as shown in Fig. 5.18.

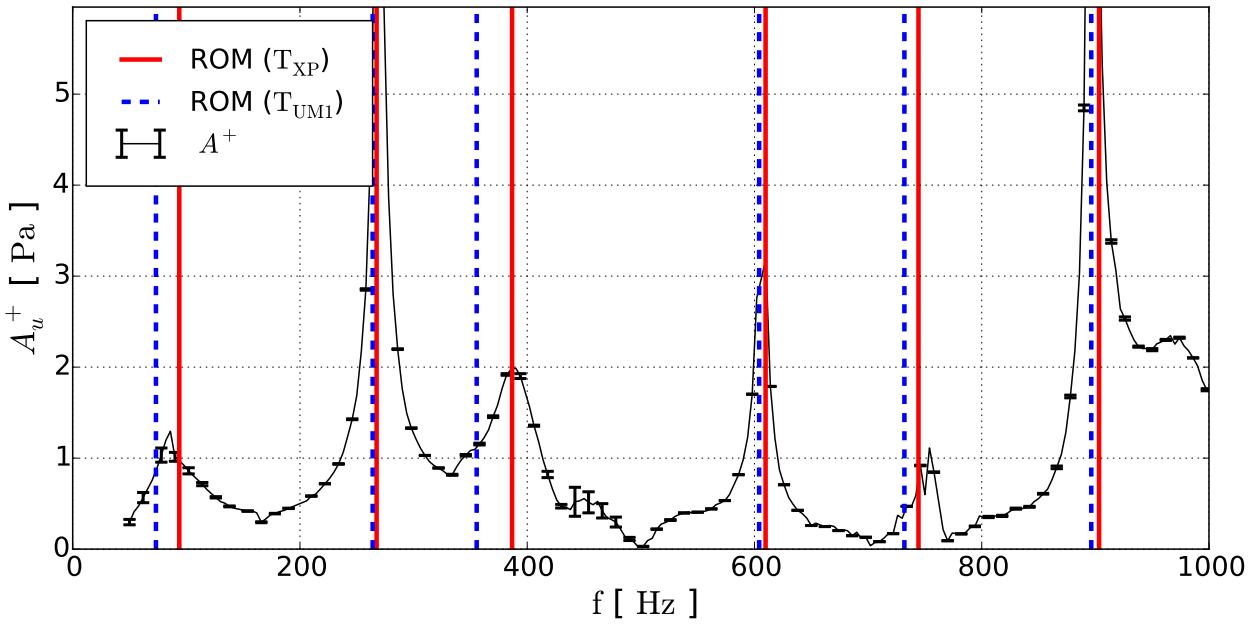

Figure 5.18: $|A_d^+|^2$ as a function of frequency for the diaphragm configuration at U_u = 0.344 $m.s^{-1}$. vertical lines denote ROM resolution with UM1 model (dashed blue lines) and experimental transfer matrices (solid red lines).

As all the real part f of the complex frequencies are accurately predicted by resolution of the ROM based on the experimental two-port. It is now possible to investigate on acoustic losses. Comparison between experimental and predicted acoustic modes is shown in table 5.2 for U_u = 0.344 $m.s^{-1}$. One can first notice the good agreement for the real part of the frequencies. Except for the first mode, which is over damped for this configuration, all relative errors are below two percent. Concerning the acoustic losses, the damping rate of modes M1 and M5 could not be measured properly as they were over-damped (see fig 5.17) In order to take into account the other sources of dissipation occurring in the

Parameters	M1	M2	M3	M4	M5	M6
f_{xp}	86.6	268.6	390.7	606.5	754.2	897.3
$f_{predicted}$	81.8	268.1	384.2	611.5	747.5	903.3
ν_{xp}	x	26.6	103.3	18.9	x	25.6
$\nu_{xp} - \nu_{xp,U_u=0}$	x	13.4	69.0	-0.5	x	3.3
$\nu_{predicted}$	x	13.4	96.8	9.7	x	5.4

Table 5.2: Frequencies and damping rates obtained from equation 5.3.2 for upstream and downstream sections compared with numerical resolution of equation 5.3.1

rig, it is possible to subtract the damping rates measured at rest to the one at obtained at U_u = 0.344 $m.s^{-}1$. Although sightly overestimated, the predicted (ROM (T_{XP})) damping rates scale well with the experimental measurements. For instance, the difference of attenuation between modes M3, which is very damped and mode M6, which is barely damped at this flow rate, is well recovered.

5.4 Conclusion

An efficient method has been presented to measure two-port matrices in both experiments and simulations in non reacting cases. The method is stable and provide uncertainties for both acoustic waves and two-port matrix coefficients by using the multi-microphone / multi-configuration technique. Once experimental two-port matrices are available for a given ACE, it is possible to study acoustic modes by solving ROMs. Academical configurations are tested here to assess the quality of the prediction of both tone and damping of acoustic modes: a good agreement is observed.

Moreover, the interesting case of swirl injector two-port matrix has been reported. However, the coupling between acoustic and hydrodynamical waves made it impossible to use the injector for an acoustic dissipation study.

Finally, this chapter closes the second part of the manuscript concerning acoustic dissipation and its implication in ROMs. In the following part, the coupling between acoustic waves and laminar flames anchored on a cylindrical rod is investigated for different temperature regimes.

Part III

Influence of flame holder temperature on combustion instabilities

This part is dedicated to the study of flame holder temperature influence on combustion instabilities. The objective is to investigate this fundamental phenomenon in a two-dimensional academic burner: the INTRIG rig, which uses a laminar, premixed air/methane V flame under atmospheric conditions. This part is decomposed into four chapters. In chapter 6, the experimental burner as well as the corresponding numerical set-up of the DNS are introduced. Flame anchoring mechanisms observed in two distinct operating regimes: a cooled flame holder and an un-cooled one are reported in chapter 7. A third case of interest is observed in the limit of transparent cylinder (low emissivity) where the flame stabilizes upstream of the flame holder. The influence of the wall temperature on combustion instabilities is assessed by the mean of FTF measurements for the three aforementioned configurations (chapter 8). Finally, these FTFs are used as input of a detailed ROM of the INTRIG burner presented in chapter 9.

Chapter 6

The INTRIG burner: experimental and numerical descriptions

The INTRIG burner was built with the support of the ERC Intecocis project (`http://intecocis.inp-toulouse.fr/en/home.html`). It is dedicated to the influence of heat transfer on the flame/acoustic coupling for a premixed, laminar, V flame attached on a cylindrical rod. Both experiments and numerical simulations (DNS) are used in this study. The objective of this chapter is to describe the INTRIG burner and the associated set-up used for the DNS. Simulations have been carried out with 3 different chemical mechanisms for methane/air flames (from 6 to 19 species) and a coupled heat transfer / flow resolution to compute not only the flow but also the temperature within the cylindrical rod for both the cooled and un-cooled cases.

Introduction

Among all the walls present in a chamber, flame holders play a special role because they control the most sensitive zone of the chamber: the place where the flames are anchored. Any temperature change of the flame holder will induce a change of position for the flame roots and therefore a change in stability and efficiency. The coupling mechanisms between heat transfer within flameholder and flame stabilization have not been analyzed in detail yet. In a series of recent papers [184, 42, 185], the MIT group has numerically studied the stabilization of premixed flames on square flame holders and shown that the location of the flame roots but also the blow-off limits were strongly affected by the temperature of the flame holder.

The present chapter focuses on a similar question: which differences in both flame anchoring and flame/acoustic coupling are observed when the temperature of the flame holder varies from a low (typically 300 K for a flame holder which will be water cooled) to a high value (700 K for an uncooled solid flame holder). In the present chapter, we first focus on the INTRIG burner, which is described in section 6.1. The setup of the DNS is described in the following sections. For the sake of clarity, the setup of the DNS is detailed only for the un-cooled cylinder case. However, all results presented here were also used to setup the cooled cylinder case. The choice of the geometry and the meshes are detailed in section 6.2 while the heat transfer coupling methodology between the solid bluff-body and the reactive flow is described in section 6.3. Finally, the choice of the chemical kinetic scheme, which appeared to be a key ingredient in the DNS, is detailed in section 6.4.

6.1 INTRIG workbench

Following the work of Mejia et al [52] concerning the influence of heat transfer on the flame dynamics, it has been decided to design a new laminar burner called INTRIG, in which heat transfer could be monitored precisely. The experimental rig is shown in Fig. 6.1: a lean premixed methane/air V-flame is stabilized over a steel cylindrical bluff-body (radius of $r = 4\ mm$).

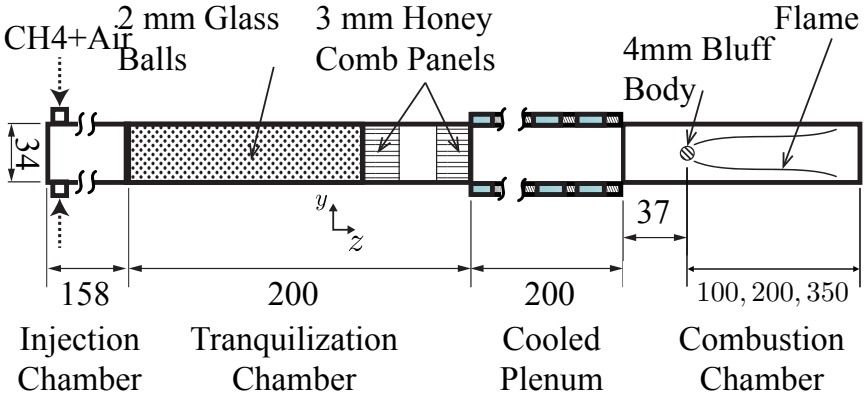

Figure 6.1: Transverse cut of the burner. The length of the combustion chamber can be varied from 0.1 up to 0.35 m.

The burner has a constant cross section of $h = 34$ by $l = 94\ mm$ so that the flame remains two-dimensional, a very interesting property for the DNS. The operating conditions are given in Tab. 6.1. In these conditions, the flame is steady for all cases (even if it exhibited unsteady Kármán Street vorticies for non reacting flow) and the power of the burner is 7 kW for $\Phi = 0.75$ and $u_\mathrm{b} = 1.07\ m.s^{-1}$. Individual mass flow meters are used to control air and methane flow rates. Fuel and oxidizer are premixed before entering the injection chamber though six holes. Glass wool, small glass balls and two honeycombs panels are used to laminarize the flow.
The flow passes through a water-cooled plenum to ensure a constant fresh-gases temperature. Hot wire measurements downstream of the plenum show that the flow is laminar: the fluctuation level remains below 1% everywhere in the chamber. The mean velocity profile, measured 35 mm upstream of the cylinder, is displayed in Fig. 6.2.

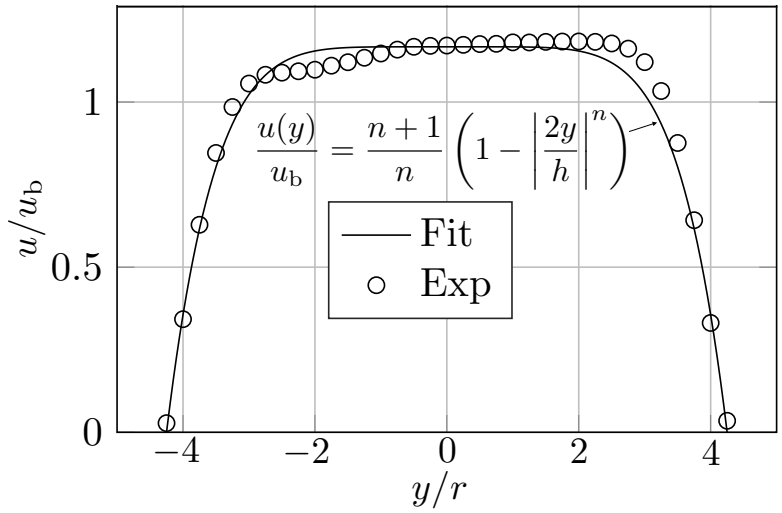

Figure 6.2: Comparison between experimental measurement and fit for the inlet velocity profile

As expected, the velocity profile is still flat as the plenum is not long enough to obtain a Poiseuille velocity profile after the glass balls. A power law fit has been performed on these data to provide an inlet boundary condition for the DNS:

$$\frac{u(y)}{u_\mathrm{b}} = \frac{n+1}{n}\left(1 - \frac{2y}{h}^{n}\right) \tag{6.1.1}$$

where the only fitting parameter is n, which is equal to 6 in this case. After the plenum, the flow enters the combustion chamber where the flame holder is located. Two different bluff-bodies have been used to stabilize the flame. The first one is a cooled steel cylinder (Fig. 6.3, left) maintained at 285 K by a 37 $g.s^{-1}$ mass flow rate of cooling water. The second flame holder is a solid steel cylinder, which has exactly the same external geometry as the cooled one (Fig. 6.3, right). In the following, these cases will be denoted as CBB (Cooled Bluff-Body) and UBB (Uncooled Bluff-Body) respectively. Finally, the combustion chamber has a quartz window in the front, and one on each lateral side wall, for visualization. Flames are imaged on an intensified PCO-Sensicam camera equipped with a CH^* narrow band-pass filter and a f/16 180 mm telecentric lens [186] (Fig. 6.3).

Name	Quantity	Value
Φ	equivalence ration	0.75
u_b	bulk velocity	1.07 $m.s^{-1}$
s_l	laminar flame speed	0.24 $m.s^{-1}$
T_u	injection temperature	292 K
T_adia	adiabatic flame temperature	1920 K

Table 6.1: Operating conditions for the CBB and UBB cases.

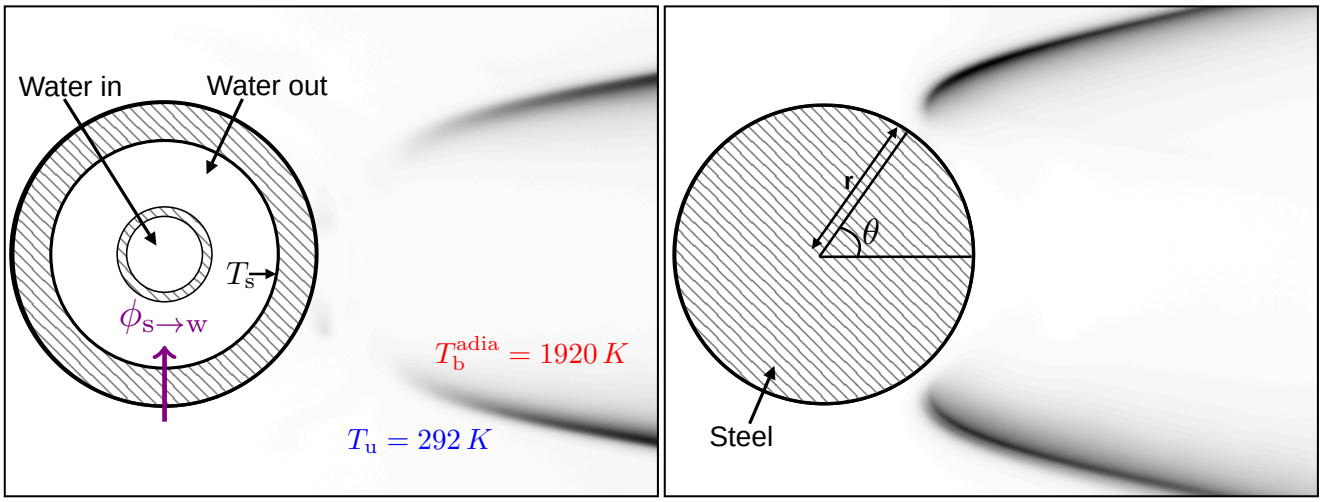

Figure 6.3: CBB: cooled bluff-body (left) and UBB: uncooled bluff-body (right). Experimental fields of CH^* are displayed for the two cases.

In the UBB case, the full cylinder is attached on only one side of the combustion chamber. On the other side, there is a gap of approximately 3 mm between the cylinder and the quartz window when the rig is cold. This gap drops to 1 mm at steady state during flame runs because of thermal expansion. The flame holder temperature has been measured with a K-type thermocouple: $T_\mathrm{cyl}^\mathrm{UBB} = 670 \pm 40\ K$. A temperature difference of about 70 K has been measured between the two extremities of the cylinder. This corresponds to a gradient of $\partial T/\partial x \approx 750\ K.m^{-1}$. The corresponding heat transfer is below 2 W so that axial heat flux is not taken into account in the DNS.

In the CBB case, the temperature elevation of the water used for cooling is equal to $\Delta T = 0.15 \pm 0.05$ K so that the cooling water temperature can be assumed to be constant. It leads to a total flux taken from the flame $\Phi^{xp}_{s\rightarrow w} = mC_p\Delta T = 24 \pm 8$ W.

The thermal properties of the steel used in both UBB and CBB cases are recalled in Tab. 6.2. The emissivity of the bluff body is directly linked to its surface state. In the present experiments, the bluff-bodies are oxidized so that an emissivity of $\epsilon = 0.9$ is retained. The effects of ϵ are discussed using DNS in chapter 7. Simulations (DNS) of the INTRIG burner have been planned in the early stages

Material	ρc_p $[K^{-1}m^{-3}]$	λ $[W/m/K]$	ϵ
35NCD16	$3.5\,10^6$	32	0.2 - 0.9

Table 6.2: Thermal properties of the steel used for the bluff-bodies. The emissivity ϵ ranges from 0.2 for polished surfaces to 0.9 for oxidized surfaces.

of its conception: the rig is designed by taking into account numerical simulations requirements. For example, the flow remains two-dimensional and steady, which eases the computations. Moreover, no sudden change of section occurs in the vicinity of the flame holder to avoid sources of acoustic losses. The setup of the DNS is described in the following sections focusing on the UBB case.

6.2 Flow solver

The Navier Stokes equations are solved with the AVBP solver using a third-order scheme for spatial differencing on a two-dimensional hybrid mesh and an explicit two-step scheme for time advancement [187, 188]. The NSCBC [11, 188] formulation is used for the boundaries.

This flow solver is particularly well adapted to study thermo-acoustic problems on large unstructured meshes. Three chemical schemes have been tested from 6 to 19 species. Details about the chemical kinetics are provided in section 6.4. Here, AVBP is used as a DNS solver which means that no LES models nor flame thickening are used.

Studying anchoring mechanisms of the laminar flame does not require to simulate all the geometry of the INTRIG burner. Indeed, only the region close to the bluff-body must be simulated accurately as long as a correct velocity is prescribed at the inlet (as shown in Fig. 6.2). Simulating only a portion of the flame has two advantages:

- Reduction of the computational cost of the simulation. A small cost allows to run parametric studies.
- Suppression of combustion instabilities as the unsteady heat release is generated close to the external boundaries, where the flame touches the walls (see section 8).

As a consequence, the geometry used in this chapter as well as in chapter 7 starts 35 mm upstream of the rod and ends 50 mm after. The size of the finer cells is fixed to 70 μm. This is enough to correctly resolve the flame front. The flame thickness is defined by:

$$\delta_{th} = \frac{T_{adia} - T_u}{\max\left(dT/dx\right)} \tag{6.2.1}$$

For a methane/air premixed flame at $\Phi = 0.75$ and with $T_u = 292K$: $\delta_{th} = 580$ μm so that at least 8 cells are obtained in the flame region. At this resolution, all transported species are accurately resolved across the flame front. The mesh size of 70 μm also allows to capture both dynamic and thermal boundary layers along the cylinder. The thermal boundary layer thickness at the stagnation point is $L_{th} = 700$ μm and is thickened as the flow passes around the cylinder. It is meshed with at least 10 cells. The dynamic boundary layer is thicker than the thermal one ($P_r < 1$).

6.2.1 Tetrahedral mesh

Fully tetrahedral meshes have been first considered for two reasons:

- Simplicity of mesh creation with unstructured meshing tools such as Centaur[1].
- Possibility to use the automatic mesh refinement chain tool HIP/MMG3D, which only works for tetrahedral meshes now.

The automatic mesh refinement chain tool makes it possible to refine the mesh only where it is needed: close to the bluff-body, but also in the flame region. This permits to control locally the size of mesh elements, according to previous simulations.

However, using tetrahedral meshes did not provide accurate results, especially close to cold boundaries such as around the rod: its steady state temperature measured experimentally is about 670 K, which is cold when compared to the adiabatic flame temperature T_b = 1900 K. The longitudinal velocity field obtained on a tetrahedral mesh is displayed in Fig. 6.4: velocity oscillations are observed in the vicinity of the bluff-body. It appears that such non-physical behaviour only occurs close to iso-thermal boundaries, where heat transfer is intense. By taking a closer look at the velocity field, one observes that the glitches are mesh dependent. Indeed, the velocity glitches occur when the mesh topology changes

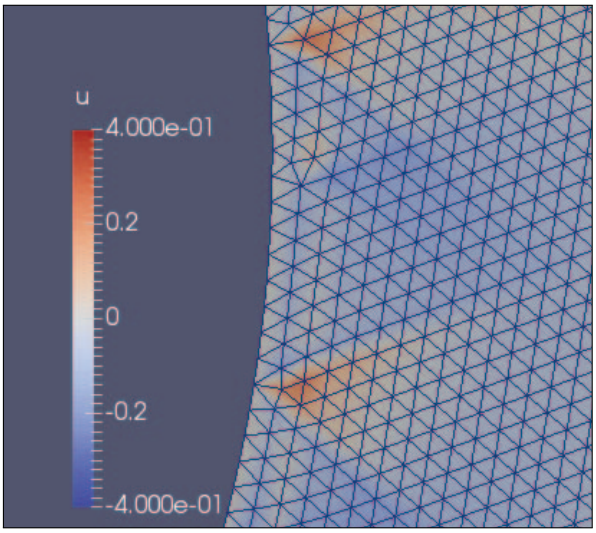

Figure 6.4: Zoom on the velocity field downstream of the bluff-body. (Reacting flow)

at the boundary. This problem is observed independently of the numerical scheme used.

6.2.2 Hybrid mesh

The tetrahedral grid approach did not provide good results, mainly because of the non-uniformity of the cells close to the bluff-body where heat fluxes are very large. This difficulty was overcome by using structured grids close to the cold boundaries. Indeed, hybrid meshes containing 5 layers of quadrilateral cells at the boundary were generated with Centaur and used for the DNS. The hybrid mesh and the corresponding velocity field are displayed in Fig. 6.5. As expected, all velocity glitches disappeared. Additional information about numerical pressure and velocity oscillations and their suppression is provided in the Appendix E.

Using hybrid meshes imply that the automated mesh refinement chain tool described in chapter 4 for cold flows in swirl injectors cannot be used anymore. The hybrid mesh should be generated carefully

[1]Centaur is a unstructured meshing tool which outputs grids compatible with AVBP

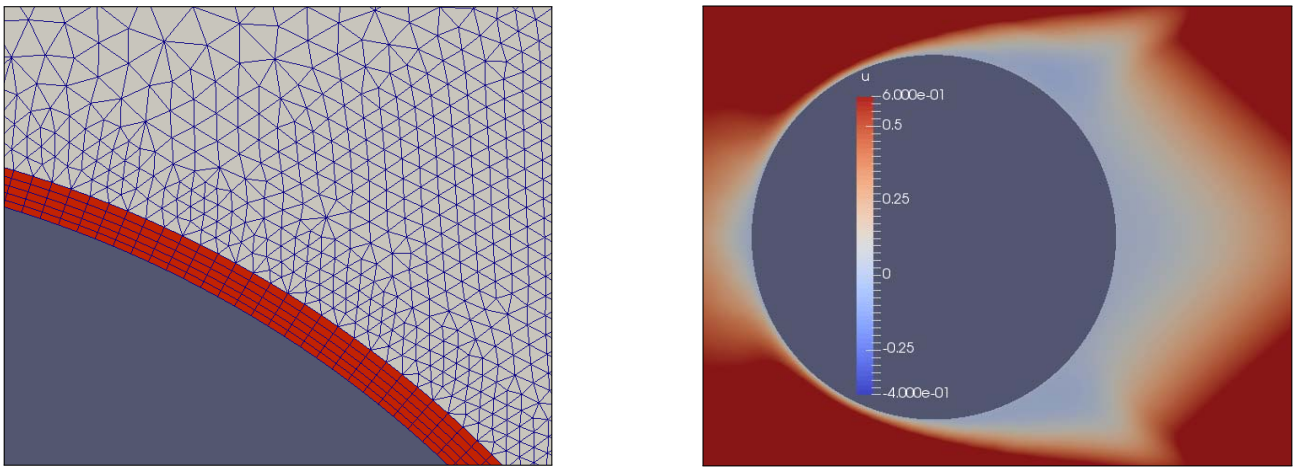

Figure 6.5: Left: hybrid mesh closed to the flame holder; Right: Velocity field obtained on the hybrid mesh.

with smooth variations of cells size between the refined regions (bluff-body, flame) and the others. This can be achieved in Centaur by creating a large number of refinement sources, with continuous bi-linear variations for the cells size criteria.

6.2.3 Mesh independence

A typical size of 70 μm has been chosen in the flame regions as well as along the cylinder in order to correctly capture the small length scales of the reactive flow. The choice of this size is based on physical criteria (boundary layer, flame thickness). In order to validate this choice, simulations have been carried out on a finer mesh: 40 μm in the flame front and boundary layers. A comparison is shown in Fig. 6.6 in the most complex zone of the flow, where velocity streamlines are displayed for the two grids. One may observe that the small recirculation zone located upstream of the flame is identical for both meshes. The topology of the flames will be discussed in details in chapter 7. This section only shows that the DNS are mesh independent: this is one of the advantages of being able to run 2D DNS.

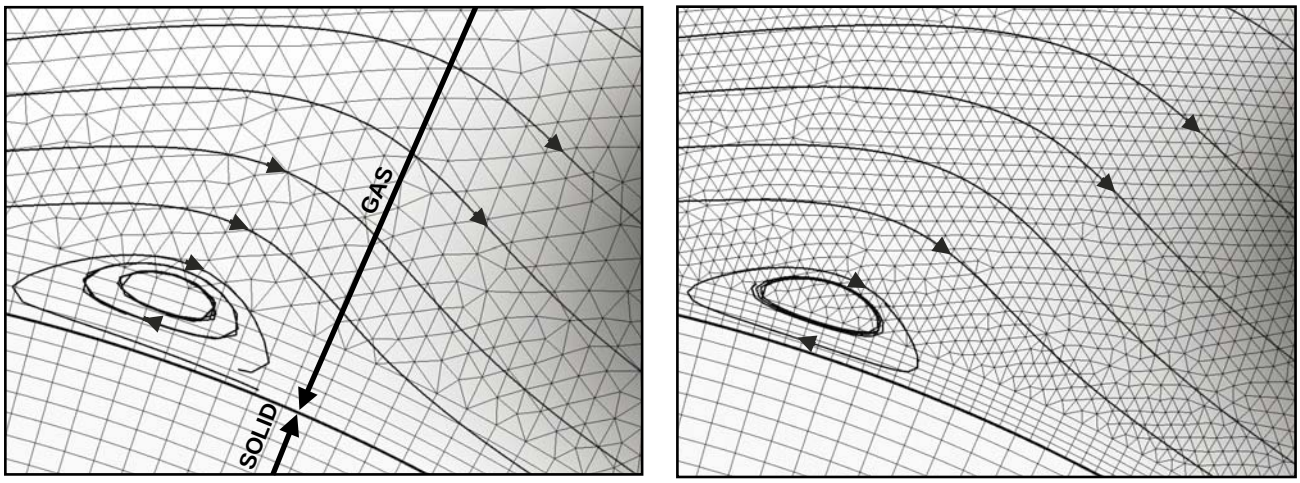

Figure 6.6: Comparison of the DNS with two different meshes. Left: the mesh used in the following. Right: the finer mesh used for validation. The recirculation zone is well captured by both meshes.

6.3 Heat transfer in the bluff-body

This section focuses on the heat transfer occurring between the reactive flow and the flame holder. As the bluff-body is completely immersed in the flow and end effects can be neglected, its mean temperature is imposed by the surrounding heat fluxes. Three contributions must be taken into account to accurately predict the mean temperature of flame holder. The first two are the convective heat transfer: one from the burnt gases to the downstream face of the flame holder, which cools the reactive flow and the other from the upstream face of the flame holder to the unburnt gases, which heats up the latter. The last contribution is the radiative heat transfer emitted by the flame holder surface which must be accounted for when relatively high temperatures are reached:

$$\phi_{\text{rad}} = \sigma\epsilon(T^4 - T_{\text{ext}}^4) \tag{6.3.1}$$

where T is the local temperature at the cylinder surface. Radiation from the gas (H_2O, CO_2) and from the hot walls downstream of the combustion zone is neglected. Furthermore, walls surrounding the flame holder (which are cooled) have a temperature close to the fresh gas and are assumed to behave as black bodies: $T_{\text{ext}} = T_{\text{u}}$.

When compared to simulations where the temperature at the walls are imposed, an accurate resolution of heat transfer provides two advantages. First, the temperature of the bluff-body is not imposed and can freely adapt to the surrounding flow. Second, the bluff-body temperature can fluctuate when the flow is pulsed or experiences instabilities. Two methods can be used to take into account heat transfer in the bluff-body:

- **Homogeneous adaptive boundary condition (HABC)**
  In this method, an iso-thermal boundary condition is used for the bluff-body. Its temperature T_c, which is assumed to be uniform, is advanced in time according to the sum of the surrounding heat fluxes. This allows a cheap coupling of the flow with the cylinder temperature. It is justified by the large heat diffusivity of the bluff-body.

- **Coupling with a solid heat transfer solver (CSHT)**
  This strategy allows to fully compute the temperature field in the flame holder by coupling the flow solver (AVBP) with a heat transfer solver (AVTP): continuity of temperature and heat fluxes is ensured between the two solvers. Here, one has access to the local temperature and heat fluxes fields inside of the flame holder [189, 190].

6.3.1 Homogeneous adaptive boundary condition (HABC)

A new iso-thermal boundary condition has been introduced in AVBP to compute the temperature of the cylinder T_{c} (supposed to be homogeneous). The cylinder temperature T_{c}, which is imposed everywhere in the cylinder and also all along the boundary, satisfies:

$$\frac{\partial T_{\text{c}}}{\partial t} = \frac{1}{C_{\text{p}}} \oint_S \vec{\phi}_{\text{c}} - \sigma\epsilon(T_{\text{c}}^4 - T_{\text{ref}}^4)\vec{n} \;\; \vec{ds} \tag{6.3.2}$$

where C_{p} is the heat capacity of the bluff-body, T_{c}: its temperature and $\vec{\phi}_{\text{c}}$ is the convective heat flux. Both $\vec{ds}$ and $\vec{n}$ are pointing inside of the cylinder so as the convective heat flux. In order to reach a steady state rapidly, the heat capacity can be decreased by several orders of magnitude. Equation 6.3.2 is advanced in time by a first order finite difference Euler scheme every iteration of the CFD solver. Computing the integrals appearing in the RHS of equation 6.3.2 causes performance issues in AVBP. Indeed, this computation requires gather/scatter MPI communications which are costly. As a consequence, the integral is computed only once every n_{temp} iterations. This does not alter the time advancement as long as $n_{\text{temp}}dt \quad \min(t_{\text{flow}}, t_{\text{solid}})$.

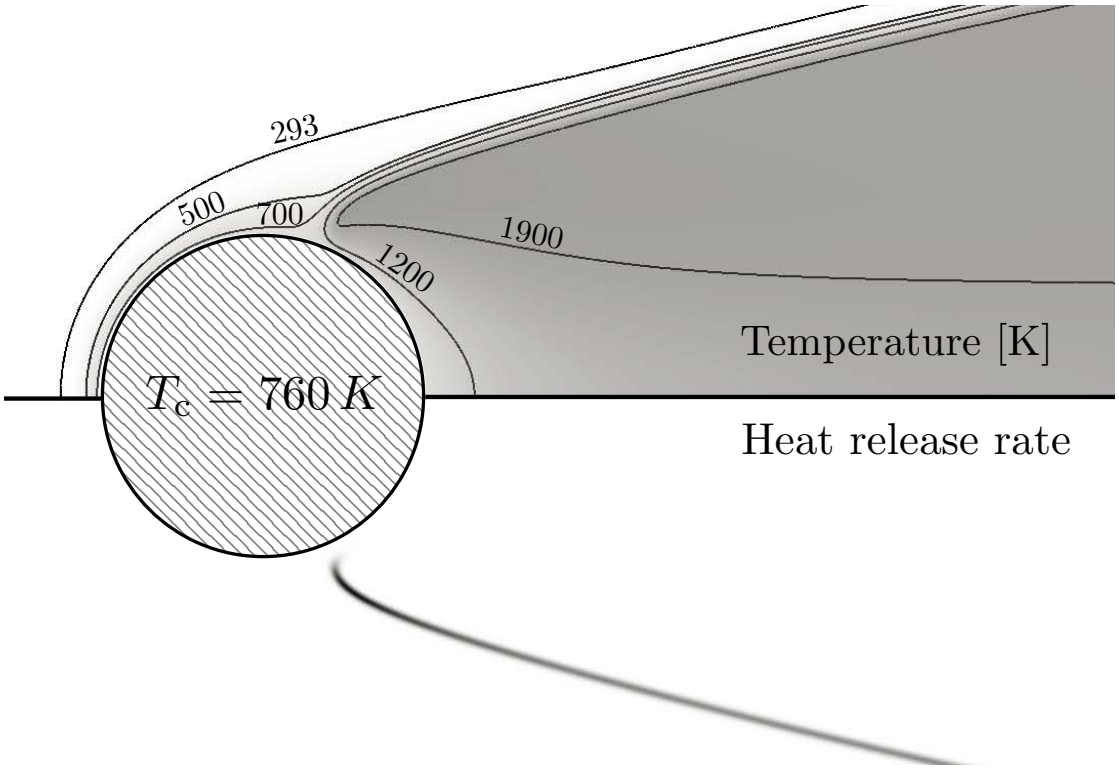

Figure 6.7: Temperature and heat release field obtained with the homogeneous adaptive boundary condition for the un-cooled case (BFER chemical scheme).

With the 2S_CH4_BFER kinetic mechanism (see section 6.4), the steady state temperature of the bluff-body is T_{HABC} = 760 K. The associated heat release field is displayed in Fig. 6.7. As expected, the temperature of the bluff-body stabilizes between the temperatures of burnt and unburnt mixtures. Contrary to adiabatic bluff-body, the flame foots are extinct close to the cylinder while the unburnt gases are heated all along the bluff-body due to the heat transfer. A detailed explanation of the flame anchoring mechanism is provided in chapter 7.

6.3.2 Coupling with a solid heat transfer solver (CSHT)

In the second method (CSHT), one more step is takem and we now want to obtain the temperature field in the cylinder. To do this, the resolution of the heat transfer equation (with a solver called AVTP) inside of the bluff-body relies on an implicit first-order forward Euler scheme for time integration [191] and a second-order Galerkin scheme [192]. Local heat fluxes ϕ_{s} are imposed in the solid solver at the boundary shared between the solid and the fluid domains. The AVTP solid solver then sends skin temperatures back to the DNS code for the next iteration.

Both codes are coupled with a software called OpenPALM [193] which exchanges the thermal information (temperature and fluxes) at the external face of the bluff-body. The local temperature obtained by the solid solver on the cylinder surface is applied through an isothermal NSCBC boundary condition [194] in the fluid solver whereas the local convective heat flux and the radiative flux are imposed in the solid solver. The characteristic flow time τ_{f} is of the order of 50 ms while the solid characteristic time τ_{s} is of the order of 10^3 s. The simulation of the flame for several τ_{s} times is impractical. The coupling strategy to accelerate the convergence towards steady state is that each domain (flow and solid) is advanced at its own characteristic time using a time step $\alpha_{\mathrm{f}}\tau_{\mathrm{f}}$ for the fluid and $\alpha_{\mathrm{s}}\tau_{\mathrm{s}}$ for the solid with $\alpha_{\mathrm{f}} = \alpha_{\mathrm{s}}$ [190]. This is equivalent to decreasing the heat capacity of the solid while preserving its conductivity, as done for the homogeneous adaptive boundary condition.

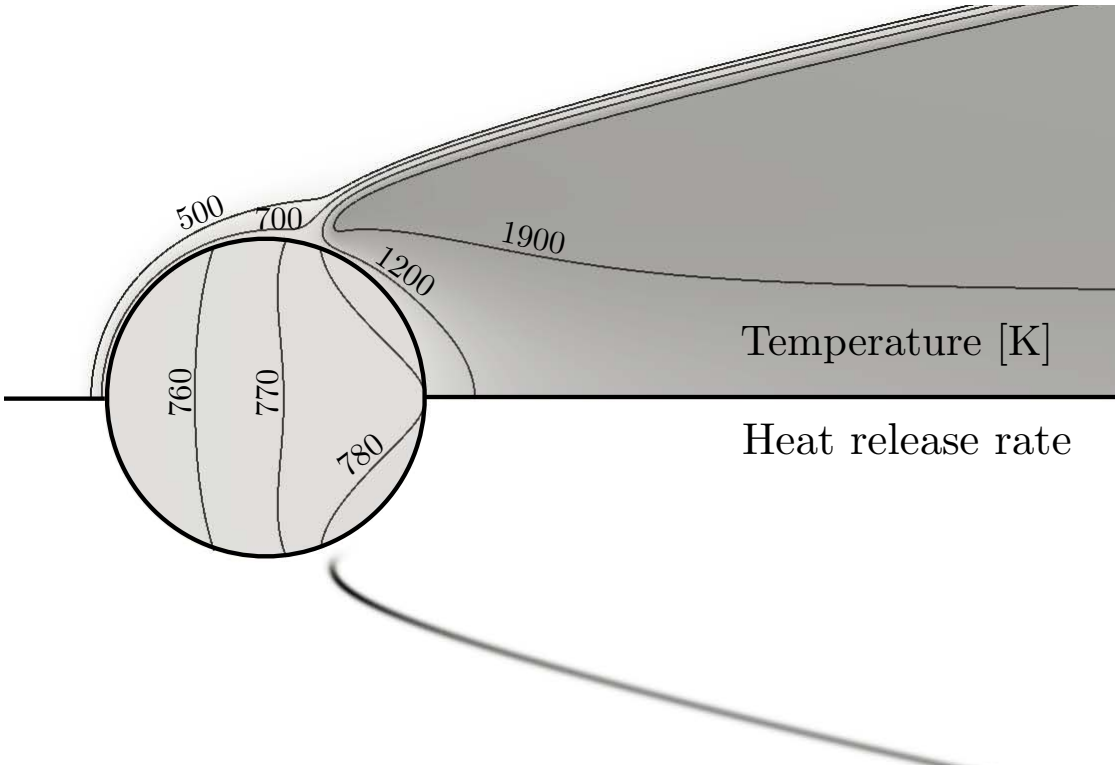

Figure 6.8: Temperature and heat release field for the coupled boundary condition.

Heat release and temperature fields obtained with the coupled boundary condition are displayed in Fig. 6.8 for the un-cooled cylinder and the 2S_CH4_BFER scheme. These fields are very similar to the ones obtained for the homogeneous adaptive boundary condition (Fig. 6.7). This method also provides the temperature distribution inside of the flame holder. It varies between 758 and 777 K with an average temperature of 766 K which is very close to the value obtained for the homogeneous adaptive boundary condition (760 K). However, the mean temperature is overestimated by about $100K$ when compared to experimental measurements.

The temperature extent across the bluff-body ($\Delta T = 777 - 758 = 19\ K$) is small when compared to flow temperature variation: $\Delta T \quad T_\mathrm{b} - T_\mathrm{u}$. This can be recovered with a one dimensional model of the flame-holder in which thermal resistances are connected in series:

$$R_\mathrm{tot} = R_\mathrm{cu} + R_\mathrm{s} + R_\mathrm{cd} \tag{6.3.3}$$

where $R_\mathrm{cu} = 1/h_\mathrm{cu}$ is the heat resistance associated with the convective heat transfer upstream of the flame-holder, $R_\mathrm{s} = 2r/\lambda$ is the heat resistance associated with the conduction of heat in the bluff-body: $R_\mathrm{s} \approx 2\,10^{-4}\ m^2K/W$ and $R_\mathrm{cd} = 1/h_\mathrm{cd}$, for the downstream convective heat transfer. Both convective heat transfer coefficients are supposed equal: $h_\mathrm{cu} = h_\mathrm{cd} \approx 100\ Wm^{-2}K^{-1}$ so that $R_\mathrm{cd} = R_\mathrm{cu} \approx 10^{-2}\ m^2K/W$. A one-dimensional sketch of this simple model is provided in Fig. 6.9. The variation of temperature between the upstream and downstream faces of the flame holder is:

$$\Delta T = \frac{R_\mathrm{s}}{R_\mathrm{tot}}(T_\mathrm{b} - T_\mathrm{u}) \approx \frac{1}{100}(T_\mathrm{b} - T_\mathrm{u}) \tag{6.3.4}$$

This corresponds to a temperature difference $T_2 - T_1 \approx 16\ K$ which is close to the value observed in the coupled DNS: $|777 - 758| = 19\ K$. As a consequence, both CSHT and HABC methods provide similar results and these results are also consistent with the simple model of Fig. 6.9. The CSHT approach has been retained in the following of the manuscript as it provides more information for a negligible additional computational cost: AVTP is an implicit solver and the solid mesh only contains a few cells ($< 10^4$). It adds a negligible computational effort to the flow solver AVBP.

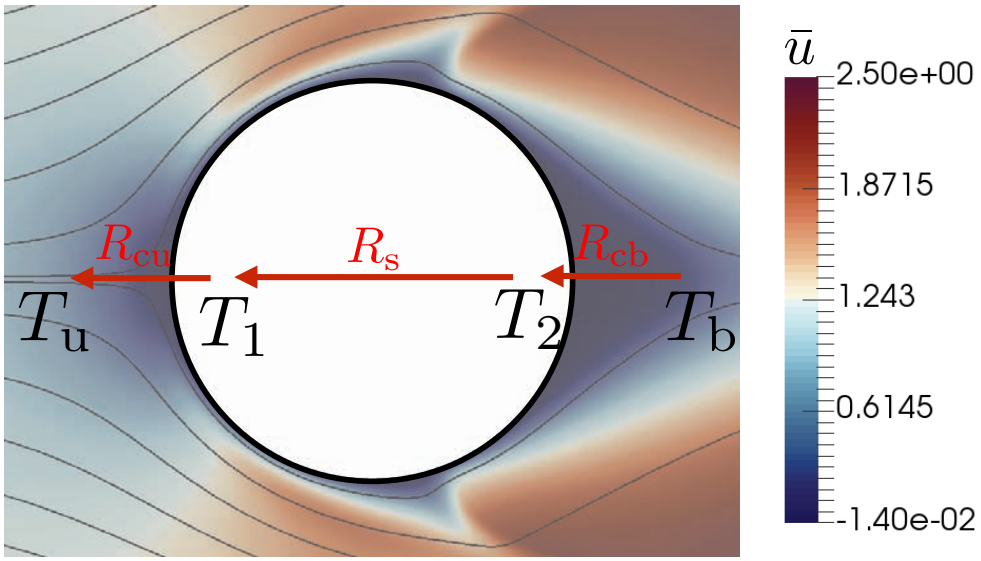

Figure 6.9: Sketch of the one-dimensional approximated model for heat transfer.

6.4 Chemical kinetic mechanisms

In the previous sections, the geometry has been properly meshed with an hybrid grid and a coupled flow/solid solver approach has been retained to capture heat transfer between the flow and the bluff-body. It is now possible to focus on the choice of the chemical kinetic scheme. This topic is especially important in the context of non-adiabatic flames, such as the ones anchored in both UBB and CBB cases. These flames will come very close to the cylinder and low temperature chemistry will play a role. Tabulation methods become difficult to use and we have focused on schemes which are compatible with DNS accuracy.

Designing a new chemical kinetic mechanism is a complex task [195, 196, 197]. However, some interesting schemes have already been developed for air/methane combustion. In this sections 6.4.1 and 6.4.2, such schemes will be validated on one-dimensional configurations with both AVBP and Cantera [198] and then used in INTRIG simulations as sketched in Fig. 6.10. Cantera is a one dimensional Navier-Stokes reactive solver featuring automatic mesh refinement and an accurate molecular transport model.

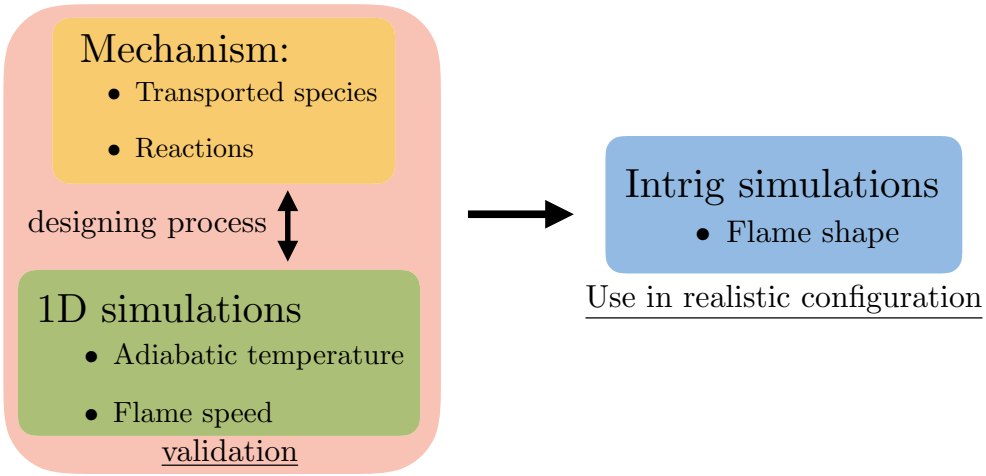

Figure 6.10: Workflow for designing and using chemical kinetic mechanisms in AVBP.

To begin with, the 2S_CH4_BFER [199] global mechanism is investigated in section 6.4.1. Two other mechanisms[200, 195] are then scrutinized in sections 6.4.2.
Detailed kinetic mechanisms are based on Arrhenius equations, which link the progress rates of individual reactions with the respective molar concentration of reactants and products[11]. A chemical scheme can contain as many reactions as needed. However, in order to lower the computational effort, simplified schemes with as few reactions as possible are always preferred. In the case of a single step chemistry with N species, the following conservation equation is obtained:

$$\sum_{k=1}^{N_r+N_p} \nu_k M_k = 0 \tag{6.4.1}$$

where M_k stands for the different species involved in the reaction and ν_k is the molar stoichiometric coefficients of both reactants (positive) and products (negative). The probability that a reaction occurs between two distinct species A and B to form C: $P_{A+B\rightarrow C}$, is proportional to the probability that both molecules encounter, so that $P_{A+B\rightarrow C}$ $[A][B]$, where [] stands for the molar concentration. These results can only be applied to elementary reactions, which cannot be decomposed into simpler ones. In the general case, the progress rate of the reaction PR is a function of the molar concentrations of each species involved in the reaction:

$$PR = K_f \prod_{k=1}^{N_r} [X_k]^{n_k} - K_r \prod_{k=1+N_r}^{N_p+N_r} [X_k]^{n_k} \tag{6.4.2}$$

where K_f and K_r are the forward and backward rates of reaction. It is convenient to link the molar concentrations and mass fractions as only the latter are computed in CFD codes: $[X_k] = \rho Y_k / W_k$ with W_k, the molar mass of the species. In this law, the exponents of the molar concentration terms are equal to their molar stoichiometric coefficients for elementary reactions. Both forward and backward rates of reaction may be expressed by the Arrhenius equation:

$$K = AT^{\beta} \exp(-\frac{E_a}{RT}) \tag{6.4.3}$$

where the pre-exponential constant A, the temperature exponent β and the activation energy E_a are tabulated for each reaction.

6.4.1 2S_CH4_BFER global scheme

Simulations have been first conducted with a two-step global mechanism fitted for air/methane combustion called 2S_CH4_BFER [199]. This scheme is built to reproduce both the correct adiabatic flame temperature and laminar flame velocity for lean air/methane premixed flows over a wide range of conditions. It contains two chemical reactions and 6 species: CH_4, O_2, N_2, H_2O, CO_2, CO. The first step produces carbon monoxide and water from methane and dioxygen:

$$CH_4 + \frac{3}{2}O_2 \rightarrow CO + 2H_2O \tag{6.4.4}$$

The second step is the CO-CO_2 equilibrium reaction:

$$CO + \frac{1}{2}O_2 \quad CO_2 \tag{6.4.5}$$

These two reactions are not elementary. As a consequence, the exponents of equation 6.4.2 are not equal to the stoichiometric coefficients of the species. The first validation of a scheme is to compute laminar

flame velocities. The latter can be measured accurately in 1D simulations by using the conservation equation of fuel mass fraction integrated over the entire domain for a lean flame:

$$\rho_u s_l Y_u^F = \int_{-\infty}^{\infty} \omega_F \, \mathrm{d}x \tag{6.4.6}$$

where the subscript u stands for unburnt quantities and Y_u^F the mass fraction of fuel in the unburnt mixture.

As Shown in equation 6.4.6, the laminar flame speed s_l may be retrieved my measuring the total fuel reaction rate integrated over the entire domain. In the following, two parametric studies are presented.

ϕ	0.7	0.75	0.8	0.85	0.9
s_l $[cm\,s^{-1}]$	18.2	22.0	25.5	29.0	32.3

Table 6.3: Laminar flame speed against the equivalence ratio at $T_u = 298\ K$ with Cantera.

First, the influence of equivalence ratio on s_l is investigated in table 6.3. As expected, the flame velocity increases with the equivalence ratio. These flame velocities are compared to experimental measurements in Fig. 6.14.

The second parametric study concerns the influence of the fresh gases temperature T_u over the laminar flame velocity. Indeed, heating of the unburnt mixture (of the order of 100 to 300 K) is observed in simulations which take into account heat transfer from the flame holder to the fresh mixture. The

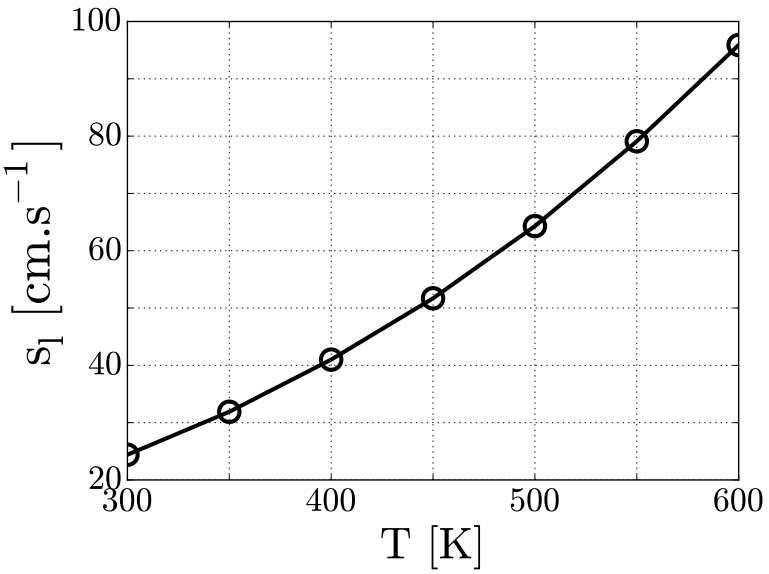

Figure 6.11: Laminar flame velocity against the fresh gas temperature at $\phi = 0.75$ and $\Delta x = 50\,\mu m$

fresh gases temperature T_u strongly influences the laminar flame velocity and the kinematic scheme must account for this. For instance, a heating of 150 K doubles the laminar flame velocity. The results of the two-step scheme can be compared with the following asymptotic model:

$$s_L(T_1) = s_L(T_0)\left(\frac{T_1}{T_0}\right)^{\alpha_T} \tag{6.4.7}$$

Expected values of α_T are close to 2 for this operating regime. A monomial regression applied to the data displayed in Fig. 6.11 leads to $\alpha_{T,BFER} = 2.05$ which is close to the expected value: $\alpha_T = 2.1$ [201].

6.4.2 Reduced mechanisms

In addition to the global two-step scheme of section 6.4.1, two additional mechanisms have been used in this study: the LU13 [202] and LU19 [195] reduced mechanisms. These mechanisms were deduced from two detailed kinetic schemes [203, 204], which contain too many species to be directly used in CFD solvers but include all the best chemical knowledge available today. The reduction procedure occurs in three steps [195]:

reduction of a detailed mechanism

1. **Skeletal reduction**
   Unimportant species as well as the participating reactions are removed. Simulations are carried out to assess the need of each species in typical operating regimes: auto-ignition and perfectly stirred reactor. Both LU13 and LU19 mechanisms have been obtained by neglecting the NO chemistry. This assumption has a negligible impact on the main mechanism acording to Lu [195].

2. **Identification of Quasi Steady State (QSS) species**
   In the next reduction step, species with low concentration which are consumed very fast can be treated separately. These are called the QSS species for which a (quasi) constant assumption can be proposed: $\partial A/\partial t \approx 0$ so that the concentration of species A can be expressed as a simple function of other non QSS species. This is done by combining all the elementary kinetic equations in which the QSS species is implied.

3. **Analytical resolution of the QSS equations**
   Most of the time, the QSS equations are solved with an iterative procedure, which provides an approximation of the solution. Here, the QSS equations are transformed so that the concentrations can be derived analytically. This reduces the computational time required to compute the chemical kinetics.

Reduced mechanisms are very convenient for CFD codes: as few species as possible are transported and stiff elementary reactions are removed while remaining very close to the detailed mechanism. Two reduced mechanisms have been used and compared to the 2S_CH4_BFER mechanism.

Among them, the LU13 mechanism has been used to describe the chemical kinetics of the methane-air combustion [202]. It is reduced from the GRI-1.2 mechanism [203]. Only 13 species are retained: the species present in the 2S_CH4_BFER scheme plus H, H_2, O, OH, HO_2, CH_2O and CH_3. As expected, all these species are reaction intermediates and take non negligible values only in the vicinity of the flame front. This property allows to start a computation with a global scheme such as the 2S_CH4_BFER and then switch to a reduced scheme by adding all the reaction intermediates to the solution (*add_spec* procedure in AVBP). This mechanism has been validated with one-dimensional flames with both Cantera and AVBP. For instance, the laminar flame velocity as a function of the grid resolution is displayed in table 6.4 and profiles of heat release rate and temperature are shown in Fig. 6.12.

Δx $[\mu m]$	12.5	33	50	62.5	83
s_L $[cm\,s^{-1}]$	24.1	24.0	24.0	24.0	24.1

Table 6.4: Laminar flame velocity against the mesh resolution for a lean premixed configuration: ϕ = 0.75, T_u = 298 K. Computations with LU13 scheme (13 species) and AVBP. The value predicted with the 2S_CH4_BFER scheme is 22 $cm.s^{-1}$. The flame thickness based to the maximum temperature gradient is 580 μm.

On the one hand, the laminar flame velocity of the LU13 mechanism is close to the one of the 2S_CH4_BFER scheme at the equivalence ratio of interest: ϕ = 0.75. An other interesting fact is that

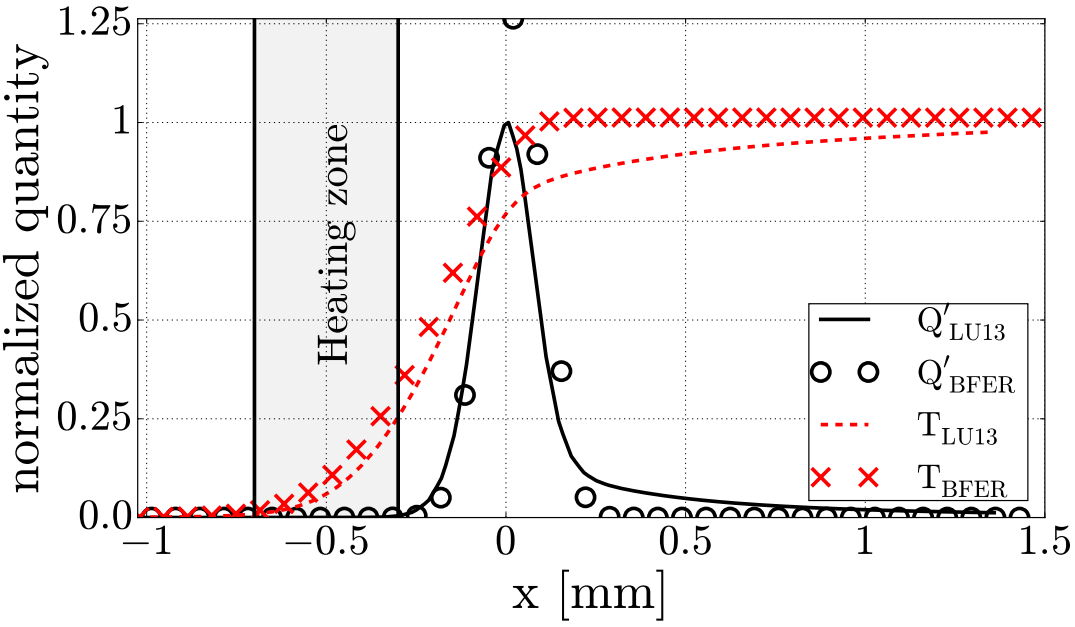

Figure 6.12: Comparison between 2S_CH4_BFER and LU13 mechanism for both temperature and heat release profiles.

the required mesh resolution is the same as the one for the 2S_CH4_BFER scheme. As a consequence, switching to a reduced mechanism only implies the transport of more species and the resolution of more complex chemical kinetic equations. For instance, in AVBP, switching from the 2S_CH4_BFER scheme to the LU13 scheme increases the computational cost by a factor two in INTRIG simulations.

On the other hand, differences are observed for the temperature profile as shown in Fig. 6.12: the reactive region can be decomposed into two zones. In the first one ($x \in [-0.3, 0.2]$ mm in Fig. 6.12, left), heat release is very important and the temperature increases rapidly. In the second region ($x > 0.2$ mm), the heat release rate is smaller but non zero and the temperature slowly converges to the adiabatic temperature $T_b = 1920$ K. This is due to the slow consumption of reaction intermediates such as O and OH. This result exhibits the ability of the LU13 scheme to reproduce a more realistic flame front.

The LU19 mechanism has been later proposed by Lu [195]. Contrary to the LU13 scheme, it is reduced from the GRI-3.0 mechanism [204] and validated on perfectly stirred reactors as well as auto-ignition cases. It is designed to be efficient for both lean and rich operating regimes by adding 6 new reaction intermediates to the LU13 mechanism: H_2O_2, CH_3OH, C_2H_2, C_4H_2, C_6H_2 and CH_2CO. As stated earlier, the NOx chemistry is not modelled in both LU13 and LU19 reduced mechanisms but can be easily added is done by Jaravel [205].

Both reduced mechanisms have been tested in Cantera and in AVBP where the increase of computational time is approximately proportional to the number of transported quantities. For instance, 5 + 6 = 11 variables[2] are transported for the 2S_CH4_BFER mechanism while 5 + 19 = 24 variables are transported for the LU19 mechanism. In practice, the computational overhead is sightly higher because more time is devoted to compute the chemical kinetics [205].

6.4.3 Comparison of chemical kinetic schemes for 1D flames

A quantitative comparison between the 2S_CH4_BFER, LU13, and LU19 mechanisms is now carried out. We first compare the mass fractions of relevant species as shown in Fig. 6.13 with AVBP. Concerning

[2] 5 for the NS equation and 6 species in the 2S_CH4_BFER scheme.

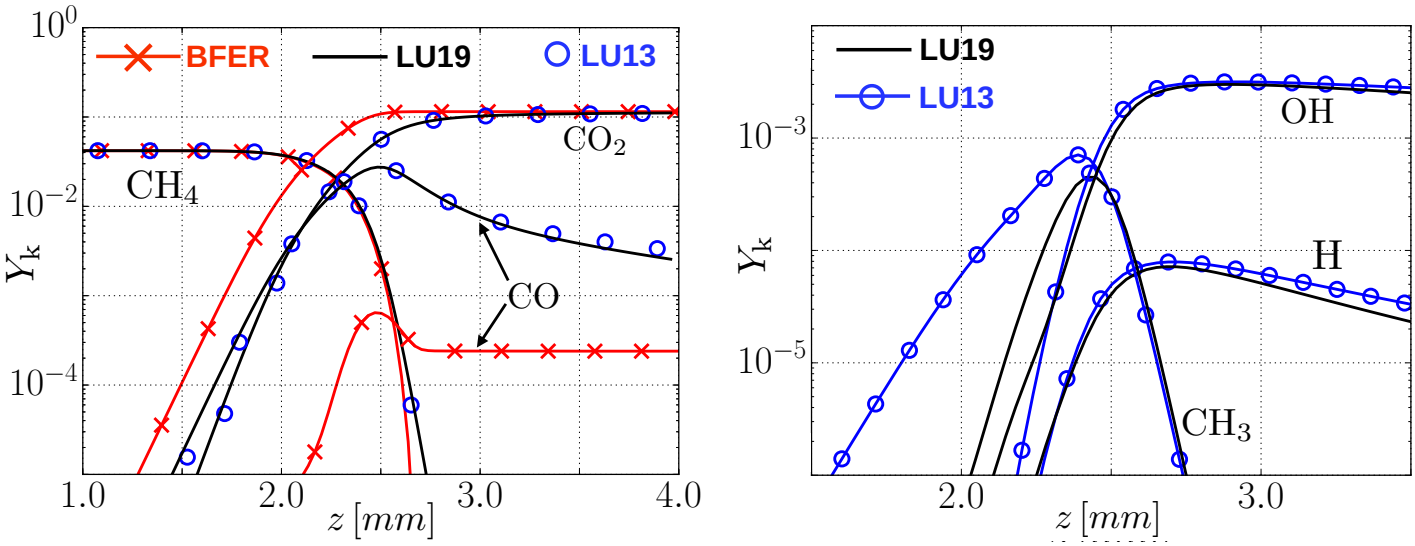

Figure 6.13: Mass fractions of some species across the flame front (AVBP). Left: species present in the three mechanisms. Right: reaction intermediates only present in LU13 and LU19 mechanisms.

the species transported in all mechanism such as CH_4, CO or CO2, one may observe some discrepancies, especially concerning the peak of CO and its value in the burnt gas, which is under-estimated with the 2S_CH4_BFER scheme. However, no differences are observed between both LU13 and LU19 mechanisms for the same species. These two reduced mechanisms exhibit slight differences for some reaction intermediates such as CH_3 or OH (Fig. 6.13, Right).

We then compare laminar flame velocities for various equivalence ratios by studying 1D flames. Using Cantera allows to obtain results for the GRI3.0 mechanism, which is not available in AVBP.

Laminar flame velocities provided by Cantera simlulations for 2S_CH4_BFER, LU13 and LU19 mechanisms are shown in Fig. 6.14 for the following operating condition: T = 298 K and P = 101300 Pa. These schemes are compared with the detailed GRI-3.0 mechanism [204] but also with experimental results of Dirrenberger et al[206]. The error bars in the experimental measurements correspond to the envelope of four different measurements performed by different authors. These measurements were realised using counter flow flames [207, 208] or spherical flame [209].

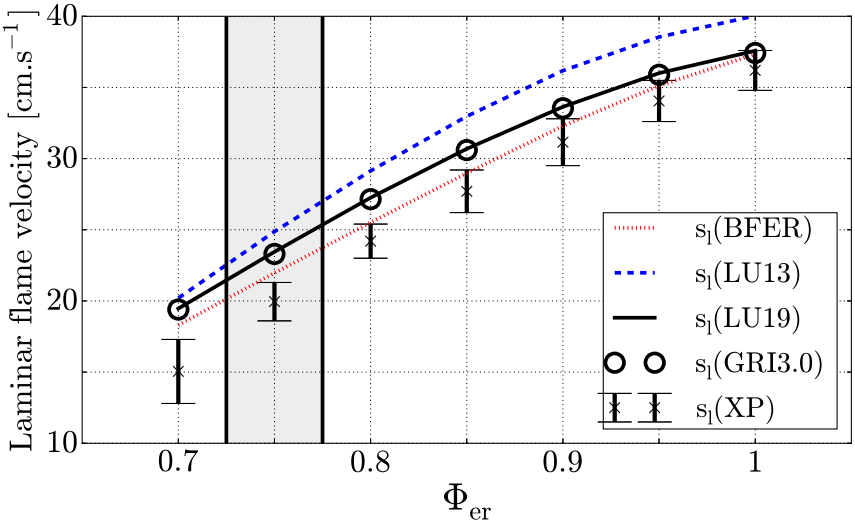

Figure 6.14: Laminar flame velocity comparison between different chemical kinetic mechanisms and experimental results extracted from [206] for methane/air lean flames at T = 298 K.

The laminar flame velocity from the LU13 mechanism is 6% higher than the one from the GRI-3.0 mechanism while the error is below 1% for the LU19 mechanism. This was expected as only the LU19 mechanism is reduced from GRI-3.0. However, a difference of about 14 % is observed between the mean experimental measurement and the LU19 reduced mechanism at $\Phi = 0.75$. All chemical schemes over-estimate flame velocities in this case except 2S_CH4_BFER which was actually tuned to match experimental data.

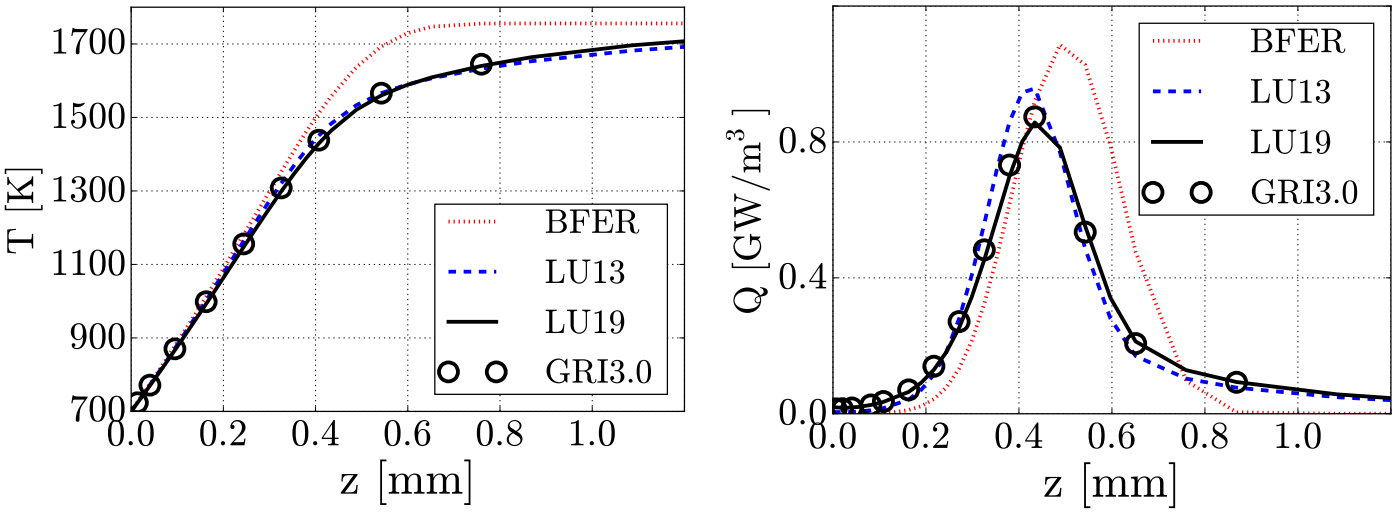

Figure 6.15: Temperature (Left) and heat release rate (Right) comparison for a flame stabilized on a burner at 700 K.

The influence of heat losses over the flame topology is now investigated. Flame stabilized over porous burners with constant rim temperature (here at 700 K with $\phi = 0.75$) have been simulated with Cantera. Contrary to freely propagating flames, stabilized ones are affected by the heat losses occurring at the burner rim. Both temperature and heat release rate profiles obtained downstream of the hot burner are reproduced in Fig. 6.15.

Similarly to the laminar velocity study, both LU19 and GRI3.0 schemes provide identical results. Discrepancies are observed with both LU13 and 2S_CH4_BFER mechanisms. These may be explained by the difference in laminar flame velocity. For instance, the 2S_CH4_BFER mechanism has a lower flame velocity than the GRI3.0 mechanism so that the corresponding flame is stabilized downstream where the heat loss is less intense.

6.4.4 Application to the INTRIG burner

In addition to the 2S_CH4_BFER scheme, the two reduced mechanisms LU13 and LU19 have been used in the simulations of the INTRIG configuration. A detailed comparison of LU13 and LU19 schemes is provided in Fig. 6.16. Species transported in the LU13 mechanism (except N_2) are displayed on the left while all the corresponding species in the LU19 mechanism are displayed on the right. Most of them are very similar. However, some differences exist close to the bluff-body: the reaction intermediate CH_3 is less intense.

The flames simulated with the three different mechanisms are then compared to experimental measurements of the flame front location. Heat transfer is taken into account thanks to the coupled strategy (section 6.3.1) on a hybrid, unstructured mesh (section 6.2). The experimental field of radical CH^* is represented in Fig. 6.17 in addition with the three flame fronts curves obtained in the DNS. Both reduced mechanisms perform better than the 2S_CH4_BFER global scheme. Moreover, the LU19 mechanism

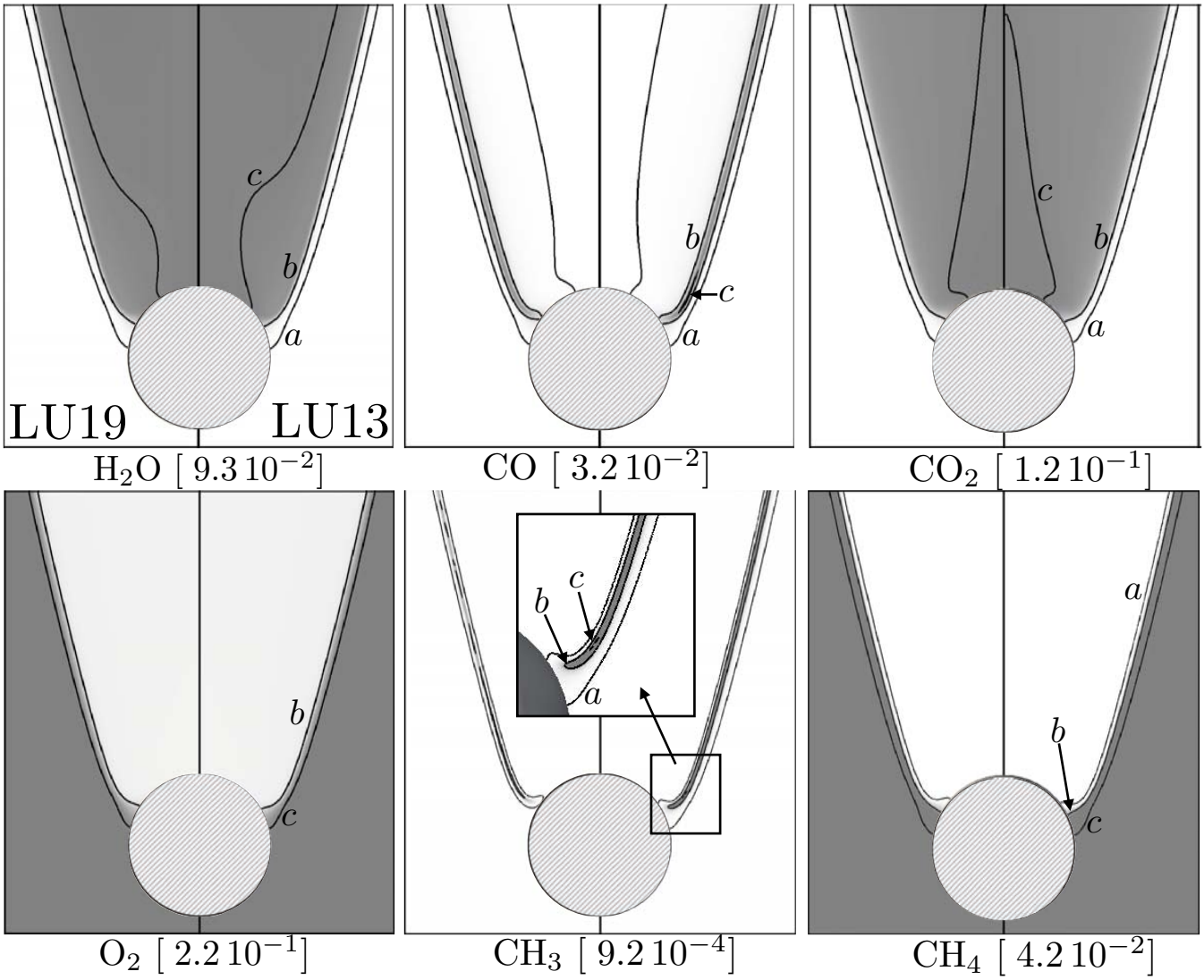

Figure 6.16: Comparison between the (normalized by max value) mass fraction fields obtained with both LU13 (Right) and LU19 (Left) mechanisms in the INTRIG configuration. The value associated with each species represent the maximum mass fraction Y_{k}. Three iso-contours are provided: $a = 0.02$, $b = 0.5$ and $c = 0.98$. The color scale starts from white ($Y_k/Y_{k,\max} = 0$) up to gray ($Y_k/Y_{k,\max} = 1$) to ease the reading of the iso-contours.

provides the best results: this is consistent with the fact that it is taking into account more species and reactions than the LU13 mechanism and predicting a more precise flame velocity (Fig. 6.14).

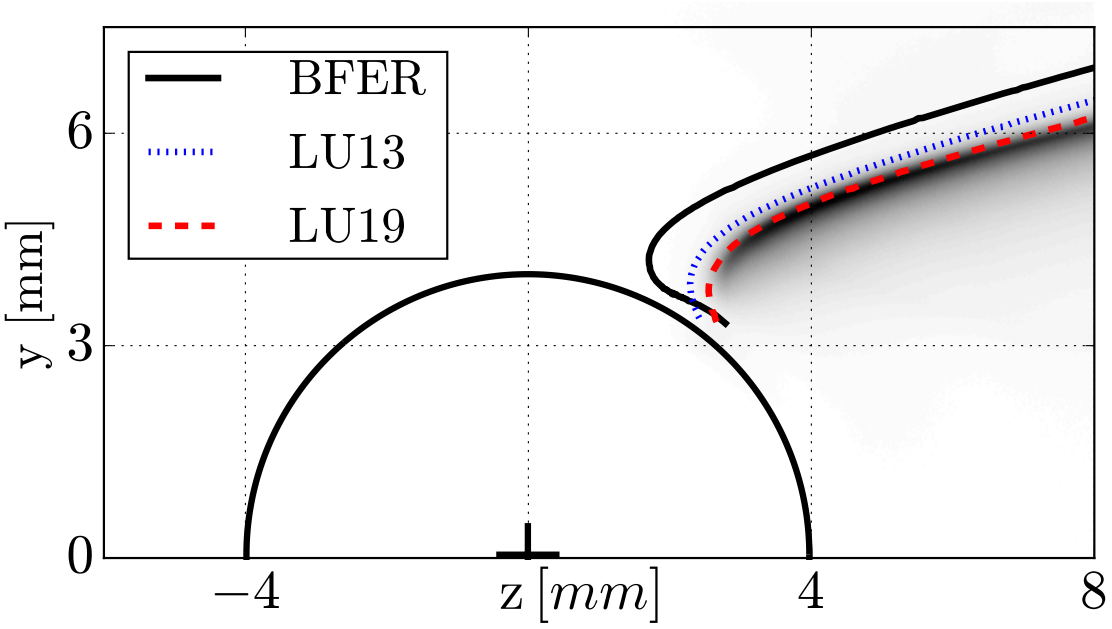

Figure 6.17: Comparison of the three chemical kinetic mechanisms. The lines correspond to flame fronts obtained with the different kinetic mechanisms while the gray field is the CH field measured experimentally for the UBB flame (un-cooled case).

6.5 Conclusion

The objective of this chapter was to describe the INTRIG burner, which is built to study the influence of heat transfer on flame dynamics. Along with the experiments, numerical simulations (DNS) have been conducted to get more insight into the physical mechanisms involved in both flame stabilisation and dynamics. Concerning the mesh, the heat transfer and the kinetic mechanisms, several options have been confronted. The final choices are recalled in Fig. 6.18. In this chapter, emphasis has been placed on numerical issues encountered in the UBB case. The strategy depicted here is used in the two following chapters to study anchoring mechanisms (chapter 7) and flame dynamics (chapter 8).

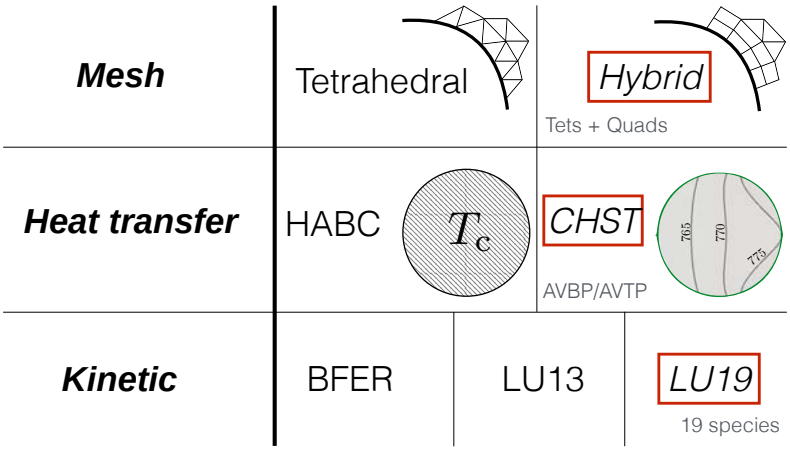

Figure 6.18: Overview of the DNS strategy. Rectangles isolate the best options retained.

Chapter 7

Mechanisms of flame anchoring on cylindrical bluff-bodies

Chapter 6 has allowed us to determine the best numerical strategy for DNS (Hybrid mesh, coupled strategy, LU19). Now, the mechanisms controlling laminar flame anchoring on a cylindrical bluff-body can be investigated using DNS and experiments. Two configurations are examined: water-cooled (CBB) and uncooled (UBB) steel bluff-bodies. Comparisons between experimental measurements and DNS show good agreement for the steady flame root locations in the two configurations. In the cooled case, the flame holder is maintained at about 300 K and the flame is stabilized in the wake of the cylinder, in the recirculation zone formed by the products of combustion. In the uncooled case, the bluff-body reaches a steady temperature of about 700 K in both experiment and DNS and the flame is stabilized closer to it. The fully coupled DNS of the flame and the temperature field in the bluff-body also shows that capturing the correct radiative heat transfer from the bluff-body is a key ingredient to reproduce experimental results. Finally, upstream stabilized flames can be obtained in the DNS for very hot bluff-bodies, when radiative heat transfer is reduced (TBB).

Introduction

In the previous chapter, both experimental and numerical setup of the INTRIG burner have been presented. It has been shown that using a coupled flow/solid DNS solver is a key ingredient to study flame anchoring mechanism as heat transfer occurs at the interface between the reactive flow and the cylinder. Among all the chemical kinetic schemes tested, the LU19 mechanism was retained as it provided the best results.

Here, both experiments and DNS are used to analyze the differences in flame structure for two different operating regimes. The simulations, performed for cooled and uncooled flame holders, reveal drastic differences in flame root location and flow topologies. They also show that radiative heat transfer must be taken into account to predict the flame topology for the uncooled case. Finally, a parametric study is performed for the emissivity ϵ of the cylinder. As this parameter decreases, radiative heat transfer is reduced and the cylinder temperature increases. A discontinuous transition is observed between flames stabilized on the sides of the bluff-body and flames stabilized upstream of it at $T_{\text{cyl}} \approx 1600$ K when the emissivity, ϵ goes from large to small values.

Results for the cooled flame holder (CBB) are discussed in section 7.1 before presenting the uncooled case (UBB) in section 7.2. Section 7.3 discusses the influence of radiative heat fluxes on the flame stabilization when the flame holder is uncooled. Finally, two simple theoretical models are introduced to predict the existence of flames stabilized upstream of the bluff-body, which is a third possibility predicted by the DNS.

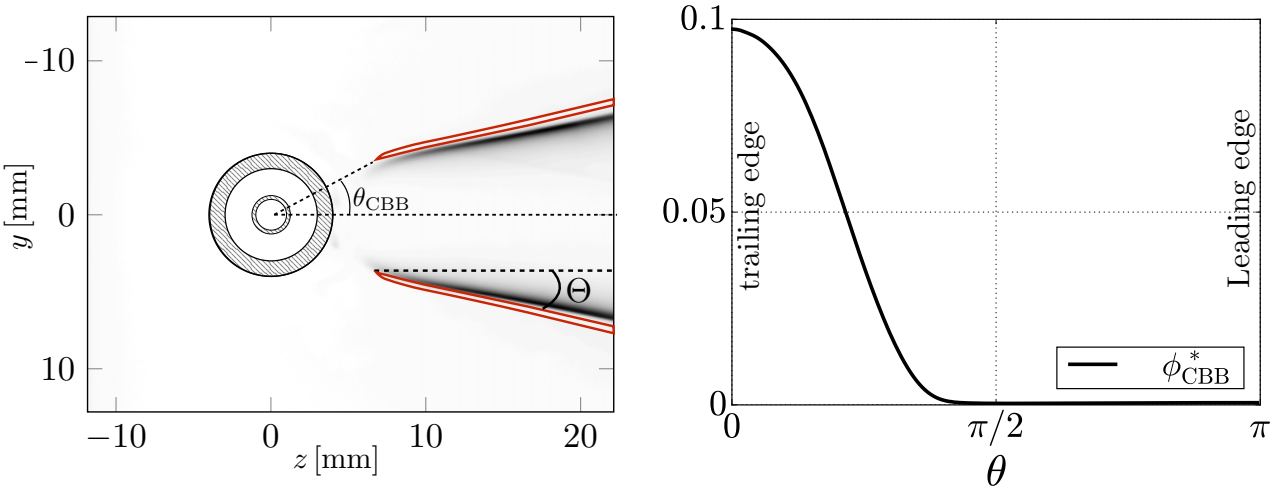

Figure 7.1: Left: Comparison between DNS (solid line: iso-contour of heat release rate) and experimental (CH^* field) flame fronts in the CBB configuration. Right: Normalized wall heat flux along the cooled cylinder external boundary.

7.1 CBB configuration

Since the bluff-body temperature is controlled by a water flow which is not computed, a boundary condition at the inner diameter of the flame holder is required. This is simple here because the water temperature is almost constant ($T_{\mathrm{w}} \approx 293\ K$) so that the convective inner flux $\phi_{\mathrm{s}\to\mathrm{w}}$ (Fig. 6.3) can be modeled through a Newton law at the solid/water boundary:

$$\phi_{\mathrm{s}\to\mathrm{w}} = h_{\mathrm{turb}}(T_{\mathrm{s}} - T_{\mathrm{w}}) \tag{7.1.1}$$

where T_{s} is the local inside skin temperature of the cylinder, T_{w} is the mean temperature of the cooling water in the outer passage and h_{turb} is the heat transfer coefficient. The water flow is turbulent with a Reynolds number of $Re \approx 5800 > Re_{\mathrm{c}} \approx 2400$ according to [210]. The heat transfer coefficient h_{turb} for a turbulent flow in an annulus is obtained by a correlation [211]:

$$h_{\mathrm{turb}} = c_p \rho v \frac{0.023}{Re^{0.2} Pr^{2/3}}\ ,\ Pr = \frac{\mu c_p}{\lambda_{\mathrm{l}}} \tag{7.1.2}$$

where c_p and μ are the specific heat at constant pressure and the dynamic viscosity of the cooling water respectively and v is the bulk velocity in the outer annulus. The corresponding turbulent heat transfer coefficient is $h_{\mathrm{turb}} \approx 3\,10^4\ W.m^{-2}.K^{-1}$.

Experimental and DNS results are compared by superposing iso-contours of the heat release rate (20 % of maximum) and CH* field obtained in the experiments (Fig. 7.1, left). The location of the flame root is accurately reproduced in the DNS. Flame angles (Θ) from DNS and experiments are close to each other: $\Theta_{\mathrm{DNS}} = 0.072\pi \pm 0.003\pi$ and $\Theta_{\mathrm{XP}} = 0.065\pi \pm 0.003\pi$. This result is coherent with the differences in laminar flame velocity: Fig. 6.14 shows that LU19 overestimates mean experimental flame velocities by 14 %.

In this configuration, the flame roots are located 3 mm downstream of the bluff-body at the angle of $\theta_{\mathrm{CBB}} \approx 0.15\pi$. Figure 7.1, right shows the normalized heat flux entering the cylinder:

$$\phi^*_{\mathrm{r}} = \frac{\vec{\phi}_{\mathrm{fluid}}.\vec{n}}{\rho_u Y_{\mathrm{CH_4}} s_{\mathrm{l}} Q} \tag{7.1.3}$$

where $\rho_u = 1.2\ kg.m^{-3}$ and $Y_{\mathrm{CH_4}} = 0.042$ are the gas density and methane mass fraction in the unburnt side respectively, $Q = 50100\ J.g^{-1}$ is the mass heat of reaction for methane/air combustion. This flux is

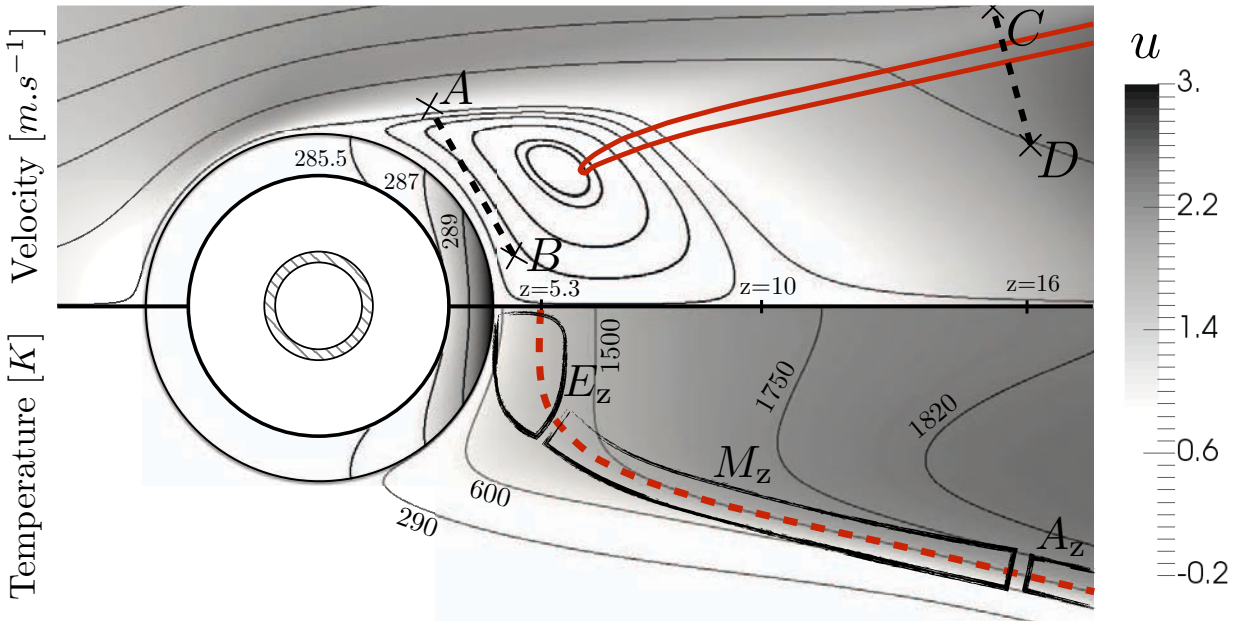

Figure 7.2: Temperature (iso-contours, solid and lower part of the fluid) and flow (stream lines, upper part of the fluid) visualization in the CBB case. The flame front location is marked by the iso-contour of 20% of the maximum heat release in the upper part and by its centerline in the lower part.

positive at all angles as the cylinder remains cooler than the unburnt mixture. It peaks at $\phi_r^* = 0.1$, a value comparable to maximum fluxes reached during SWQ (Side Wall Quenching) flame/wall interaction where reduced fluxes can reach 0.15 [11].

The flame root is located in the recirculation zone (Fig. 7.2) in the wake of the cylinder. Similar results were previously observed by Kedia et al [42] for a flame stabilized behind a square bluff-body in ceramic. The temperature is quasi uniform inside the flame holder. It ranges between 285 K, the temperature of the cooling water and 291 K. The DNS data can be used to compute the total heat transfer between the cylinder and the cooling water:

$$\Phi_{s\to w} = \int_\theta \phi_r(r_{int})\, l r_{int} \mathrm{d}\theta \tag{7.1.4}$$

where $r_{int} = 3\ mm$ is the radius of the inner boundary of the cooled flame holder. This flux is equal to 29 W and is consistent with the experimental measurement based on the cooling water heating: $\Phi^{exp}_{s\to w} = m_w c_p (T_w^{out} - T_w^{in}) = 24\ W$.

The ratio between the heat losses along the cooled cylinder (29 W) and the total power of the burner (7 kW) shows that less than 0.5 percent of the thermal energy released by combustion is transferred to the cooled flame holder. This is a negligible quantity but its effects on the flame itself, in term of stabilization and dynamics, are large

The flame structure can be analyzed by visualizing the maximum heat release rate along the flame front (Fig. 7.3, left). This quantity has been normalized by the heat release rate of the equivalent laminar un-stretched adiabatic flame. Three different zones can be identified:

- The adiabatic zone (A_z). Downstream of the cylinder ($z > 16\ mm$), the heat release rate goes to unity showing that the flame has forgotten its stabilization zone and is not affected by the cooled flame holder. Typical profiles of mass fractions of one reactant (CH_4), one product (H_2O) and one reaction intermediate (CH_3) are displayed in Fig. 7.3, right, along the path $[CD]$ of Fig. 7.2.

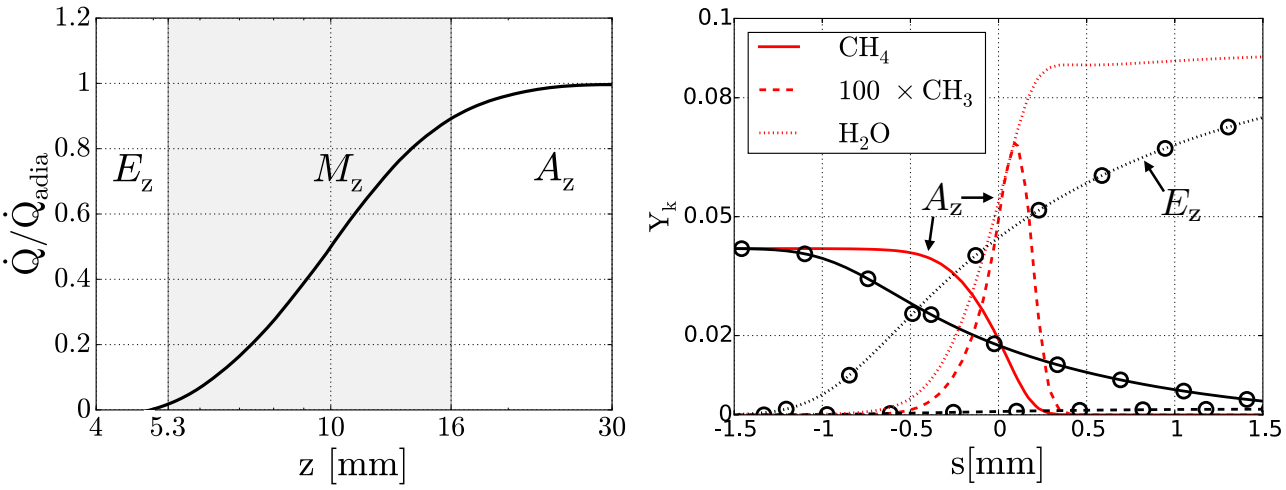

Figure 7.3: Left: Normalized maximum heat release rate along the flame front (dashed line in Fig. 7.2) for the CBB case. $z = 4\ mm$ corresponds to the cylinder external wall.
Right: Mass fractions of CH_4, CH_3 and H_2O along the paths $[AB] \in E_z$ (curve with markers) and $[CD] \in A_z$ (curves). The mass fraction of CH_3 is multiplied by a factor 100.

- The extinction zone (E_z). Close to the bluff-body ($z < 5.3\ mm$), the flame is quenched. In this region (path $[AB]$ in Fig. 7.2), the flow is dominated by diffusion processes since no production nor consumption of reaction intermediates is observed. The reactants present away from the wake of the cylinder (point A, Fig. 7.2) are mixed with the products of combustion convected in the recirculation zone (point B).

- The mixed zone (M_z). This zone is located downstream of the center of the recirculation zone ($z \in [5.3, 16]\ mm$). Here, the combustion is less intensive because the fresh mixture has been mixed with products of combustion so that the local equivalence ratio is decreased. This is the zone where the flame roots are located. Fig. 7.3, left, shows that the transition from the quenched state (zone E_z) to the fully burning state (zone A_z) is progressive in the zone M_z and takes place over a length of approximately 1 cm.

7.2 UBB configuration

This section describes the steady flame obtained for an uncooled configuration where the cooled bluff-body of Fig. 6.3, Left is replaced by a solid steel cylinder (Fig. 6.3, Right).

7.2.1 Anchoring mechanisms

For the uncooled flame holder, a steady symmetrical flame is also observed. The comparison between DNS and experiments is very good (Fig. 7.4, left). Compared to the CBB case (Fig. 7.1, left), the flame is much closer to the flame holder. The radial heat flux in the fluid region can be used to determine its angle. The angle θ_{UBB} corresponds to the azimuthal point where the heat flux changes sign: $\theta_{UBB} = \theta \,/\, \vec{\phi}_{fluid}.\vec{n} = 0$ where $\vec{n}$ is the normal unit vector pointing inside of the cylinder. As shown in Fig. 7.4, right: $\theta_{UBB} = 0.37\pi$ while θ_{CBB} was 0.15π (section 7.1). Furthermore, the flame roots are located at 0.3 mm of the flame holder instead of 1.6 mm for the CBB case.

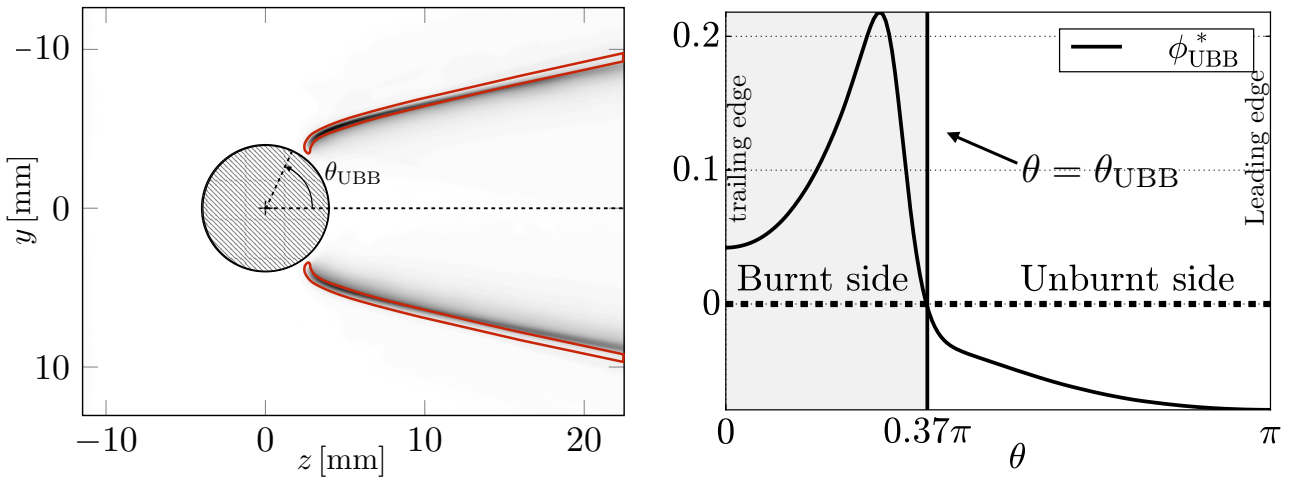

Figure 7.4: Left: Comparison of DNS (iso-contours of heat release rate) and experimental (CH^* field) flame fronts in the UBB case. Right: normalized wall heat flux along the uncooled cylinder.

Temperature and velocity fields obtained in DNS for both solid and fluid zones are displayed in Fig. 7.5.

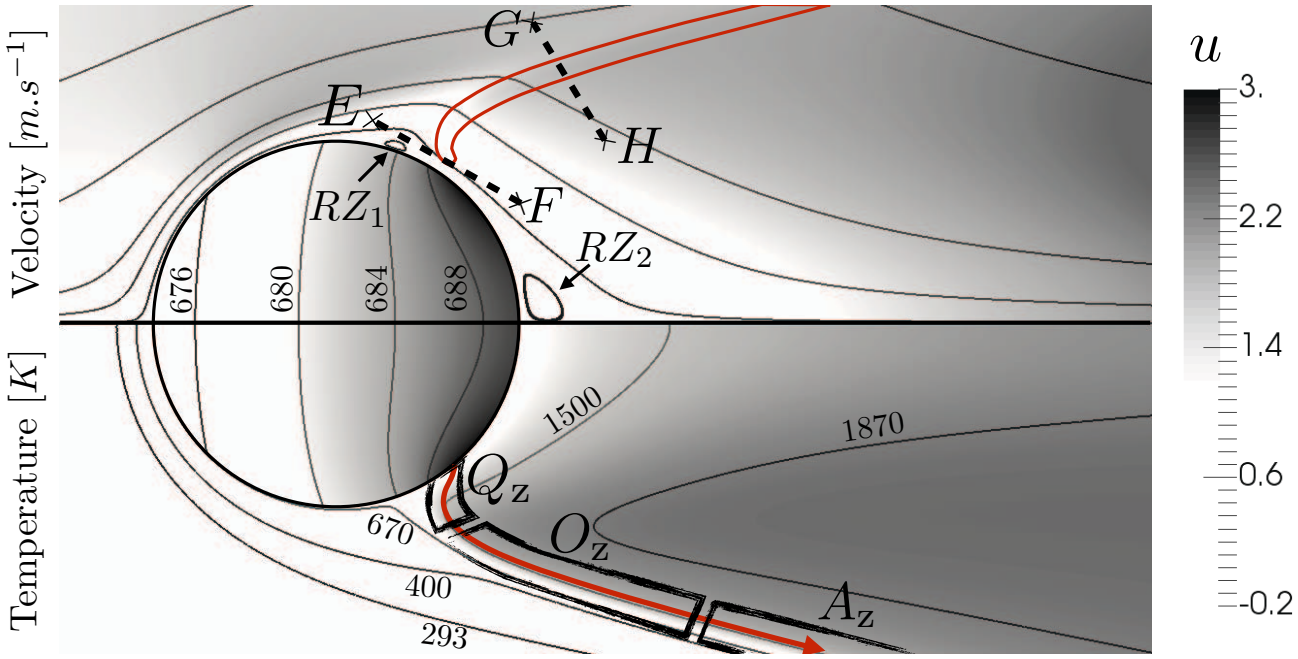

Figure 7.5: Temperature (iso-contours in the lower part of the flow and the solid) and flow (streamlines in the upper part of the flow) visualisation in the UBB case. The flame front location is recalled by the iso-contour of 20% of the maximum heat release and by its centerline.

Color scales used to visualize the temperature fields have been separately adapted for both regions. At steady state, the mean temperature of the bluff-body is close to 680 K with a minimum of 675 K at the stagnation point and a maximum of 690 K at the trailing edge. This result is consistent with experimental measurements of 670 ± 40 K obtained with a thermocouple just after stopping the flame. Close to the cylinder, the temperature field in the fluid region indicates that the fresh gases are heated by the hot cylinder on the upstream side. Two small recirculation zones are observed instead of one for the CBB case (Fig. 7.2). The first one (RZ_1) is located upstream of the flame front, where the laminar

unburnt flow separates. Its temperature is very close to the one of the bluff-body. The second one (RZ_2) is located behind the wake of the cylinder but it is much smaller than it was for the CBB case (Fig. 7.2) due to the flow expansion. Contrary to the CBB case, the flame roots are located upstream of the back recirculation zone (RZ_2) showing that this stabilization follows different mechanisms.

The DNS data can be used to establish an energy balance for the uncooled flame holder. To do this, it is useful to separate the skin of the bluff-body into two zones: upstream ($\theta > 0.37\pi$ in Fig. 7.4), a large part of the bluff-body is cooled by the incoming gases, taking a flux $\Phi_{s\to g}$ away from it:

$$\Phi_{s\to g} = \int_{\phi_r<0} \phi_r \, l r \mathrm{d}\theta \tag{7.2.1}$$

where $\phi_r = \vec{\phi}_{\text{fluid}}.\vec{n}$ is the radial heat flux in the fluid region taken at the boundary of the bluff-body and $\vec{n}$ is the normal unit vector pointing inside of the cylinder. Downstream of the bluff body ($\theta < 0.37\pi$), the burnt gases heat up the cylinder, injecting a flux $\Phi_{g\to s}$:

$$\Phi_{g\to s} = \int_{\phi_r>0} \phi_r \, l r \mathrm{d}\theta \tag{7.2.2}$$

The separation of the two zones is simply obtained from the sign of the local heat flux (Note that this flux was positive everywhere for the CBB case: see Fig. 7.1). The radiative flux lost by the cylinder Φ_{rad} is:

$$\Phi_{\text{rad}} = -\oint \epsilon\sigma(T^4 - T_{\text{ext}}^4) \, l r \mathrm{d}\theta \tag{7.2.3}$$

DNS results show that $\Phi_{g\to s} = 62.0\ W$ while $\Phi_{s\to g} = -36.0\ W$ and $\Phi_{\text{rad}} = -26.0\ W$ so that the global budget is closed: $\Phi_{g\to s} + \Phi_{s\to g} + \Phi_{\text{rad}} = 0$. The input heat transfer $\Phi_{g\to s}$ is larger than it is for the CBB case (29 W) due to the vicinity of the flame. Figure 7.6 shows the flux line inside the bluff-body. One can see that heat coming from the burnt gases is participating to the heating up of the fresh gases.

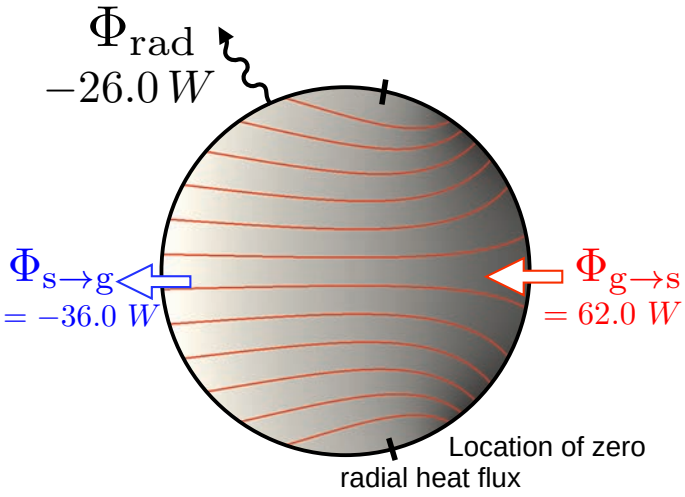

Figure 7.6: Thermal budget of the uncooled cylinder (all fluxes are counted positive when entering the cylinder). Flux lines are represented inside of the cylinder.

Similarly to the CBB case, three zones are identified for the flame front structure (see Fig. 7.7, left):

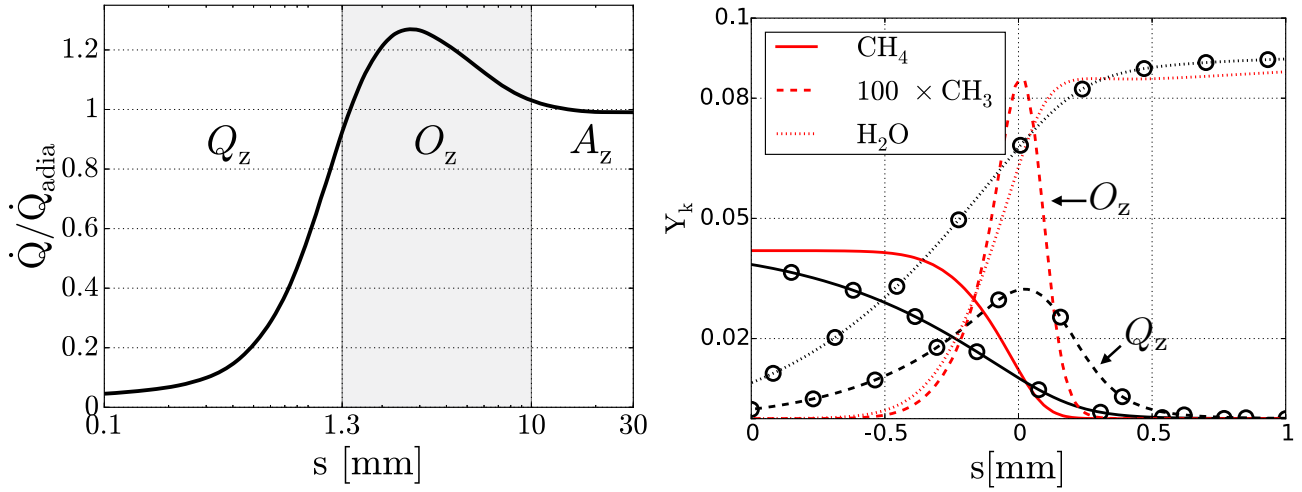

Figure 7.7: Left: Normalized maximum heat release rate along the flame front centreline (curvilinear abscissae). Three regions of interest are denoted: the quenching zone (Q_z), the over-reactive zone (O_z) and the adiabatic zone (A_z).
Right: Mass fractions of CH_4, CH_3 and H_2O along the paths $[EF] \in Q_z$ (curves with markers) and $[GH] \in O_z$(curves) plotted against their normalized curvilinear abscissae in the UBB case.

- The adiabatic zone (A_z). In this zone, the fresh reactants have not been heated by the hot bluff-body or diluted by burnt gases. As a consequence, an adiabatic, almost un-stretched laminar flame is observed and the heat release rate values are similar to the equivalent one-dimensional adiabatic flame. The adiabatic zones encountered in both the UBB and the CBB cases are similar in terms of flame dynamics.

- The over-reactive zone (O_z). Here, the flame is more intense than the corresponding un-stretched adiabatic flame. The excess in burning rate is about 25 percent since the unburnt mixture is heated by the hot cylinder (Fig. 7.6). This increases the burning rate by accelerating kinetics: the peak mass fraction of CH_3 is 20 percent greater than in the adiabatic zone as shown in Fig. 7.7, right, on the path $[GH]$.

- The quenching zone (Q_z). Close to the bluff-body, the flame is quenched due to the conjugate heat transfer from the fluid to the bluff-body. This region may be compared with the academical flame/wall interaction zone discussed in both experimental and theoretical studies by Von Kármán et al[212], Lu et al[27] and more recently by Buckmaster and Vedarajan[213, 214], who introduced the concept of edge flame. Flame/wall interaction has also been investigated numerically in Head On or Side Wall quenching configurations [215, 216] and more recently in a turbulent channel [217, 218]. The mass fraction profiles of CH_4, CH_3 and H_2O are displayed in Fig. 7.7, right, along the path $[EF]$, described in Fig. 7.7, left. The presence of the reaction intermediate CH_3 proves that chemical reactions are still occurring close to the cylinder. Furthermore, the flame front is thicker in the quenching zone than the adiabatic or the over reactive zones. This is due to thermal losses which slow kinetics down. Finally, the normalized heat flux between the fluid and the solid ϕ_r^* is shown in Fig. 7.4, right, along the cylinder. It reaches a maximum of 0.24, which is coherent with values obtained during stagnation quenching events on a cold wall: $\phi_{SQ}^* \approx 0.33$ [219]. It is also much higher than it was for the CBB case $\phi_r^* = 0.1$ (Fig. 7.1).

7.2.2 Determination of the flame anchoring angle

Many physical phenomena are involved in the stabilization of the flame roots such as extinction (in the Q_z zone of Fig. 7.7, left), fresh mixture pre-heating (occurring in both Q_z and O_z zones) and convective heat transfer along the cylinder. As a consequence, providing a model which predicts the flame anchoring angle θ_{UBB} but also the bluff-body mean temperature T_{cyl} is difficult.

In the Q_z zone, the local flame velocity is decreased because of heat losses. One dimensional models exist to predict the evolution of the flame velocity with the temperature of the cylinder [220, 221] but are difficult to use in practice as the characterization of heat losses relies on the flame/wall distance: the closer the flame is from the wall, the more intense is the heat transfer. However, this quenching distance is not known a priory.

Similarly, modeling the flame in the O_z (Fig. 7.7, left), requires to predict correctly the preheating of the fresh mixture caused by the cylinder. This implies to model both mechanic and thermal boundary layers around the cylinder with care. As long as accurate models are provided for the flame in both Q_z and O_z zones, it is possible to obtain a relation between the temperature of cylinder and the flame anchoring angle by assuming that the flame stabilizes where the local velocity compensates the laminar flame velocity as shown in Fig. 7.8. This relation is called the **dynamical equilibrium condition** [222, 223].

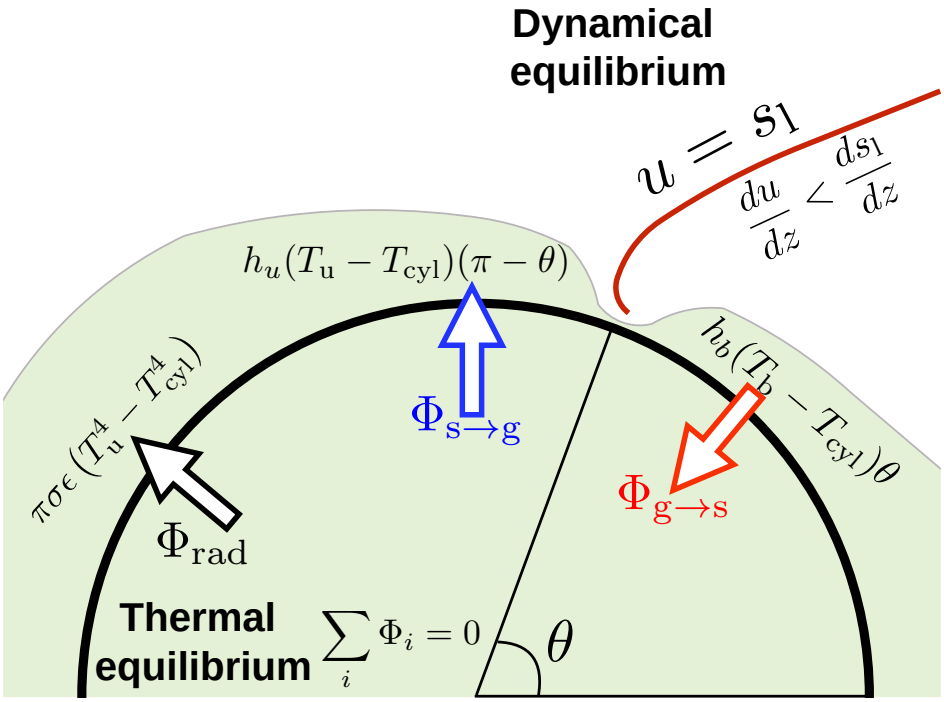

Figure 7.8: Dynamical and thermal equilibrium conditions

To close this problem, another relation must be provided to link the temperature of the flame holder with the flame anchoring angle. This can be achieved by considering the energy budget equation of the cylinder: the **thermal equilibrium condition** where simple models are provided for all heat transfer occurring across the cylinder. After assuming constant convective coefficients h_u and h_b for both unburnt and burnt sides respectively, the convective heat transfer is obtained by rewriting equations 7.2.2 and 7.2.1:

$$\Phi_{conv,i} = h_i(T_i - T_{cyl})lr\Delta\theta i \tag{7.2.4}$$

where $i \in [u, b]$ stands for burnt or unburnt sides. In the burnt side ($i = b$): $T_b = T_{adia}$ and $\Delta\theta_b = \theta$ whereas in the unburnt side ($i = u$), $T_u = T_u$ and $\Delta\theta_u = \pi - \theta$ as shown in Fig. 7.8. After combining

equation 7.2.4 with equation 7.2.3, one finally obtains:

$$\Phi_{g\to s} + \Phi_{s\to g} + \Phi_{rad} = 0 \qquad \theta = \pi\left(1 + \frac{\sigma\epsilon T_{cyl}^3}{h_u}\frac{1-\alpha^4}{1-\alpha}\right)/\left(1 + \frac{h_b}{h_u}\frac{\beta-1}{1-\alpha}\right) \tag{7.2.5}$$

where $\alpha = T_u/T_{cyl}(\approx 0.4)$ and $\beta = T_{adia}/T_{cyl}(\approx 2.8)$. Convective heat coefficients have been measured in the DNS: $h_b = 58$ and $h_u = 62\ Wm^{-2}K^{-1}$. The predicted flame foot angle is then equal to $\theta \approx 0.38\pi$ which is in very good agreement with the measured angle ($\theta_{UBB} = 0.37\pi$). Equation 7.2.5 can be inverted numerically in order to retrieve the temperature of the bluff-body as a function of the flame angle and the cylinder emissivity ϵ.

7.3 Influence of the cylinder emissivity

Section 7.2 showed that radiative heat transfer represents 45 % of the bluff-body heat losses for the UBB case. This suggests that changes in stabilization mechanisms may be induced by changing the flame holder emissivity and its temperature. Different computations have been carried out for cylinder emissivities ranging between 0.02 and 1. DNS results show that the flame root position (Fig. 7.9)

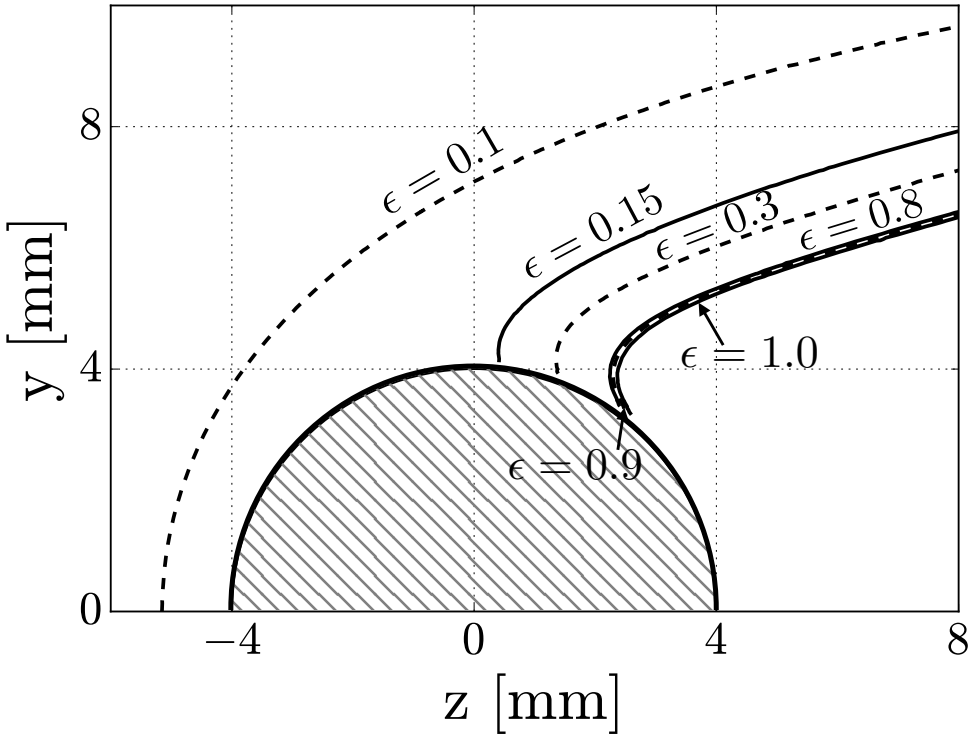

Figure 7.9: Flame shapes for emissivity ranging from $\epsilon_{min} = 0.1$ to $\epsilon_{max} = 1$.

is roughly independent of the emissivity between $\epsilon = 0.8$ (weakly oxidized bluff-body) and $\epsilon = 1.0$ (perfect black body). The corresponding averaged temperatures of the bluff-body computed in the DNS are $T_{\epsilon=0.8} = 705\ K$, $T_{\epsilon=0.9} = 682\ K$ and $T_{\epsilon=1.0} = 672\ K$. All these results are contained within the upper bound of the confidence interval of the experimental measurement of the uncooled bluff-body temperature.

Once the emissivity of the flame holder decreases below $\epsilon = 0.8$, the flame roots move upstream. For a low emissivity ($\epsilon = 0.15$), the flame is stabilized at $\theta_{\epsilon=0.15} \approx \pi/2$. In this case, half of the bluff-body is immersed in the burnt gases and its mean temperature increases to $T_{\epsilon=0.15} = 1035\ K$. A dramatic change occurs when the emissivity goes below 0.15: the flame jumps ahead of the cylinder and is called

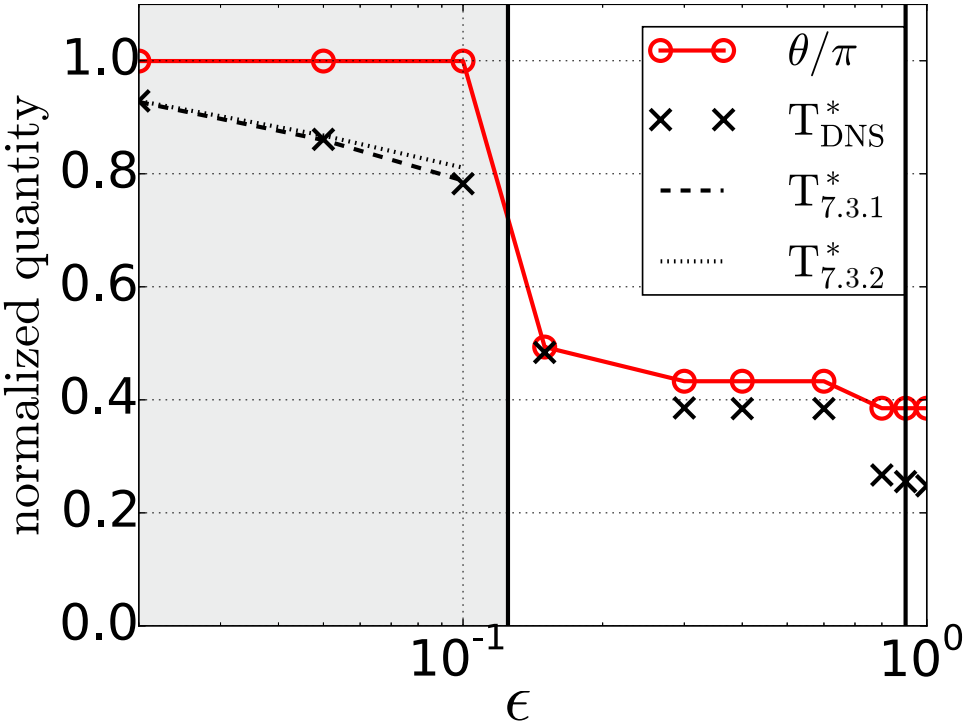

Figure 7.10: Flame root angle θ and normalized temperature $(T - T_u)/(T_{adia} - T_u)$ for cylinder emissivity between 0.02 and 1. The temperature predicted by the model 7.3.1 and its approximation 7.3.2 are also displayed when the flame is stabilized upstream.

Upstream Stabilized . In this case, the temperature of the bluff-body, which is completely immersed in the burnt gases ranges between 1500 and 1900 K, depending on the emissivity. Flame root angles and the corresponding normalized mean cylinder temperature are displayed in Fig. 7.10 for $\epsilon \in [0.02, 1]$. The temperature of the cylinder increases with the flame root angle as the cylinder is surrounded by more burnt gases. When the flame is upstream stabilized , the bluff-body mean temperature can be predicted by equation 7.2.5 by setting $\theta = \pi$. Here, we use $h \approx 100\ W.m^{-2}.K^{-1}$ which is in agreement with the value measured in the DNS for this regime:

$$\frac{\sigma \epsilon T_{cyl}^3}{h} = \beta - 1 \tag{7.3.1}$$

where radiative fluxes absorbed by the hot cylinder have been neglected. The temperature T_{cyl} of the cylinder is solution of the fourth order polynomial in equation 7.3.1. In the limit where $\epsilon < 0.1$, the temperature of the cylinder remains close to the adiabatic flame temperature. A Taylor expansion of $(T_{adia} - T_{cyl})/T_{adia}$ provides :

$$\frac{T_{adia} - T_{cyl}}{T_{adia}} \approx \frac{1/4}{1 + h/(4\sigma\epsilon T_{adia}^3)} \tag{7.3.2}$$

According to Eq, 7.3.2, an increase of the emissivity decreases the cylinder temperature as expected. Mean temperatures in the UBB case for the DNS, the model of equation 7.3.1 and its approximation 7.3.2 are displayed in Fig. 7.10 where ϵ goes from 0.002 to 1. This figure confirms the topology discontinuity at $\epsilon = 0.15$ and shows that the simple equation 7.3.2 is sufficient to predict the variations of the flame holder temperature with ϵ when the flame is stabilized upstream of the cylinder.

In the following chapters concerning flame dynamics, the TBB[1] case which corresponds to $\epsilon = 0.05$ will be investigated along with CBB and UBB cases. Obviously, this case has not been studied experimentally and only numerical results will be provided.

[1]TBB stands for Transparent Bluff-Body.

7.4 Bifurcation to upstream stabilized flames

In section 7.3, flames stabilized upstream of the bluff-body have been observed in the DNS for the regime of low emissivity, i.e. when the cylinder is sufficiently hot. Note that such stabilization points have also been observed in the experiment of IMFT when the cylinder was rotated [66]. Such phenomena have also been observed on flames stabilized on rods [224]. In this section, two models based on different physical arguments are established to assess this phenomenon. The objective of such models is to predict whether a flame can stabilize upstream of the bluff-body or not, a situation which is potentially dangerous in practical burners as the flame holder can melt.

7.4.1 Dynamic equilibrium of the flame front (DEFF)

The basis of the DEFF model is to look at the stability of a flame stabilized on the leading edge ($\theta = \pi$) of the cylinder. If the flame is able to remain in this position, it implies that its velocity s_l is equal to that of the mean flow u_z [222, 223] and that this low velocity zone is large enough for the flame to remain in this zone as sketched in Fig. 7.11:

$$|z'| \,/\, [u(z') = s_\mathrm{l}] > \delta \tag{7.4.1}$$

where all parameters are defined in Fig. 7.11. After assuming a simple model[2] for the velocity upstream of the cylinder: $u(z') = -u_b z'/r$, equation 7.4.1 can be recast into the following ratio of non-dimensional parameters:

$$(u_b/s_\mathrm{l})/(r/\delta) < 1 \tag{7.4.2}$$

This expression can be further simplified by using the Blint correlation [225], which links flame velocity and thickness:

$$s_\mathrm{l}\delta = 2\left(\frac{T_\mathrm{b}}{T_\mathrm{u}}\right)^{0.7} D_\mathrm{th} \tag{7.4.3}$$

Finally, the flame can stabilize upstream when:

$$\frac{s_\mathrm{l}}{u_b} > a = \frac{\sqrt{2}}{(P_r Re_r)^{0.5}}\left(\frac{T_\mathrm{b}}{T_\mathrm{u}}\right)^{0.35} \tag{7.4.4}$$

In the UBB configuration, $Re_r = Re/2 = 260$, $P_r = 0.7$ and $T_\mathrm{b}/T_\mathrm{u} = 6.3$ so that $a = 0.2$. The order of magnitude seems to be correct as quasi adiabatic flames encountered for $\epsilon \quad 0.05$ are upstream stabilized with $s_{\mathrm{l,adia}}/u_b = 0.24/1.07 = 0.22 > a$. Cases where the flame is upstream stabilized or not are depicted in Fig. 7.11. As shown in section 7.3, the parameter that controls the transition between upstream to downstream flame stabilization, is the temperature of the cylinder (through the emissivity of the bluff-body). When radiative transfer is taken into account, both flame velocity and bluff-body temperature decrease and equation 7.4.4 is not fulfilled anymore. In other words, the criterion for upstream stabilization 7.4.4 is purely kinematic and cannot translate directly into a criterion involving the bluff-body temperature T_cyl. In order to close this model, one must provide a law for the flame velocity as a function of the bluff-body temperature as sketched in Fig. 7.12. Providing such a law is out of the scope of this manuscript.

[2] In the case of a potential flow, the exact solution in the vicinity of the cylinder is $u(z') \approx -(2u_b)/rz'$ but the factor 2 is omitted for the sake of simplicity

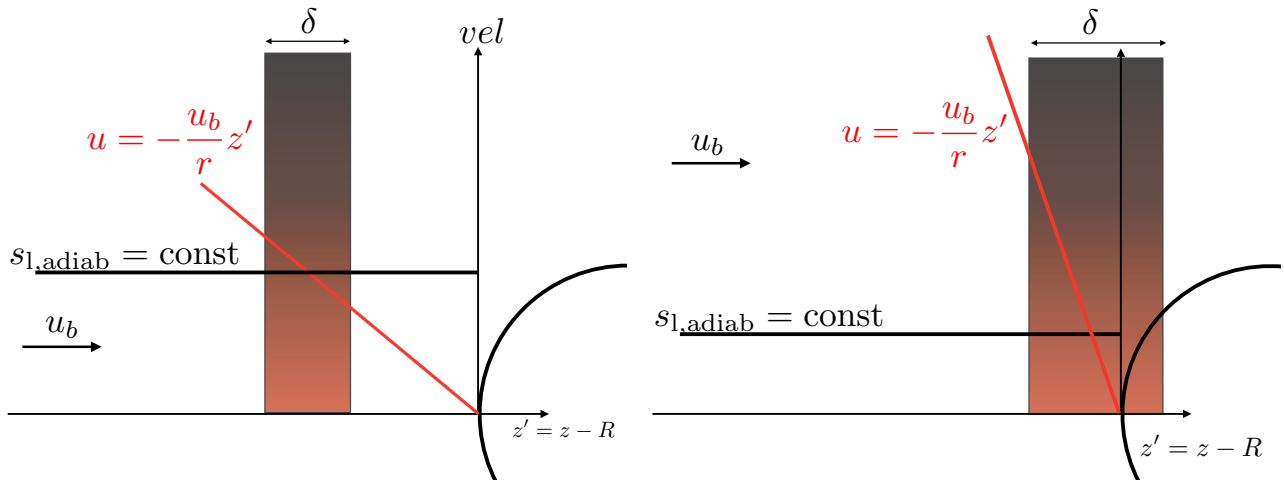

Figure 7.11: Left: Sketch of a flame stabilized upstream of the cylinder. Right: Case where a flame cannot stabilize upstream of the cylinder.

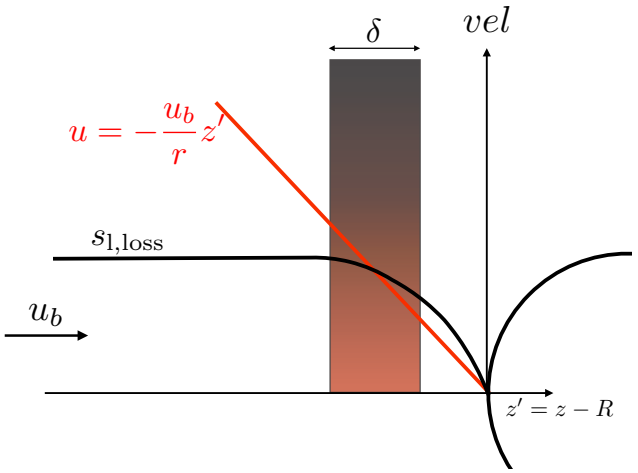

Figure 7.12: Flame stabilized upstream of the flame-holder in the non adiabatic case.

7.4.2 Thermal extinction of the flame front (TEFF)

In this second theoretical model for flame stabilization upstream of the flame holder, a much more powerful machinery can be used if the leading edge of the flame ($\theta = \pi$) is viewed as a stagnation point flame stabilized on burnt under-adiabatic gases. This case has been studied extensively using asymptotic techniques [220]. Suppose that in the region located upstream of the cylinder, the flow configuration can be approximated by a counter-flow flame (Fig. 7.13). Following the work of Libby and Williams [226], the complete flow and flame structure can be described using asymptotic analysis for a single-step chemistry premixed flame. This theory shows that extinction is observed when:

$$H = (T_{\text{adia}} - T_{\text{cyl}})(T_{\text{adia}} - T_u)T_{\text{act}}/(T_{\text{adia}}^3) > 3 \tag{7.4.5}$$

where T_{act} is the activation temperature and T_{cyl} is the temperature of the cylinder which is supposed to correspond to the burnt gas side in Fig. 7.13.
This leads to a critical cylinder temperature for extinction:

$$T_{\text{cyl}} = T_{\text{a}}(1 - 3\frac{T_{\text{adia}}^2}{T_{\text{act}}(T_{\text{adia}} - T_u)}) = 1200K \tag{7.4.6}$$

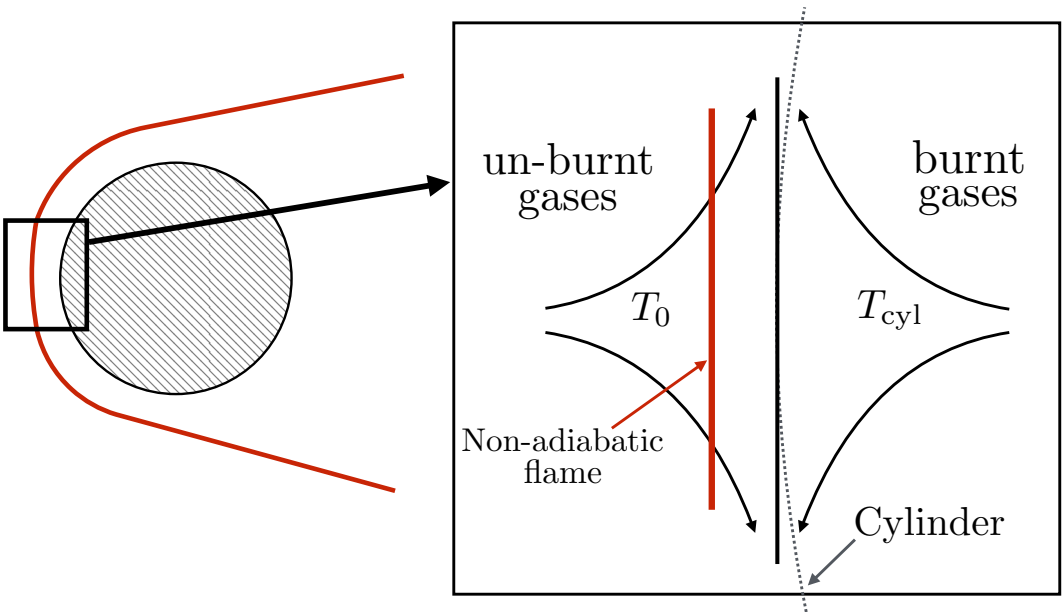

Figure 7.13: Sketch of the equivalent counter-flow flame configuration. The plane separating both jets mimics the cylinder upstream face. The burnt gases are supposed to be at the cylinder temperature T_{cyl}.

This model sightly under-estimates the minimal temperature observed for upstream stabilized flames in the DNS ($\approx$ 1500 K in section 7.3). Indeed, it is designed for flows with reduced strain $k > 1$ where $k = \partial^2 v/\partial y^2 \alpha_\infty/(v_\infty^2)$ where α_∞ is the heat diffusion coefficient taken in the burnt side and v_∞^2 is the laminar flame velocity also taken in the burnt side. In the INTRIG case, the reduced strain is equal to 0.05 so that the model cannot be applied. However, it would be appropriate to study cases with higher strain rate (larger velocity or smaller cylinder).

Both attempts to model the bifurcation between downstream and upstream stabilized (equations 7.4.4 and 7.4.6) show that there is a potential for theoretical analysis here and a nice field for future research.

7.5 Conclusions

A comparison between DNS and experiments has been carried out to study the anchoring mechanism of a flame attached on a cylindrical bluff-body. Two distinct configurations have been studied. In the cooled bluff-body case (CBB) the flame holder temperature is about 300 K and the flame is stabilized approximately one radius downstream of the cylinder at an angle $\theta_{\text{CBB}} \approx 0.15\pi$ and attached at the center of the recirculation zone in which products and reactants are mixed. In the uncooled bluff-body case (UBB), the temperature of the flame holder reaches 670 K and the flame is attached closer to the cylinder at $\theta_{\text{UBB}} \approx 0.37\pi$. A good agreement between DNS and experiments is obtained for the shape for both cases. Finally, it has been shown that the cylinder temperature is controlled by the equilibrium of the convective and radiative heat fluxes occurring along the bluff body: the emissivity of the flame holder can change the flame stabilization location (upstream or downstream of the flame holder). A change of emissivity (a decrease) can lead to a flame jumping upstream of the flame holder and its destruction. More generally, these results show that the temperature of flame holders has a major effect on the flame topology and must be included in simulations as an important control parameter.

Chapter 8

Influence of flame holder temperature on flame acoustic coupling

In the previous chapters, three different stabilization scenarios have been reported for laminar flames anchored on a cylindrical flame holder. The first one is obtained for a cooled cylinder and is referred to as the CBB (Cooled Bluff-Body) case. The two others are obtained with an uncooled cylinder: the UBB case ($\epsilon = 0.9$) where the flame is stabilized downstream but very close to the cylinder and the TBB case ($\epsilon = 0.05$) where the flame stabilizes upstream of the cylinder. We now focus on the flame dynamics for these three flames by studying the coupling between acoustic waves and unsteady heat release rate in a forced regime where flames are excited by inlet acoustic waves.

Introduction

From small scale apparatus such as domestic water heaters [227] up to rocket motors [228], combustion chambers are often subject to thermo-acoustic instabilities. These instabilities exhibit some similarities: acoustic waves perturbate the flame front, which generates unsteady heat release. The latter may generate acoustic energy when it is in phase with acoustic pressure [4]. The coupling between acoustic waves and the flame front is two sided: the generation of sound by unsteady heat release perturbation q' is predicted by a simple acoustic theory which is recalled in chapter 1. However, the heat release response q' to an acoustic velocity perturbation u' is much more complicated to predict. For instance, the G-equation framework [81, 227, 51] provides such models in very simple configurations.

As a consequence, measurements are still needed to obtain Flame Transfer Functions (FTF), which relate the ratio of unsteady heat release to the acoustic velocity perturbation. These measurements can be performed either in experiments [52, 6] or in CFD [84, 83, 82, 229].

Here, we focus on laminar lean premixed flames and investigate the flame dynamics by the mean of simulations and experiments. The first objective is to study the effect of the flame holder temperature on the FTFs. Only few studies have been performed on the same topic. Kedia et al [83] investigated the influence of the flame holder material on the FTF by using DNS data while Mejia et al [52] carried out experiments at IMFT to study the influence of flame holder temperature on the flame dynamics. However, both studies where limited because only small variations of bluff-body temperature could be created. The second objective of this study is to answer to the following question: *Is DNS able to predict the dynamics of non adiabatic flames ?*

The INTRIG burner has been designed to study lean premixed laminar flames stabilized on a cylindrical bluff-body where the temperature can be controlled over a wide range. The mechanisms leading to flame stabilization have been previously detailed in chapter 7 and three cases have been identified. Two regimes are obtained in both experiments and DNS: the cooled (CBB: $T \approx 300\ K$) and

uncooled (UBB: $T \approx 700\ K$) bluff-bodies while a third one is only available in DNS: the transparent bluff-body (TBB) for which the temperature reaches a very high temperature ($\approx 1600\ K$). The method used to measure FTFs in the DNS is described in section 8.1. The flame dynamics are scrutinized with a special attention to the flame root motion (section 8.2). A model is then provided for the INTRIG flames by using the G-equation framework in section 8.2.3 and finally, a comparison with experimental measurements is provided (section 8.3).

8.1 Measurement of Flame Transfer Function (FTF)

This section describes the numerical methods used to compute FTFs. Results are provided for the three cases of interest CBB, UBB and TBB described in chapter 7. There are many methods to measure FTFs and FDFs[1] [230, 52, 231, 82]. Here, two methods were used and compared:

- Forcing with a broad band signal and using Wiener-Hopf system inversion [82, 23, 232] to retrieve the FTF.
- Forcing with a single frequency and obtain both FTF [84, 80] or FDF [233, 231, 234, 235].

The operating point is similar to chapters 6 and 7 (see table 6.1).

8.1.1 Steady baseline flames for FTF simulations

In the previous chapter, all simulated flames were stable because flame/wall interaction had been suppressed: the chemistry was deactivated 3.5 cm downstream of the cylinder. This method is efficient as long as steady regimes are considered. However the computation of realistic flame dynamics responses must take into account flame/external wall interaction and a larger geometry must be simulated as shown in Fig. 8.1.

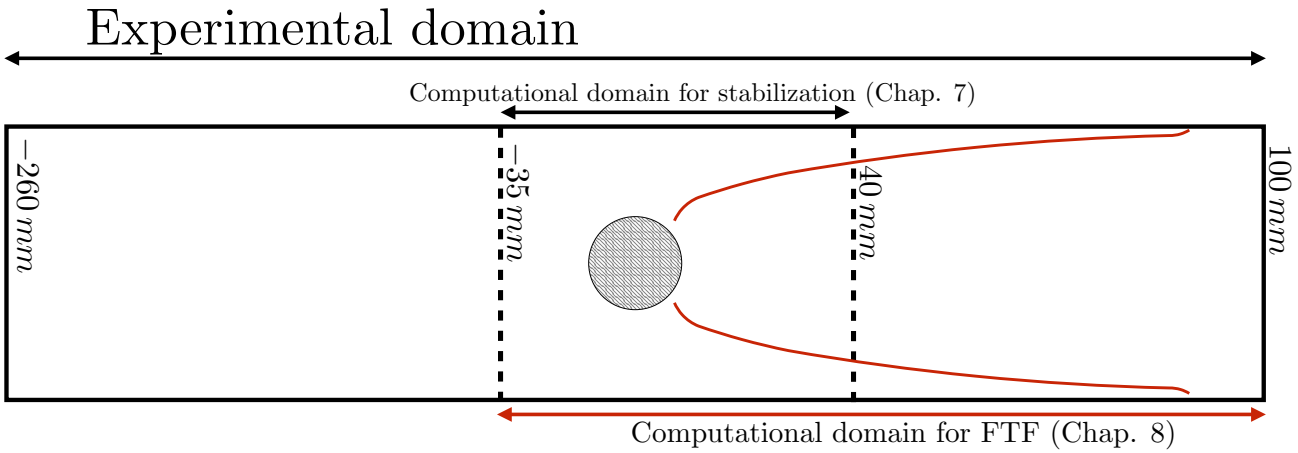

Figure 8.1: sketch of the computational domain used to obtain the FTFs.

Generally, steady flames are obtained by lowering the amplitude of both inlet and outlet reflection coefficients. In the INTRIG burner, it appeared that stable flames were only obtained with reflective boundary conditions: a velocity node is imposed at the inlet while a pressure node is imposed at the outlet. A similar phenoma has been previsouly reported by Silva et al [236].

[1]The concept of FDF, which stands for Flame Describing Function, is described in section 8.3.3.

In chapter 7, a small domain of computation was used as only the flame anchoring mechanisms were investigated: this corresponds to the region denoted as computational domain for stabilization in Fig. 8.1. In the experiment, both plenum and chamber are larger as observed in Fig. 8.1.

The geometry used to measure FTFs has been specifically adapted: the plenum has been kept as short as possible while the chamber was kept identical to the experimental one. This region is denoted as Computational domain for FTF in Fig. 8.1. This permits to increase the frequency of the first acoustic mode (from 200 Hz up to $\approx$ 1350 Hz) and avoid self-excited modes. It is important to note that chamber and plenum sizes do not impact the FTF. The mean velocity profile has been measured experimentally 3.5 cm upstream of the cylinder and is imposed at the DNS inlet while the combustion chamber walls are cooled. Cooling the external walls simplifies the set-up of the DNS because a simple isothermal boundary condition is imposed at the DNS side walls.

The three steady flames are displayed in Fig. 8.3. The specific meshes associated with each case are represented in the upper part of each images. These meshes are refined along the flame front and close to the bluff-body, as prescribed in chapter 6. All flames are steady, with limited spurious oscillations at high frequencies ($\approx$ 1350 Hz) of amplitudes below 1 $mm.s^{-1}$.

8.1.2 System identification method

When the flame is pulsated with broad band noise, Flame Transfer Functions (FTF) can be measured in DNS by using the system identification method [232, 229] which is suitable for discretized signals. The flame is considered as a black-box system: its input $s_j = s(j\Delta t)\,, j \in [\![0, N]\!]$ is the normalized upstream acoustic velocity u' taken at a reference location (2 cm upstream of the cylinder) and its output r_j is the normalized unsteady heat release rate Ω_T(Fig. 8.2):

$$r_j = \sum_{l>\mathbb{R}} h_l s_{j-l} \tag{8.1.1}$$

$$\text{with} \quad \begin{matrix} r_j = \frac{\dot{\Omega}_{T,j}}{\bar{\Omega}_T} \\ s_j = \frac{u'_j}{\bar{u}} \end{matrix}$$

where h is the impulse response of the system.

Figure 8.2: The flame viewed as a dynamical system: its input is an upstream acoustic velocity while its output is an unsteady heat release rate.

The flame response is causal: its response at time t_0 does not depend on acoustic velocity fluctuations at time $t > t_0$. As a consequence, the impulse response h is equal to zero for negative times: $h_l = 0\,, l < 0$. Moreover, h contains only a finite number of coefficients: $h_l = 0\,, l > L_{\max}$. $\Delta t L_{\max}$ quantifies the time over which the input s is used to construct the output r. Once known the discrete impulse response h of the system, the FTF is retrieved by taking the Z transform of equation 8.1.1:

$$\text{FTF}(\omega) = \mathcal{Z}_+\{h\} = \sum_{l=0}^{L_{\max}} h_l e^{-il\omega\Delta t} \tag{8.1.2}$$

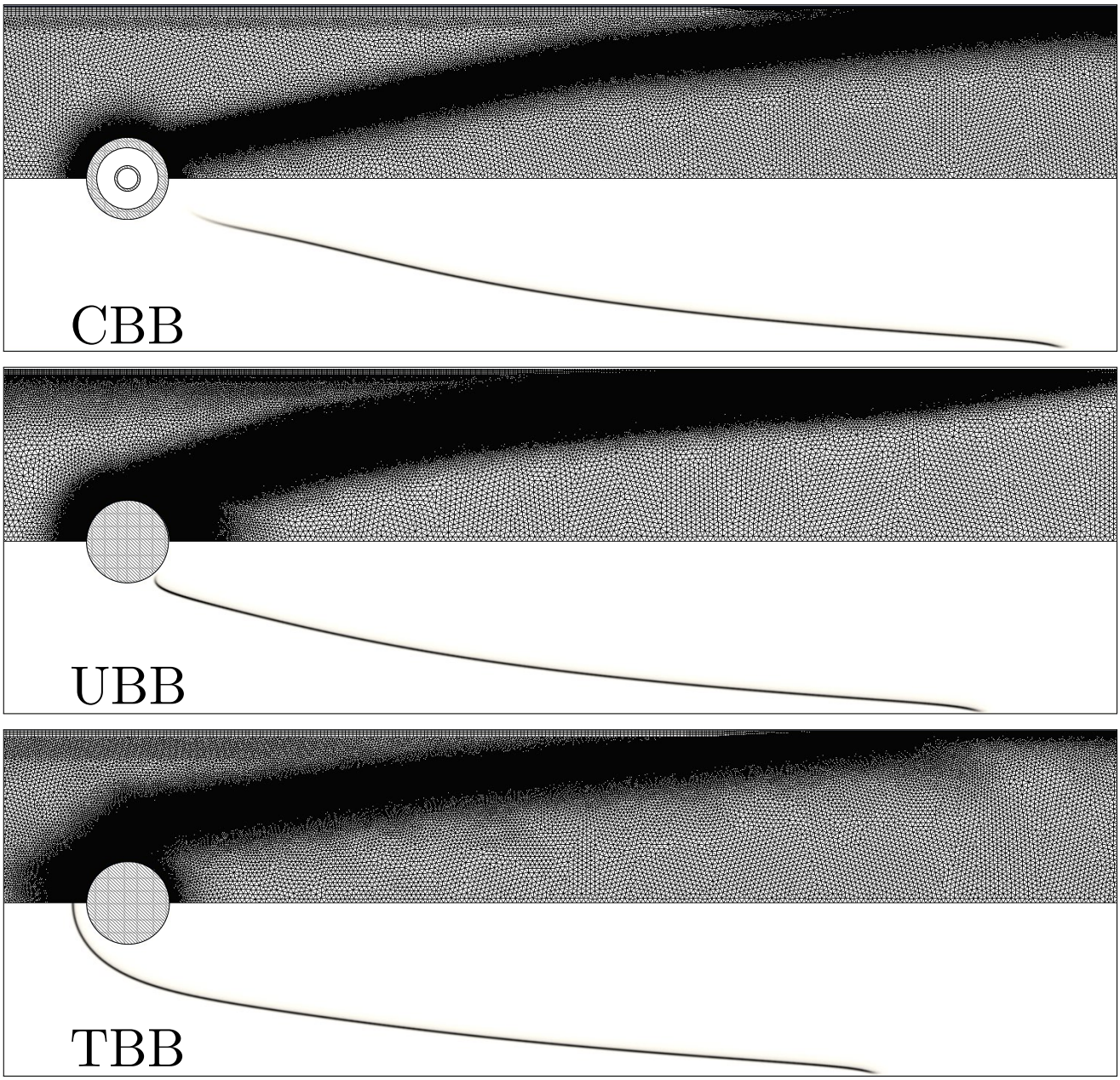

Figure 8.3: Stable flame in CBB (top), UBB (middle) and TBB (bottom) cases. The mesh is displayed in the upper part and the heat release rate in the lower part

The impulse response is solution of the Wiener-Hopf equation[237]:

$$\Gamma h = c \tag{8.1.3}$$

where Γ is the auto-correlation matrix of the input signal and c is the cross-correlation vector between the input and the output [82]:

$$c_j = \frac{1}{M} \sum_{l=L_{\max}}^{N} s_{l-j} r_j \tag{8.1.4}$$

$$\Gamma_{j,k} = \frac{1}{M} \sum_{l=L_{\max}}^{N} s_{l-j} s_{l-k} \text{ where } (j,k) \in [\![0, L_{\max}]\!]^2 \tag{8.1.5}$$

case	$N\Delta t\,[ms]$	$\Delta t\,[ms]$	N	$L_{\max}$	$T_{\max}\,[ms]$
CBB	440	0.55	792	130	71.5
UBB	750	0.55	1348	115	63.2
TBB	885	0.55	1594	90	49.5

Table 8.1: Parameters for the Wiener-Hopf system construction for the three cases CBB, UBB and TBB.

with N, the number of temporal samples and $M = N - L_{\max} + 1$. In the case of a perfect white-noise input, the auto-correlation matrix Γ reduces to the unit matrix and the impulse response is directly equal to the cross correlation matrix c. In the INTRIG configurations, fully reflective boundary conditions were employed to stabilize the flames and this introduces an undesired correlation in the input signal s. As a consequence, equation 8.1.3 must be inverted numerically:

$$h = \Gamma^{-1} c \tag{8.1.6}$$

Starting from a steady initial solution, the system is excited by a broad-band signal u', which is superimposed to the steady inlet velocity. This input signal is displayed in Fig. 8.4, left. It has been obtained by low pass filtering a random discrete binary signal [238]. This method permits to avoid the occurrence of significant peaks, which could trigger non-linear heat release response. The power spectral density of the input signal is also displayed in Fig. 8.4, right. The cut-off frequency has been set to $f_{\max} = 900\ Hz$ so that the first acoustic mode of the shortened chamber (at 1350 Hz) is not excited in the DNS.

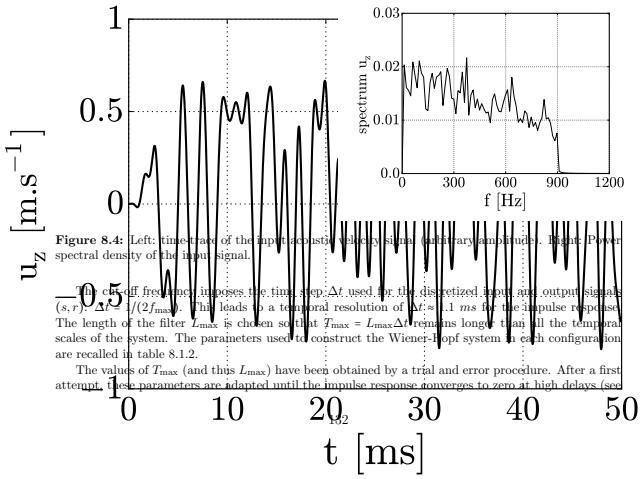

Figure 8.4: Left: time trace of the input acoustic velocity signal (arbitrary amplitude). Right: Power spectral density of the input signal.

The cut-off frequency imposes the time step Δt used for the discretized input and output signals (s, r): $\Delta t = 1/(2f_{\max})$. This leads to a temporal resolution of $\Delta t \approx 1.1\ ms$ for the impulse response. The length of the filter $L_{\max}$ is chosen so that $T_{\max} = L_{\max}\Delta t$ remains longer than all the temporal scales of the system. The parameters used to construct the Wiener-Hopf system in each configuration are recalled in table 8.1.2.

The values of $T_{\max}$ (and thus $L_{\max}$) have been obtained by a trial and error procedure. After a first attempt, these parameters are adapted until the impulse response converges to zero at high delays (see

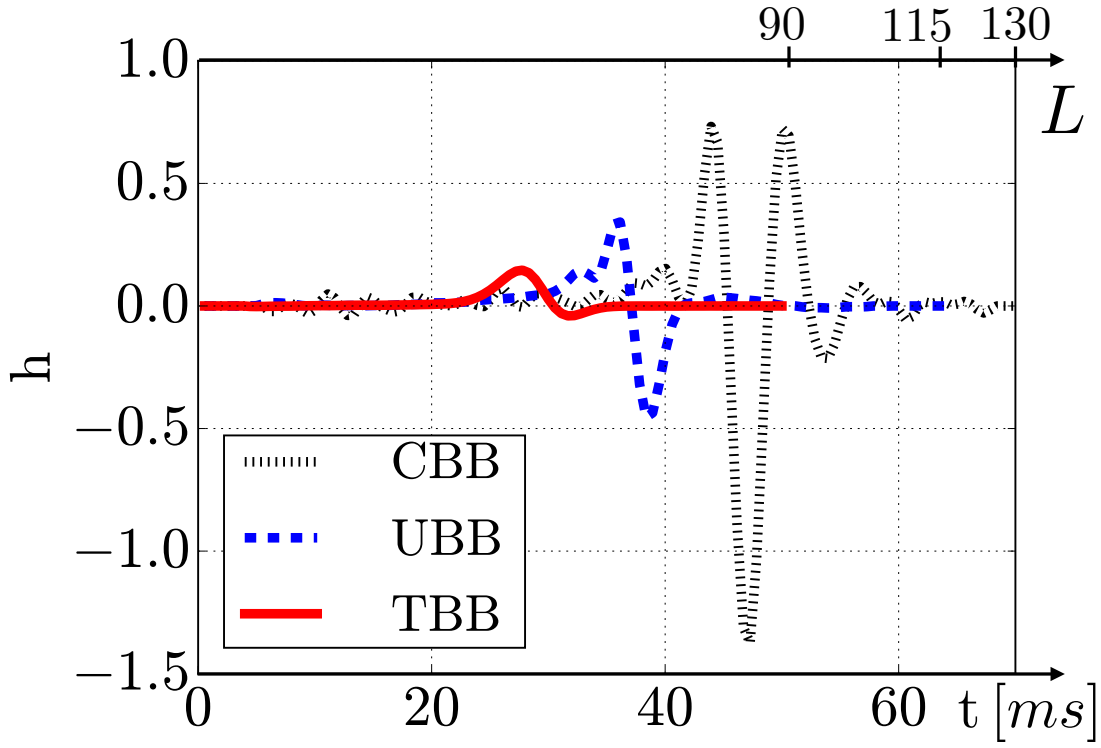

Figure 8.5: Impulse response for the three cases CBB, UBB and TBB.

Fig. 8.5). The impulse responses measured for the three configurations CBB (cooled cylinder), UBB (uncooled cylinder) and TBB (transparent cylinder) are gathered in Fig. 8.5.

The three impulse responses exhibit a similar global behavior: it is zero before a certain delay (25 ms in the TBB case, 32 ms in the UBB case and 40 ms in the CBB case). One or more peaks are then observed and finally, all impulse responses return to zero. In all cases, the sum of the impulse responses is equal to unity. This is consistent with the theoretical low frequency limit of FTFs [85] as $\mathrm{FTF}(\omega = 0) = \sum_l h_l$ (see equation 8.1.2).

Differences are also observed: the delay of the peaks decreases as the temperature of the bluff-body is increased. The increase in delay directly influences the phase lag of the FTFs and will be scrutinized in section 8.2.3. In addition, both the number and the width of the peaks vary from one case to another. When more peaks are present, the flame response experiences a richer behavior with strong gain variations. Moreover, as the width of the peaks increases, the FTF returns faster to zero[2].

The FTFs in frequency space $\mathrm{FTF}(\omega)$ can now be deduced from the impulse responses (equation 8.1.2). In order to improve the frequency resolution of the FTF, the impulse responses are prolonged with zeros: $\Delta f = 1/(T_{\max})$. Contrary to the zero-padding technique, here, adding zeros can be seen as a continuous prolongation of the impulse responses so that the frequency resolution is really increased.

Gains and phases of the FTFs are displayed in Fig. 8.6. As stated previously in this section (8.3.3), all FTFs start from unity at low frequencies ($f < 10\ Hz$) and return to zero at high frequencies ($f > 300Hz$). This behavior validates the choice of the cut-off frequency $f_{\max} = 900\ Hz$: all flames exhibit no fluctuations at high frequencies. The amplitude of the peaks greatly varies from one case to another:

- In the case of the upstream stabilized flame (TBB case), which is obtained for a quasi-transparent bluff-body ($\epsilon = 0.05$), the gain starts at unity and decreases to zero monotonically

[2]Justifications of these observations are provided in chapter 9.

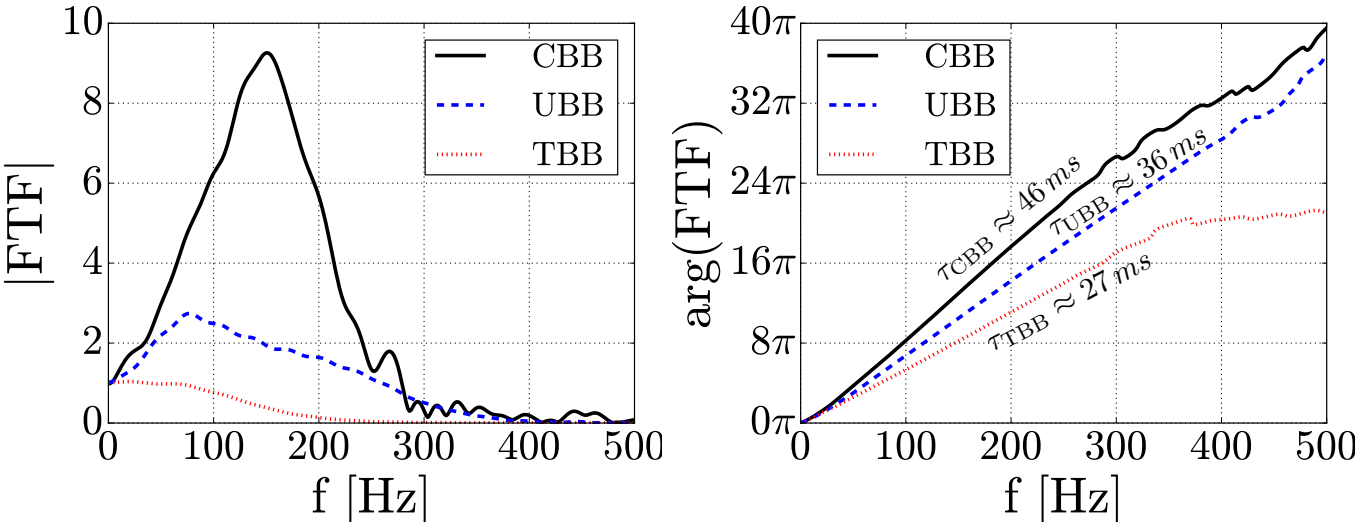

Figure 8.6: Left: Gain of the FTFs for the three cases. Right: phase of the FTFs with the corresponding delays: $\arg(\text{FTF}) = \omega\tau$

- Concerning the uncooled flame holder (UBB case with $\epsilon = 0.9$), a peak of amplitude 2.5 is observed for $|\text{FTF}(\omega)|$ at $f = 80\ Hz$. Such gains have already been reported experimentally at EM2C for conical V flames [239, 6].
- For the cooled cylinder (CBB case with $T_{\text{cyl}} \approx 300\ K$), the peak in the FTF occurs at a slightly higher frequency ($f = 140\ Hz$) and reaches a value of 9. Such large values have not been reported so far in previous publications but very few experiments have been performed for cooled flame holders

A simple conclusion arises from these observations:

> As the temperature of the bluff-body decreases (TBB → UBB → CBB), the gain of the FTF increases. The changes of the FTF are large and the maximum gain of $\text{FTF}(\omega)$ can change by an order of magnitude when the bluff-body temperature goes from 300 to 1800 K.

Phases ($\phi = \arg(\text{FTF})$) vary almost linearly until the gains tend to zero: the heat release response to an acoustic perturbation comes after a certain delay τ such that $\phi = \omega\tau$. This observation will be validated in section 8.2.3 by using the G-equation framework to model the flame dynamic response. Finally, the phases saturate at high frequencies as observed experimentally by Cuquel et al [51] or numerically by Duchaine et al [84].

8.1.3 Harmonic forcing

The Wiener-Hopf method described in section 8.1.2 is only suitable for flames excited linearly: i.e. when the heat release perturbation remains small. The influence of non-linearities on the flame response is scrutinized in section 8.3.3. Here, we simply check with harmonic velocity forcing that the heat release response remains linear[3]. Comparisons between FTFs obtained with harmonic forcing (method detailed in the present section) and by the Wiener-Hopf method (method detailed in section 8.1.2) are provided in this section and show that both results are coherent in all cases.

[3]For a linear system, the response to an harmonic input is also harmonic.

The harmonic forcing technique has been widely used to measure FTF: actually most of the experimental studies concerning FTF measurements used harmonic forcing [230, 52, 6, 227]. Concerning simulations (DNS or LES), the harmonic method remains costly: one simulation must be performed per frequency. The physical time which must be simulated must be at least grater than the flame delay (mean delay of the peaks in the impulse response as shown in section 8.3.3) plus a few periods of acoustic fluctuations where both input and output reach a permanent regime [240, 80] (see Fig. 8.7).

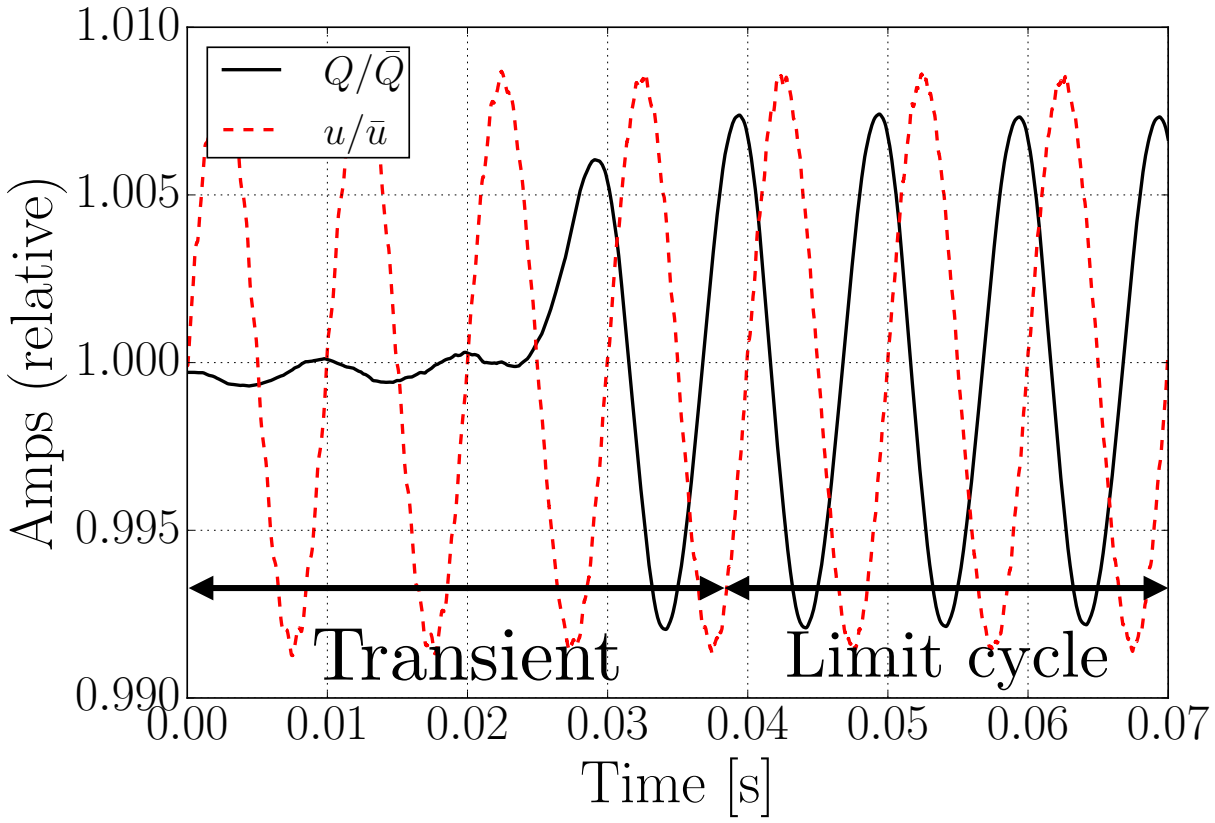

Figure 8.7: Time series of acoustic and heat release fluctuation for a low amplitude forcing at 100 Hz for the TBB case.

As a consequence, only results at a few selected frequencies will be presented here (80 and 100 Hz). The procedures employed to retrieve both gains and phases of the FTF in the three cases TBB, UBB and CBB have already been reported elsewhere [240]: the inlet is forced with harmonic acoustic waves and both amplitudes and phases of acoustic velocity at the reference location u' and heat release rate Ω_T are retrieved using Fourier transforms performed on exactly 3 periods of input and output signals as shown in Fig. 8.7 for the TBB case.

Amplitudes of excitation are small ($u'/\bar{u} \approx 0.6\%$) to avoid non-linear fluctuations of the heat release rate. One may notice that the heat release response shown in Fig. 8.7 is purely sinusoidal. The FTF measured harmonically at 100 Hz are displayed in Fig. 8.8. A very good agreement is observed between harmonic and broad-band excitation methods tested in section 8.1.2.

A second critical question for FTFs is the location of the reference point where u is measured [80]. The influence of the velocity reference location was scrutinized in the UBB case (uncooled cylinder with high emissivity). Several locations upstream of the cylinder have been chosen (see Fig. 8.9) and the results (gains and phases) are gathered in table 8.2. The last case (location $10i$) refers to a lateral location 10 mm at the side of the flame holder.

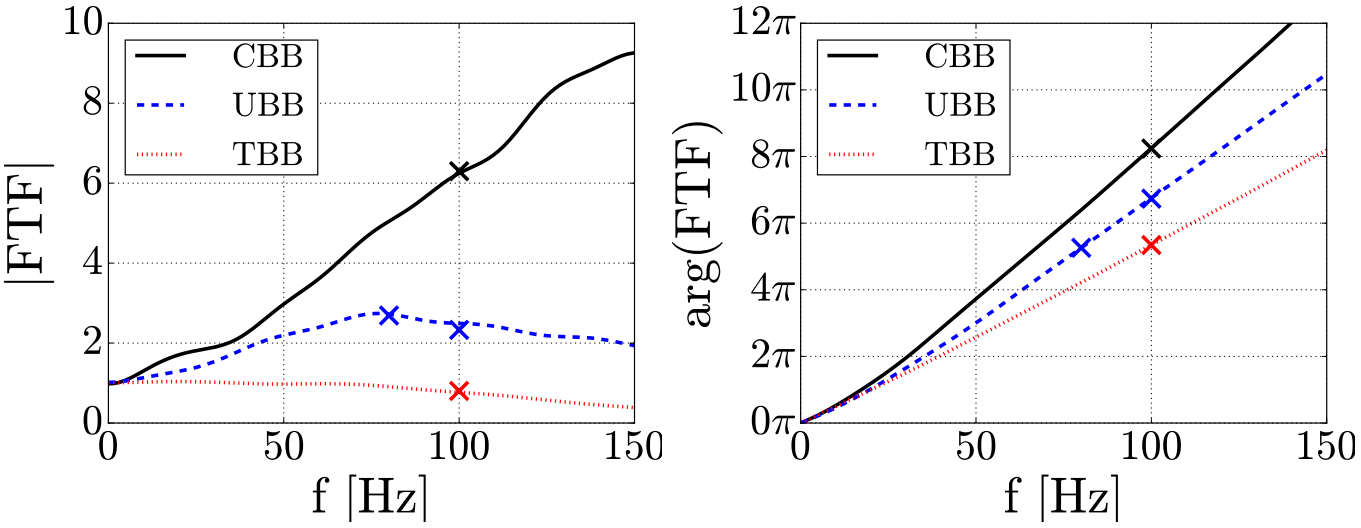

Figure 8.8: Left: Gains of the FTFs for the three cases. Right: phases of the FTFs. Results for the harmonic forcing are represented by markers. Solid lines correspond to the Wiener-Hopf data of Fig. 8.6.

Except for the two last cases, where two-dimensional effects must be considered, the gains are similar and the phases do not change. This is coherent with the results of Truffin et al [80] where it is shown that the ratio between the velocity reference displacement Δz_{ref} and the acoustic wavelength λ controls the FTF. In this case, $\Delta z_{\text{ref}}/\lambda \approx 10^{-3}$ which is negligible. Results for the two other cases concerning the influence of the velocity reference are similar and not shown here for the sake of clarity.

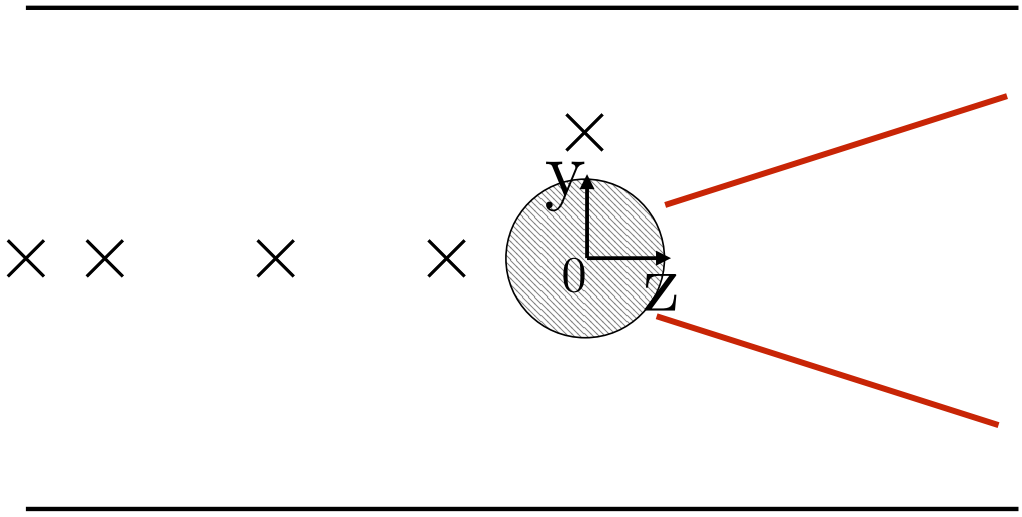

Figure 8.9: Velocity reference locations used as inputs of the FTFs.

z+iy [mm]	-35	-30	-20	-10	10i
FTF	2.37	2.37	2.39	2.62	2.25
arg(FTF)	0.75π	0.75π	0.75π	0.76π	0.72π

Table 8.2: Influence of the velocity reference location for the UBB case. The locations used for the velocity reference are sketched in Fig. 8.9

8.2 Flame roots mechanisms

The FTFs of the INTRIG burner have been measured in DNS for three distinct operating regimes (Flame holder temperature from 292 K up to 1750 K). Both gain and phase results exhibited differences which can be analysed by using DNS data to understand the underlying mechanisms.

8.2.1 Description of flame roots dynamics

The flame holder temperature is the only parameter varying in the three different cases and all other parameters such as bulk velocity or equivalence ratio remain constant. As a consequence, one may expect that it is the flame root motion which causes the change in FTF. This can be observed by looking at instantaneous fields of heat release rate sampled over one acoustic period. The acoustic velocity amplitude was set to a sufficiently high value (5%) for the three cases so that flame surface variations can be easily detected.

Heat release rate but also velocity streamlines[4] are displayed in Fig. 8.10 for the CBB case, Fig. 8.11 for the UBB case and Fig. 8.12 for the TBB case for four different excitation phases.

[4]The technique employed to display the streamlines is called Line Integral Convolution [241]

8.2.1.1 Cooled case CBB: $T_{cyl} \approx 300\ K$

Wrinkles are convected along the flame front at a convective speed (Fig. 8.10, grey circles). These wrinkles are created in the vicinity of the flame holder, where the flame is attached. The flow topology encounters important changes in the wake of the cylinder. The main Recirculating Zone (RZ) decreases from step $T/4$ to step $3T/4$ while a new RZ is formed at the side of the cylinder (step $3T/4$). The latter grows and is displaced in the wake of the cylinder between steps ($3T/4$ and $5T/4$). Kinematic restoration is slow and the flame surface wrinkles are convected almost without attenuation.

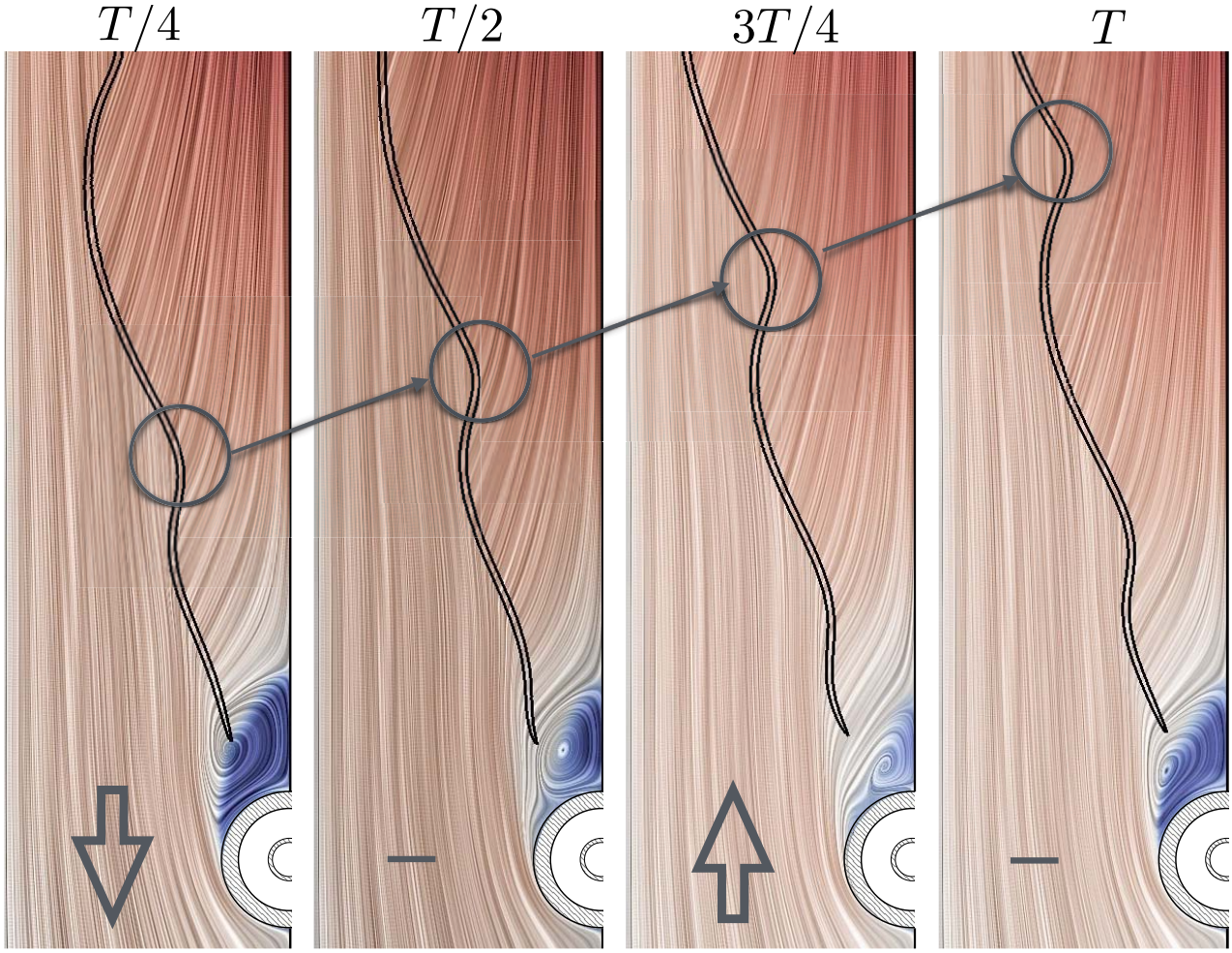

Figure 8.10: Instantaneous solutions during one acoustic period of excitation at 100 Hz for the CBB case. Heat release rate is displayed by thick black iso-lines and velocity streamlines coloured by the axial velocity are represented by using the LIC method [241]. The grey arrow represents the instantaneous direction of the acoustic velocity fluctuation at the reference velocity location (20 mm upstream of the cylinder).

As explained in chapter 7, the flame roots are attached in the center of the main RZ where fresh reactants and products of combustion mix. As this zone is strongly pulsated, the flame roots are also affected in the same proportions.

8.2.1.2 Uncooled case UBB: $T_{cyl} \approx 700\ K$

In this case, wrinkles convection is also observed (Fig. 8.11, grey circles) but at a lower amplitude than for the CBB case. The flame roots are anchored closer to the bluff-body, which temperature is T_{cyl} = 680 K and they move much less than for CBB flames. Note that the cylinder temperature does not change

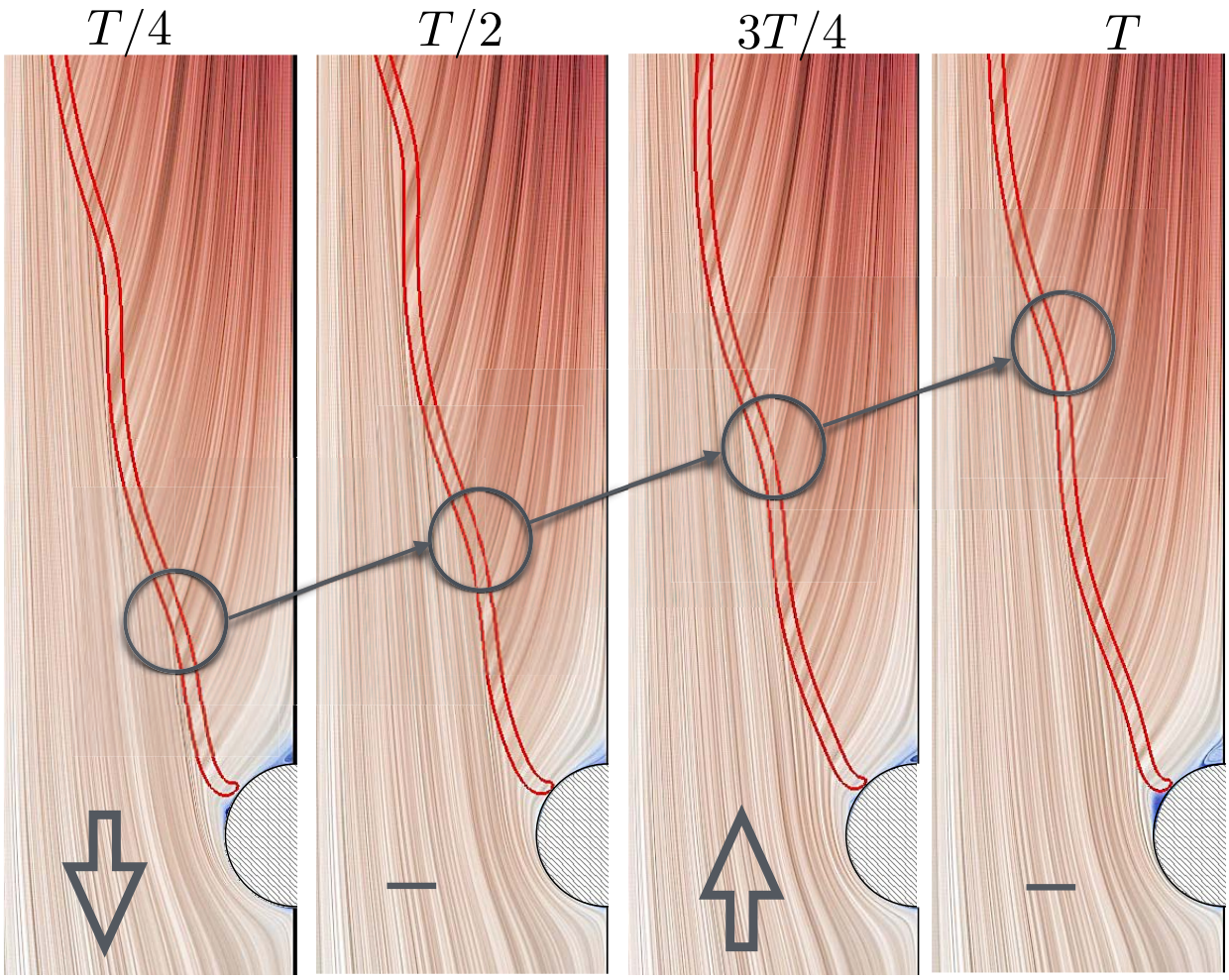

Figure 8.11: Instantaneous solutions during one acoustic period of excitation at 100 Hz for the UBB case

during forcing: acoustic waves at 100 Hz cannot alter the mean temperature of the bluff-body, which remains steady. Indeed, one can consider a thermal skin effect where external harmonic fluctuations of temperature cannot propagate into the flame holder deeper than $\delta_{\text{th}} = \sqrt{2\lambda/(\rho c_p \omega)} \approx 0.2\ mm$ at $f = 100$ Hz, which is negligible when compared to the radius $r = 4\ mm$ of the cylinder.

The two small recirculation zones RZ1 and RZ2 described in chapter 7 are still observed but their respective sizes vary during one acoustic period. Indeed, RZ1 almost disappears at $t = T/2$: the flame root motion is affected by the change in flow topology.

8.2.1.3 Transparent case TBB: $T_{\text{cyl}} \approx 1700\ K$

In the last case, where the flame holder is transparent and cannot be cooled by radiation, it becomes hot enough so that the flame stabilizes upstream. When it is forced acoustically, very small wrinkles are observed (Fig. 8.12, grey circles). Contrary to the two previous cases, the recirculation zone, which is present in the wake of the transparent flame-holder, is not really affected by the acoustic waves. Moreover, as the flame is stabilized upstream of the cylinder, it experiences no influence of the RZ displacement. As a result, the TBB flame is very weakly sensitive to acoustic forcing.

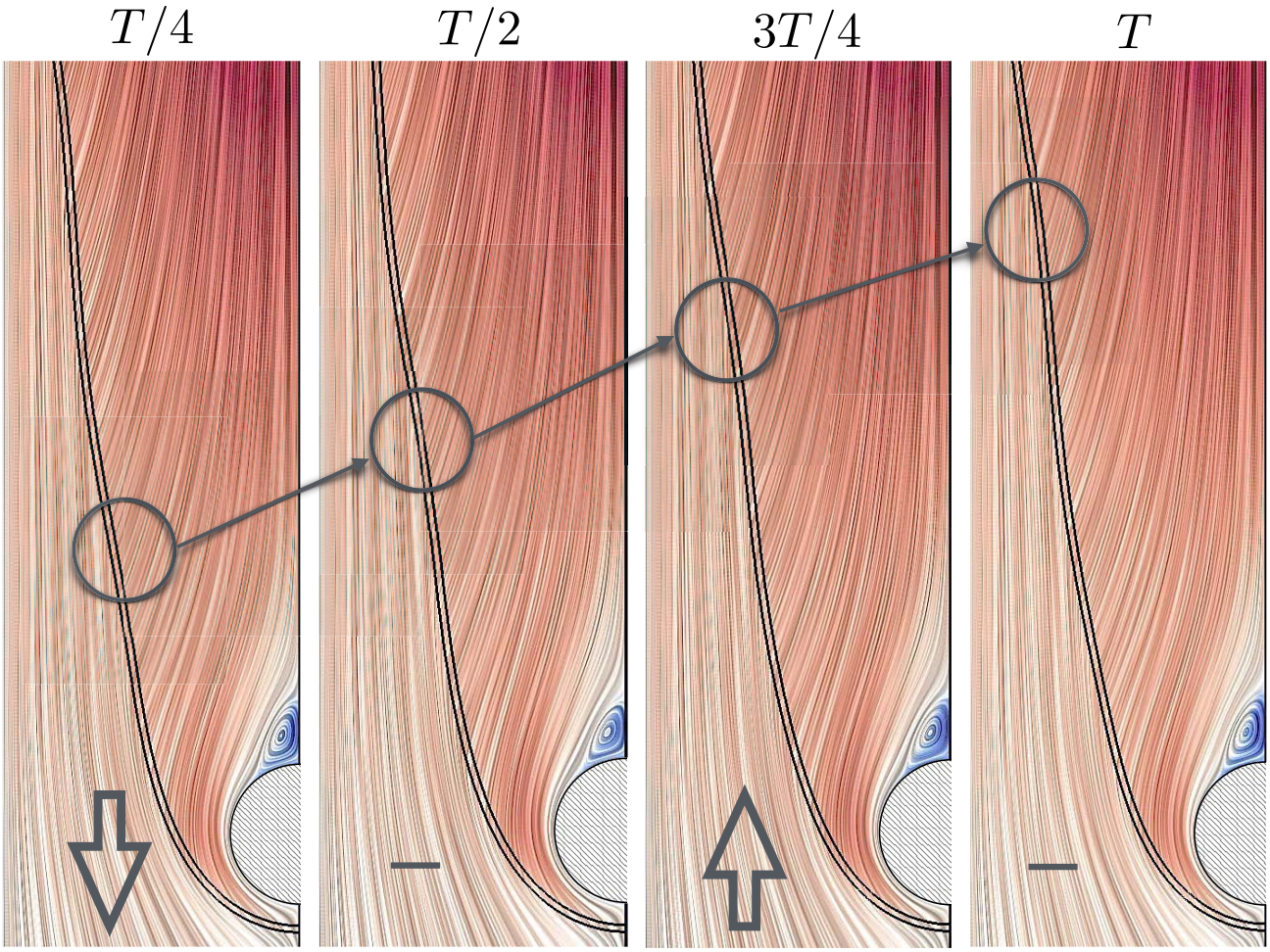

Figure 8.12: Instantaneous solutions during one acoustic period of excitation at 100 Hz for the TBB case

8.2.2 Detailed analysis of the flame roots motion

The previous section has shown the important role of the flame root dynamic in the overall flame response as already assumed by Mejia et al [52] or Kedia et al [185]. DNS allows to analyse this phenomenon in details. First, the temporal variation of the flame roots location can be extracted from DNS data. The flame root is defined as the most upstream location of the 10% iso-line of heat release rate fields displayed in Figs. 8.10, 8.11 and 8.12. Flame roots displacement for the three cases over one period of acoustic pulsation are displayed in Fig. 8.13, left. The flame roots trajectories are ellipsoidal. As for the FTFs, the colder is the bluff-body, the higher is the amplitude of displacement. For instance, the amplitude of flame root displacement is about 4 mm in the CBB case whereas it reduces down to 0.04 mm in the TBB case.

A model for the FTF taking into account the flame root displacement is provided in section 8.2.3. In this model, the quantity which controls the flame dynamics is the flame root displacement normal to the steady flame front. This quantity is called $\xi(0)$ and is displayed in Fig. 8.13, right, as a function of time. The quantity $h = 13\ mm$ is the free space between the cylinder and the flame holder as defined in Fig. 8.14. All roots motions are sinusoidal which proves that the flame roots respond linearly to the acoustic velocity forcing, even for a high amplitude of excitation (5%). Both gains and phases change from one case to another. Concerning the phase, differences of the order of $T/2 = 5\ ms$ are observed between the peaks (Fig. 8.13, right) and cannot be explained by the acoustic propagation time between

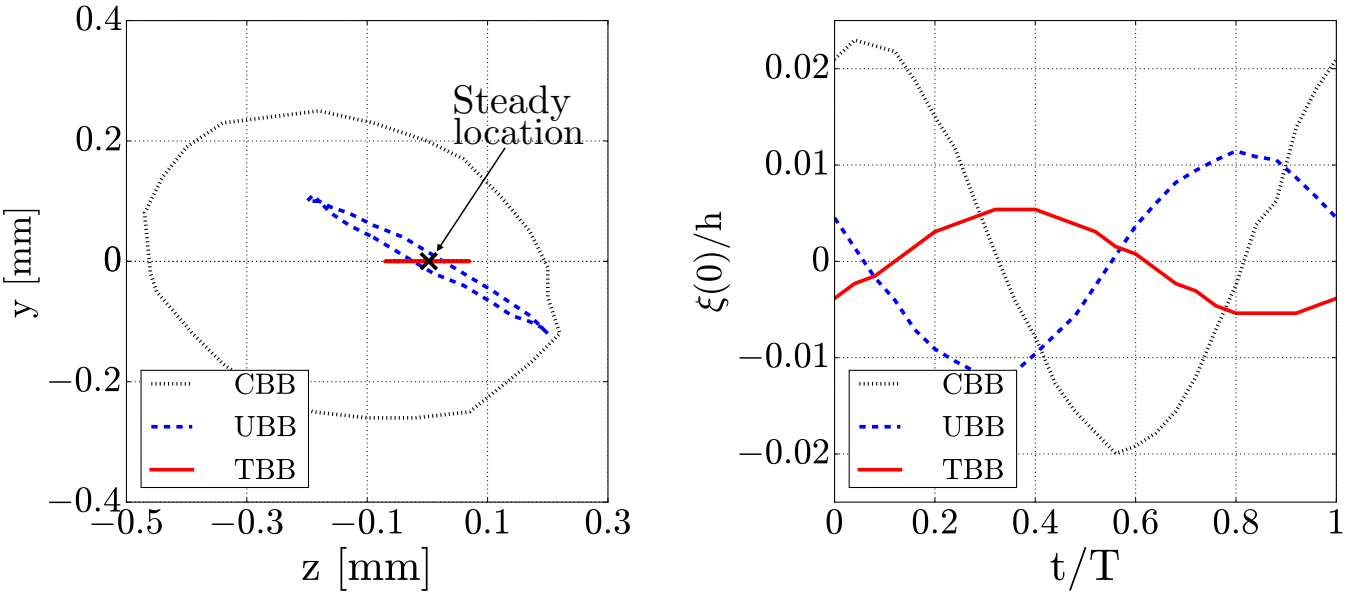

Figure 8.13: Left: relative location of the flame roots in the z,y plane. Right: temporal variation of flame displacement normal to the flame front.

the anchoring points of the three flames: $L/c \approx 0.03\ ms$ where $L \approx 10\ mm$ is the distance between the TBB and the CBB anchoring locations.

All the observations presented in this section are in agreement with the FTF measurements presented in section 8.1.2. Indeed, the flame front is more perturbed in the CBB case, where the FTF gain is higher. The next section tries to quantify the effect of the flame root motion on FTF(ω) using the G-equation framework.

8.2.3 From flame roots dynamics to FTF models

The G-equation framework [242, 81], which models the flame front as a scalar field convected by the mean flow and propagating on it at the displacement velocity can provide physical insight into the FTFs of INTRIG flames. In a recent study from Cuquel et al [51], the particular importance of flame roots motion has been succefully taken into acount in the case of a conical flame. These results have been adapted more recently to the IMFT slot flame by Mejia et al [52] to take into account the influence of the burner rim temperature. The objective of this section is to provide a basic model for the FTFs of the cylinder stabilized flame, measured in the DNS according to the flame representation of Fig. 8.14.

We start from the general G-equation adapted to the INTRIG cases UBB, CBB and TBB defined in equation 8.2.1. The interface between burnt and unburnt gases is represented by the iso-level $G = 0$ of the scalar G field. This field is solution of a convective equation which takes into account both flame displacement speed s_l and velocity field $\vec{U}$:

$$\frac{\partial G}{\partial t} + \vec{U}.\vec{\nabla}G = s_l|\vec{\nabla}G| \tag{8.2.1}$$

Equation 8.2.1 can be solved by assuming a simplified velocity field $\vec{v}$ and a constant flame displacement speed which is taken equal to the laminar flame velocity $s_d = s_l$:

$$\vec{U} = (u_0 + u_1(t))\vec{e_z} \tag{8.2.2}$$

Both mean and acoustic velocity profiles are assumed to be uniform in the $\vec{e_z}$ direction. Equation 8.2.1 can be rewritten in the frame of the flame (Y, Z as defined in Fig. 8.14) for harmonic perturbations [81].

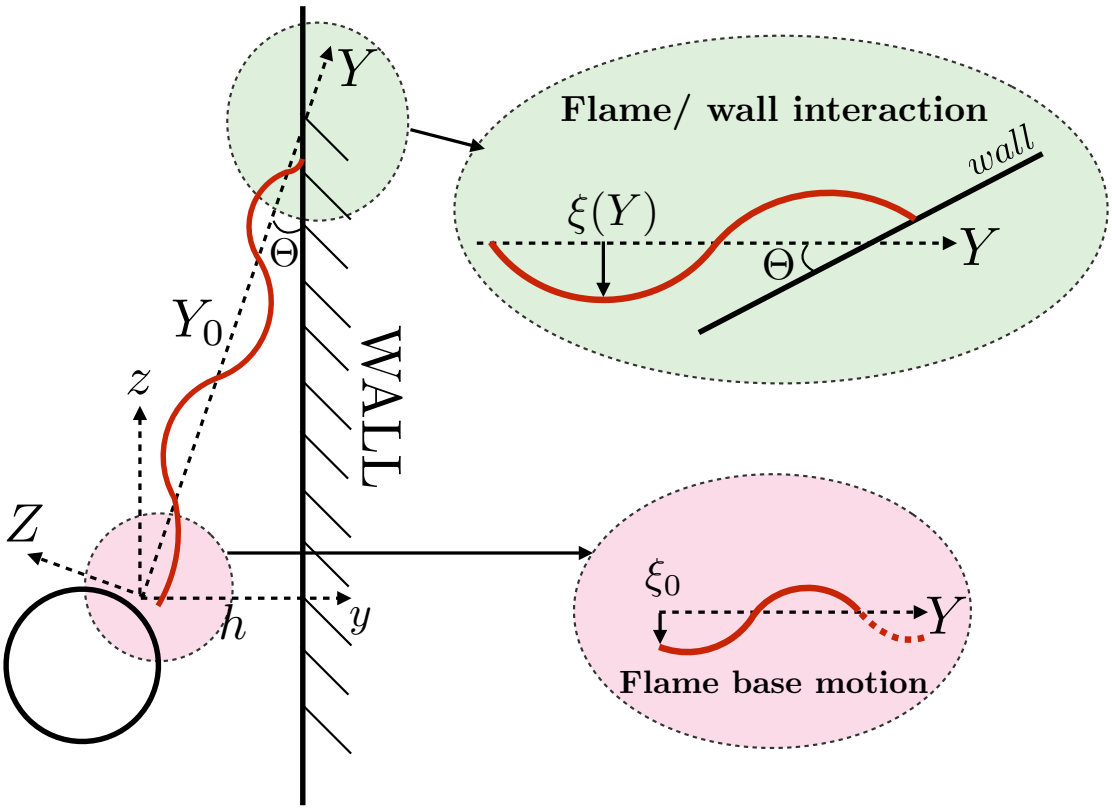

Figure 8.14: Sketch of the perturbed flame represented in the G-equation framework

The location of the flame front is evidenced by applying the change of variable $G = Z - \xi(Y,t)$:

$$\frac{\partial \xi}{\partial t} - (U_0 + U_1) + V\frac{\partial \xi}{\partial Y} = -s_l\left[1 + \left(\frac{\partial \xi}{\partial Y}\right)^2\right]^{1/2} \tag{8.2.3}$$

where $U = U_0 + U_1$ is the velocity normal to the flame front and $V = V_o + V_1$ is the velocity tangential to it: $V_0 = u_0\cos(\Theta)$. This equation can be simplified by keeping terms at first order and noticing that $U_0 = S_l$ (steady state equation):

$$\frac{\partial \xi}{\partial Y} = iK\xi + \frac{U_1(Y)}{V_0} \tag{8.2.4}$$

where ξ is the harmonic perturbation of the flame front normal to its steady shape, Finally, $K = \omega/V_0$ is the wave number associated with the convection of perturbations along the flame front. The solution of Equation 8.2.4 is provided by the Telegraph integral[5] [243]:

$$\xi(Y) = e^{iKY}\left(\xi_0 + \frac{1}{V_0}\int_0^Y U_1(Y)e^{-iKY'}dY'\right) \tag{8.2.5}$$

The first term of the RHS in equation 8.2.5 concerns the flame root motion ($Y = 0$) while the second term measures how the external velocity excitation affects the convection of the wrinkles along the flame front. In all three cases, the flame angle Θ is imposed by the ratio between flow and flame speed and is close to 0.07π. As the lateral distance $h \approx 13\ mm$ is common for all cases, one retrieves the steady length of the flames: $Y_0 \approx h/\sin(\Theta) \approx 60\ mm$. Some variations around this value are observed for the

[5]The resolution is eased by applying the following change of variable: $\xi(Y) = f(Y)\exp(iKY)$.

three cases but this estimation is valid at first order. In the frequency range of interest $f \in [10, 500]$ Hz, acoustic wavelengths remain longer than $\lambda_{\min} = c/f_{\max} \approx 0.7\ m$ so that $Y_0 \quad \lambda_{\min}$ for all frequencies considered here. As a consequence, the velocity perturbation U_1 is supposed uniform: $U_1(Y) = U_1$. It is thus possible to integrate the second term in the RHS of equation 8.2.4:

$$\frac{1}{V_0}\int_0^Y U_1 e^{-iKY'} dY' = i\frac{U_1}{V_0}\frac{e^{-iKY} - 1}{K} \tag{8.2.6}$$

This term is equivalent for all three cases and is thus not responsible for the differences observed in the FTFs. However, as shown in Fig. 8.13, the flame root motion is deeply impacted by the temperature of the bluff-body which affects the motion of the flame base ξ_0. This behavior has also been mentioned for flames stabilized on rectangular slot burners [52] or conical flames [51]. The coupling between flame root motion and acoustic velocity perturbation can be described by the Flame Base Motion Transfer Function (FBMTF):

$$\Xi(\omega) = (\xi_0/h)/(u/u_0) \tag{8.2.7}$$

which relates the flame root motion amplitude to the upstream acoustic velocity amplitude.

The global FTF is obtained by dividing the flame surface fluctuation by the velocity perturbation. The surface of the perturbed flame writes:

$$A(Y) = \int_0^Y \quad \overline{1 + \left(\frac{\partial \xi}{\partial Y'}\right)^2} dY' \approx \int_0^Y dY' = Y \tag{8.2.8}$$

To first order, flame front displacements play no role in the surface fluctuation. However, the length of the flame varies when wrinkles reach the wall as shown in Fig. 8.14. The fluctuating flame length is solution of the following equation:

$$Y_f = Y \mid \xi(Y_0 + \delta) = \delta \sin(\Theta) \tag{8.2.9}$$

where $\delta = Y - Y_0$ is the additional length of the flame caused by the wrinkles convection and $\xi(Y)$ is provided by equation 8.2.5. In the limit of small perturbations, $\delta \to 0$ so that:

$$\delta = \frac{h}{\sin(\Theta)}\left(\Xi(\omega)\frac{u}{u_0}e^{iKY_0} + i\frac{U_1}{V_0}\frac{1 - e^{iKY_0}}{Kh}\right) \tag{8.2.10}$$

It is then possible to combine equations 8.2.10 and 8.2.8 to retrieve the FTF:

$$\mathrm{FTF}(\omega) = \frac{A(Y_f)/A_0}{u/u_0} = \underbrace{\Xi e^{iKY_0}}_{\text{Flame root}} + \underbrace{\frac{e^{iKY_0} - 1}{iKY_0}}_{\text{Surface perturbation}} \tag{8.2.11}$$

Equation 8.2.11 exhibits two terms which contribute to the FTF. The first term is linked with flame root motion and is controlled by the FBMTF (Ξ) while the second is linked to the perturbation of the flame front away of the bluff-body by the acoustic wave. As shown in Fig. 8.6, peaks are present in the FTF for both UBB and CBB cases in the frequency range $f \in [80, 150]$ Hz so that $KY_0 = \omega Y_0/V_0 > 25$.

A model also exists for the FBMTF of a conical flame [51]. In this model, the FBMTF has a band-pass behavior and peaks at values close to unity. However, in the INTRIG configuration, the flame is attached on a cylinder and no models are available. The study of flame roots motion presented in Fig. 8.13 provides values for the FBMTF at 100 Hz which are summarized in table 8.3. These values are close to unity, especially for the CBB case. As a consequence equation 8.2.11 is dominated by the flame base motion term.

Two simple models (one for low frequencies and the other for large ones) can be established to predict the FBMTF in the TBB case (where the flame is upstream stabilized). At low frequency, the

	CBB	UBB	TBB
Ξ	0.6	0.3	0.14

Table 8.3: Flame Base Motion Transfer Function (FBMTF) measured in the DNS at 100 Hz for the three cases.

velocity field varies slowly and the flame can adapt quasi-steadily. The dynamic equilibrium equation of the flame front expresses that the flame stabilizes where the flow velocity $u(z')$ is equal to the laminar flame velocity s_l:

$$s_l = u(z') = -\frac{u_0}{r}(z_0 + \xi(0)) + u \tag{8.2.12}$$

where z_0 is the steady location of the flame root ($z' = 0$ at the cylinder center as defined in Fig. 7.12). After subtracting the steady state equation ($s_l = u_0 z_0/r$), one obtains the FBMTF of the TBB flame in the low frequency regime:

$$\Xi^1_{\mathrm{TBB}}(\omega) = r/h \tag{8.2.13}$$

In the INTRIG burner, the ratio between the flame holder radius r and the free lateral space h is equal to $r/h = 0.31$. As frequency is increasing, the acoustic velocity reverts before the flame reaches its steady state equilibrium: the characteristic time needed by the flame to return to equilibrium becomes higher than the temporal period of the signal. At high frequencies, the flame never reaches equilibrium and its location is predicted by the convection equation $\partial\xi/\partial t = u_0 + u_1(t) - s_l$ or equivalently in the frequency domain $i\omega\xi(0) = u$ as $u_0 = s_l$. This condition leads to the high frequency limit of the FBMTF:

$$\Xi^2_{\mathrm{TBB}}(\omega) = \frac{u_0}{i\omega h} \tag{8.2.14}$$

At high frequencies, the FBMTF decreases to zero. The flame switches from a quasi-steady to a dynamic behavior for $f_s = v_0/(2\pi r) \approx 50Hz$. This frequency is in agreement with the FTF obtained in the TBB case (see Fig. 8.6) where the gain starts decreasing close to f_s. As a consequence, the second model is valid at $f = 100\ Hz$: the FBMTF value predicted ($|\Xi^2_{\mathrm{TBB}}| = 0.13$) is in good agreement with the measured value: 0.14 (see table 8.3).

As shown in equation 8.2.11, the gain of the FTFs should be close to the gain of the FBMTF. Here, the gains of FBMTFs at 100 Hz are lower than the corresponding gains of the FTFs: for instance, in the CBB case, the FTF gain is equal to 5.5 while the FBMTF gain is equal to 0.6. However, the ratio between the FTF and FBMTF gains is roughly constant: $|\mathrm{FTF/FBMTF}| \in [6, 9]$. The assumption that the flame base motion controls the overall FTF of the flames is thus validated and that this zone must be modelled precisely, taking into account heat transfer to the flame holder.

A better modeling of the flames, especially close to the cooled external walls, would probably help to retrieve the gains of the measured FTFs in the G-equation framework. Indeed, the model presented here is valid for adiabatic external boundaries. For instance, when the walls are cold, the flames angle decreases so that FTF gains increase.

A general scenario for the flame dynamics can be established after considering the observations of Figs. 8.10,8.11 and 8.12 but also the FTF derived theoretically in section 8.2.3:

Flame dynamics

- The flame roots oscillate when the flow is acoustically forced. As the temperature of the flame holder decreases, the amplitude of the flame base motion increases. This motion is due to the coupling between the flame root and the recirculation zones and can be measured by the mean of the Flame Base Motion Transfer Function (FBMTF) which changes drastically with the flame holder temperature.
- Perturbations issued from the roots are convected down to the end of the flames. No heat release rate fluctuations are associated with the convection of these perturbations at first order.
- As these perturbations reach the external walls, the flame length varies when quenching takes place, which leads to unsteady heat release rate.

8.3 Comparison with experimental measurements

In this section, a comparison is performed between the FTF obtained in DNS and in the experiment. The influence of the bluff-body temperature is globally retrieved. Higher gains are obtained when the flame-holder is cooled while DNS and experimental phases are in very good agreement for both cooled and uncooled cases. However, the FTFs measured in the experiments goes to zero at lower frequencies than the ones obtained in DNS. The detailed comparison is provided in section 8.3.1 while some possible reasons explaining these discrepancies are introduced in sections 8.3.2 and 8.3.3.

8.3.1 Cooled and uncooled cases

The experimental method employed to measure the flame response to acoustic perturbations have already been described by Mejia et al [52, 181]. Acoustic waves are generated by a 160 mm loudspeaker located outside of the combustion chamber while acoustic velocity perturbation and heat release rate are recorded simultaneously by a hot wire probe and a photomultiplier equipped with CH filter. The hot wire probe is located 8 mm upstream of the bluff-body in order not to alter the flow. Temporal signals are then processed as described in section 8.1.3 to provide the FTF for frequencies above 100 Hz.

The corresponding FTFs are displayed in Fig. 8.15 and compared to DNS results. First, FTF obtained experimentally as well as numerically show a remarkable result: they change drastically when the temperature of the flame holder changes. The cooled case (CBB) leads to a flame which responds much more than the uncooled case (UBB). The maximum gain of the CBB case can be 2 to 3 times larger than the UBB case. This maximum gain is also obtained at a different frequency. This shows that the bluff-body temperature controls the flame response. The second issue is to compare DNS and experiments. Here, the phases are in very good agreement: the phase shift between UBB and CBB cases is well reproduced up to 200 Hz and slight discrepancies are observed at higher frequencies. Second, gain differences are observed in the experiments between the CBB and the UBB cases. However, these gains are lower than the corresponding gains in the DNS and the difference increases with the frequency.

Two effects may explain the discrepancies observed between the FTFs measured in the experiments and the DNS:

- Three dimensional effects influence the FTF in the three cases of interest. Because of thermo-diffusive instabilities [220], the flame height is not uniform and phase averaging of the FTF is produced.

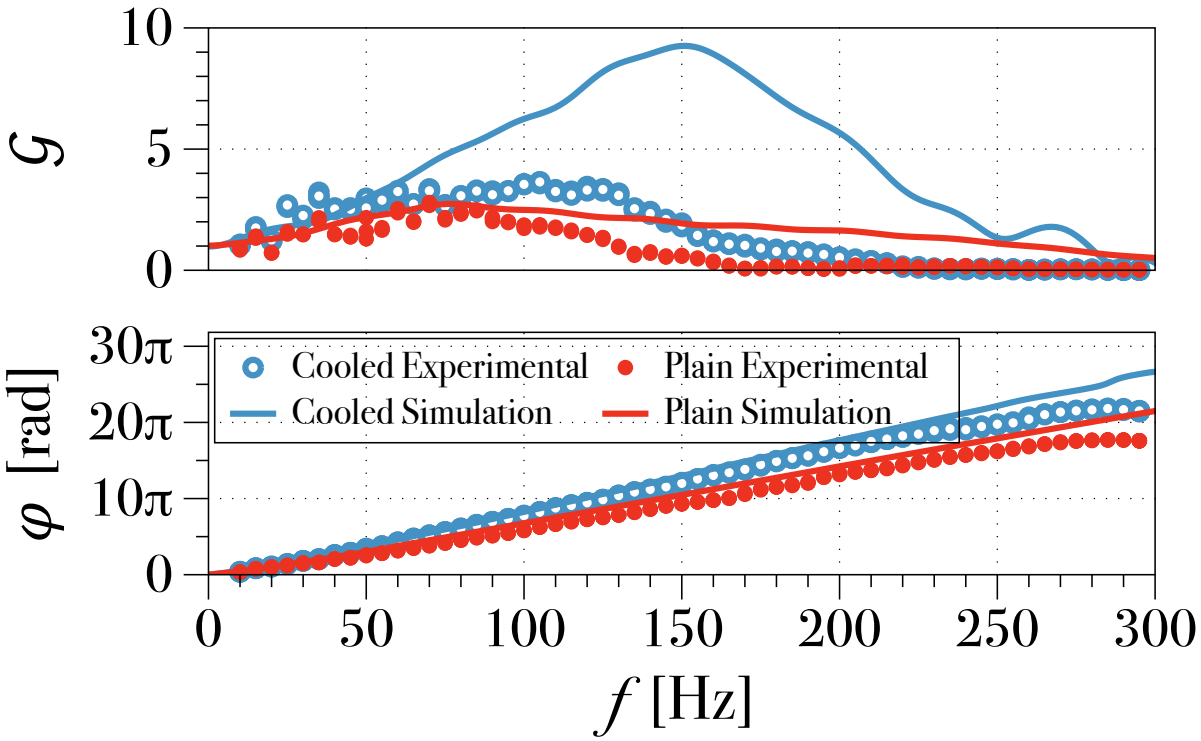

Figure 8.15: Experimental measurements of the FTF.

- Non linear perturbations of the flame front are observed, even at low excitation amplitude. In the DNS, the ratio between acoustic and bulk velocities was about 1 percent while it was about 5 percent in the experiments. These effect can be synthetized in the framework of Flame Describing Functions (FDF)[244].

8.3.2 Three dimensional effects

As observed in Fig. 8.16, left, the flame height is not uniform in the x direction. One possible reason for this is the occurence of instabilities [220], which lead to a flame surface which is not perfectly flat (see Fig. 8.16, left). These instabilities may be hydrodynamic, thermodiffusive (this is unlikely here because $Le \approx 0.95$) or due to the geometrical imperfections or 3D end effects. The objective of this section is not to focus on the physical mechanisms leading to flame front perturbations in the transverse direction but to investigate their impact on FTFs.

A sketch of the flame front in the transverse direction is provided in Fig. 8.16, right. The steady height of the flame in the frame Y, Z is represented by the variable $Y_0(X)$. In order to account for three-dimensional effects in UBB, CBB and also TBB cases, one may decompose the flame sheet into infinitesimal 2D flames. Their respective contributions can be integrated to retrieve the global FTF:

$$\mathrm{FTF}_{3D} = \frac{1}{|x_{\max} - x_{\min}|} \int_{x_{\min}}^{x_{\max}} \mathrm{FTF}_{2D}(Y_0(X))dX \tag{8.3.1}$$

Equation 8.3.1 can be closed by providing a model for the two-dimensional local flame transfer function $\mathrm{FTF}_{2D}(Y_0)$. This can be achieved by keeping the root motion term in the FTF model provided in section 8.2.3:

$$\mathrm{FTF}_{2D}(\omega) = \Xi(\omega)e^{i\omega Y_0/V_0} \tag{8.3.2}$$

The two-dimensional FTF provided in equation 8.3.2 is convenient because it first exhibits a linear behavior for the phase which is in good agreement with both experimental and numerical measurements.

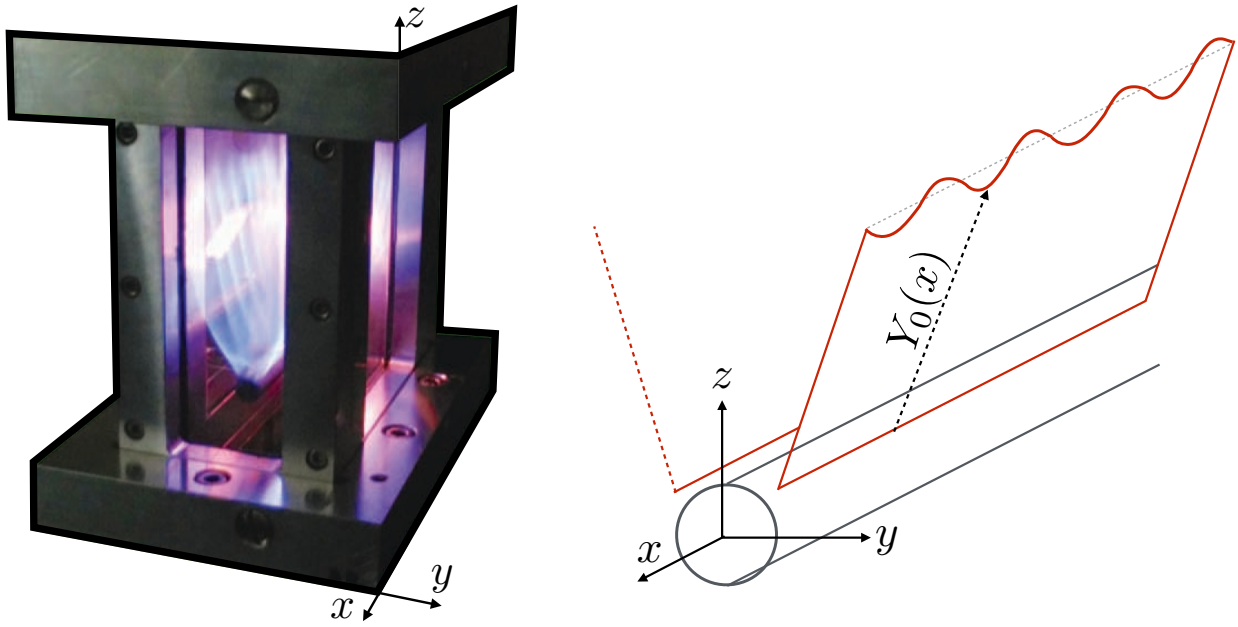

Figure 8.16: Right: Three dimensional sketch of the INTRIG flame. Left: picture of the INTRIG burner showing the transverse perturbation.

Moreover, it is clear the FMBTF does not depend on the flame length so that only the phase of the FTF varies with this quantity. The following calculations are further simplified by assuming a Gaussian distribution for the flame height in the transverse direction:

$$P(Y_0) = \frac{1}{\sigma\sqrt{2\pi}} \exp\left(-\frac{1}{2}\left(\frac{Y_0 - Y_m}{\sigma}\right)^2\right) \tag{8.3.3}$$

where Y_m is the mean value of the flame height and σ its standard deviation. The ratio σ/Y_m has been approximately measured to 0.04 ± 0.015 (see Fig. 8.16, left). It is now possible to rewrite equation 8.3.1:

$$\mathrm{FTF_{3D}} = \frac{1}{|x_{\max} - x_{\min}|} \int_{x_{\min}}^{x_{\max}} \Xi e^{iKY_0(X)} dX = \Xi(\omega) \int_{\mathcal{R}} e^{iKY} P(Y) dY \tag{8.3.4}$$

where one recognizes the Fourier transform of the Gaussian distribution:

$$\mathrm{FTF_{3D}} = \Xi(\omega) e^{iKY_m} e^{-\frac{1}{2}(K\sigma)^2} =< \mathrm{FTF_{2D}} > e^{-\frac{1}{2}(K\sigma)^2} \tag{8.3.5}$$

Finally, taking into account the steady flame height variation alters the global FTF by multiplying it by a low-pass filter of cut-off frequency $f_c = V_0/(2\pi\sigma) \approx 65\ Hz$. The more important are the flame height variations, the lower is the cut-off frequency. In order to simplify the calculations, the choice of a Gaussian function for the flame height density function has been retained. However, similar results in term of cut-off frequency would have been obtained with other distributions.

This effect helps to understand the differences between FTFs measured in the DNS and in the experiments. For frequencies lower than f_c, experimental and numerical data are in excellent agreement (in gain and phase). However, for frequencies higher than f_c, the gains measured in the experiments start decreasing faster than the ones in the DNS. This is because phase averaging only operates for the experimental flame.

8.3.3 Non linear forcing: Flame Describing Function

As shown in the previous section, three dimensional effects may damp the gain of the FTF obtained by a 2D approximation. Here, an other source of FTF gain attenuation is considered. As the excitation

Amplitude	TBB	UBB	CBB
≤ 1 %	0.8	2.38	5.5
5 %	0.76	1.63	2.35

Amplitude	TBB	UBB	CBB
≤ 1%	-2.06	2.36	0.75
5 %	-2.11	1.86	-1.16

Table 8.4: Left: Gain, Right: phases of FTF for the three cases at two forcing amplitudes for $f = 100$ Hz

amplitude increases, the gain of the FTF decreases, this non-linear effect leads to the concept of Flame Describing Functions (FDF). The latter have been first described by Dowling [244] and EM2C [233, 231, 234, 235]. It states that the heat release response to an acoustic perturbation is also a function of the amplitude of excitation:

$$\mathrm{FDF}(\omega, |u|) = \frac{\Omega_T(\omega, |u|)/\bar{\Omega}_T}{u/\bar{u}} \tag{8.3.6}$$

where $|u|$ refers to the amplitude of the acoustic forcing velocity. Examples of time-traces of velocity and heat release rate monitored in the UBB case are displayed in Fig. 8.17. First, a small forcing (below 1% of bulk velocity) is applied and one observes an harmonic response of the heat release rate. Second, a stronger forcing is applied (5%) and the heat release response ceased to be harmonic. Consequently, high frequency oscillations are also observed in the velocity signal as soon as the heat release rate reaches its limit cycle. The heat release rate response to the sinusoidal forcing exhibits higher frequencies harmonics which in turn generate acoustic waves.

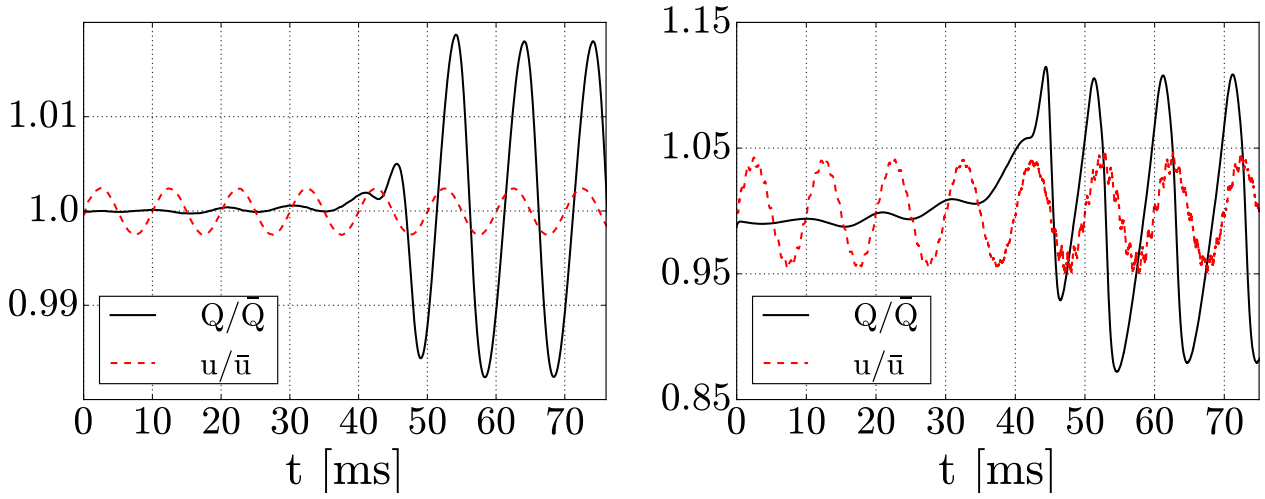

Figure 8.17: Left: time traces of reference velocity and heat release in a linear case (the heat release is still harmonic). Right: same but with a higher forcing amplitude.

The influence of the forcing amplitude is scrutinized for the three cases CBB, UBB and TBB and results are shown in table 8.4. One can observe that the damping effects are more important in the CBB case, where the heat release fluctuations are higher. This suggests that non-linear responses are obtained when the heat release rate fluctuations are important. Such a result is coherent with the FTF model proposed in section 8.2.3: when important flame displacements $\xi(Y)$ are observed, the assumption used to linearize equations 8.2.9 and 8.2.8 does not hold anymore. One may also notice that the FBMTF may also exhibit non-linear behavior when the forcing amplitude increases.

After combining both three dimensional and non-linear effects, it is possible to understand why the FTFs obtained in the DNS exhibit higher gains than those measured experimentally. However, all the

mechanisms presented in this section are independent of the flame base motion transfer function, which controls flame dynamics in the frequency range of interest. As a consequence, both experiments and DNS provide higher gains for the cooled case when compared to the un-cooled one.

Conclusion

Results concerning flame transfer functions for three different topologies of flames stabilized on a cylindrical bluff-body have been reported. In the first case (CBB), the flame is attached in the wake of a cooled flame holder and its FTF experiences a high gain (close to 9) around to 100 Hz. In the second case (UBB), the cylindrical bluff-body is not cooled and the flame is attached closer to it: the FTF peaks at a lower amplitude (about 2.5). In the last case (TBB), the flame is attached upstream of a quasi-transparent bluff-body of same dimensions. No peaks are observed in the FTF: it starts from one and gently decreases to zero. Obviously the flame roots play a major role in the FTF, For the TBB flame, there is no flame root and the flame is stabilized upstream of the flame holder so that is is much less sensitive to forcing. As the roots appear and are convected downstream close to the cylinder (UBB) or far away (CBB), the flame response increases. The differences between these FTFs have been explained within the G-equation framework: it has been shown that the flame base motion plays an important role in all cases and is responsible for the changes in flame dynamics between the different cases. Finally, comparisons between experimental and numerical FTFs show that the cooled cylinder has a more intense response than the un-cooled one but discrepancies for the gain values have been reported and justified by both non-linear (FDF) and three-dimensional effects (phase averaging).

Chapter 9

Reduced Order Model of the INTRIG burner

This chapter is dedicated to thermo-acoustic modeling of the INTRIG burner. As its geometry is simple (quasi one dimensional), the ROM approach has been retained. The latter is built on top of FTF measured in the DNS (see chapter 8) and takes into account the non compactness of the flame. The solutions of the ROM (obtained with the A_{RL} algorithm) are compared to experimental measurements for the three flames CBB, UBB and TBB, and a good agreement is observed for three different geometries: the combustion chamber length is varied from 0.1 (stable configuration) up to 0.35 m (unstable configuration). Finally, the modal structure observed in both ROM and experimental results is explained by introducing a new family of acoustic modes: the Quasi Intrinsic Thermo-Acoustic (QITA) family. This family originates from the coupling between the Intrinsic Thermo-Acoustic (ITA) family, which play an important role in anechoic burners, and the chamber family, which concerns all the modes that exist without flame/acoustic interaction.

Introduction

As stated in the introduction, one of the main objectives of thermo-acoustic studies is to predict the stability of a given system prior to building it. To do this, several approaches exist including CFD [108] or Helmholtz solvers [70, 92] and ROMs [57]. The two latter approaches need additional information about acoustic losses and flame/acoustic interaction to provide predictive results.

The INTRIG geometry is simple: Sudden change of section and swirl injectors have been avoided to limit the impact of acoustic dissipation. Moreover, the burner is one dimensional (excepted around the small cylindrical bluff-body), which simplifies the design of an accurate ROM.

This chapter is decomposed into four parts. Section 9.1 describes the post-processing of experimental and DNS data to provide the information required to the ROM. FTFs are converted into analytical functions which contain no poles in order to comply with RootLocker requirements. Once they are fittd using analytical functions, the three FTFs are introduced into a non compact acoustic transfer matrix. Indeed, the temperature linearly increases from the root to the end of the flame over a length z_{f} = 0.07 m which is non negligible when compared to the burner length ($\approx$ 0.5 m). In addition, the unsteady heat release rate is only located at the end of the flame whereas the velocity reference location is taken upstream of the bluff-body.

In the second section (9.2), the acoustic boundary conditions required in the ROM are inferred from experimental measurements in the INTRIG burner. It is shown that acoustic waves are partially reflected by the small glass balls used to laminarize the flow (R = 0.7). Concerning the outlet, three configurations are introduced where the length of the combustion chamber is varied: short (z_{end} = 0.1

m), medium ($z_{\text{end}} = 0.2\ m$) and long ($z_{\text{end}} = 0.35\ m$).

A comparison between ROM predictions and experimental measurements is provided in section 9.3: the short configuration, where no acoustic activity is observed in the experiment is predicted stable by the ROM while the other configurations exhibit acoustic instabilities. Experimental measurements and ROM solutions are in good agreement. In addition, more than ten modes are observed before the first cavity mode for each configuration.

This intriguing result is explained in section 9.4, where the concept of mode family is introduced. The modes observed in the INTRIG burner can be separated into three families:

- The classical chamber modes [11], which exist for non reacting flows and are sightly affected by the flame/acoustic interaction.
- The Intrinsic Thermo-Acoustic (ITA) modes [245, 240, 246], which have been first observed in anechoic chambers and result from an internal feedback mechanism of the {bluff-body + flame} system. More generally, these modes can still exist in non anechoic chambers but are less affected by the BCs than the chamber modes.
- The Quasi Intrinsic Thermo-Acoustic (QITA) modes, which are introduced in this PhD work, and result from the coupling between the two previous families.

These results are similar to the recent analysis performed by Emmert et al [247] at the last symposium (not published yet).

9.1 Flame/Acoustic coupling

As shown in chapters 1 and 2, FTF is the key ingredient needed to predict thermo-acoustic instabilities. Most of the time, FTFs are only known for a discrete set of real valued frequencies. However, ROM (and even Helmholtz solvers) need an analytical representation, which must be valid not only for all values of real frequencies but also for complex frequencies (i.e. for signals growing or decaying in time) [248]. An automated procedure which answers to this question is presented in 9.1.1.

After that, the FTF is introduced in a two-port representation, which links acoustic variables at both sides of the element. In the case of the INTRIG burner, the flames are quite long (from 60 to 70 mm) so that the compact approximation developed in chapter 1 does not apply perfectly. As a consequence, a more accurate description of the two-port, which differentiates the location of the velocity reference (upstream of the cylinder) to that of the unsteady heat release production (end of the flames, as shown in chapter 8), is provided in section 9.1.2. This approach also assumes a linear temperature profile from the root to the end of the flame.

9.1.1 Analytical representation of FTFs

Analytical representation $f(\omega)$ of FTFs are needed as inputs of ROMs and this topic has already been addressed in various studies. Empirical models have been used by Kopitz et al [54] and Noiray et al [249]. In these cases, a fractional polynomial multiplied by a delay function was used:

$$f_{\text{fp}}(\omega) = \frac{\sum_{k=0}^{n} a_k \omega^k}{\sum_{k=0}^{p} b_k \omega^k} e^{i\omega\tau} \tag{9.1.1}$$

where $a_k\ k \in [1, n]$, $b_k\ k \in [1, p]$ and τ are the fitting coefficients. As all FTFs decrease to zero at high frequencies, we impose $p > n$. The optimal coefficients are obtained by performing a non linear regression of the discrete FTF. However, using this kind of model for FTFs comes with two major drawbacks:

- This model is not based on physical insights and the correct values for n and p are not easy to guess. Most of the time, a trial and error method is used. Even when these parameters are fixed, it is also complicated to find correct guesses for the $n + p + 3$ fitting coefficients of the model required by minimization algorithms.

- This model introduces poles in the ROM (when $p > 0$). Indeed, a pole present in the analytical representation of the FTF, unless balanced by a root, will induce a pole in the ROM. However, methods based on the argument principle such as the A_{RL} algorithm presented in chapter 2 are not adapted to ROMs with poles.

As a consequence, an other methodology is adapted from [250] and [251] to solve the two aforementioned issues. In this procedure, the fitting is performed in the time domain on the impulse response of the flame as shown in Fig. 9.1. Indeed, it is simpler to fit a real valued function such as the impulse response than the complex FTF.

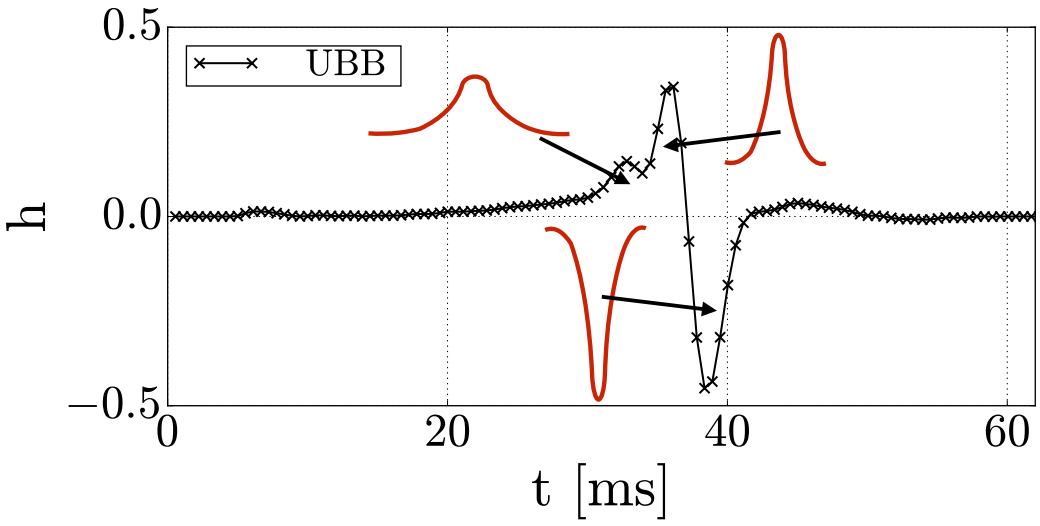

Figure 9.1: Discrete Impulse Response (DIR) in the UBB case: Gaussian peaks can be used to fit the data.

The Discrete Impulse Response (DIR) contains peaks of various amplitudes and widths, which can be easily identified. These peaks can be fitted with multiple Gaussian functions $h_{g,\tau,\sigma}$ which are summed to obtain the complete impulse response[1]:

$$h_{np}(t) = \sum_{k=1,n_p} h_{g,\tau,\sigma}(t) \tag{9.1.2}$$

$$\text{with } h_{g,\tau,\sigma} = g e^{-\frac{(t-\tau)^2}{2\sigma^2}} \tag{9.1.3}$$

where the number of peaks n_p will be determined later. The three parameters g, τ, σ corresponds to the amplitude, the center and the standard deviation of the Gaussians functions respectively. Guesses for these values can be easily obtained:

[1]Contrary to Polifke et al [252], who used a single Gaussian function to describe the DIR.

Peaks detection method

- The local maxima of the absolute DIR τ_k are identified and reordered from larger to lower. Among them, only the first n_p peaks are retained: $\{\tau_1, \tau_2, \dots \tau_{n_p}\}$.
- Starting from the peaks center, the amplitudes $\{g_1, g_2, \dots g_{n_p}\}$ are simply obtained: $g_k = \mathrm{DIR}(\tau_k)$
- Finally, the standard deviation σ_k is obtained for each peak by using the second order discrete derivative of the impulse response $d_2(\mathrm{DIR})(\tau_k)$ which is computed with a fourth order centered stencil[a]:

$$\sigma_k = \sqrt{\frac{-g}{d_2(\mathrm{DIR})(\tau_k)}} \tag{9.1.4}$$

[a] Indeed, $h''(\tau) = -g/\sigma^2$

Finally, the Gaussian based model provided in equation 9.1.2 is fitted on the DIR: examples are provided in Fig. 9.2 with four different number of peaks: $n_p \in [1, 3, 8, 15]$. One observes that with $n_p \geq 8$, the discrete data are well reproduced by the analytical model.
In practice, it is useful to increase n_p until the integral of h_{np} converges to unity[2]:

$$\int_{t=0}^{\infty} h_{np}(t)dt = \sqrt{2\pi} \sum_{k=1}^{n_p} g_k \sigma_k \tag{9.1.5}$$

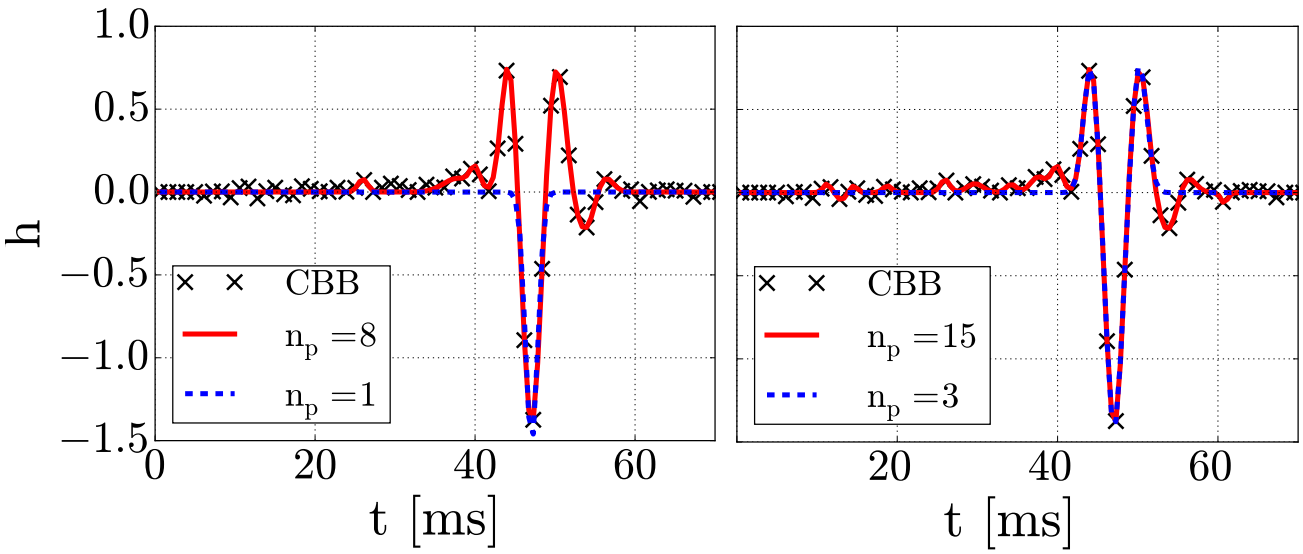

Figure 9.2: Model fitting on discrete impulse response (CBB case). Left: the parameter n_p is set to 1 and 8. Right: the parameter n_p is set to 3 and 15.

When the analytical representation h_{np} of the impulse response is obtained, it is possible to retrieve the corresponding analytical FTF by using Fourier Transform (FT). Each Gaussian $h_{g,\tau,\sigma}$ terms can be easily recast into the frequency domain:

$$FT(\underbrace{g e^{-\frac{(t-\tau)^2}{2\sigma^2}}}_{\mathrm{h}_{g,\tau,\sigma}}) = \underbrace{g\sigma\sqrt{2\pi}}_{\text{gain}} \underbrace{e^{i\omega\tau}}_{\substack{\pm \\ \text{delay}}} \underbrace{e^{-\frac{1}{2}(\omega\sigma)^2}}_{\text{envelope}} \tag{9.1.6}$$

[2] The integral of the impulse response is equal to the low frequency limit of the FTF (see chapter 8) and must be equal to unity [85].

Equation 9.1.6 shows that the Fourier Transform of a Gaussian function is decomposed into a product of three terms. The first one characterizes the gain in the frequency domain. The second one corresponds to a delay while the third one relates to the range of influence of the peak in the frequency domain: for frequencies above $\omega > 1/\sigma$, this term vanishes. As a consequence, a peak with a large width in the impulse response (large σ) only influences the low frequency range of the FTF.

The analytical representations of the FTFs deduced from the h_{np} functions displayed in Fig. 9.2 (n_p =1, 3, 8 and 15) are shown in Fig. 9.3. A good agreement is observed for the fit function as long as n_p 8. Taking into account more than 8 peaks improves the gain accuracy for low frequencies as well as the phase accuracy for high frequencies.

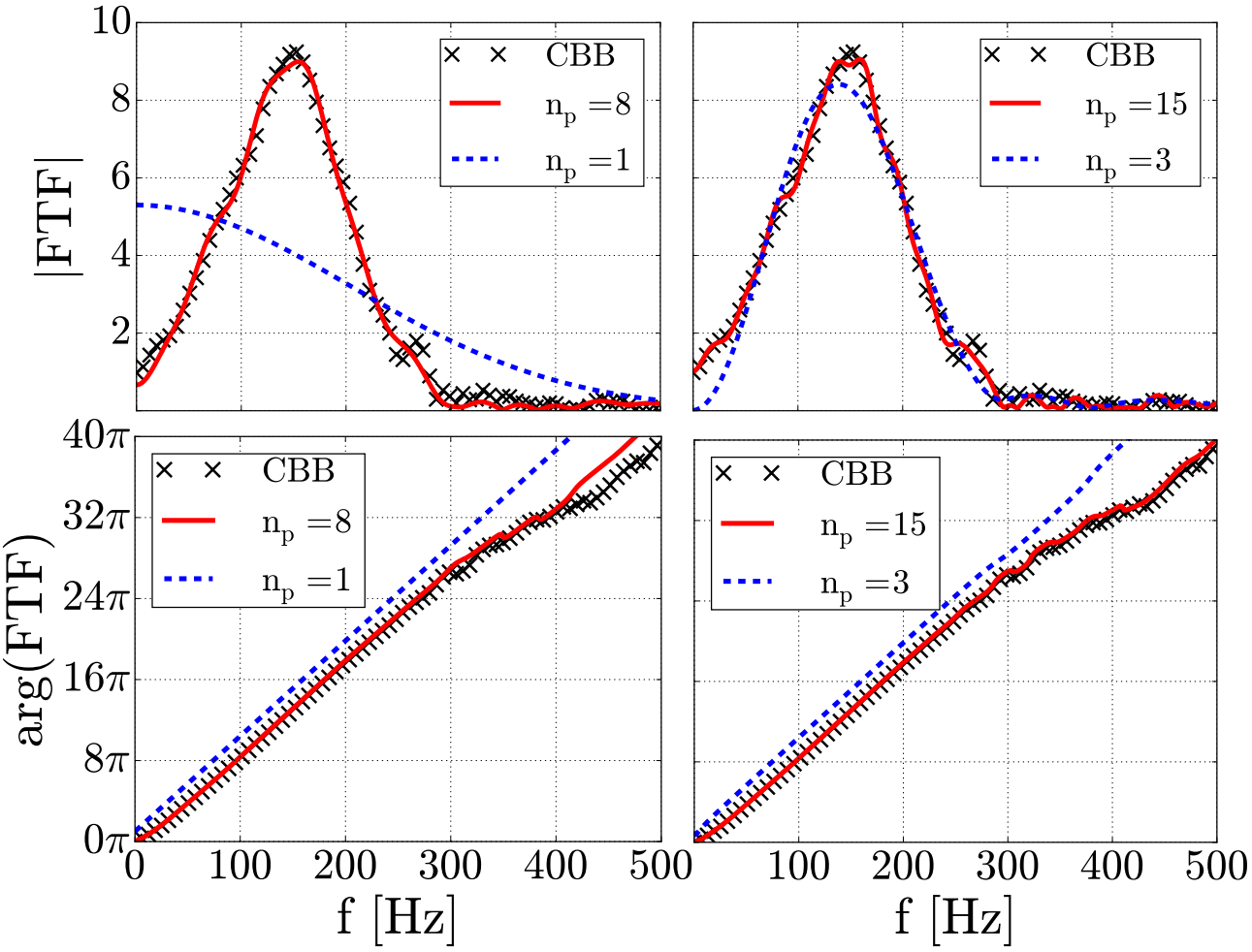

Figure 9.3: Model fitting on FTF (CBB case). Left: the parameter n_p is set to 1 and 8. Right: the parameter n_p is set to 3 and 15.

A value of n_p = 15 will be retained for this case (CBB) but smaller ones are sufficient for the two other cases: n_p = 8 for the UBB case and n_p = 2 for the TBB case. Using more peaks than needed increases the computational time needed by the ROM numerical solver RootLocker without modifying significantly the FTF.

9.1.2 Transfer Matrix of a non compact flame

The mechanisms leading to flame front perturbation in the presence of acoustic forcing have been detailed in chapter 8. In the three cases CBB, UBB and TBB, unsteady heat release rate was only

observed in the region where the flame interacts with the external walls. However, the amplitude of flame front perturbations was impacted by the flame root dynamic, close to the cylindrical bluff-body. These two regions are separated by about 70 mm: the three flames are thus not perfectly compact. A two-port description can still be proposed and is based on two assumptions:

- **A1** Unsteady heat release rate is mainly generated at the wall (z_f) according to the acoustic velocity reference taken at z_ref.
- **A2** The temperature profile increases linearly from T_u at $z = 0$ up to T_b at $z = z_\mathrm{ref}$ so that the sound speed field can be simply evaluated.

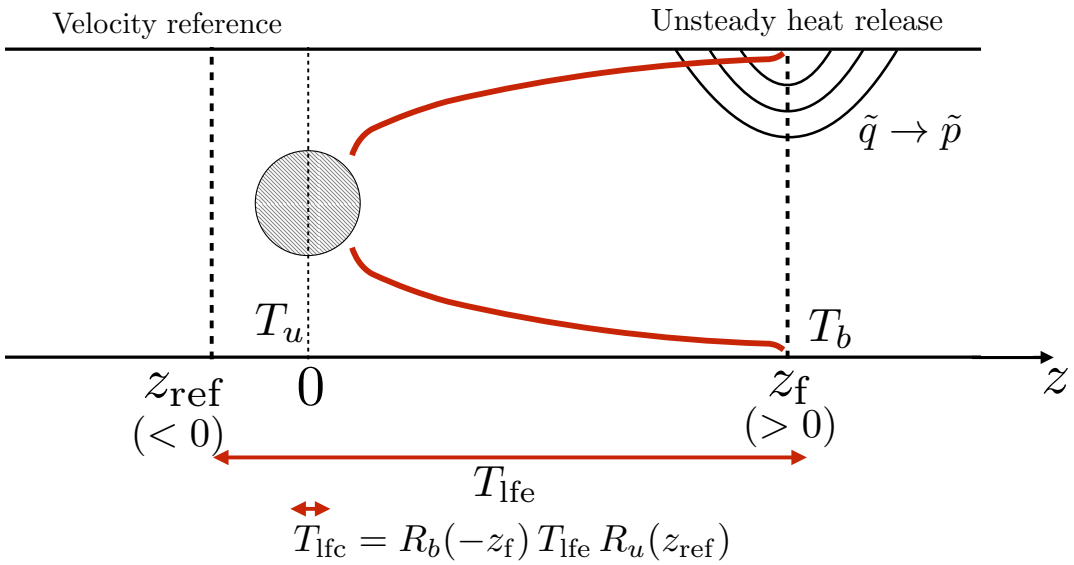

Figure 9.4: Sketch of the flame region. The velocity reference location used to measure FTFs is located at z_ref while unsteady heat release occurs at z_f. Two transfer matrix are defined: T_lfe links acoustic waves at z_ref and z_f stations while T_lfc links them at 0^- and 0^+ by using matrix transformation.

A sketch of the flame region is provided in Fig. 9.4 where all the parameters of interest are introduced. Two transfer matrices are defined: the long flame extended transfer matrix T_lfe links the acoustic waves $(A^+, A^-)_\mathrm{ref}$ taken at the velocity reference location with the acoustic waves $(A^+, A^-)_\mathrm{f}$ taken at the end of the flame. Starting from this transfer matrix, the long flame compact transfer matrix T_lfc can be obtained by using matrix transformation:

$$T_\mathrm{lfc} = \mathrm{R}_b(-z_\mathrm{f})\, T_\mathrm{lfe}\, \mathrm{R}_u(z_\mathrm{ref}) \tag{9.1.7}$$

where $\mathrm{R}_{b,u}$ is the rotation matrix defined in equation 1.4.8 for burnt/unburnt gases respectively. Both T_lfe and T_lfc take into account the whole flame with a linear temperature profile variation. However, the T_lfc matrix is denoted as compact because its ports are located right upstream and downstream of the bluff-body thanks to matrix transformation.

The T_lfc transfer matrix can be directly introduced into a ROM in place of the flame transfer matrix F defined in equation 1.5.6 as it links acoustic waves at $z = 0^-$ and $z = 0^+$.

The objective is now to provide an analytical expression of the long flame extended transfer matrix T_lfe. This can be achieved by starting from equation 1.5.4 in which the reference velocity location has been re-defined:

$$[u]_{z_\mathrm{f}}^{z_\mathrm{f}} = \frac{\Delta T}{T_u} \mathrm{FTF}(\omega) u_{z_\mathrm{ref}} \tag{9.1.8}$$

This equation states that the acoustic velocity jump occurring at $z = z_\mathrm{f}$ is only caused by the flame response through the FTF. Equation 9.1.8 can be combined with the conservation equation of acoustic pressure across the interface at $z = z_\mathrm{f}$ and recast into acoustic wave formalism to obtain:

$$\begin{pmatrix} A_\mathrm{f}^+ \\ A_\mathrm{f}^- \end{pmatrix} = \underbrace{\begin{pmatrix} 1 & 0 \\ 0 & 1 \end{pmatrix}\begin{pmatrix} A_\mathrm{f}^+ \\ A_\mathrm{f}^- \end{pmatrix}}_{\text{passive}} + \underbrace{\frac{1}{2}\Gamma g \begin{pmatrix} 1 & -1 \\ -1 & 1 \end{pmatrix}\begin{pmatrix} A_\mathrm{ref}^+ \\ A_\mathrm{ref}^- \end{pmatrix}}_{\text{active}} \tag{9.1.9}$$

where $\Gamma g = (\rho_0 c)_d/(\rho_0 c)_u(\Delta T/T_u)\mathrm{FTF}(\omega)$ is the product of the ratio of downstream and upstream impedances with the reduced FTF. The RHS of equation 9.1.9 is decomposed into a passive part (scattering of acoustic waves without the flame) and an active part (acoustic waves generated by the unsteady heat release). The long flame extended transfer matrix T_lfe can be thus obtained by providing a model for the acoustic waves passive propagation between z_ref and z_f .

This region is decomposed into two zones: from $z = z_\mathrm{ref}$ to $z = 0^-$ (see Fig. 9.4), acoustic waves are simply advanced by using a rotating matrix $\mathrm{R}_u(0 - z_\mathrm{ref})$. At the interface between the two zone (center of the bluff-body), acoustic waves are continuous: the contraction ratio caused by the cylinder is to small to alter the acoustic propagation significantly. However, in a general case, one can use a transfer matrix for the flame holder: T_fh. For instance, using a flame holder transfer matrix can be very useful in the case of flames stabilized over multi-perforated plates or swirl injectors. The second zone, which ranges from $z = 0$ to $z = z_\mathrm{f}$, has a non uniform temperature profile. The propagation of acoustic waves in one dimensional ducts with an axial temperature gradient has been investigated numerically by various authors [253, 254, 255]. More recently, Sujith et al [256] derived an exact solution in the case of a linear mean temperature $\bar{T}$ variation in the duct, as it is the case in the INTRIG configuration (assumption **A2**). However, this approach, which is described in appendix F, cannot be retained because it implies the use of Bessel functions of first and second order which are not available in RootLocker.

Another approach is preferred: the problem is discretized into n smaller regions, in which the mean temperature T_i , $i \in [1, n]$ is supposed uniform as shown in Fig. 9.5.

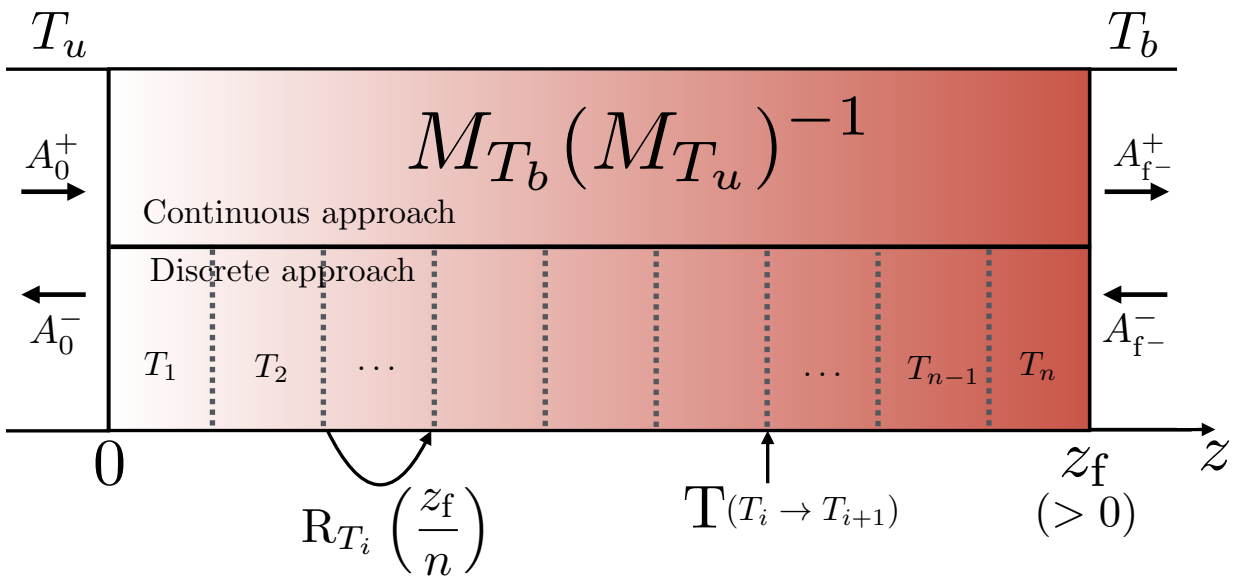

Figure 9.5: Detailed sketch for the inhomogeneous zone between $z = 0$ and $z = z_\mathrm{f}$. Both continuous and discrete approaches are represented for the propagation of acoustic waves. A comparison between the two approaches is provided in appendix F. Note that the unsteady combustion takes place only at $z = z_f$.

The corresponding discrete transfer matrix is obtained by combining all rotation (R) and temperature jump[3] (T) transfer matrices:

$$\mathrm{T}_{\mathrm{disc}} = \mathrm{T}_{n,T_b}\mathrm{R}_{T_n}\left(\frac{z_\mathrm{f}}{n}\right)\left(\prod_{i=n-1}^{1}\mathrm{T}_{i,i+1}\mathrm{R}_{T_i}\left(\frac{z_\mathrm{f}}{n}\right)\right)\mathrm{T}_{u,1} \tag{9.1.10}$$

where the intermediates temperature are $T_i = T_u + (T_b - T_u)(i - 0.5)/n$. Here, the discrete approach does not require the use of unusual functions and can also be easily adapted to the case of a non-linear variation of the mean temperature profile. A comparison between the continuous (equation F.1.4) and the discrete (equation 9.1.10) approaches is provided in appendix F where it is shown that both methods provide similar results when $n > 5$.

Finally, it is possible to combine equations 9.1.10 and 9.1.9 to obtain the long flame extended transfer matrix T_{lfe}:

$$T_{\mathrm{lfe}} = \mathrm{T}_{\mathrm{disc}}T_{\mathrm{fh}}\mathrm{R}_{T_u}(-z_{\mathrm{ref}}) + \frac{1}{2}\frac{(\rho_0 c)_b}{(\rho_0 c)_u}\frac{T_b - T_u}{T_u}\mathrm{FTF}(\omega)\begin{pmatrix} 1 & -1 \\ -1 & 1 \end{pmatrix} \tag{9.1.11}$$

The long flame compact transfer matrix T_{lfc} which was derived from T_{lfe} in equation 9.1.7 can be used in a ROM. To sum it up, this two-port matrix takes into account the length of the flame as well as the reference location for the acoustic velocity. It supposes that the temperature increases linearly starting from the flame holder at $T = T_u \approx 300\ K$ up to $T = T_b \approx 1900\ K$ at the end of the flame where the unsteady heat is released.

9.2 Boundary conditions and ROM of the INTRIG burner

The flame region has been accurately modeled in the previous sections 9.1.1, where the discrete FTFs have been recast into analytical representations, and 9.1.2, where these analytical FTFs have been included in a two-port matrix which takes into account the length of the flame. A complete ROM can be formed by combining the burner compact transfer matrix T_{lfc} with a set of boundary conditions.

9.2.1 Inlet and outlet BCs

Concerning the outlet boundary conditions, the chamber outlet is left open to let the burnt mixture flow out. As a consequence, an acoustic pressure node is imposed right after the chamber exit. Similarly to what has been done in chapter 5, an acoustic end correction [257, 12] can be taken into account: $\delta_{\mathrm{out}} = h/2$ where $h = 34\ mm$ refers to the burner width.

As small glass balls are used in the plenum to laminarize the flow (see chapter 6 for a complete description of the burner), the definition of the inlet acoustic boundary is more difficult. In order to characterize it, the multi-microphone technique described in chapter 5 has been employed in the experimental INTRIG burner to reconstruct the acoustic velocity profiles for frequencies ranging between 50 and 1000 Hz as shown in Fig. 9.6. These measurement have been performed in a non reacting configuration, and at rest. For the sake of clarity, the acoustic velocity profiles have been normalized by their maximum value. One observes that all velocity curves collapse in the vicinity of $z = -0.26\ m$, which corresponds to the end of the small glass balls. This result was expected: small glass balls form a porous wall where acoustic waves are partially reflected. This situation can be modeled by a reflection R_{in} applied at $z = -0.26\ m$, which phase[4] φ is equal to 0.

[3] This matrix is defined in equation 1.5.6 after setting $g = 1$.

[4] The reflection coefficient must be real to obtain an extremum of velocity for each frequencies. $\varphi = \pi$ corresponds to a maximum while $\varphi = 0$ corresponds to a minimum, which is observed here.

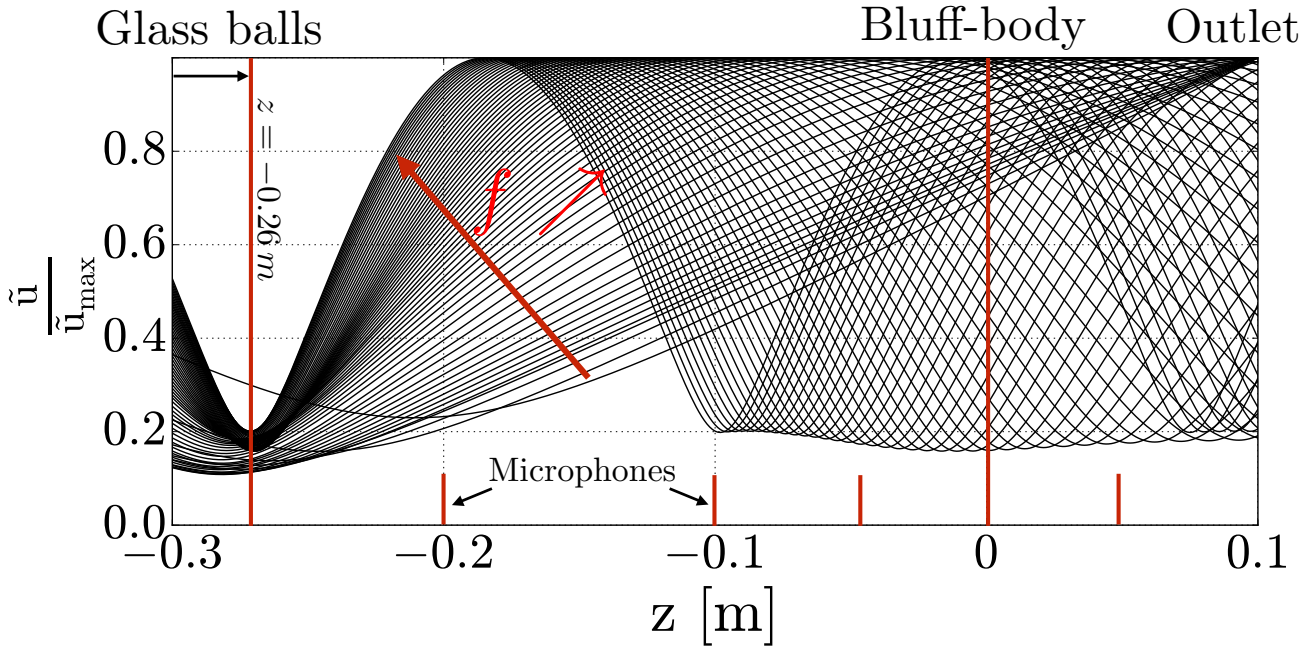

Figure 9.6: Normalized acoustic velocity field reconstructed with the multi-microphone method in the INTRIG burner for $f \in [50, 500]\ Hz$. A velocity node is clearly observed at $z = -0.26\ m$, which corresponds to the final location of the small glass balls used to laminarize the flow.

Moreover, the modulus of the reflection coefficient R_{in} can be deduced from Fig. 9.6 by considering the Standing Wave Ratio (SWR) of u. Equation 1.4.7 can be recast by using the reflection coefficient R_{in}:

$$\rho_0 c u = a^- \quad Re^{ikz} - e^{-ikz} \tag{9.2.1}$$

where $k = \omega/c$ is the wave number and a^-, the Riemann invariant of the upstream propagating wave measured at $z = -0.26\ m$. The ratio between maximum and minimum of $|u|$ is:

$$\text{SWR} = \frac{\max|u|}{\min|u|} = \frac{1 + R_{\text{in}}}{1 - R_{\text{in}}} \tag{9.2.2}$$

so that:

$$R_{\text{in}} = \frac{\text{SWR} - 1}{\text{SWR} + 1} \tag{9.2.3}$$

Figure 9.6 shows that the standing wave ratio is about SWR = 1/0.17 = 5.9 so that the amplitude of the reflection coefficient is $R_{\text{in}} \approx 0.7$. However, an important uncertainty (± 0.1) is associated with this measurement.

$|R_{\text{in}}| < 1$ means that the acoustic waves which are transmitted upstream of the inlet are dissipated by the small glass balls. This constitutes the only source of dissipation occurring in the INTRIG burner.

9.2.2 Detailed ROM of the INTRIG burner

A simplified ROM of the INTRIG burner has already been proposed in section 1.6.3. Although not accurate, this model permitted to introduce the concept of thermo-acoustic low order modeling. Moreover, it was used as a benchmark for the A_{NR} (stochastic method presented in chapter 1) and the A_{RL} (exact method presented in chapter 2) algorithms.

Here, we propose to establish a detailed ROM of the INTRIG burner, based on the knowledge acquired in the previous chapters. The corresponding sketch of the INTRIG burner is depicted in Fig. 9.7 where all important parameters are recalled.

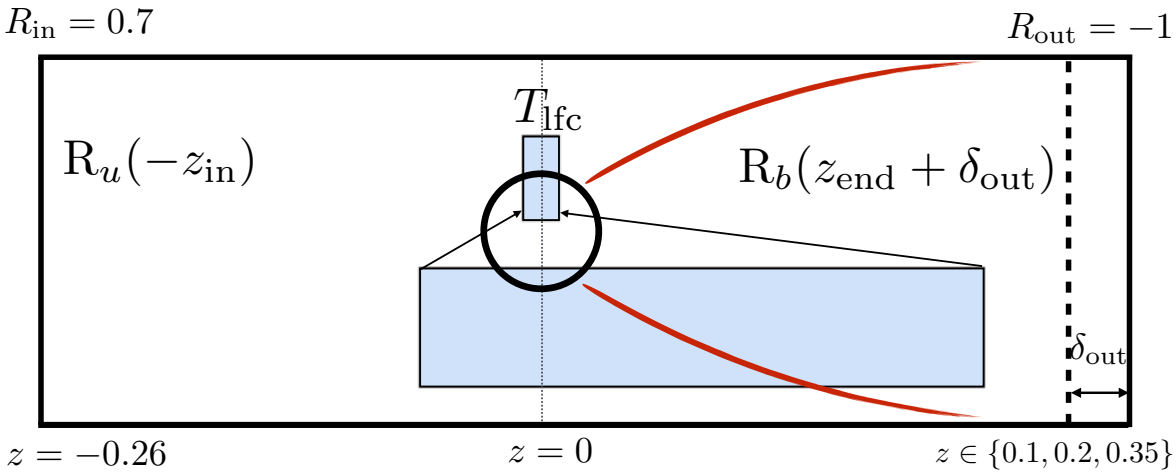

Figure 9.7: Sketch of the INTRIG burner used to build the ROM. All the lengths are given in m

The detailed ROM of the INTRIG burner is then:

$$\det\left(\mathrm{R}_b(z_{\text{out}} + \delta_{\text{out}})T_{\text{lfc}}(z_{\text{ref}}, z_{\text{f}})\mathrm{R}_u(-z_{\text{in}})\begin{pmatrix} R_{\text{in}} \\ 1 \end{pmatrix}, \begin{pmatrix} 1 \\ R_{\text{out}} \end{pmatrix}\right) = 0 \tag{9.2.4}$$

where $\mathrm{R}_{u,b}$ denotes the rotation matrix in the unburnt/burnt gases and T_{lfc} is the long flame compact transfer matrix defined in section 9.1.2. Solutions of this ROM are provided in the next section for the three cases CBB (cooled bluff-body), UBB (un-cooled bluff-body) and TBB (transparent bluff-body). These solutions, which correspond to the acoustic modes of the INTRIG rig, are then compared to experimental measurements.

9.3 Acoustic modes prediction in INTRIG

In the previous chapters (6, 7 and 8) a very short ($z_{\text{end}} = 0.1\ m$) combustion chamber has been used in the experimental set-up to avoid self-excited acoustic modes. In this configuration, referred as short in the following, the absence of unstable mode can be understood by considering the Rayleigh criterion provided in equation 0.1.1 which relates the variation of acoustic energy in the chamber. The source term of acoustic energy caused by the coupling with the flame (see equation 0.1.2) which is recalled here for the sake of clarity:

$$S = \frac{1}{T}\int_0^T \frac{\gamma - 1}{\rho_0 c^2} p'q'dt \tag{9.3.1}$$

is proportional to the product of the fluctuating pressure and heat release rate $p'q'$. It was shown in chapter 8 that the unsteady heat release rate was located at the end of the flame ($z_{\text{f}} \approx 0.07\ m$). In this region, which is very close from the outlet ($p' = 0$ at $z_{\text{end}}^{\text{short}} = 0.1\ m$), the pressure fluctuation remains very small so that $S \approx 0$. As a consequence, no unstable modes are expected because of acoustic dissipation and radiation.

The absence of unstable mode can also be understood quantitatively by solving the ROM equation of the INTRIG burner in the short configuration as done in section 9.3.3. Moreover, two other chamber lengths have been studied. A medium chamber of length $z_{\text{end}}^{\text{medium}} = 0.2\ m$, which roughly corresponds to three lengths of the flame and a long chamber of length $z_{\text{end}}^{\text{long}} = 0.35\ m$. Contrary to the short configuration, self-excited acoustic modes have been observed in the experiment for both UBB and CBB flames in the medium and long configurations. Determining whether the ROM can reproduce this behavior is an interesting test of quality.

configuration	chamber length	stable (CBB, UBB, TBB)	XP	ROM
short (section 9.3.3)	0.1 m	, ,		
medium (section 9.3.2)	0.2 m	- , ,		
long (section 9.3.1)	0.35 m	- , - ,		

Table 9.1: Summary of the different configurations studied in this manuscript. Only CBB and UBB cases have been studied in the experiments. However, the ROM approach was used with the three flames (CBB, UBB and TBB).

A brief summary of the configurations is provided in table 9.1. In the experiment, only the cooled (CBB) and un-cooled (UBB) flames were investigated. The three flames topologies (CBB, UBB and the transparent bluff-body TBB) were investigated with the ROM approach. Note tht all FTF used for the ROM come from the DNS. Even if they partially match the experimental FTF, none of the experimental FTF results was used to determine the stability map given in the next sections. In other words, the whole procedure can be performed without running the experiment, allowing to determine the stability map before operating the burner, the usual ideal target of all instability studies.

Acoustic modes in the experiments are recovered by a Power Spectral Density (PSD) of a pressure signal, measured inside of the plenum: each peak in the PSD corresponds to an acoustic mode[5]. Both frequencies (real part) and stable/unstable behavior recovered from the PSDs are then compared to the solutions of the ROM.

9.3.1 Long configuration

ROM can be first used to predict the passive acoustic modes of the burner, that is to say the modes obtained without flame/acoustic coupling (FTF(ω) = 0), but taking into account the temperature variation. In the long configuration, the first two ROM modes are: f_1^l = 228 and f_2^l = 620 Hz. The frequency of the second mode is not three times that of the first one (expected behavior for the quarter wave family of modes) as the temperature field is not uniform.

The comparison between experiments and ROM solutions is shown in Fig. 9.8 for active flames. Experimental results are provided for both CBB (black solid line) and UBB (blue dashed line) flames, while the solutions of the ROM are denoted by black circles (CBB) and blue crosses (UBB). This representation will be maintained in the following sections for the medium and short configurations. A different scale is used for experimental and ROM modes. The objective is to verify of each peaks observed in the experimental measurements correspond to a solution of the ROM.

Experimental measurement are represented by a PSD of a pressure signal (Pa^2) while ROM solutions are represented by their imaginary part $\Im(f)$ in Hz. A positive imaginary part stands for an unstable mode. Although different, these scales represent similar quantities. A high peak in the PSD represents an acoustic mode which must be unstable, and thus, with a positive growth rate $\Im(f)$. Several observations can be made from Fig. 9.8:

- First, there is a significant number of modes, both in the experiment and in the ROM. For instance, in the frequency range $f \in [0 : f_1^l]$, one observes 11 modes for the CBB case in the experimental spectrum (12 predicted by the ROM) and 9 modes for the UBB case (10 predicted by the ROM). The agreement between the experiment and the resolution of the ROM is good and highlights a point which is rarely observed: the existence of multiple possible modes in the low frequency range. This topic will be addressed in section 9.4.

[5]This statement must be tempered by the existence of harmonics. When an acoustic mode reaches a limit cycle, non linear effects arise and harmonics at multiple frequencies appear.

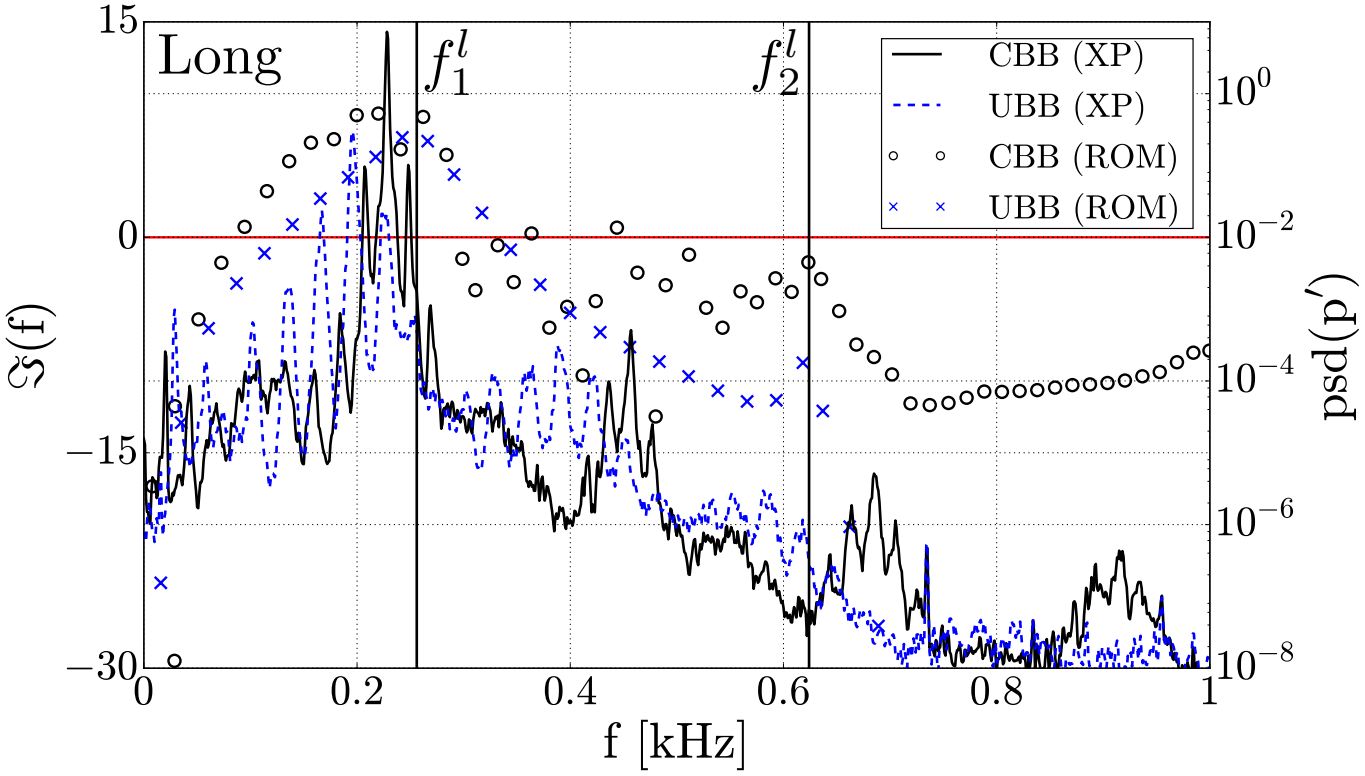

Figure 9.8: Acoustic modes obtained in the INTRIG burner in the long configuration ($z_{\text{end}} = 0.35\ m$), Vertical black lines corresponds to the modes obtained without acoustic/flame coupling. Experimental results (PSD) are represented by lines (solid black for the CBB case and dashed blue for the UBB case) while ROM solutions are denoted by markers. The solid red horizontal line denote the limit of stability for ROM solutions.

- Very unstable modes are observed in the experiment (peaks in the PSD close to 1 Pa^2) between $f \in [200 : 250]\ Hz$ for both CBB and UBB flames. These frequencies are close to the first mode of the cavity $f_1^l = 228\ Hz$ in the absence of an active flame. Moreover, the resolution of the ROM exhibits acoustic modes with a positive growth rate in the same region. Finally, one may observe that the instability is more important (higher limit cycle) in the CBB case.

- For higher frequencies ($f > f_1^l$), damped acoustic modes are observed in both experiment (PSD 1 Pa^2) and ROM solutions ($\Im(f) < 0$). This behavior is similar for both UBB and CBB flames.

- The frequency difference between two consecutive modes is about $\Delta f_{\text{CBB}} = 25\ Hz$ for the cooled case CBB in the experiment (about 20 Hz in the ROM) while it is $\Delta f_{\text{UBB}} = 31\ Hz$ for the uncooled case UBB in the experiment (about 25 Hz in the ROM). It is interesting to note that the ratio between the CBB and the UBB gap is the same in the experiment as well as in the ROM: $\Delta f_{\text{UBB}}/\Delta f_{\text{CBB}} \approx 1.25$.

9.3.2 Medium configuration

The medium configuration is now investigated ($z_{\text{end}} = 0.2\ m$). Here, the first two passive modes are: $f_1^m = 281$ and $f_2^m = 794\ Hz$ and are sightly higher than those obtained for the long chamber ($f_1^m > f_1^l = 228$ and $f_2^m > f_2^l = 620\ Hz$). The comparison between experiments and ROM solutions is shown in Fig. 9.9 where the same axes as in the long configuration comparison (see Fig. 9.8) are used.

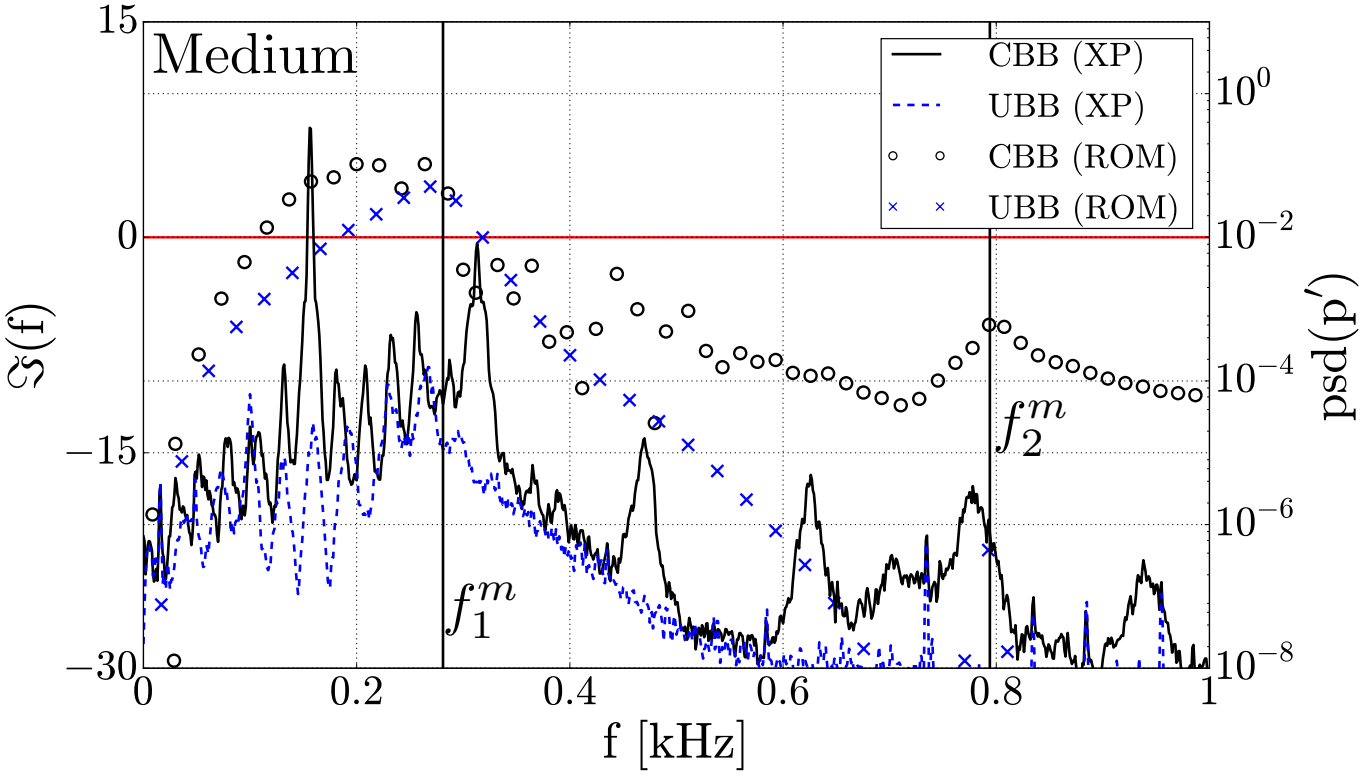

Figure 9.9: Acoustic modes of the INTRIG burner in the medium configuration (z_{out} = 0.20 m). Vertical black lines corresponds to the modes obtained without acoustic/flame coupling.

As done in section 9.3.1 for the long configuration, several observations can be realized in Fig. 9.9 for the medium chamber:

- There are still an important number of modes, both in the experiment and in the ROM and the agreement is still very good in the low frequency range ($f \in [0:300]$ Hz).
- Unstable modes are only observed with the cooled bluff-body (CBB case, solid black lines). The amplitudes of the peaks observed for UBB case (dshed blue lines) are very small when compared to those observed in the CBB case. However, the resolution of the ROM predicts sightly unstable modes in both cases, although they should only appear above 200 Hz for the UBB case.
- Finally, the frequency spacing between two consecutive modes are similar to those obtained in the long configuration.

9.3.3 Short configuration

Only results from ROM are provided in the short configuration. Indeed, no instabilities where observed in the experiment for both CBB and UBB flames. In this configuration, the first two passive modes are: f_1^s = 297 and f_2^s = 883 Hz and are also higher than those obtained for the medium chamber ($f_1^s > f_1^m$ = 256 and $f_2^s > f_2^m$ = 794 Hz). The solutions of the ROM for these two flames are displayed in Fig. 9.10.

In this configuration, all the solutions of the ROM are stables (except some marginally unstable modes in the CBB case) which validates the absence of self-excited acoustic oscillations in the experiments for both CBB and UBB flames as required in chapter 8 to measure FTFs.

This configuration proves that the ROM approach is suitable to design a stable chamber, once the FTF of the flame is known accurately.

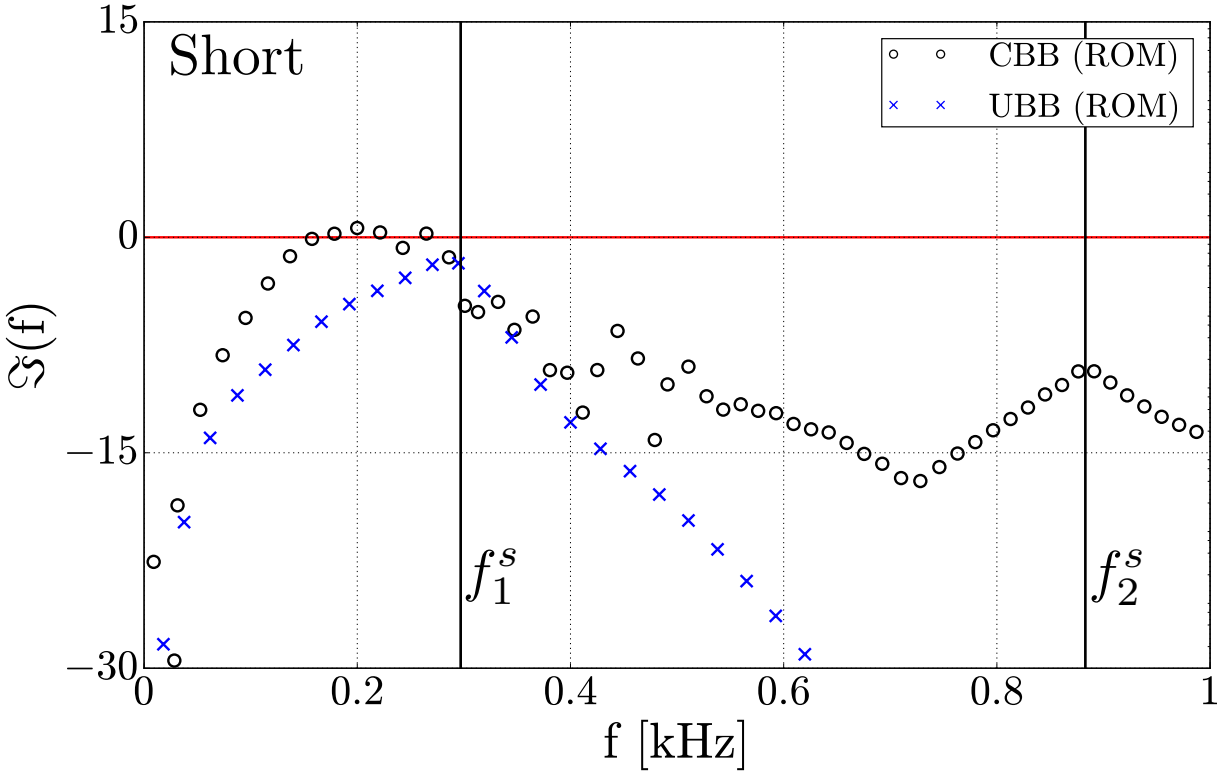

Figure 9.10: Acoustic modes of the INTRIG burner in the short configuration ($z_{\text{out}} = 0.10\ m$). Vertical black lines corresponds to the modes obtained without acoustic/flame coupling. All modes are stables with negative imaginary parts.

9.3.4 TBB case

Finally, results concerning the transparent bluff-body (TBB case), for which the flame is upstream stabilized, are provided in this section. All these results were obtained with the ROM approach as such flames were not studied in the experimental burner[6] and are gathered in Fig. 9.11.

First, one observes that for the TBB flames, all modes are stable, independently of the chamber length. A closer look at the acoustic modes provides an interesting classification: two distinct families of modes seem to exist with the TBB flame. The first one, denoted as chamber family in Fig. 9.11, contains two modes which are clearly affected by the change in length of the chamber: the longer the chamber the lower the frequency. The frequencies (real part) of the chamber family of modes are very close to the one obtained with a passive flame (denoted by dashed gray vertical lines in Fig. 9.11).

Second, an other set of acoustic modes, gathered here under the name of Unknown family is observed at low frequencies. Contrary to the chamber family of modes, only their growth rates vary with the chamber length. Here again, the frequency gap between the unknown family modes is small and independent of the chamber length : $\Delta f \approx 34\ Hz$.

9.4 Discussion

In the previous sections, comparisons between experimental measurements and ROM predictions have been provided. Short, medium and long chambers has been investigated and a very good agreement was obtained. The objective of this section is to first, explain these findings, and discuss especially the exis-

[6] the flame holder temperature measured in the DNS is about 1600 K for the TBB case

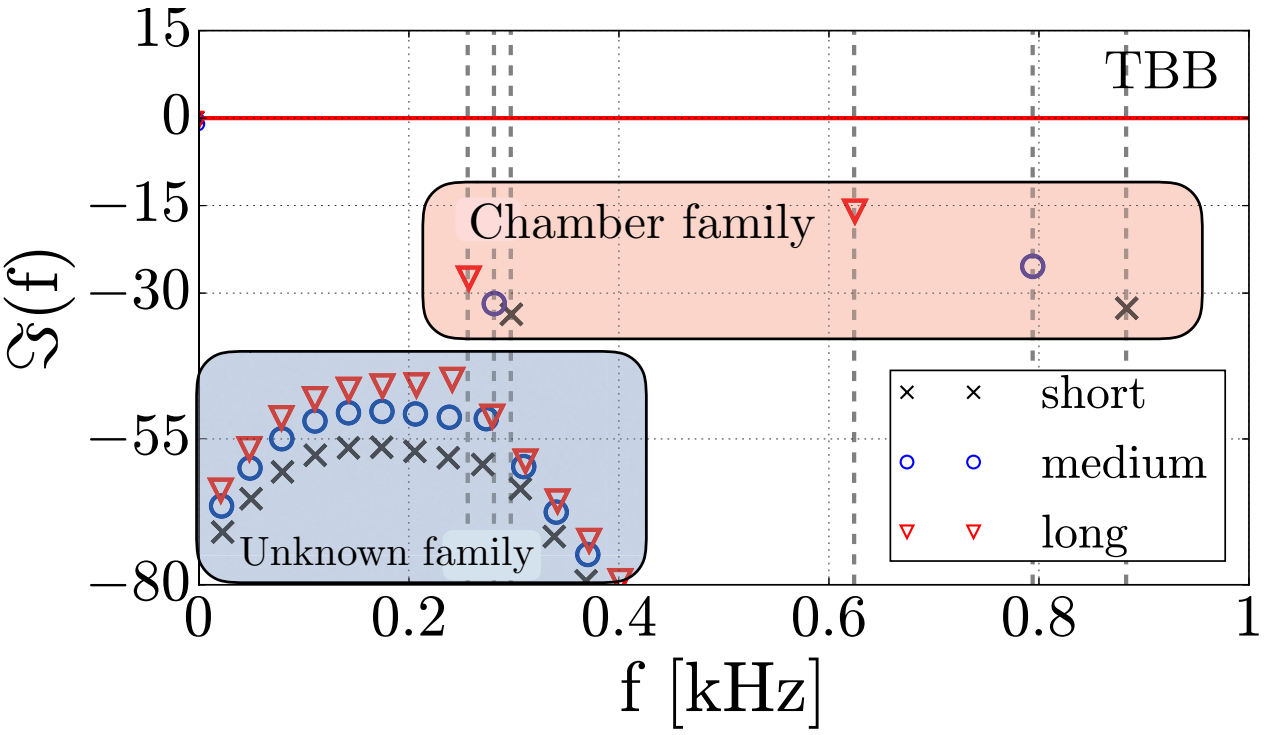

Figure 9.11: Acoustic modes predicted by using the ROM approach for the transparent bluff-body (TBB case). The modes are displayed for the three chamber lengths and vertical lines symbolizes the acoustic modes $f_{1,2}^{l,m,s}$ of the passive systems.

tence of distinct families of modes. After that, the small discrepancies observed between experimental results and ROM predictions will be discussed.

9.4.1 Chamber and Intrinsic families of modes

The modal structures observed in section 9.3 can be understood by considering the block diagram of the INTRIG burner. In a recent study, Emmert and Bomberg [246, 258] provided block diagrams of the region in which a flame was anchored on a swirl injector. Such diagrams link in and out-coming acoustic waves outside of the region of interest. This formalism is reproduced here in Fig. 9.12 with the notations adapted to those of the manuscript and several simplifications. Indeed, the bluff-body is transparent for acoustic waves[7] so that the scattering matrix appearing in [246] is replaced by an unit matrix, which greatly simplifies the diagram.

Two distinct loops are observed in this diagram. First, the chamber loop, which takes into account the propagation of acoustic waves all along the chamber. This loop is still present in the absence of combustion.

Second, the intrinsic loop, which relies only on the flame response. This intrinsic loop, has been studied recently by many authors [245, 246, 240] in the context of (quasi) anechoic combustion chambers, that is to say for vanishing reflection coefficients. Indeed, only the intrinsic loop remains when both upstream and downstream boundary conditions tend to zero. The modes associated to this loop are called the Intrinsic Thermo-Acoustic (ITA) modes [240]. Prior to studying the fully coupled system described in Fig. 9.12, it is important to isolate the intrinsic loop, as done in section 9.4.1.1. The coupling ITA and

[7] Acoustic reflection at the flame holder caused by the change of impedance are neglected here for the sake of simplicity without altering the purpose of the discussion.

[8] Assuming a compact flame do not alter the results of this section.

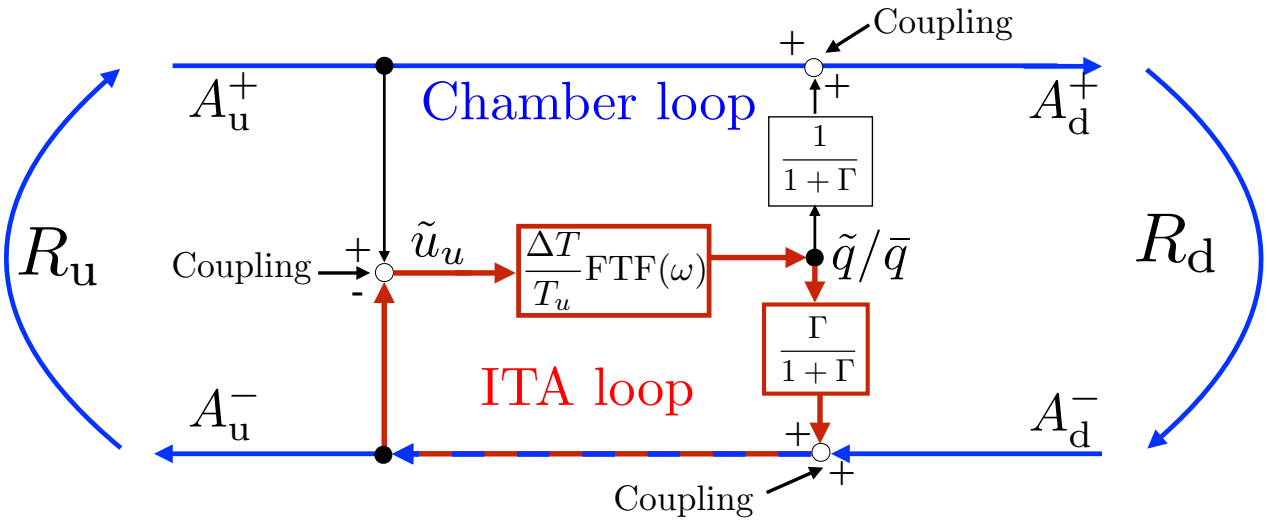

Figure 9.12: Simplified block diagram of the INTRIG burner. This diagram is adapted from [246] from which several simplifications have been adopted: the passive scattering matrix of the flame holder is set to unity and the flame is supposed compact[8].

and Chamber modes will lead to QITA modes, which are introduced in section 9.4.1.2.

9.4.1.1 ITA modes

In the context of fully anechoic combustion chamber, the ITA modes can be retrieved from the intrinsic loop of Fig. 9.12 by considering the following equation:

$$u_u = -\frac{\Gamma}{1+\Gamma}\frac{\Delta T}{T_u}\mathrm{FTF}(\omega)u_u \tag{9.4.1}$$

which has non trivial solutions only when:

$$\frac{\Gamma}{1+\Gamma}\frac{\Delta T}{T_u}\mathrm{FTF}(\omega) = -1 \tag{9.4.2}$$

where Γ is the ratio of downstream and upstream impedances and $\Delta T = T_b - T_u$. The solutions of equation 9.4.2 can be derived by assuming a local $n-\tau$ representation for the flame response ($\mathrm{FTF}(\omega) \approx n\exp(i\omega\tau)$):

$$\Re(f_{\mathrm{ITA}}) = \frac{1}{\tau}\left(\frac{1}{2}+k\right) \tag{9.4.3}$$

$$\Im(f_{\mathrm{ITA}}) = \frac{1}{\tau}\ln\left(\frac{n\Gamma\Delta T}{T_u(1+\Gamma)}\right) \tag{9.4.4}$$

The frequency spacing between ITA modes depends only on the FTF local phase delay: $\Delta f_{\mathrm{ITA}} = 1/\tau$. In addition, the stability of these modes rely on the FTF gain through the interaction index n. An ITA mode is unstable only when:

$$n > n_u = \frac{T_u}{\Delta T}\frac{1+\Gamma}{\Gamma} = \frac{\Gamma}{1-\Gamma} \tag{9.4.5}$$

In the case of the INTRIG burner, $\Gamma = \sqrt{T_u/T_b} \approx 0.4$ so that unstable ITA modes are expected when $n > n_u = 0.66$. As noted by Emmert [246], Courtine [240] or Hoeijmakers [245], unlike usual CI modes, ITA modes are not unstable when a phase condition is satisfied but when a gain criterion n_c is fulfilled. In real burners, boundary conditions are never fully anechoic and one must take into account the coupling between the Intrinsic and the Chamber acoustic modes. The resulting solutions of the ROM are called Quasi Intrinsic Thermo-Acoustic (QITA) modes and are investigated in the following section.

9.4.1.2 QITA modes

In the INTRIG burner, acoustic waves are reflected at the boundaries: $|R_{\text{in}}| = 0.7$ and $|R_{\text{out}}| = 1$ so that a coupling between intrinsic and chamber loops must occur. Instead of solving analytically the ROM equation 9.2.4, it is easier to identify the coupling by performing parametric studies with the safe parametric mode defined in section 2.6 (chapter 2). This coupling is investigated in the long chamber configuration ($z_{\text{end}} = 0.35\ m$), for the UBB flame. Similar results are obtained in the other configurations.

The QITA modes can be obtained by a continuation strategy: starting from a fully anechoic chamber, where ITA modes are expected, the reflection coefficients are varied up to their respective values ($R_{\text{in}} = 0.7$ and $R_{\text{out}} = -1$) according to the following transformation:

$$\begin{pmatrix} R_{\text{in}} \\ R_{\text{out}} \end{pmatrix}_{\text{param}} = \alpha \begin{pmatrix} R_{\text{in}} \\ R_{\text{out}} \end{pmatrix} \tag{9.4.6}$$

where α is varied from 0 to 1. The corresponding parametric study is displayed in Fig. 9.13 where the anechoic solutions ($\alpha = 0$) are denoted by red crosses while reflective ones ($\alpha = 1$) are represented by blue circles. The anechoic solutions correspond to the ITA modes which are solutions of equation 9.4.2.

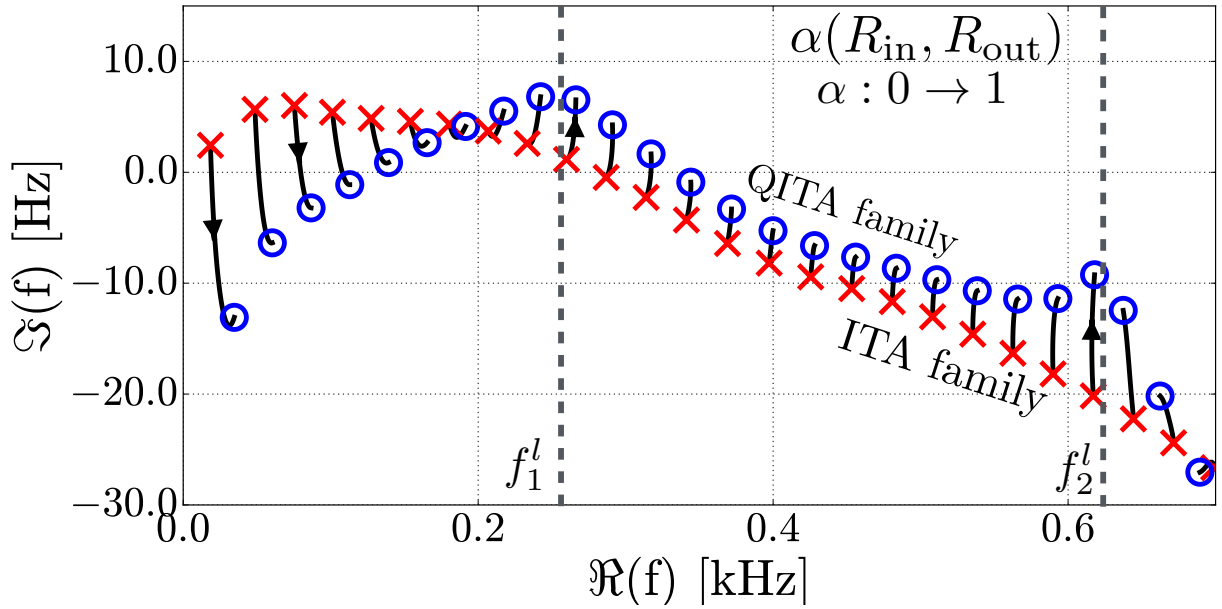

Figure 9.13: Parametric study realized with the ROM approach described in chapter 2. The reflection coefficients are multiplied by a scalar α which is varied from 0 (fully anechoic) up to 1 (reflective experimental burner). Red crosses denote the origin of a mode ($\alpha = 0$) while blue circles denote the end of a mode ($\alpha = 1$).

These solutions are then shifted to form the QITA modes when the reflection coefficients retrieve their original values. This parametric study does not differentiate modes from chamber and QITA families. Indeed, as the coupling remains strong ($\text{FTF}(\omega) > n_c$), both burner and intrinsic loops are fully coupled. However, one may observe than the QITA modes are amplified for frequencies close to that of the passive modes (obtained without flame/acoustic coupling): f_1^l and f_2^l. Close to these frequencies, the chamber reflects acoustic waves in phase with the ITA modes and the growth rate of the corresponding QITA modes is increased. In other words, for $\alpha = 0$, ITA modes do not know of the chamber modes but as α goes to unity, the ITA modes close to the acoustic passive modes are the ones with the largest growth rates. Moreover, the frequency spacing between ITA and QITA modes remains similar.

An second parametric study allows to separate the QITA modes into two distinct sets of modes: those coming from the chamber family and those originating from the ITA family. Here, the FTF is varied from zero (where only chamber modes are expected) up to its original value (where QITA modes are expected) according to the following transformation:

$$\mathrm{FTF}(\omega)_{\mathrm{param}} = \beta \mathrm{FTF}(\omega) \tag{9.4.7}$$

where β is varied from 0 up to 1. The corresponding study is displayed in Fig. 9.14 where the passive solutions ($\beta = 0$) are denoted by red crosses while active ones ($\beta = 1$) are represented by blue circles. Only two modes are obtained when $\beta = 0$ and correspond to the passive chamber modes: f_1^l and f_2^l.

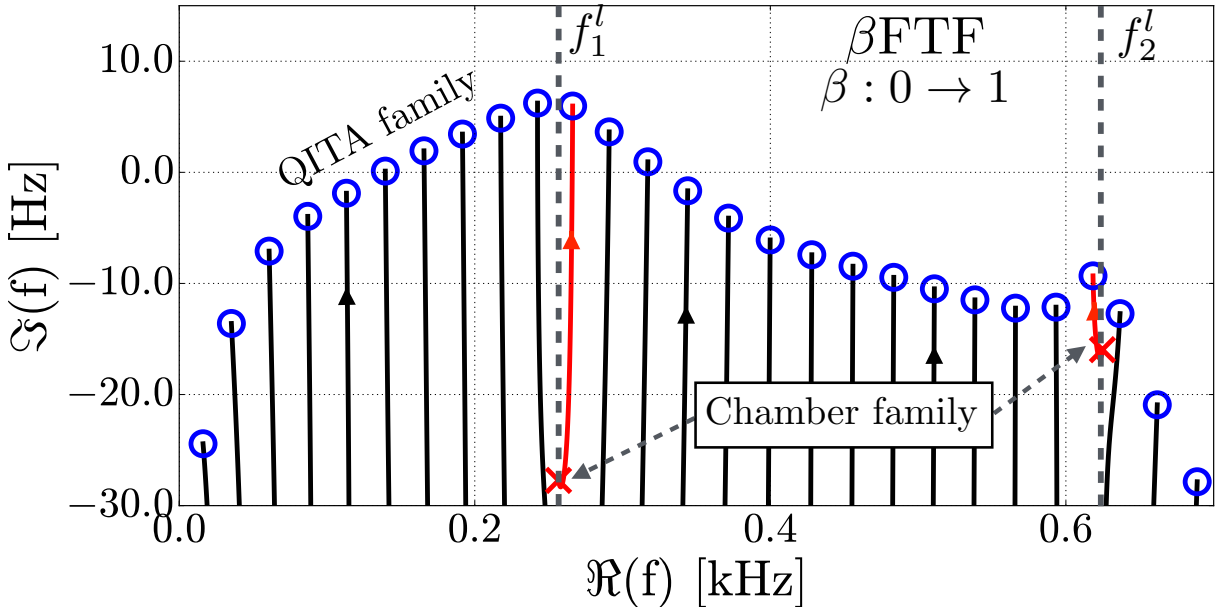

Figure 9.14: Parametric study realized with the ROM approach described in chapter 2. The FTF of the UBB flame is multiplied by a scalar β which is varied from 0 (passive flame) up to 1 (fully active flame). Red crosses denote the origin of a mode ($\beta = 0$) while blue circles denote the end of a mode ($\beta = 1$).

However, as the gain of the FTF increases, other modes appear. Their frequencies ($\Re(f)$ and $\Im(f)$) roughly match the ITA prediction of equations 9.4.3 and 9.4.4. When $\beta = 1$, it is no more possible to separate the modes coming from the chamber or from the intrinsic loops.

According to these observations (parametric studies for the FTF and the reflection coefficients), it is possible to infer a condition for the existence of QITA modes, which result from the coupling of chamber and ITA families. From Fig. 9.14, one observes that the two families begin to couple when their imaginary part (damping/growth rate) become similar which leads to the following condition for the apparition of QITA modes:

$$C = \frac{\Im(f_{\mathrm{ITA}})}{\Im(f_{\mathrm{Chamber}})} = 1 \tag{9.4.8}$$

where $\Im(f_{\mathrm{ITA}})$ is defined by equation 9.4.4. The growth/damping rate of the chamber modes can be approximated by the following formula, which is exact in the case of a purely quarter wave mode for isothermal flows:

$$\Im(f_{\mathrm{Chamber}}) = \frac{f_c}{\pi} \ln\left(R_{\mathrm{in}} R_{\mathrm{out}}\right) \tag{9.4.9}$$

where f_c is the frequency (real part) of the first chamber mode. The coupling criterion defined in equation 9.4.8 provides a critical threshold n_c for the gain of the FTF at the frequency f_c of the first

chamber mode:

$$n_c = \frac{\Gamma}{1-\Gamma}\left(R_{\text{in}}R_{\text{out}}\right)^{\tau f_c/\pi} \tag{9.4.10}$$

As a consequence, QITA modes must be accounted for to predict the stability of a burner when $\text{FTF}(2\pi f_c) \quad n_c$. Finally, all the families of acoustic modes encountered in the INTRIG burner are gathered in table 9.2.

	$\text{FTF}(2\pi f_c) \leq n_c$		$\text{FTF}(2\pi f_c) \quad n_c$
Mode family	ITA	Chamber	QITA
Characteristic	Controlled by FTF	Controlled by geometry	coupled

Table 9.2: Families of modes encountered in the INTRIG burner according to the criteria defined in equation 9.4.10.

9.4.1.3 Interpretation of the modal structure of the INTRIG burner

In this section, a re-interpretation of the modal structure observed in both experimental measurements and ROM solutions for the three configurations (short, medium and long) as well as the three flames (CBB, UBB and TBB) is provided.

The coupling criterion provided in equation 9.4.10 is applied to all of the aforementioned cases to check whether ITA, Chamber or QITA modes are expected. Values of FTFs (measured in the DNS) and critical threshold are provided in table 9.3. The direct application of the criterion of equation 9.4.10 shows that no coupling is expected in the three configuration for the transparent bluff-body (TBB). This is coherent with the results provided in Fig. 9.11 where the two families (ITA and chamber) were clearly separated. In addition, the CBB and UBB cases exhibit a coupled behavior with the QITA family. Indeed, no distinction between ITA and chamber modes can be performed in Figs. 9.8, 9.9 and 9.9.

These results prove that the criterion provided in equation 9.4.10 is a good indicator for the existence of QITA modes. For the three cases, QITA or ITA modes are observed. It is possible to verify that an important property of these families is verified in the experiment: the spacing between two consecutive modes must be a function of the flame dynamics only. Following the ITA theory developed in section 9.4.1.1, which is assumed to be also valid for QITA modes as shown in Fig. 9.13, the predicted spacing writes:

$$\Re \quad f_{(\text{Q})\text{ITA}}(k+1) - f_{(\text{Q})\text{ITA}}(k) \quad = \frac{1}{\tau} \tag{9.4.11}$$

It has been shown in section 9.3 that the spacing between acoustic modes did not depend on the chamber length. A comparison between frequency spacing measurements and equation 9.4.11 is provided in table 9.4:

The agreement between equation 9.4.11 and the ROM spacing is very good, which also proves that ITA/QITA modes are obtained in the INTRIG burner. However, there is a small difference with the spacing obtained in the experiment. Indeed, the ROM is based on FTFs measured in the DNS, where the flame delays[9] are sightly higher than those observed in the experiment as shown in Fig. 8.15.

Finally, the difference in gain between FTFs measured in DNS and experiments (Fig. 8.15) can explain why the ROM approach predicts unstable modes for the UBB flame in the medium configuration while the experimental burner remains stable (see Fig. 9.9). Indeed, in the frequency range $f \in [200, 300]$, the FTF gain in the experiment is much lower than the one in the DNS, which stabilizes the QITA modes, as shown in equation 9.4.4.

[9]The flame delay is the slope of the phase of the FTF.

Conf / Case	Short		Medium		Long	
	$\lvert FTF(2\pi f_c)\rvert$	n_c	$\lvert FTF(2\pi f_c)\rvert$	n_c	$\lvert FTF(2\pi f_c)\rvert$	n_c
CBB	0.1	0.14 weak coupling	0.9	0.15	1.7	0.17
UBB	0.5	0.2	0.6	0.21	0.9	0.23
TBB	$7\ 10^{-6}$	0.26 un-coupled	10^{-5}	0.28 un-coupled	$3\ 10^{-5}$	0.30 un-coupled
f_c	297 Hz		281 Hz		256 Hz	

Table 9.3: FTF (left, black) and critical (right, red) threshold for all the cases/configurations investigated in this chapter. A coupling between ITA and chamber modes is expected when the gain of the FTF is greater than the threshold at the frequency f_c of the first passive mode.

Case	CBB	UBB	TBB
XP spacing $[Hz]$	25	31	-
ROM spacing $[Hz]$	20	25	34
ITA spacing $(1/\tau)$ $[Hz]$	21	27	37

Table 9.4: Comparison between mode spacing predicted (see equation 9.4.11) and measured (see section 9.3). The delay τ are obtaned from the FTF data of section 8.1.2. The experimental spacing is measured in the experimental pressure spectra. The ROM spacing is simply deduced from ROM solutions.

Conclusion

Here, the knowledge acquired in the previous chapter about reduced order modeling, acoustic losses and flame/acoustic interaction has been used to output a detailed ROM of the INTRIG burner. Its solutions have been compared to experimental measurements for different flames (CBB, UBB and TBB) and for different configurations (short, medium and long) and a good agreement was obtained.

It was shown that the flame holder temperature greatly influences the stability of the chamber. For instance, in the medium length chamber, the flame stabilized on a cooled cylinder ($T_c \approx 300\ K$) was unstable for the ROM as well as in the experiment while the flame stabilized on the un-cooled cylinder ($T_c \approx 700\ K$) was stable. The TBB case, where the flame was stabilized upstream of the bluff-body, was stable for all configurations.

In order to understand the modal structure observed, a new family of acoustic mode has been introduced: the Quasi-Intrinsic Thermo-Acoustic (QITA) family, which results from the coupling between chamber and intrinsic modes. These modes are barely affected by the boundary conditions which would make acoustic dampers useless to temper CIs. Finally, a critical threshold n_c has been derived to determine when these modes must be accounted for to predict the stability of the burner.

Concluding remarks

This PhD work has been carried out with three primary objectives: 1) Defining a clear methodology to derive and solve reduced order models in thermo-acoustic studies, 2) Incorporating sources of acoustic losses in these models and 3) investigate on the flame holder temperature influence on both anchoring mechanisms and flame dynamics. All these objectives are linked by the motivation to predict and better understand thermo-acoustic instabilities.

From an other point of view, this work has also been dedicated to the design of numerical tools to predict thermo-acoustic instabilities. For instance, comparisons between CFD codes (DNS and LES) and experiments have been provided in parts II and III with a constant desire to obtain a good agreement. Using simulations permits to: a) better understand underlying physical mechanisms by providing quantitative data and b) help to design new efficient and stable combustion chambers. Figure 9.15 summarizes the experimental set-ups investigated during this PhD work. Both PREINTRIG and INTRIG rigs were studied with numerical solvers (DNS or LES) and validated with experimental measurements (PIV, OH* imaging).

In order to accomplish these objectives, new concepts, methods and physical mechanisms have been introduced. Among them, the most important are recalled here:

Major advances realized during this PhD work

- A numerical algorithm (A_{RL}) has been designed to solve analytical equations. This method ensures that all the roots lying in a specific portion of the complex plane are enclosed properly. This algorithm is particularly useful to solve ROM equations.
- An automated mesh refinement procedure has been introduced to predict mean pressure losses in Large Eddy Simulations (LES). This method is based on a physical criterion: the loss in kinetic energy.
- Acoustic transfer matrices have been measured and introduced in a dedicated ROM: the predicted frequencies and damping rates matched experimental measurements carried out on the PREINTRIG workbench.
- The mechanisms of flame anchoring on cylindrical bluff-bodies have been investigated in DNS, with analytical chemistry and heat transfer taken into account in the solid. It was shown that the radiative heat transfer played a crucial role in the stabilization mechanisms.
- The flame dynamic (FTF) is greatly influenced by flame holder temperature. This topic has already been addressed in former experimental studies and we confirm the existing results with DNS data.
- A new family of acoustic modes: the Quasi-Intrinsic Thermo-Acoustic (QITA) has been introduced to explain the modal structure encountered in the INTRIG burner. We also showed that the flame holder temperature influenced the stability of the burner.

Thanks to the work accomplished, several advices can be proposed to design stable combustion chambers. First, the use of acoustic dampers must be used with caution. Indeed, it has been shown that good acoustic dissipation properties always come with mean pressure losses, which reduce engines

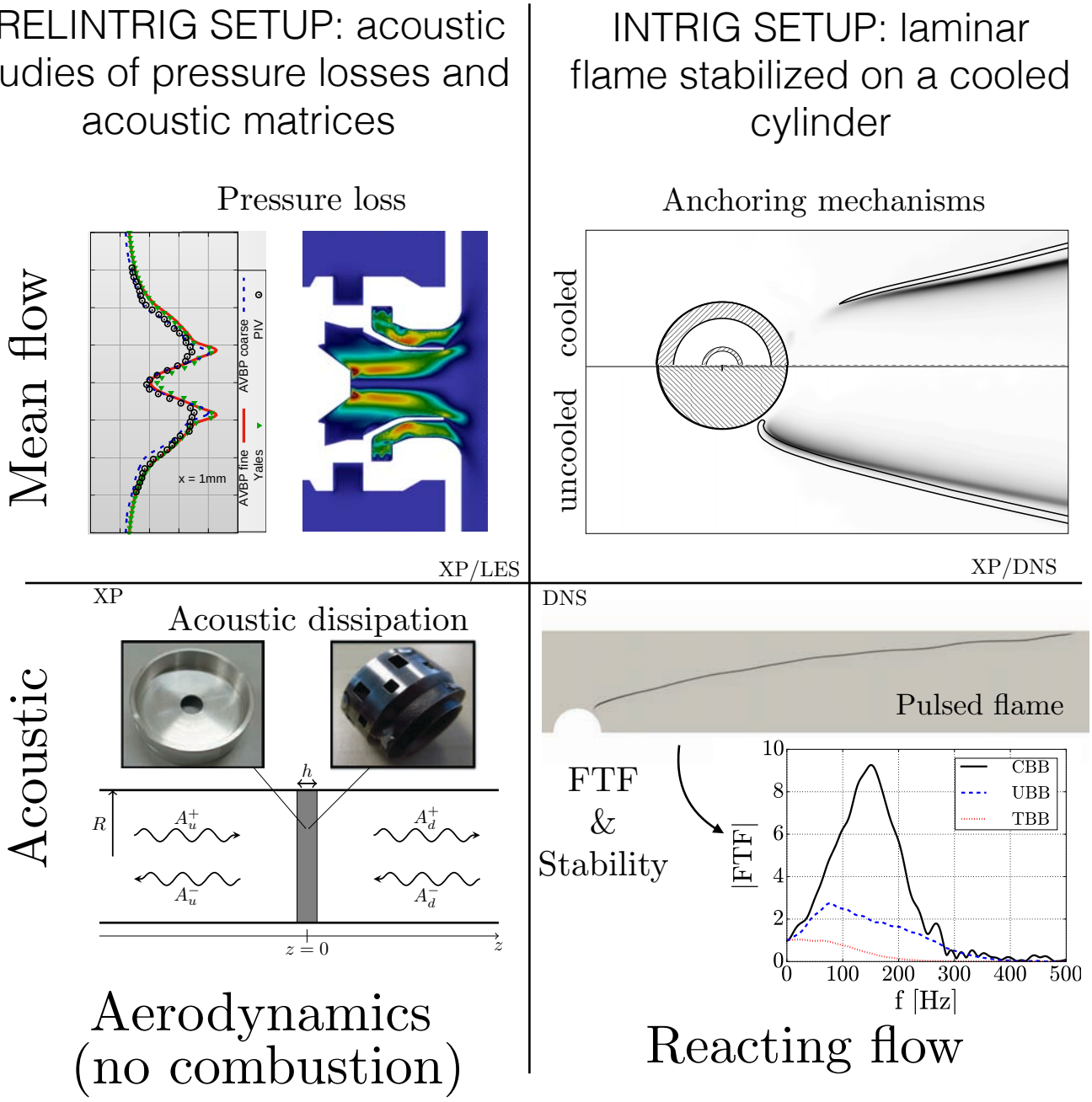

Figure 9.15: Experimental set-up used during this PhD work.

efficiency. Second, two effects has been identified to control flame dynamics. An increase in flame holder temperature permits to attach flames outside of recirculation zones, and reduces their responses to acoustic perturbations. Moreover, combining flames with different delays causes phase averaging in the overall response of the burner: this also reduces the unsteady heat release outputted by the burner and may suppress instabilities. For instance, these advices are applied here to design a laminar burner: flames are stabilized on a multi-perforated plate presented in Fig. 9.16. s

In this design (Fig. 9.16, right), the radii of the holes are not uniformly distributed in order to obtain a Gaussian distribution for the flame delays. Indeed, the pressure drop is constant for each hole and is

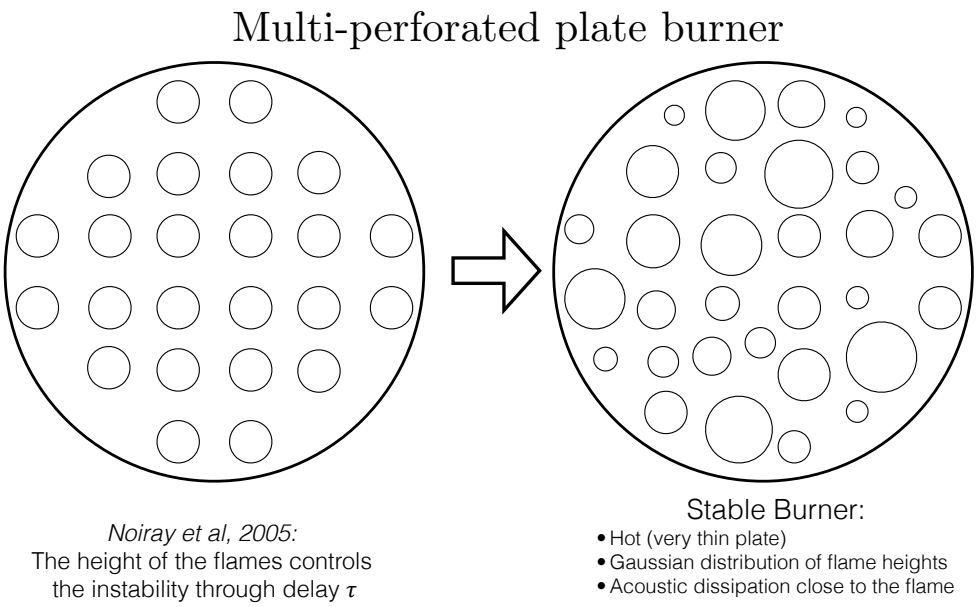

Figure 9.16: sketch of a laminar burner inspired by a study performed by Noiray et al [259]

a function of the hole bulk velocity u_b and radius r (see chapter 6 for the exact relation):

$$\Delta P \quad \frac{u_b^2}{r^4} \tag{9.4.12}$$

Moreover, the flame delay is proportional to the ratio between the flame height and the velocity:

$$\tau \quad \frac{L}{u_b} \approx \frac{r}{2s_L} \tag{9.4.13}$$

which does not depend on the velocity: the flame delay is proportional to the hole radius: $\tau \quad r$

This parameter (r) must follow a Gaussian distribution. In addition, a thin plate will attain higher temperature and thus, help to reduce the magnitude of flame responses. Finally, the multi-perforated plate will dissipate acoustic energy. As a consequence, one expects that this burner will remain stable for a wide range of operating regimes.

Publications

During this Phd work, five articles have been submitted. Most of these articles are related to chapters presented here and two of them are already published. This section also allows me to thanks colleagues who contributed to my PhD work.

The first article was realized in collaboration with D. Mejia at IMFT and provides a comparison between different experimental methods to measure acoustic growth/damping rates in a combustion chamber. These measurements are then compared to the solutions of a ROM and an excellent agreement is obtained. I realized the post-processing of pressure signals in obtained in both stable and un-stable operating regimes, for which a broad band acoustic fluctuation was superimposed (one of the method tested) while Daniel took care of the other methods and the ROM design.

On the experimental determination of growth and damping rates for combustion instabilities. D. Mejia, M. Miguel-Brebion, L. Selle. **2016**, Combustion and Flame 169, 287-296.

The next article is about the introduction of acoustic dissipation in a Helmholtz solver and has been realised in collaboration with F. Ni at CERFACS, who used the experimental measurements of acoustic two-ports of the diaphragm and the swirl-injector that I realized at IMFT to predict acoustic damping in three dimensional configurations.

Accounting for acoustic damping in a Helmholtz solver. F. Ni, M. Miguel-Brebion, F. Nicoud and T. Poinsot. **2016**, AIAA Journal, 1-16.

An article has been submitted in the journal *Flow, Turbulence and Combustion* in the collaboration with G. Daviller (CERFACS) about the automatic mesh refinement procedure dedicated to predict pressure losses in LES. I helped G. Daviller to design the mesh refinement criteria, which is based on mean kinetic energy dissipation and I carried out experimental measurements of the pressure losses as well as PIV imaging (with P. Xavier). This article is still under reviews.

A mesh adaptation strategy to predict pressure losses in LES of swirled flows. G. Daviller, M. Miguel-Brebion, P. Xavier, G. Staffelbach, J.D. Muller, T. Poinsot. **2016**, FTAC.

The next article is about the stabilization mechanisms of laminar flames on cylindrical rod and the influence of the flame holder temperature. I performed the DNS (with a chemical mechanism less accurate than the one presented in chapter 7: LU13) and wrote the article while D. Mejia and P. Xavier carried out the experimental measurements.

Joint experimental and numerical study of the influence of flame holder temperature on the stabilization of a laminar methane flame on a cylinder. M. Miguel-Brebion, D. Mejia, P. Xavier, F. Duchaine, B. Bedat, L. Selle, T. Poinsot, **2016**, Combustion and Flame, 172, 153-161

Finally, the last article has been published to the *Journal of Fluid Mechanics* and is about the

anchoring mechanisms of flames stabilized on rotating cylinders. P. Xavier carried out DNS with the LU19 chemical mechanism and the Homogeneous adaptive boundary condition (HABC), which I developed during my PhD work (see chapter 6). These results were compared to experimental measurements for various rotating speeds and compared to academical one dimensional flames configurations by A. Ghani.

*Experimental and numerical investigation of flames stabilised behind rotating cylinders: interaction of flames with a moving wall.*P. Xavier, A. Ghani, D. Mejia, M. Miguel-Brebion, L. Selle, T. Poinsot, **2017**, Journal of Fluid Mechanics, 813, 127-151.

Appendices

Appendix A

Checking procedure of the roots

The checking procedure guarantees that all roots found (distinct or multiple) are solutions of the initial problem to ϵ. The roots $z_i\,, i \in [|1, N|]$, obtained after the application of the algorithm detailed in section 2.2 must be controlled in an efficient way. Indeed, The accuracy of the roots found by solving the equivalent polynomial problem is controlled by the stop criteria used to compute the integrals of equation 2.1.9. Applying the NR method on these guesses may then leads to erroneous results, especially when multiple distinct solutions are extracted from a single mesh.
When all roots $z_i^\star$ are distinct: $|z_i - z_j| > \epsilon\,, \quad (i, j)$, we check that $I_0(\mathbf{C_i}) = 1 \quad i \in [|1, N|$ where $\mathbf{C_i}$ is a square of size 2ϵ centred around z_i.
When a cluster of roots is encountered: $\{z_i, z_j\}, \quad j \,/\, |z_i - z_j| < \epsilon$, we check that $I_0(\mathbf{C_{eq}})$ is equal to the corresponding multiplicity. In this case, $\mathbf{C_{eq}}$ is centred on the mean of the multiple root obtained after the NR step. In both cases, a failing check leads to a new mesh split.

Appendix B

Design of a non intrusive lateral loudspeaker system

This appendix reports the development of an analytical model to study eigen-frequencies of a tube when a loudspeaker is connected to it. A network approach is developed, thus leading to consider only longitudinal waves. Finally, a validation is performed experimentally, with the n-microphones technique. This study was realized with the help of Dr. Xavier from IMFT.

The objective of this study is to prove that a loudspeaker attached at the side of the PREINTRING rig do not alter the acoustic modes in the frequency range of interest: $f \in [0,1]\ kHz$. For the sake of simplicity, all parameters are redefined without assuming that the chapter 3 have been read.

B.1 Geometry description

Fig. B.1, left presents a photography of the experiment. It consists of a vertical closed duct, named main tube , with a length L, a section S, and equipped with several ports for microphones. In order to harmonically force the main duct, a loudspeaker system is connected at a right angle, located at a certain distance ηL from the upper part of the main tube. The loudspeaker casing can be considered as a duct, of length L_B and section S_B. The main duct is connected to the loudspeaker casing by an intermediate duct (length L_i, and a section S_i). The length of this junction can be varied so that the loudspeaker is either flush mounted or deported with respect to the main duct lateral wall.

A network model approach is used to model the entire experiment (Fig B.1, right). In this ROM, only longitudinal modes are taken into account. No flame is present in the experiment so that sound speed, noted c, is constant in all tubes. The network consists of 4 elements: 1 and 2 for the main duct (the separation corresponds to the location of the loudspeaker system port), i for the connecting junction, and B for the loudspeaker casing.
Table B.1 summarizes dimensions of the experimental setup.

	Main Tube 1, 2	Connection i	Casing B
Length L [m]	$9.27.10^{-1}$	$5.4\,10^{-1}\,8\,10^{-2}$	8.10^{-2}
Diameter [m]	8.10^{-2}	1.10^{-2}	$9.1.10^{-2}$
Section [-]	5.10^{-3}	$7.85.10^{-5}$	$6.5.10^{-3}$
η		0.28	

Table B.1: Dimensions of the experimental setup. Note that two lengths are tested for the connection tube i

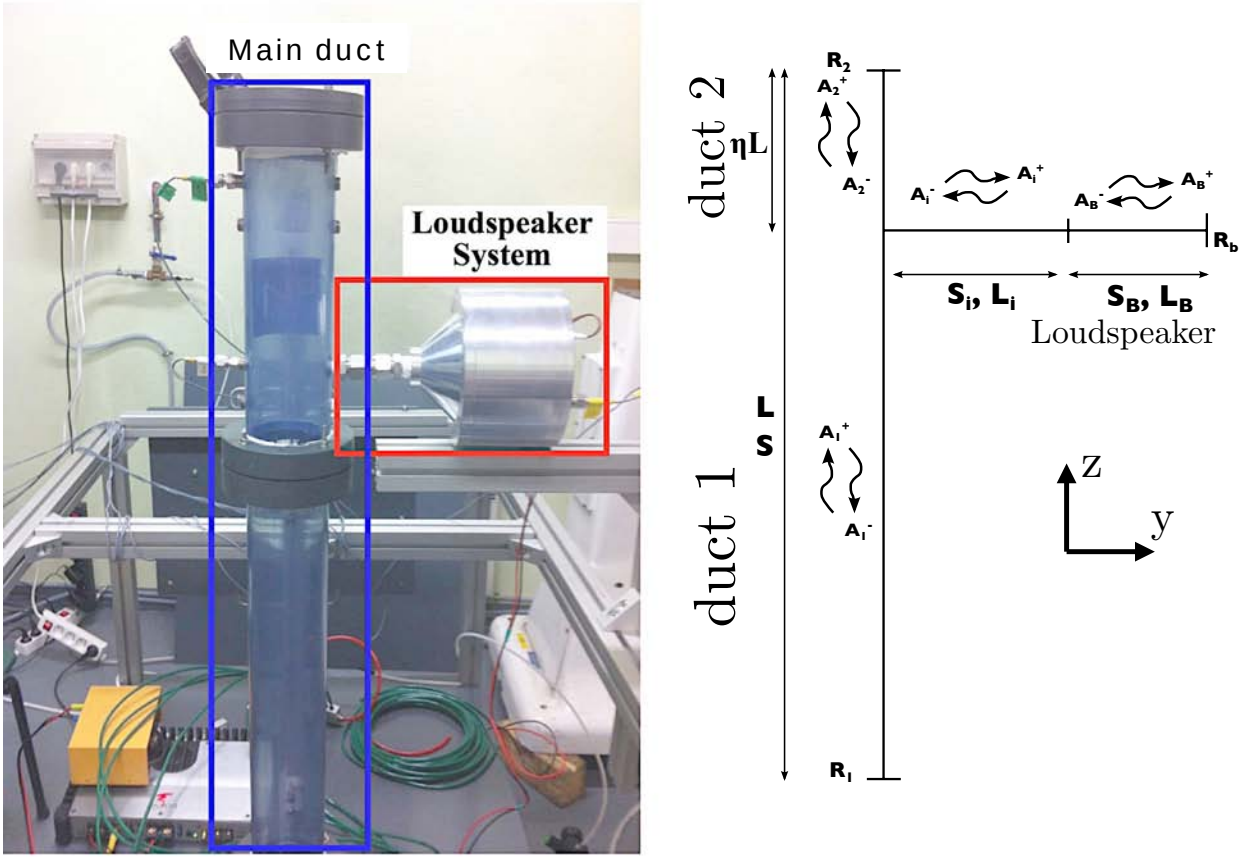

Figure B.1: Left: photography of the experimental setup. Coloured rectangles depict the different parts of the system. Right: Schematic illustration of the acoustic system recalling the notations used.

B.2 ROM derivation

In order to obtain the ROM for the system of Fig. B.1, a transfer matrix for the main tube (between ducts 1 and 2) is first derived, separately from the whole loudspeaker system (ducts i and B). The interaction with duct i at the T intersection is taken into account by considering:

$$A_i^- = F A_i^+ \tag{B.2.1}$$

Where F is determined in Sec. B.2.2, when deriving the transfer matrix between tubes i and B .

B.2.1 Main tube transfer matrix

Note that in this section, the origin is taken at the T intersection ($z = 0$ and $y = 0$). Both ends of ducts 1 and 2 are considered as walls, then leading to zero velocity fluctuations (i.e., $u_2(z = \eta\ L) = 0$ and $u_1(z = (\eta\text{-}1)L) = 0$). However, other boundary conditions may be tested by defining two reflection coefficients :

$$\frac{A_1^+}{A_1^-} e^{2ikL(1-\eta)} = R_1 \tag{B.2.2}$$

$$\frac{A_2^-}{A_2^+} e^{2ikL\eta} = R_2 \tag{B.2.3}$$

Jump conditions are written at the T intersection:

$$A_2^+ + A_2^- = A_1^+ + A_1^- = A_i^+ + A_i^- \tag{B.2.4}$$

$$(A_2^+ - A_2^-) = (A_1^+ - A_1^-) + \alpha(A_i^+ - A_i^-) \tag{B.2.5}$$

with $\alpha = S_i/S$. Eq. B.2.5 is simplified with the assumption that the section in ducts 1 and 2 is constant and equal to S. Equation B.2.4 states that the acoustic pressure is continuous across the interface while Equation B.2.5 expresses the conservation of the acoustic flux. After combining equations B.2.5 and B.2.1, one obtains

$$(A_2^+ - A_2^-) = (A_1^+ - A_1^-) + \alpha Z(A_1^+ + A_1^-) \tag{B.2.6}$$

where $Z = \dfrac{1-F}{1+F}$ is an impedance, appearing with the addition of the loudspeaker system (tubes i and B) to the main duct. As a consequence, equations B.2.4 and B.2.6 only contain acoustic wave amplitudes of ducts 1 and 2 so that a transfer matrix T can be derived:

$$\begin{pmatrix} A_2^+ \\ A_2^- \end{pmatrix} = \underbrace{\begin{pmatrix} 1+\alpha Z/2 & \alpha Z/2 \\ -\alpha Z/2 & 1-\alpha Z/2 \end{pmatrix}}_{\mathrm{T}} \begin{pmatrix} A_1^+ \\ A_1^- \end{pmatrix} \tag{B.2.7}$$

Note that if Z is equal to zero, waves travelling in ducts 1 and 2 are identical. Such a situation corresponds to a normal velocity node imposed at the junction and thus, does not alter the acoustic of the main duct. However, setting $F = -1$ leads to an undefined transfer matrix. In this case, a pressure node is imposed at the junction, and there is thus no relation between acoustic waves from both sides of the duct. Using the boundary conditions of the main duct (Eqs. B.2.2 and B.2.3), Equation B.2.7 can be re-written as a function of only two waves:

$$\underbrace{\begin{pmatrix} (1+\alpha Z/2)R_1 e^{2ikL(1-\eta)} + (\alpha Z/2) & 1 \\ (-\alpha Z/2)R_1 e^{2ikL(1-\eta)} + (1-\alpha Z/2) & R_2 e^{2ikL\eta} \end{pmatrix}}_{\mathrm{T'}} \begin{pmatrix} A_1^- \\ A_2^+ \end{pmatrix} = \begin{pmatrix} 0 \\ 0 \end{pmatrix} \tag{B.2.8}$$

System B.2.8 leads to non-null solutions if and only if the determinant of T' is null:

$$R_2 R_1 e^{2ikL} - 1 = -\alpha Z/2[1 + R_1 e^{2ikL(1-\eta)} + R_2 e^{2ikL\eta} + R_1 R_2 e^{2ikL}] \tag{B.2.9}$$

Before solving Eq. B.2.9, the coupling factor Z must be obtained by considering the loudspeaker system.

B.2.2 Loudspeaker system transfer matrix

The objective of this section is determine the coupling factor Z (or F). Note that the origin is taken at the intersection between tube i and B ($z = 0$ and $y = 0$). End of tube B (at $y = L_B$) is considered as a wall[1] which leads to zero velocity fluctuation (i.e., $u_B(y = L_B) = 0$):

$$A_B^+ = \gamma A_B^- \tag{B.2.10}$$

with $\gamma = e^{-2ikL_B}/R_B$. Jump conditions are written at the intersection between tube i and B :

$$A_i^+ + A_i^- = A_B^-(1+\gamma) \tag{B.2.11}$$

$$(A_i^+ - A_i^-) = A_B^-\varepsilon(\gamma - 1) \tag{B.2.12}$$

with $\varepsilon = S_B/S_i$. After combining Eqs. B.2.11 and B.2.12, one can obtain the equation for F:

[1]This is a strong assumption as we do not consider the impedance of the loudspeaker itself.

$$F = \frac{\varepsilon(1-\gamma)+(1+\gamma)}{(1+\gamma)+\varepsilon(\gamma-1)} \tag{B.2.13}$$

Therefore, Z can be easily determined with Eq. B.2.13:

$$Z = \frac{z_1}{z_2} = \frac{(1+\gamma)+\varepsilon(\gamma-1)-\beta_i[\varepsilon(1-\gamma)+(1+\gamma)]}{(1+\gamma)+\varepsilon(\gamma-1)+\beta_i[\varepsilon(1-\gamma)+(1+\gamma)]} \tag{B.2.14}$$

A particular attention must be taken when using Eq. B.2.13. The latter is valid at the intersection between tube i and B ($y = 0$). Therefore, a correction has been added in Eq. B.2.14 to account for the length of tube i and to estimate this coupling factor at the T intersection, i.e.:

$$\frac{A_i^+}{A_i^-}_{T} = \underbrace{\frac{A_i^+}{A_i^-}_{x=0}}_{F} e^{2ikL_i}_{\beta_i} \tag{B.2.15}$$

B.2.3 Characteristic equation

With the model of the coupling impedance $Z = z_1/z_2$, the dispersion relation in Eq. B.2.9 can be closed, and written as:

$$2z_2[R_2R_1e^{2ikL}-1]+\alpha z_1[1+R_1e^{2ikL(1-\eta)}+R_2e^{2ikL\eta}+R_1R_2e^{2ikL}] = 0 \tag{B.2.16}$$

The methodology used in this appendix can be applied to more general configurations. It relates the derivation of ROM of non linear geometries which contain branches. All branches are modeled as reduced impedances, which are taken into account in modified transfer matrices inside of the main branch .

Equation B.2.16 cannot be solved analytically. The numerical solver Rootlocker described in chapter 2 is then used in section B.4.

B.3 Experimental acoustic modes

As shown in Fig. B.1, experiments have been carried out to identify the frequencies of the acoustic modes of the complete system. Two distinct geometries have been scrutinized: the first one used a long junction ($L_i \approx 0.5\ m$) while the second used a smaller one ($L_i \approx 8\ cm$). The geometrical parameters are recalled in tableB.1.

Four microphones have been placed in duct 1 to retrieve the amplitude of the acoustic waves following the multi-microphone methodology described in chapter 5 and the results are shown in Fig. B.2. The modes family $f_0, 2f_0, \ldots$ correspond to the natural modes of the main duct: $f_0 = c/(2L) = 185\ Hz$. Unwanted modes (f_1) are observed in the long configuration and might be caused by the coupling between the main duct and the loudspeaker system.

According to these two measurements, one can deduce that the length of the intermediate duct L_i plays a role in the coupling between the main duct and the loud speaker system. This coupling is investigated in section B.4 by comparing the experimental results with a numerical resolution of the ROM derived in section B.2.3.

B.4 Discussion

The frequencies of the acoustic modes obtained experimentally are now compared to the numerical resolution of the ROM (equation B.2.16). The frequencies obtained in the two configurations are gathered in table B.2

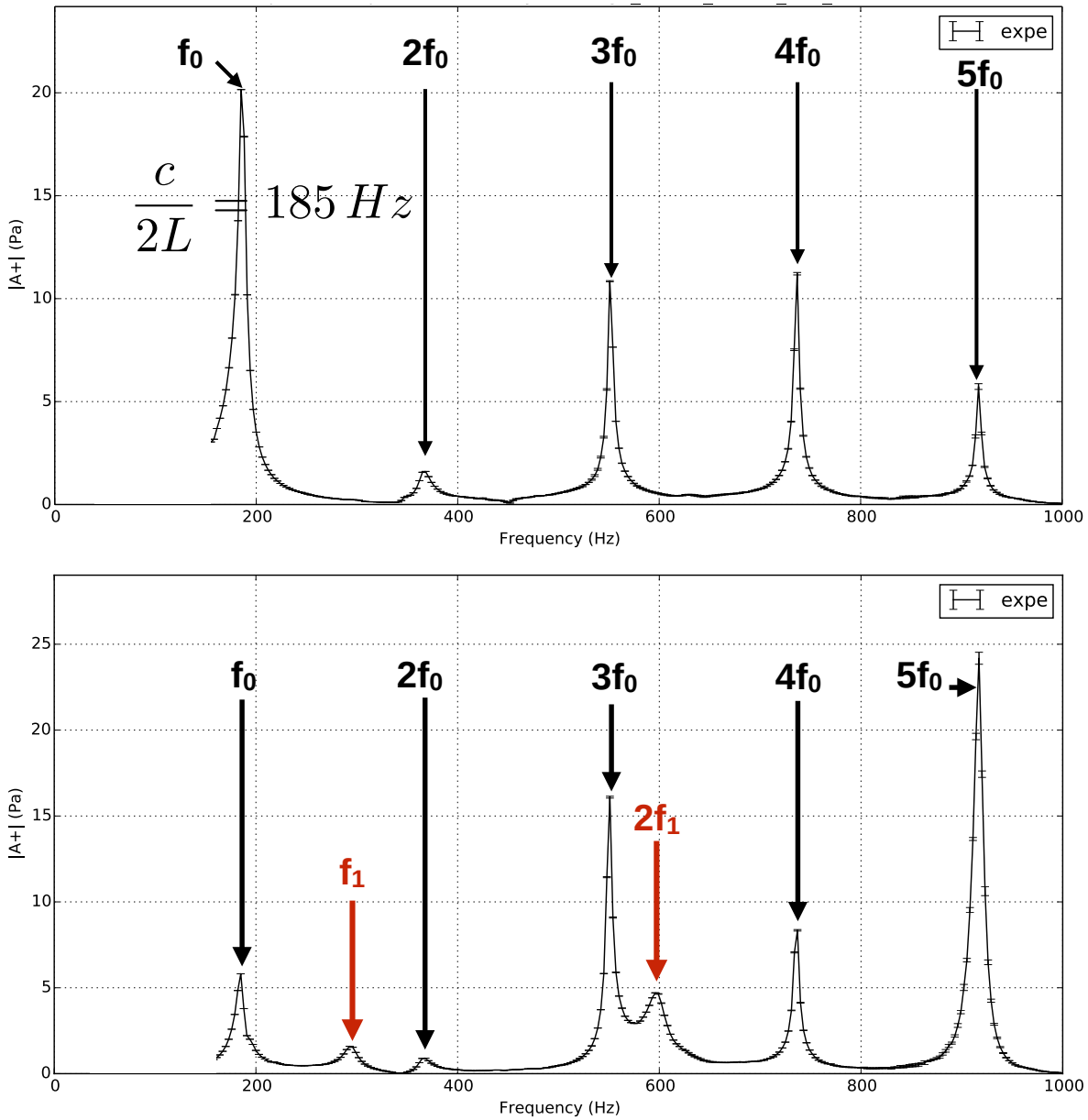

Figure B.2: acoustic wave amplitude in the duct 1 in the short configuration (up, $L_i = 8\ cm$) and the long configuration (bottom, $L_i = 50\ cm$). Error bars represent the uncertainty on the acoustic wave amplitude. The experiment is forced harmonically with the loudspeaker of Fig. B.1.

The numerical resolution of the ROM with Rootlocker provide results in excellent agreement with the experiment. The agreement is perfect for the half wave $f_0 = c/(2L)$ family of mode. The next family of modes observed (f_1) seems to depend on the connection duct length L_i: they disappear when the junction is shortened. Finally, a last mode, called f_{Helm} is associated to the Helmholtz mode [11] of the system formed by the loudspeaker casing and the connection duct:

$$f_{\text{H}} = \frac{c}{2\pi} \quad \overline{\frac{S_i}{L_i V_B}} \tag{B.4.1}$$

where $V_B = S_B L_B$ is the volume of the loudspeaker casing. The corresponding frequencies are $f_{\text{H}}^{\text{short}} = 74$

	long		short	
	$L_i = 50\ cm$		$L_i = 8\ cm$	
name	f_{xp}	f_{ROM}	f_{xp}	f_{ROM}
f_{Helm}	-	26	-	66
f_0	185	183	185	182
f_1	294	315	x	x
$2f_0$	365	366	368	366
$3f_0$	551	550	551	549
$2f_1$	596	627	x	x
$3f_0$	737	733	737	733
$4f_0$	917	917	917	916
$3f_1$	917 ?	939	x	x

Table B.2: Summary of the acoustic modes $[Hz]$ obtained in the two configurations. The symbol – means that the measurement was not performed at this frequency while the symbol x means that the mode was not observed.

Hz for the short junction and $f_{\text{H}}^{\text{long}} = 31\ Hz$ for the long one. These results are in good agreement with the modes obtained by the ROM resolution (66 and 26 Hz) displayed in table B.2.

Finally, a parametric study, as described in section 2.6, is performed for $L_i \in [0.022 : 0.6]\,m$. Figure B.3 shows that for a given length L_i, the PREINTRIG modes (f_0 family) but also others are expected. Below $L_i^c = 18\ cm$, only the Helmholtz and the f_0 family modes are present. This situation is suitable for an acoustic study of the main duct: except the first mode, which is predicted by the Helmholtz equation B.4.1, the only modes observed are the one of the main duct, unperturbed by the loudspeaker system.

However, with a longer intermediate duct ($L_i > 20\ cm$), other parasite modes are observed. These modes appear for both high frequencies f and large length L_i. By taking a closer look at equation B.2.16, one observes that the intermediate length L_i only appear in an non-dimensioned form: $L_i\omega/c$ and the parametric study shows that this parameter control the coupling between the two families of modes f_0 and f_1. Concerning the design of a lateral loudspeaker system which does not perturb the main acoustic modes , the following conclusions arise:

Design of a lateral loudspeaker system

- An optimal lateral loudspeaker system should not modify the acoustic modes of the main system.
- ROMs can easily be established for such systems and the present study demonstrates that the agreement with experimental measurements is very good.
- This study also proves that the length L_i of the intermediate duct, which link the main chamber to the loudspeaker casing, controls the coupling of the acoustic modes: When this parameter is small ($\omega L_i/c \quad 1$), the modes of the chamber and the loudspeaker do not mix.
- The frequency of the Helmholtz mode occurring at low frequency can be predicted by a simple model (equation B.4.1).

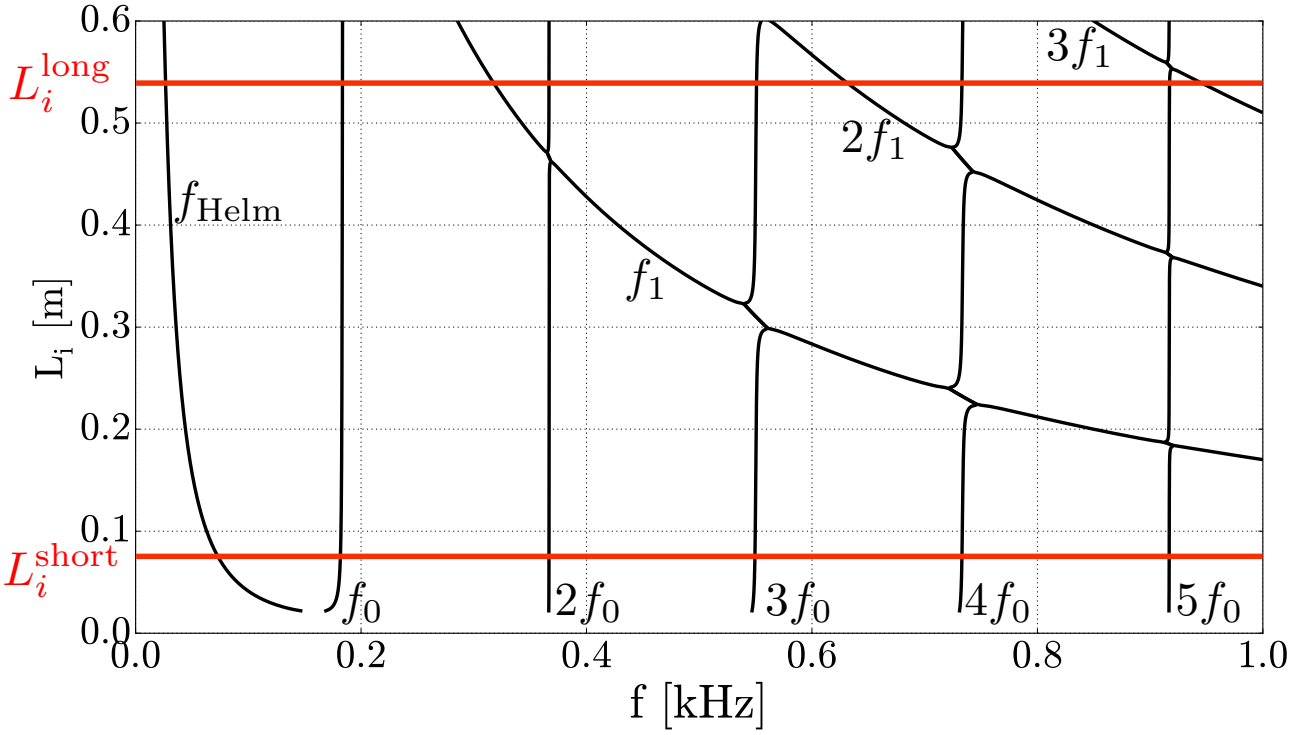

Figure B.3: Parametric study realized with RootLocker (see chapter 2). The intermediate duct size L_i is varied from 22 up to 600 mm and several families of modes are denoted (black solid lines).

Appendix C

Application of the viscous dissipation QOI Φ to compressible flows

The objective of this appendix is to demonstrate that the viscous dissipation term Φ which has been identified in incompressible flows is still a good mesh refinement sensor in compressible flows. Even in low Mach number flows, compressibility effects can be observed. For instance, in an isothermal expansion, pressure and density variations are proportional, as a consequence, in mechanism leading to pressure drop will also cause a density fluctuation.

The kinetic energy equation analogous to equation 4.1.1 for compressible flows writes:

$$\frac{\partial E_c}{\partial t} + \frac{\partial}{\partial x_j}\left(u_j\left(E_c + P\right)\right) - \underbrace{P\frac{\partial u_j}{\partial x_j}}_{\text{Pressure dilatation}} = \frac{\partial\left(\tau_{ij}u_i\right)}{\partial x_j} + \tau_{ij}\frac{\partial u_i}{\partial x_j} \tag{C.0.1}$$

where a new pressure dilatation term is introduced. Similarly to what has been done in chapter 4, equation C.0.1 is integrated over a control volume delimited by an inlet, outlet and non-moving walls:

$$\underbrace{\int_\Sigma P_t u_i n_i d\sigma}_{\alpha} + \underbrace{\int_\Delta P\frac{\partial u_j}{\partial x_j}dV}_{\beta} = \int_\Delta \Phi dV \tag{C.0.2}$$

For incompressible flows, it has been shown in chapter 4 that the pressure drop is expressed in the term α which reduces to $Q_v\Delta P_t$. This term can be calculated in the context of isothermal compressible flows[1]. One may combine the mass conservation ($[\rho u] = 0$) equation with the real gas relation ($P \quad \rho$) to show the the product of pressure and volume flow rate is conserved: $[PQ_v]_{\text{outlet}} = [PQ_v]_{\text{inlet}}$. As a consequence, the term α is equal to zero in the case of isothermal compressible flows.

Similarly, it is possible to show that β approximately reduces to $Q_v\Delta P$ for an isothermal compressible flow. As a consequence, equation C.0.2 shows that the viscous dissipation term is responsible for pressure drop in both compressible and incompressible flows, although the mechanisms are sightly different.

[1]The flows simulated in chapter4 across both the diaphragm and the swirl injector have been reported to be quasi-isothermal with $\Delta T/T \quad \Delta P\ P$

Appendix D

Microphone spacing and acoustic forcing in PREINTRIG

This appendix deals with two important issues concerning the multi-microphones method used to measure acoustic two-port matrices.

D.1 Microphone spacing

The choice of the locations of the pressure taps is of primary importance. Singularities may occur when the distance between the microphones is a multiple of the half acoustic wavelength (see [21]). In this case, all microphones measure the same acoustic pressure (with the same or opposite phase):

$$e^{ik(x+p\lambda/2)} = (-1)^p e^{ikx} \ , \ p \in \mathbb{Z} \tag{D.1.1}$$

as a consequence, the matrix defined in equation 5.1.5 is constituted of co-linear line vectors and is thus ill-conditioned. Best results are obtained by ensuring that the minimal distance between two microphones is lower than the half of the lowest acoustic wavelength considered. In chapter 5, this inequality is verified for $\Delta z_{\text{mic}} < c/(2f_{\text{max}}) \approx 0.15$ m. In practical, a value of $\Delta z_{\text{min}} = 0.04$ m has been retained. Jang et al [171] recommended an equidistant spacing for the microphones in order to lower the uncertainties. However, with only three microphones at each sides of the ACE, it was preferred to use a non equidistant spacing which is adapted for low frequencies (long wavelengths) as well as high frequencies (short wavelengths): Abom et al [260] recommended that the spacing between two microphone was roughly equal to $\Delta z = \lambda/4$ to reduce the uncertainties.

D.2 Acoustic forcing

The four configurations exhibited in figure 3.10 are associated with quasi-reflective acoustic boundary conditions. The loudspeaker, which imposes an acoustic velocity, acts like a wall, and both opened and closed end are almost fully reflective. The sound level inside of the ducts is then greatly modified as the frequency crosses one of the multiple acoustic modes of the rig. Two solutions exist to maintain a quasi-constant sound level in the ducts:

1. Using an absorbing media such as a muffler at the end of the downstream duct to lower the modulus of the end reflection coefficient. This can damp the acoustic modes of the configuration and lower the variations of sound level as done by Holmberg et al [175].

2. Fixing the sound level at a given reference microphone M_{REF} by adapting the voltage amplitude transmitted to the loudspeaker as described by Scarpato et al [25].

The second solution has been chosen in this manuscript as it allows to use various boundary conditions at the outlet (opened or closed) and thus increase the number of independent states used to reconstruct the two-port matrix.

Appendix E

Suppression of pressure and velocity oscillations

As mentioned in section 6.2, velocity but also pressure spurious oscillations were observed in the vicinity of walls hotter than the surrounding flow. Using hybrid meshes helped to damp the velocity oscillations which occurred in regions where the topology of the unstructured mesh changed. Numerical pressure oscillations are observed in Fig. E.1 close to the downstream face of the bluff-bodies. The associated wavelength scales with the grid resolution: This phenomenon is clearly a numerical artefact. Multiple possibilities have been investigated to solve this problem. Among them, the use of NSCBC [194] boundary conditions for the isothermal cylinder wall (WALL_WAVE_NOSLIP_ISOT) completely damped the oscillations.

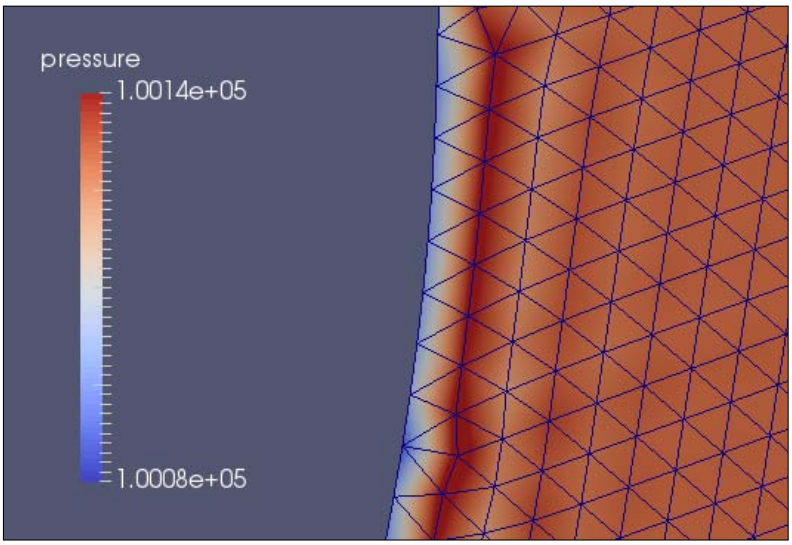

Figure E.1: Pressure oscillations close to the cylinder boundary.

Both heat loss and iso-thermal boundary conditions are suitable for AVBP/AVTP coupling. In the case of heat loss BCs (WALL_NOSLIP_LOSS), the choice of the thermal resistance is of primordial importance: this parameter must be lower than any other thermal resistance encountered in the solid region. Iso-thermal (WALL_NOSLIP_ISOT) boundary conditions act in a different way: the temperature is directly imposed so that the mass conservation equation might be violated. Post processing of the simulations showed that less than 0.1% of the mass flow is lost through the iso-thermal boundary condition.

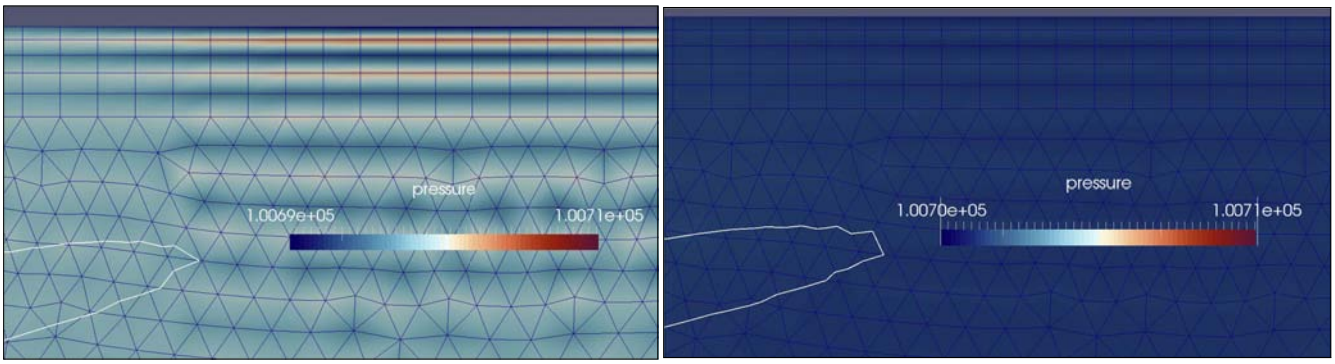

Figure E.2: Influence of the fourth order artificial viscosity over pressure oscillations. The flame is represented by an iso-contour of heat release rate. Left: $Smu_4 = 4\,10^{-4}$ and $\Delta P \approx 25\ Pa$. Right: $Smu_4 = 0$ and $\Delta P \approx 0\ Pa$.

Pressure oscillations have also been reported in the case of the flame/wall interaction encountered in chapter8. However, switching between iso-thermal NSCBC and heat loss BCs did not solve the problem. It appeared that the amplitude of these pressure wiggles was linked to the strength of the fourth order numerical dissipation term [187]. This term is dedicated to damp numerical oscillations that may occur in very low dissipative solvers such as AVBP. However, in the present simulations, decreasing the fourth order dissipation reduced the amplitude of the pressure oscillations as shown in Fig. E.2. In the second case, the artificial viscosity was removed ($Smu_4 = 0$) and the pressure wiggles completely disappeared. However, the simulation crashed after 1 ms elsewhere close to the inlet probably because of a numerical instability. As a consequence, a compromise was need between global stability of the reacting flow and pressure wiggles. The value of $Smu_4 = 4\,10^{-4}$ was retained in all simulations.

Finally, one may observe in Fig. E.2 that the flame front is not affected by the pressure wiggles. These oscillations do not propagate nor interact with the flow.

Appendix F

Continuous and discrete approaches for acoustic propagation in non homogeneous media

The objective of this appendix is to compare both continuous and discrete approaches for the passive (flame/acoustic coupling is not considered here) propagation of acoustic waves in a duct with a constant gradient of temperature. The analytical approach is first briefly recalled here in section F.1 Second, a test case is used to compare both approaches in section F.2.

F.1 Analytical two-port matrix for a linear temperature profile

In this section, we provide a brief overview of the analytical two-port representation derived by Sujith et al [256]. Both velocity u and pressure p acoustic fields can be expressed by using Bessel functions of first (J_0, J_1) and second (Y_0, Y_1) order:

$$p = (c_1 J_0(s) + c_2 Y_0(s)) \tag{F.1.1}$$

$$u = (c_1 J_1(s) + c_2 Y_1(s)) \frac{\epsilon}{i\rho c(\bar{T})} \tag{F.1.2}$$

where c_1, c_2 are two constant, $\epsilon = \text{sign}\,(m = \partial T/\partial z)$ and s is function of the mean temperature field:

$$s(T(z)) = \frac{2\omega}{m} \quad \overline{\frac{\bar{T}(z)}{\gamma \mathrm{r}}} \tag{F.1.3}$$

where m is the gradient of mean temperature and $\mathrm{r} = R/W = 287\ J.K^{-1}.Kg^{-1}$ the reduced perfect gas constant. Equations F.1.1 and F.1.2 can be recast into the two-port formalism:

$$\begin{pmatrix} A_{\mathrm{f}}^{+} \\ A_{\mathrm{f}}^{-} \end{pmatrix} = \underbrace{M_{T_b} M_{T_u}^{-1}}_{\mathrm{T_{cont}}} \begin{pmatrix} A_0^{+} \\ A_0^{-} \end{pmatrix} \tag{F.1.4}$$

where:

$$M_T = \begin{pmatrix} [J_0(s) - i\epsilon J_1(s)] & [Y_0(s) - i\epsilon Y_1(s)] \\ [J_0(s) + i\epsilon J_1(s)] & [Y_0(s) + i\epsilon Y_1(s)] \end{pmatrix} \tag{F.1.5}$$

Although exact, this transfer matrix can be approximated as done in chapter 9 in order to avoid the use of Bessel functions. The original geometry is discretized into n smaller regions, in which the mean

temperature $T_i\,, i \in [1, n]$ is supposed uniform as shown in Fig. 9.5. These two approaches are compared in the following section.

F.2 Validation of the discrete approach

Sujith et al [256] provided a test case constituted by a duct ($L = 4\ m$) with a close inlet ($u = 0$, $R_{\text{in}} = 1$) and an open outlet ($p = 0$, $R_{\text{out}} = -1$), in which a linear temperature axial distribution was imposed: $T_{in} = 1100\ K$ and $T_{out} = 300\ K$. Acoustic modes provided by a Helmholtz solver were compared to the solution of a ROM based on the continuous transfer matrix T_{cont} (see equation F.1.4) and an excellent agreement was obtained.

Here, we compare the results of the continuous approach developed by Sujith et al [256] with a ROM based on the discrete transfer matrix T_{disc} defined in equation 9.1.10. The two ROMs are recalled here for the sake of clarity:

$$\det\left(\mathrm{T}_{\text{cont,dict}}\begin{pmatrix}R_{\text{in}}\\1\end{pmatrix},\begin{pmatrix}1\\R_{\text{out}}\end{pmatrix}\right) = 0 \tag{F.2.1}$$

In the discrete approach, one can choose the number n of discrete units used to reproduce the temperature profile as shown in Fig. 9.5. The frequencies of the five first modes solutions of equation F.2.1 are displayed in table F.1.

Continuous	$n = 2$	$n = 5$	$n = 10$
27.7	30.9	29.7	27.6
93.7	97.4	97.1	94.6
157.5	160.1	154.7	158.5
221.0	224.9	221.9	221.4
284.5	289.8	288.2	284.2

Table F.1: Frequencies $[Hz]$ of the five first acoustic quarter waves modes in the presence of an axial uniform temperature gradient. Both continuous and discrete approaches provide good results when $n > 5$

An excellent agreement is obtained for $n = 10$ which means that both discrete and continuous approaches are equivalent as long as the temperature variation is sufficiently discretized.

Bibliography

[1] R. F. Sawyer, Science based policy for adressing energy and environmental problems, Proc. Combust. Inst. 32 (2009) 45 56.

[2] J. Penner, D. Lister, D. Griggs, D. Dokken, M. McFarland, Aviation and the global atmosphere a special report of ipcc working groups i and iii. intergovernmental panel on climate change (1999).

[3] N. Docquier, S. Candel, Combustion control and sensors: a review, Progress in energy and combustion science 28 (2) (2002) 107 150.

[4] L. Rayleigh, The explanation of certain acoustic phenomena, Nature July 18 (1878) 319 321.

[5] F. Nicoud, T. Poinsot, Thermoacoustic instabilities: should the rayleigh criterion be extended to include entropy changes ?, Combust. Flame 142 (2005) 153 159.

[6] D. Durox, T. Schuller, N. Noiray, S. Candel, Experimental analysis of nonlinear flame transfer functions for different flame geometries, Proc. Combust. Inst. 32 (1) (2009) 1391 1398.

[7] M. J. Brear, F. Nicoud, M. Talei, A. Giauque, E. R. Hawkes, Disturbance energy transport and sound production in gaseous combustion, Journal of Fluid Mechanics 707 (2012) 53 73.

[8] M. Myers, Transport of energy by disturbances in arbitrary steady flows, J. Fluid Mech. 226 (1991) 383 400.

[9] S. Candel, Combustion dynamics and control: progress and challenges, Proc. Combust. Inst. 29 (1) (2002) 1 28.

[10] T. C. Lieuwen, Unsteady combustor physics, Cambridge University Press, 2012.

[11] T. Poinsot, D. Veynante, Theoretical and Numerical Combustion, Third Edition (www.cerfacs.fr/elearning), 2011.

[12] D. Mejia, Wall-temperature effects on flame response to acoustic oscillations, Ph.D. thesis, Université de Toulouse (2014).

[13] D. Durox, T. Schuller, N. Noiray, A. L. Birbaud, S. Candel, Rayleigh criterion and acoustic energy balance in unconfined self-sustained oscillating flames, Combustion and Flame 156 (1) (2009) 106 119.

[14] a. Selamet, Acoustic Attenuation Performance of Circular Expansion Chambers With Extended Inlet/Outlet, Journal of Sound and Vibration 223 (2) (1999) 197 212.

[15] M. Atig, J. P. Dalmont, J. Gilbert, Termination impedance of open-ended cylindrical tubes at high sound pressure level, Comptes Rendus - Mecanique 332 (4) (2004) 299 304.

[16] G. Searby, A. Nicole, G. Ordonneau, M. Habiballah, A Lightweight hybrid method to estimate the linear acoustic damping of arbitrarily complex geometries, 3rd European Conference for Aerospace Sciences (EUCASS).

[17] D. W. Bechert, Sound absorption caused by vorticity shedding, demonstrated with a jet flow, AIAA, Aeroacoustics Conference, 5th, Seattle, Wash., Mar. 12-14, 1979, 11 p.

[18] M. S. Howe, Acoustics of Fluid-Structure Interaction, Cambridge University Press, 1998.

[19] C. K. W. Tam, H. Ju, M. G. Jones, W. R. Watson, T. L. Parrott, A computational and experimental study of slit resonators, Journal of Sound and Vibration 284 (3-5) (2005) 947 984.

[20] M. S. Howe, On the theory of unsteady high reynolds number flow through a circular aperture, Proc. R. Soc. Lond. A , Mathematical and Physical Sciences 366 (1725) (1979) 205 223.

[21] A. Fischer, C. Hirsch, T. Sattelmayer, Comparison of multi-microphone transfer matrix measurements with acoustic network models of swirl burners, J. Sound Vib. 298 (1-2) (2006) 73 83.

[22] A. Gentemann, A. Fischer, S. Evesque, W. Polifke, Acoustic transfer matrix reconstruction and analysis for ducts with sudden change of area, in: 9th AIAA/CEAS Aeroacoustics Conference and Exhibit, 2003, p. 3142.

[23] S. Foller, W. Polifke, Identification of aero-acoustic scattering matrices from large eddy simulation. Application to a sudden area expansion of a duct, Journal of Sound and Vibration 331 (13) (2012) 3096 3113.

[24] S. W. Rienstra, A. Hirschberg, An introduction to acoustics, Eindhoven University of Technology, 2003.

[25] A. Scarpato, N. Tran, S. Ducruix, T. Schuller, Modeling the damping properties of perforated screens traversed by a bias flow and backed by a cavity at low Strouhal number, Journal of Sound and Vibration 331 (2) (2012) 276 290.

[26] D. Durox, T. Schuller, N. Noiray, A. L. Birbaud, S. Candel, Rayleigh criterion and acoustic energy balance in unconfined self-sustained oscillating flames, Combustion and Flame 156 (1) (2009) 106 119.

[27] J. H. Lu, O. Ezekoye, R. Greif, F. Sawyer, Unsteady heat transfer during side wall quenching of a laminar flame, in: 23rd Symp. (Int.) on Combustion, The Combustion Institute, Pittsburgh, 1990, pp. 441 446.

[28] G. Bruneaux, T. Poinsot, J. H. Ferziger, Premixed flame-wall interaction in a turbulent channel flow: budget for the flame surface density evolution equation and modelling, J. Fluid Mech. 349 (1997) 191 219.

[29] G. Bruneaux, K. Akselvoll, T. Poinsot, J. Ferziger, Flame-wall interaction in a turbulent channel flow, Combust. Flame 107 (1/2) (1996) 27 44.

[30] I. Wichman, G. Bruneaux, Head on quenching of a premixed flame by a cold wall, Combust. Flame 103 (4) (1995) 296 310.

[31] K. Mahesh, G. Constantinescu, S. Apte, G. Iaccarino, F. Ham, P. Moin, Large eddy simulation of reacting turbulent flows in complex geometries, ASME J. Appl. Mech. 73 (2006) 374 381.

[32] P. Schmitt, T. Poinsot, B. Schuermans, K. P. Geigle, Large-eddy simulation and experimental study of heat transfer, nitric oxide emissions and combustion instability in a swirled turbulent high-pressure burner, J. Fluid Mech. 570 (2007) 17 46.

[33] G. Staffelbach, L. Gicquel, G. Boudier, T. Poinsot, Large eddy simulation of self-excited azimuthal modes in annular combustors, Proc. Combust. Inst. 32 (2009) 2909 2916.

[34] P. Wolf, G. Staffelbach, A. Roux, L. Gicquel, T. Poinsot, V. Moureau, Massively parallel LES of azimuthal thermo-acoustic instabilities in annular gas turbines, C. R. Acad. Sci. Mécanique 337 (6-7) (2009) 385 394.

[35] K. N. C. Bray, Turbulent flows with premixed reactants in turbulent reacting flows, Vol. 44 of Topics in applied physics, Springer Verlag, New York, 1980.

[36] C. D. Pierce, P. Moin, Progress-variable approach for large eddy simulation of non-premixed turbulent combustion, J. Fluid Mech. 504 (2004) 73 97.

[37] B. Fiorina, O. Gicquel, D. Veynante, Turbulent flame simulation taking advantage of tabulated chemistry self-similar properties, Proc. Combust. Inst. 32 (2009) 1687 1694.

[38] G. Kuenne, A. Ketelheun, J. Janicka, LES modeling of premixed combustion using a thickened flame approach coupled with FGM tabulated chemistry, Combust. Flame 158 (9) (2011) 1750 1767.

[39] R. Mercier, Turbulent combustion modeling for large eddy simulation of non-adiabatic stratified flames, Ph.D. thesis, Ecole Centrale Paris (2015).

[40] F. Duchaine, T. Poinsot, Sensitivity of flame transfer functions of laminar flames, in: N. A. U. Center for Turbulence Research (Ed.), Proc. of the Summer Program , 2011, pp. 250 258.

[41] F. Duchaine, F. Boudy, D. Durox, T. Poinsot, Sensitivity analysis of transfer functions of laminar flames, Combustion and Flame 158 (12) (2011) 2384 2394.

[42] K. S. Kedia, A. F. Ghoniem, The anchoring mechanism of a bluff-body stabilized laminar premixed flame, Combust. Flame 161 (9) (2014) 2327 2339.

[43] T. F. Guiberti, D. Durox, P. Scouflaire, T. Schuller, Impact of heat loss and hydrogen enrichment on the shape of confined swirling flames, Proceedings of the Combustion Institute 35 (2) (2015) 1385 1392.

[44] A. Sengissen, J. F. V. Kampen, R. Huls, G. Stoffels, J. B. W. Kok, T. Poinsot, LES and experimental studies of cold and reacting flows in a swirled partially premixed burner with and without fuel modulation, Combust. Flame 150 (2007) 40 53.

[45] T. Alshaalan, C. J. Rutland, Turbulence, scalar transport and reaction rates in flame wall interaction, Proc. Combust. Inst. 27 (1998) 793 799.

[46] A. Gruber, R. Sankaran, E. R. Hawkes, J. Chen, Turbulent flame wall interaction: a direct numerical simulation study, J. Fluid Mech. 658 (2010) 5 32.

[47] C. K. Westbrook, A. A. Adamczyk, G. A. Lavoie, A numerical study of laminar flame wall quenching., Combust. Flame 40 (1981) 81 99.

[48] P. Popp, M. Baum, An analysis of wall heat fluxes, reaction mechanisms and unburnt hydrocarbons during the head-on quenching of a laminar methane flame, Combust. Flame 108 (3) (1997) 327 348.

[49] K. Kedia, H. Altay, A. Ghoniem, Impact of flame-wall interaction on premixed flame dynamics and transfer function characteristics, Proc. Combust. Inst. 33 (2011) 1113 1120.

[50] K. S. Kedia, A. F. Ghoniem, An analytical model for the prediction of the dynamic response of premixed flames stabilized on a heat-conducting perforated plate, Proc. Combust. Inst. 34 (1) (2013) 921 928.

[51] A. Cuquel, D. Durox, T. Schuller, Impact of flame base dynamics on the nonlinear frequency response of conical flames, C. R. Acad. Sci. Mecanique 341 (2013) 171 180.

[52] D. Mejia, L. Selle, R. Bazile, T. Poinsot, Wall-temperature effects on flame response to acoustic oscillations, Proc. Combust. Inst. 35 (3201-3208) (2014) 3.

[53] R. Glav, M. Åbom, a General Formalism for Analyzing Acoustic 2-Port Networks, J. Sound Vib. 202 (5) (1997) 739 747.

[54] J. Kopitz, W. Polifke, CFD-based application of the Nyquist criterion to thermo-acoustic instabilities, Journal of Computational Physics 227 (14) (2008) 6754 6778.

[55] T. Sattelmayer, W. Polifke, Assessment of methods for the computation of the linear stability of combustors, Combustion Science and Technology 175 (3) (2003) 453 476.

[56] J.-F. Parmentier, P. Salas, P. Wolf, G. Staffelbach, F. Nicoud, T. Poinsot, A simple analytical model to study and control azimuthal instabilities in annular combustion chambers, Combust. Flame 159 (7) (2012) 2374 2387.

[57] M. Bauerheim, J.-F. Parmentier, P. Salas, F. Nicoud, T. Poinsot, An analytical model for azimuthal thermoacoustic modes in an annular chamber fed by an annular plenum, Combust. Flame 161 (5) (2014) 1374 1389.

[58] T. Schuller, D. Durox, S. Candel, Self-induced combustion oscillations of laminar premixed flames stabilized on annular burners, Combust. Flame 135 (2003) 525 537.

[59] J. N. Lyness, Numerical algorithms based on the theory of complex variable, Proceedings of the 1967 22nd national conference on - (1967) 125 133.

[60] S. Mendez, J. Eldredge, Acoustic modeling of perforated plates with bias flow for large-eddy simulations, J. Comput. Phys. 228 (13) (2009) 4757 4772.

[61] A. Scarpato, S. Ducruix, T. Schuller, Optimal and off-design operations of acoustic dampers using perforated plates backed by a cavity, J. Sound Vib. (2013) 1 20.

[62] L. Y. M. Gicquel, G. Staffelbach, T. Poinsot, Large Eddy Simulations of gaseous flames in gas turbine combustion chambers, Prog. Energy Comb. Sci. 38 (6) (2012) 782 817.

[63] M. Philip, M. Boileau, R. Vicquelin, T. Schmitt, D. Durox, J.-F. Bourgouin, S. Candel, Simulation of the Ignition Process in an Annular Multiple-Injector Combustor and Comparison With Experiments, J. Eng. Gas Turb. and Power 137 (3) (2015) 031501 9.

[64] V. Moureau, P. Domingo, L. Vervisch, From large-eddy simulation to direct numerical simulation of a lean premixed swirl flame: Filtered laminar flame-pdf modeling, Combust. Flame 158 (7) (2011) 1340 1357.

[65] F. Ni, M. Miguel-Brebion, F. Nicoud, T. Poinsot, Accounting for acoustic damping in a helmholtz solver, AIAA Journal (2016) 1 16.

[66] D. Mejia, M. Bauerheim, P. Xavier, B. Ferret, B. Selle, T. Poinsot, Stabilization of a premixed laminar flame on a rotating cylinder, Proceedings of the Combustion Institute (2016).

[67] S. Candel, D. Durox, T. Schuller, N. Darabiha, L. Hakim, T. Schmitt, Advances in combustion and propulsion applications, European Journal of Mechanics - B/Fluids 40 (0) (2013) 87 106.

[68] P. Wolf, R. Balakrishnan, G. Staffelbach, L. Gicquel, T. Poinsot, Using LES to study reacting flows and instabilities in annular combustion chambers, Flow, Turb. and Combustion 88 (2012) 191 206.

[69] C. Pankiewitz, A. Fischer, C. Hirsch, T. Sattelmayer, Computation of transfer matrices for gas turbine combustors including acoustics/flame interaction, in: 9th AIAA/CEAS Aeroacoustics Conference and Exhibit, 2003, p. 3295.

[70] C. F. Silva, F. Nicoud, T. Schuller, D. Durox, S. Candel, Combining a Helmholtz solver with the flame describing function to assess combustion instability in a premixed swirled combustor, Combust. Flame 160 (9) (2013) 1743 1754.

[71] E. Courtine, L. Selle, F. Nicoud, W. Polifke, C. Silva, M. Bauerheim, T. Poinsot, Causality and intrinsic thermoacoustic instability modes, in: Proceedings of the Summer Program, Center for Turbulence Research, Stanford University, 2014, pp. 169 178.

[72] J. Hirschfelder, C. Curtis, B. Bird, Molecular Theory of Gases and Liquids, 1954th Edition, John Wiley & Sons, 1954.

[73] C. Bailly, C. Bogey, S. Candel, Modelling of sound generation by turbulent reacting flows, International Journal of Aeroacoustics 9 (4) (2010) 461 490.

[74] G. Searby, A. Nicole, M. Habiballah, E. Laroche, Prediction of the efficiency of acoustic damping cavities, J. Prop. Power 24 (3) (2008) 515 523.

[75] K. Wieczorek, Numerical study of mach number effects on combustion instability, Ph.D. thesis, Université Montpellier II - Ecole Doctorale ISS - Mathématiques et Modélisation (2010).

[76] M. Bauerheim, F. Nicoud, T. Poinsot, Theoretical analysis of the mass balance equation through a flame at zero and non-zero mach numbers, Combust. Flame 162 (1) (2015) 60 67.

[77] L. S. Chen, S. Bomberg, W. Polifke, Propagation and Generation of Acoustic and Entropy Waves Across a Moving Flame Front, Combust. Flame 166 (2016) 170 180.

[78] L. Crocco, Aspects of combustion instability in liquid propellant rocket motors. part II., J. American Rocket Society 22 (1952) 7 16.

[79] D. Durox, T. Schuller, S. Candel, Combustion dynamics of inverted conical flames, Proc. Combust. Inst. 30 (2) (2005) 1717 1724.

[80] K. Truffin, T. Poinsot, Comparison and extension of methods for acoustic identification of burners, Combust. Flame 142 (4) (2005) 388 400.

[81] T. Schuller, D. Durox, S. Candel, A unified model for the prediction of laminar flame transfer functions: comparisons between conical and v-flames dynamics, Combust. Flame 134 (2003) 21 34.

[82] W. Polifke, A. Gentemann, Order and realizability of impulse response filters for accurate identification of acoustic multi-ports from transient cfd, Int. J. of Acoustics and Vibration 9 (3) (2004) 139 148.

[83] K. S. Kedia, A. F. Ghoniem, An analytical model for the prediction of the dynamic response of premixed flames stabilized on a heat-conducting perforated plate, Proc. Combust. Inst. 34 (1) (2013) 921 928.

[84] F. Duchaine, F. Boudy, D. Durox, T. Poinsot, Sensitivity analysis of transfer functions of laminar flames, Combust. Flame 158 (12) (2011) 2384 2394.

[85] W. Polifke, C. Lawn, On the low-frequency limit of flame transfer functions, Combustion and flame 151 (3) (2007) 437 451.

[86] M. Bauerheim, F. Nicoud, T. Poinsot, Theoretical analysis of the mass balance equation through a flame at zero and non-zero mach numbers, Combust. Flame 162 (1) (2015) 60 67.

[87] C. O. Paschereit, W. Polifke, B. Schuermans, O. Mattson, Measurement of transfer matrices and source terms of premixed flames, J. Eng. Gas Turb. and Power 124 (2002) 239 247.

[88] M. S. Howe, The generation of sound by aerodynamic sources in an homogeneous steady flow, J. Fluid Mech. 67 (3) (1975) 597 610.

[89] M. Hoeijmakers, Flame-acoustic coupling in combustion instabilities, Ph.D. thesis (2013).

[90] A. Ghani, F. Nicoud, T. Poinsot, Avsp active flame: Tool descriptions, Technical report, CERFACS.

[91] F. Nicoud, L. Benoit, C. Sensiau, T. Poinsot, Acoustic modes in combustors with complex impedances and multidimensional active flames, AIAA Journal 45 (2007) 426 441.

[92] S. Camporeale, B. Fortunato, G. Campa, A finite element method for three-dimensional analysis of thermo-acoustic combustion instability, J. Eng. Gas Turb. and Power 133 (1).

[93] P. Salas, Aspects numériques et physiques des instabilités de combustion dans les chambres de combustion annulaires, Ph.D. thesis, Université Bordeaux - INRIA (2013).

[94] L. M. Delves, J. N. Lyness, A numerical method for locating the zeros of an analytic function, Mathematics of Computation 21 (100) (1967) 543 560.

[95] M. Dellnitz, O. Schutze, Q. Zheng, Locating all the zeros of an analytic function in one complex variable, Journal of Computational and Applied Mathematics 138 (2) (2002) 325 333.

[96] T. Johnson, W. Tucker, Enclosing all zeros of an analytic function A rigorous approach, Journal of Computational and Applied Mathematics 228 (1) (2009) 418 423.

[97] T. Johnson, W. Tucker, On a fast and accurate method to enclose all zeros of an analytic function on a triangulated domain, Proceedings of PARA-2008, to appear in Lecture Notes in Computer Science 6126 (2009) 6127.

[98] T. Suzuki, T. Suzuki, A modification of the numerical integration error method for the zero-finding problem of an analytic function, Japan Journal of Industrial and Applied Mathematics 22 (3) (2005) 353 365.

[99] K. H. Ko, T. Sakkalis, N. M. Patrikalakis, A reliable algorithm for computing the topological degree of a mapping in R2, Applied Mathematics and Computation 196 (2008) 666 678.

[100] V. Semenov, Method for the Calculation of All Non-Multiple Zeros of an Analytic Function, Comp. Methods in Applied Mathematics 11 (1) (2011) 67 74.

[101] D. Kalman, A matrix proof of newton s identities, Mathematics Magazine 73 (4) (2000) pp. 313 315.

[102] F. Jedrzejewski, Introduction aux méthodes numériques, Springer Science & Business Media, 2006.

[103] J. N. Lyness, Notes on the adaptive simpson quadrature routine, J. ACM 16 (3) (1969) 483 495.

[104] T. Parr, The Definitive ANTLR Reference: Building Domain-Specific Languages., The Pragmatic Programmers, 2007.

[105] M. Bartholomew-biggs, S. Brown, B. Christianson, L. Dixon, Automatic differentiation of algorithms, Journal of Computational and Applied Mathematics 124 (2000) 171 190.

[106] M. Bauerheim, M. Cazalens, T. Poinsot, A theoretical study of mean azimuthal flow and asymmetry effects on thermo-acoustic modes in annular combustors, Proc. Combust. Inst. 35 (3) (2015) 3219 3227.

[107] M. A. Jenkins, J. F. Traub, A three-stage variable-shift iteration for polynomial zeros and its relation to generalized rayleigh iteration, Numerische Mathematik 14 (3) (1970) 252 263.

[108] L. Y. M. Gicquel, G. Staffelbach, T. Poinsot, Large eddy simulations of gaseous flames in gas turbine combustion chambers, Prog. Energy Comb. Sci. 38 (6) (2012) 782 817.

[109] M. Zahn, M. Schulze, C. Hirsch, M. Betz, T. Sattelmayer, Frequency domain predictions of acoustic wave propagation and losses in a swirl burner with linearized navier-stokes equations, in: ASME Turbo Expo 2015: Turbine Technical Conference and Exposition, American Society of Mechanical Engineers, 2015.

[110] R. Lacombe, S. Foller, G. Jasor, W. Polifke, Y. Aurégan, P. Moussou, Identification of aeroacoustic scattering matrices from large eddy simulation: Application to whistling orifices in duct, Journal of Sound and Vibration 332 (20) (2013) 5059 5067.

[111] M. Munjal, Acoustics of Ducts and Mufflers, Wiley, 2014.

[112] P. Davies, Practical flow duct acoustics, Journal of Sound and Vibration 124 (1) (1988) 91 115.

[113] A. Pierce, Acoustics: An Introduction to Its Physical Principles and Applications, McGraw-Hill series in mechanical engineering, McGraw-Hill Book Company, 1981.

[114] J. D. Eldredge, A. P. Dowling, The absorption of axial acoustic waves by a perforated liner with bias flow, Journal of Fluid Mechanics 485 (2003) 307 335. doi:10.1017/S0022112003004518.

[115] X. Jing, X. Sun, Effect of Plate Thickness on Impedance of Perforated Plates with Bias Flow, AIAA Journal 38 (9).

[116] T. Luong, M. Howe, R. McGowan, On the Rayleigh conductivity of a bias-flow aperture, Journal of Fluids and Structures 21 (8) (2005) 769 778.

[117] Y. Aurégan, R. Starobinski, Determination of acoustical energy dissipation/production potentiality from the acoustical transfer functions of a multiport, Acta Acustica United with Acustica 85 (6) (1999) 788 792.

[118] S. Malavasi, G. Messa, U. Fratino, A. Pagano, On the pressure losses through perforated plates, Flow measurement and instrumentation 28 (2012) 57 66.

[119] D. Miller, Internal flow systems, 2nd, BHR Information Services, Cranfield, UK.

[120] D. Laera, G. Campa, S. M. Camporeale, E. Bertolotto, S. Rizzo, F. Bonzani, A. Ferrante, A. Saponaro, Modelling of thermoacoustic combustion instabilities phenomena: Application to an experimental test rig, Energy Procedia 45 (2014) 1392 1401.

[121] K. Merkle, Einfluss gleich- und gegensinniger Drehrichtung der Verbrennungsluftstrome auf die Stabilisierung turbulenter Doppeldrall-Diffusionsflammen, Ph.D. thesis, Universitat Fridericiana Karlsruhe (2006).

[122] C. Dapogny, C. Dobrzynski, P. Frey, Three-dimensional adaptive domain remeshing, implicit domain meshing, and applications to free and moving boundary problems, J. Comput. Phys. 262 (2014) 358 378.

[123] N. Syred, A review of oscillation mechanisms and the role of the precessing vortex core (PVC) in swirl combustion systems, Prog. Energ. Combust. 32 (2) (2006) 93 161.

[124] Y. Huang, H.-G. Sung, S.-Y. Hsieh, V. Yang, Large-eddy simulation of combustion dynamics of lean-premixed swirl-stabilized combustor, J. Prop. Power 19 (5) (2003) 782 794.

[125] V. Moureau, P. Domingo, L. Vervisch, From large-eddy simulation to direct numerical simulation of a lean premixed swirl flame: Filtered laminar flame-pdf modeling, Combust. Flame 158 (7) (2011) 1340 1357.

[126] S. Roux, G. Lartigue, T. Poinsot, U. Meier, C. Bérat, Studies of mean and unsteady flow in a swirled combustor using experiments, acoustic analysis and large eddy simulations, Combust. Flame 141 (2005) 40 54.

[127] D. Barré, M. Kraushaar, G. Staffelbach, V. Moureau, L. Y. M. Gicquel, Compressible and low Mach number LES of a swirl experimental burner, CR - Mec. 341 (2013) 277 287.

[128] M. Falese, A study of the effects of bifurcations in swirling flows using Large Eddy Simulation and mesh adaptation, Ph.D. thesis, Université de Toulouse (2013).

[129] H. Choi, P. Moin, Grid-point requirements for large eddy simulation: Chapman s estimates revisited, Physics of Fluids 24 (2012) 011702 5.

[130] G. Boudier, L. Y. M. Gicquel, T. Poinsot, D. Bissières, C. Bérat, Effect of mesh resolution on Large Eddy Simulation of reacting flows in complex geometry combustors, Combust. Flame 155 (1-2) (2008) 196 214.

[131] C. Hertel, J. Frohlich, Error reduction in les via adaptive moving grids, in: Quality and Reliability of Large-Eddy Simulations II, Springer, 2011, pp. 309 318.

[132] P.-J. Frey, F. Alauzet, Anisotropic mesh adaptation for CFD computations, Computer methods in applied mechanics and engineering 194 (48) (2005) 5068 5082.

[133] A. Loseille, A. Dervieux, F. Alauzet, Fully anisotropic goal-oriented mesh adaptation for 3d steady Euler equations, Journal of computational physics 229 (8) (2010) 2866 2897.

[134] M. Rai, D. Anderson, The use of adaptive grids in conjunction with shock capturing methods, in: 5th Computational Fluid Dynamics Conference, 1981, p. 1012.

[135] M. J. Berger, J. Oliger, Adaptive mesh refinement for hyperbolic partial differential equations, J. Comput. Phys. 53 (3) (1984) 484 512.

[136] S. V. Apte, K. Mahesh, P. Moin, J. C. Oefelein, Large-eddy simulation of swirling particle-laden flows in a coaxial-jet combustor, Int. J. Multiphase Flow 29 (8) (2003) 1311 1331.

[137] M. Falese, L. Y. Gicquel, T. Poinsot, LES of bifurcation and hysteresis in confined annular swirling flows, Comput. Fluids 89 (2014) 167 178.

[138] V. Sankaran, S. Menon, Les of spray combustion in swirling flows, J. Turb. 3 (2002) 011.

[139] Y. Huang, V. Yang, Dynamics and stability of lean-premixed swirl-stabilized combustion, Prog. Energy Comb. Sci. 35 (4) (2009) 293 364.

[140] S. M. Mitran, A comparison of adaptive mesh refinement approaches for large eddy simulation, Tech. rep., DTIC Document (2001).

[141] R. Lohner, J. D. Baum, Adaptive h-refinement on 3D unstructured grids for transient problems, Int. J. Numer. Meth. Fluids 14 (12) (1992) 1407 1419.

[142] J. Majewski, J. Rokicki, Anisotropic mesh adaptation in the presence of complex boundaries, in: ADIGMA-A European Initiative on the Development of Adaptive Higher-Order Variational Methods for Aerospace Applications, Springer, 2010, pp. 441 453.

[143] J. Majewski, P. Szaltys, J. Rokicki, Anisotropic adaptation for simulation of high-reynolds number flows past complex 3d geometries, IDIHOM: Industrialization of High-Order Methods-A Top-Down Approach: Results of a Collaborative Research Project Funded by the European Union, 2010-2014 128 (2015) 101.

[144] M. Lombardini, R. Deiterding, Three-dimensional parallel adaptive mesh refinement simulations of shock-driven turbulent mixing in plane and converging geometries, Parallel Computational Fluid Dynamics: Recent Advances and Future Directions (2010) 462.

[145] B. Zhang, T. Wang, C.-G. Gu, Z.-Y. Dai, An adaptive control strategy for proper mesh distribution in large eddy simulation, J. Hydrodyn. Ser. B 22 (6) (2010) 865 870.

[146] P. Benard, G. Balarac, V. Moureau, C. Dobrzynski, G. Lartigue, Y. D Angelo, Mesh adaptation for Large-Eddy Simulations in complex geometries, Int. J. Numer. Meth. Fluids .

[147] A. Bejan, Entropy generation minimization: The new thermodynamics of finite-size devices and finite-time processes, J. Applied Phy. 79 (3) (1996) 1191 1218.

[148] F. Kock, H. Herwig, Entropy production calculation for turbulent shear flows and their implementation in CFD codes, Int. J. Heat Fluid Flow 26 (4) (2005) 672 680.

[149] D. M. McEligot, E. J. Walsh, E. Laurien, P. R. Spalart, Entropy generation in the viscous parts of turbulent boundary layers, J. of Fluids Eng. 130 (6) (2008) 1 12.

[150] I. Prigogine, Time, structure, and fluctuations, Science 201 (4358) (1978) 777 785.

[151] W. HORNE, K. Karamcheti, Extrema principles of entropy production and energy dissipation in fluid mechanics, in: 1st National Fluid Dynamics Conference, 1988, p. 3830.

[152] J. D. Denton, Loss Mechanisms in Turbomachines, J. Turbomach. 115 (1993) 621 656.

[153] P. Lax, Hyperbolic systems of conservation laws ii, Comm. Pure Appl. Math. 10 (4) (1957) 537 566.

[154] S. Osher, S. Chakravarthy, High Resolution Schemes and the Entropy Condition, SIAM J. Num. Anal. 21 (5) (1984) 955 984.

[155] O. Zeman, Dilatation dissipation: the concept and application in modeling compressible mixing layers, Phys. Fluids 2 (1990) 178 188.

[156] P. Sagaut, Large Eddy Simulation for Incompressible Flows, Springer-Science, 1998.

[157] U. Piomelli, Large-Eddy simulation: achievements and challenges, Prog. Aero. Sci. 35 (4) (1999) 335 362.

[158] R. Biswas, R. C. Strawn, Tetrahedral and hexahedral mesh adaptation for CFD problems, App. Num. Math. 26 (1998) 135 151.

[159] T. Schønfeld, M. Rudgyard, Steady and unsteady flow simulations using the hybrid flow solver avbp, AIAA J. 37 (11) (1999) 1378 1385.

[160] L. Selle, G. Lartigue, T. Poinsot, R. Koch, K.-U. Schildmacher, W. Krebs, B. Prade, P. Kaufmann, D. Veynante, Compressible large eddy simulation of turbulent combustion in complex geometry on unstructured meshes, Combust. Flame 137 (4) (2004) 489 505.

[161] O. Colin, M. Rudgyard, Development of high-order Taylor-Galerkin schemes for unsteady calculation, J. Comput. Phys. 162 (2) (2000) 338 371.

[162] T. Poinsot, S. K. Lele, Boundary conditions for direct simulations of compressible viscous flows, J. Comput. Phys. 101 (1) (1992) 104 129.

[163] F. Nicoud, H. Baya Toda, O. Cabrit, S. Bose, J. Lee, Using singular values to build a subgrid-scale model for large eddy simulations, Phys. Fluids 23.

[164] I. Idel Cik, Memento des pertes de charge, Eyrolles, 1969.

[165] F. M. White, Fluid mechanics, in si units (2011).

[166] J. Hunt, A. Wray, P. Moin, Eddies, stream, and convergence zones in turbulent flows, in: Proceedings of the summer program, Center for Turbulence Research, 1988, pp. 193 208.

[167] D. G. Lilley, Swirl Flows in Combustion: A Review, AIAA J. 15 (8) (1977) 1063 1078.

[168] K. Midgley, A. Spencer, J. J. McGuirk, Unsteady flow structures in radial swirler fed fuel injectors, J. Eng. Gas Turb. and Power 127 (4) (2005) 755 764.

[169] J. Westerweel, On velocity gradients in PIV interrogation, Exp. fluid 44 (5) (2008) 831 842.

[170] A. F. Seybert, D. F. Ross, Experimental determination of acoustic properties using a two-microphone random-excitation technique, The Journal of the Acoustical Society of America 6 (5) (1977) 1362 1370.

[171] S.-H. Jang, J.-G. Ih, On the multiple microphone method for measuring in-duct acoustic properties in the presence of mean flow, The Journal of the Acoustical Society of America 103 (3) (1998) 1520 1526.

[172] J. Kopitz, A. Huber, T. Sattelmayer, W. Polifke, Thermoacoustic stability analysis of an annular combustion chamber with acoustic low order modeling and validation against experiment, in: ASME Turbo Expo 2005: Power for Land, Sea, and Air, American Society of Mechanical Engineers, 2005, pp. 583 593.

[173] C. Sovardi, Y. Aurégan, W. Polifke, Parametric les/si based aeroacoustic characterization of tandem orifices in low mach number flows, Acta Acustica united with Acustica 102 (5) (2016) 793 803.

[174] T. Poinsot, T. L. Chatelier, S. Candel, E. Esposito, Experimental determination of the reflection coefficient of a premixed flame in a duct, J. Sound Vib. 107 (1986) 265 278.

[175] A. Holmberg, M. Å bom, H. Bodén, Accurate experimental two-port analysis of flow generated sound, Journal of Sound and Vibration 330 (26) (2011) 6336 6354.

[176] H. Boden, M. Abom, Influence of errors on the two-microphone method for measuring acoustic properties in ducts, The Journal of the Acoustical Society of America 79 (2) (1986) 541 549.

[177] E. Dokumaci, A plane wave approximation to sound transmission in parallel sheared mean flow, Journal of Sound and Vibration 284 (3 5) (2005) 551 565.

[178] H. Boden, On multi-load methods for determination of the source data of acoustic one-port sources, Journal of Sound and Vibration 180 (5) (1995) 725 743.

[179] N. Syred, A review of oscillation mechanisms and the role of the precessing vortex core (PVC) in swirl combustion systems, Progress in Energy and Combustion Science 32 (2) (2006) 93 161.

[180] C. Sovardi, S. Jaensch, W. Polifke, Concurrent identification of aero-acoustic scattering and noise sources at a flow duct singularity in low mach number flow, Journal of Sound and Vibration 377 (2016) 90 105.

[181] D. Mejia, M. Miguel-Brebion, L. Selle, On the experimental determination of growth and damping rates for combustion instabilities, Combust. Flame 169 (2016) 287 296.

[182] N. Noiray, B. Schuermans, Deterministic quantities characterizing noise driven Hopf bifurcations in gas turbine combustors, International Journal of Non-Linear Mechanics 50 (2013) 152 163.

[183] G. Searby, A. Nicole, G. Ordonneau, M. Habiballah, A lightweight hybrid method to estimate the linear acoustic damping of arbitrarily complex geometries, in: 3rd European Conference for Aerospace Sciences (EUCASS), von Karman Institute for Fluid Dynamics, 2009, pp. CDROM ISBN.

[184] K. S. Kedia, C. Safta, J. Ray, H. N. Najm, A. F. Ghoniem, A second-order coupled immersed boundary-SAMR construction for chemically reacting flow over a heat-conducting Cartesian grid-conforming solid, J. Comput. Phys. 272 (2014) 408 428.

[185] K. S. Kedia, A. F. Ghoniem, The response of a harmonically forced premixed flame stabilized on a heat-conducting bluff-body, Proc. Combust. Inst. .

[186] R. B. Price, I. R. Hurle, T. M. Sugden, Optical studies of the generation of noise in turbulent flames, Symp. (Int.) on Combustion 12 (1) (1969) 1093 1102.

[187] O. Colin, M. Rudgyard, Development of High-Order Taylor Galerkin Schemes for LES, Journal of Computational Physics 162 (2) (2000) 338 371.

[188] V. Moureau, G. Lartigue, Y. Sommerer, C. Angelberger, O. Colin, T. Poinsot, Numerical methods for unsteady compressible multi-component reacting flows on fixed and moving grids, J. Comput. Phys. 202 (2) (2005) 710 736.

[189] B. F. Duchaine, S. Mendez, F. Nicoud, A. Corpron, V. Moureau, Coupling heat transfer solvers and large eddy simulations for combustion applications, Proc. of the Summer Program .

[190] F. Duchaine, S. Mendez, F. Nicoud, a. Corpron, V. Moureau, T. Poinsot, Conjugate heat transfer with Large Eddy Simulation for gas turbine components, C. R. Méc. 7 (6-7) (2009) 550 561.

[191] V. A. L. Erie, V. Frayssé, L. Giraud, S. Gratton, A set of GMRES routines for real and complex arithmetics on high performance computers, ACM Transactions on 31 (2) (2005) 228 238.

[192] J. Donea, A. Huerta, Finite element methods for flow problems, John Wiley & Sons, 2003.

[193] S. Buis, A. Piacentini, D. Déclat, the PALM Group, PALM: a computational framework for assembling high-performance computing applications, Concurr Comput 18 (May 2004) (2006) 231 245.

[194] T. Poinsot, S. Lele, Boundary conditions for direct simulations of compressible viscous flows, J. Comput. Phys. 101 (1) (1992) 104 129.

[195] T. Lu, C. K. Law, A criterion based on computational singular perturbation for the identification of quasi steady state species: A reduced mechanism for methane oxidation with NO chemistry, Combustion and Flame 154 (4) (2008) 761 774.

[196] P. Pepiot, H. Pitsch, Systematic reduction of large chemical mechanisms, in: 4th joint meeting of the US Sections of the Combustion Institute, Philadelphia, PA, 2005.

[197] P. Pepiot-Desjardins, H. Pitsch, An automatic chemical lumping method for the reduction of large chemical kinetic mechanisms, Combustion Theory and Modelling 12 (6) (2008) 1089 1108.

[198] D. G. Goodwin, H. K. Moffat, R. L. Speth, Cantera: An object-oriented software toolkit for chemical kinetics, thermodynamics, and transport processes, `http://www.cantera.org`, version 2.2.1 (2016).

[199] B. Franzelli, E. Riber, L. Y. M. Gicquel, T. Poinsot, Large Eddy Simulation of combustion instabilities in a lean partially premixed swirled flame, Combust. Flame 159 (2) (2012) 621 637.

[200] R. Sankaran, E. Hawkes, J. Chen, T. Lu, C. K. Law, Structure of a spatially developing turbulent lean methane air bunsen flame, Proc. Combust. Inst. 31 (2007) 1291 1298.

[201] X. J. Gu, M. Z. Haq, M. Lawes, R. Woolley, Laminar burning velocity and markstein lengths of methane-air mixtures, Combust. Flame 121 (2000) 41 58.

[202] R. Sankaran, E. R. Hawkes, J. H. Chen, T. Lu, C. K. Law, Structure of a spatially developing turbulent lean methane-air Bunsen flame, Proc. Combust. Inst. 31 I (2007) 1291 1298.

[203] M. Frenklach, H. Wang, M. Goldenberg, G. P. Smith, D. M. Golden, C. T. Bowman, R. K. Hanson, W. C. Gardiner, V. Lissianki, GRI-mech: an optimized detailed chemical reaction mechanism for methane combustion, Tech. Rep. GRI-Report GRI-95/0058, Gas Research Institute (1995).

[204] G. P. Smith, D. M. Golden, M. Frenklach, N. W. Moriarty, B. Eiteneer, M. Goldenberg, C. T. Bowman, R. K. Hanson, S. Song, W. C. Gardiner Jr, et al., Gri 3.0 mechanism, Gas Research Institute.

[205] T. Jaravel, Prediction of pollutants in gas turbines using large eddy simulation, Ph.D. thesis, CERFACS (2016).

[206] P. Dirrenberger, H. Le Gall, R. Bounaceur, O. Herbinet, P. A. Glaude, A. Konnov, F. Battin-Leclerc, Measurements of laminar flame velocity for components of natural gas, Energ. Fuel 25 (9) (2011) 3875 3884.

[207] M. I. Hassan, K. T. Aung, G. M. Faeth, Measured and predicted properties of laminar premixed methane/air flames at various pressures, Combust. Flame 115 (4) (1998) 539 550.

[208] C. M. Vagelopoulos, F. N. Egolfopoulos, Direct experimental determination of laminar flame speeds, Symp. (Int.) on Combustion 27 (1) (1998) 513 519.

[209] I. Dyakov, A. A. Konov, J. D. Ruyck, K. J. Bosschaart, E. C. M. Brock, L. P. H. De Goey, Measurement of Adiabatic Burning Velocity in Methane-Oxygen-Nitrogen Mixtures, Combust. Sci. Tech. 172 (1) (2001) 81 96.

[210] H. S. Dou, B. C. Khoo, H. M. Tsai, Critical Condition for Flow Transition in a Full- Developed Annulus Flow, J. Petr. Sci. Eng.71 (2000) 1 6.

[211] W. H. MacAdams, Heat transmission, McGraw-Hill New York, 1954.

[212] M. Von Kármán, Theoretical and Experimental Studies on laminar combustion and detonation waves, Symp. (Int.) on Combustion.

[213] J. Buckmaster, Edge-flames, Prog. Energy Comb. Sci. 28 (5) (2002) 435 475.

[214] T. Vedarajan, J. Buckmaster, Edge-flames in homogeneous mixtures, Combust. Flame 114 (1) (1998) 267 273.

[215] G. M. Makhviladze, V. I. Melikhov, Flame propagation in a closed channel with cold side walls, Combust. Explo. Shock W.27 (2) (1991) 176 183.

[216] I. S. Wichman, G. Bruneaux, Head-on quenching of a premixed flame by a cold wall, Combust. Flame 103 (4) (1995) 296 310.

[217] A. Gruber, R. Sankaran, E. R. Hawkes, J. H. Chen, Turbulent flame wall interaction: a direct numerical simulation study, J. Fluid Mech. 658 (2010) 5 32.

[218] A. Gruber, J. H. Chen, D. Valiev, C. K. Law, Direct numerical simulation of premixed flame boundary layer flashback in turbulent channel flow, J. Fluid Mech. 709 (2012) 516 542.

[219] J. H. Lu, O. Ezekoye, R. Greif, R. F. Sawyer, Unsteady heat transfer during side wall quenching of a laminar flame, Symp. (Int.) on Combustion 23 (1) (1991) 441 446.

[220] F. A. Williams, Combustion Theory, Benjamin Cummings, Menlo Park, CA, 1985.

[221] T. Takeno, K. Sato, K. Hase, A theoretical study on an excess enthalpy flame, Symp. (Int.) on Combustion 18 (1) (1981) 465 472.

[222] T. Kawamura, K. Asato, T. Mazaki, Reexamination of the blowoff mechanism of premixed flames-inverted flames, Combust. Flame 45 (C) (1982) 225 233.

[223] K. S. Kedia, A. F. Ghoniem, Mechanisms of stabilization and blowoff of a premixed flame downstream of a heat-conducting perforated plate, Combustion and Flame 159 (3) (2012) 1055 1069.

[224] M. Drkos, C. Leung, C. Cheung, Flame stability of rod stabilised premixed butane/air flames, Journal of the Energy Institute.

[225] R. J. Blint, The relationship of the laminar flame width to flame speed, Combust. Sci. Tech. 49 (1986) 79 92.

[226] P. A. Libby, F. A. Williams, Strained premixed laminar flames under non-adiabatic conditions, Combust. Sci. Tech. 31 (1983) 1 42.

[227] C. Coats, Z. Chang, P. Williams, Excitation of thermoacoustic oscillations by small premixed flames, Combust. Flame 157 (2010) 1037 1051.

[228] F. E. C. Culick, Combustion instabilities in liquid-fueled propulsion systems- an overview, in: AGARD 72B PEP meeting, 1988.

[229] L. Tay-Wo-Chong, S. Bomberg, A. Ulhaq, T. Komarek, W. Polifke, Comparative validation study on identification of premixed flame transfer function, Journal of Engineering for Gas Turbines and Power 134 (2) (2012) 021502.

[230] V. Kornilov, R. Rook, J. ten Thije Boonkkamp, L. de Goey, Experimental and numerical investigation of the acoustic response of multi-slit bunsen burners, Combust. Flame (2009) 1957 1970.

[231] F. Boudy, D. Durox, T. Schuller, S. Candel, Nonlinear mode triggering in a multiple flame combustor, Proc. Combust. Inst. 33 (2011) 1121 1128.

[232] L. Chong, T. Komarek, R. Kaess, S. Foller, W. Polifke, Identification of flame transfer functions from les of a premixed swirl burner, in: A. P. GT2010-22769 (Ed.), ASME Turbo expo, Glasgow, UK, 2010.

[233] N. Noiray, D. Durox, T. Schuller, S. Candel, A unified framework for nonlinear combustion instability analysis based on the flame describing function, J. Fluid Mech. 615 (2008) 139 167.

[234] S. Candel, D. Durox, T. Schuller, J.-F. Bourgouin, J. P. Moeck, Dynamics of Swirling Flames, Ann. Rev. Fluid Mech. 46 (1) (2014) 147 173.

[235] J.-F. Bourgouin, D. Durox, J. P. Moeck, T. Schuller, S. Candel, Characterization and Modeling of a Spinning Thermoacoustic Instability in an Annular Combustor Equipped With Multiple Matrix Injectors, J. Eng. Gas Turb. and Power 137 (2) (2015) 021503 11.

[236] C. F. Silva, T. Emmert, S. Jaensch, W. Polifke, Numerical study on intrinsic thermoacoustic instability of a laminar premixed flame, Combustion and Flame 162 (9) (2015) 3370 3378.

[237] L. Ljung, System identification: Theory for the user, ptr prentice hall information and system sciences series (1999).

[238] A. Huber, W. Polifke, part I : model structure and identification, International journal of spray and combustion dynamics 1 (2) (2009) 169 198.

[239] A. L. Birbaud, D. Durox, S. Ducruix, S. Candel, Dynamics of confined premixed flames submitted to upstream acoustic modulations, Proc. Combust. Inst. 31 (2007) 1257 1265.

[240] E. Courtine, L. Selle, T. Poinsot, DNS of Intrinsic ThermoAcoustic modes in laminar premixed flames, Combust. Flame 162 (11) (2015) 4331 4341.

[241] B. Cabral, L. C. Leedom, Imaging vector fields using line integral convolution, in: Proceedings of the 20th Annual Conference on Computer Graphics and Interactive Techniques, SIGGRAPH 93, ACM, New York, NY, USA, 1993, pp. 263 270.

[242] M. Fleifil, A. M. Annaswamy, Z. A. Ghoneim, A. F. Ghoniem, Response of a laminar premixed flame to flow oscillations: A kinematic model and thermoacoustic instability results, Combust. Flame 106 (4) (1996) 487 510.

[243] L. Boyer, J. Quinard, On the dynamics of anchored flames, Combust. Flame 82 (1990) 51 65.

[244] A. P. Dowling, Nonlinear self-excited oscillations of a ducted flame, J. Fluid Mech. 346 (1997) 271 290.

[245] M. Hoeijmakers, V. Kornilov, I. L. Arteaga, P. de Goey, H. Nijmeijer, Intrinsic instability of flame-acoustic coupling, Combust. Flame 161 (2014) 2860 2867.

[246] T. Emmert, S. Bomberg, W. Polifke, Intrinsic thermoacoustic instability of premixed flames, Combust. Flame 162 (1) (2015) 75 85.

[247] T. Emmert, S. Bomberg, S. Jaensch, W. Polifke, Accounting for acoustic damping in a helmholtz solver, 36th International Symposium on Combustion (not published yet).

[248] M. Schmid, R. S. Blumenthal, M. Schulze, W. Polifke, T. Sattelmayer, Quantitative Stability Analysis Using Real-Valued Frequency Response Data, Journal of Engineering for Gas Turbines and Power 135 (12) (2013) 121601.

[249] N. Noiray, D. Durox, T. Schuller, S. Candel, Self-induced instabilities of premixed flames in a multiple injection configuration, Combust. Flame 145 (3) (2006) 435 446.

[250] T. Komarek, W. Polifke, Impact of swirl fluctuations on the flame response of a perfectly premixed swirl burner, Journal of Engineering for Gas Turbines and Power 132 (6) (2010) 061503.

[251] L. Tay-Wo-Chong, W. Polifke, Large eddy simulation-based study of the influence of thermal boundary condition and combustor confinement on premix flame transfer functions, J. Eng. Gas Turb. and Power 135 (2013) 021502.

[252] W. Polifke, J. Kopitz, A. Serbanoviv, Impact of the fuel time lag distribution in elliptical premix nozzles on combustion stability, in: 7th AIAA/CEAS Aeroacoustics Conference and Exhibit, 2001, p. 2104.

[253] K. Peat, The acoustical impedance at discontinuities of ducts in the presence of a mean flow, J. Sound Vib. 127 (1988) 123 132.

[254] M. L. Munjal, Acoustics of Ducts and Mufflers, John Wiley & Sons, 1986.

[255] A. Kapur, A. Cummings, P. Mungur, Sound propagation in a combustion can with axial temperature and density gradients, Journal of Sound and Vibration 25 (1) (1972) 129 138.

[256] R. I. Sujith, G. A. Waldherr, B. T. Zinn, An exact solution for one-dimensional acoustic fields in ducts with an axial temperature gradient, Journal of Sound and Vibration 184 (1995) 389 402.

[257] S. W. Rienstra, A small strouhal number analysis for acoustic wave-jet flow-pipe interaction, J. Sound Vib. 86 (1983) 539 556.

[258] S. Bomberg, T. Emmert, W. Polifke, Thermal versus acoustic response of velocity sensitive premixed flames, Proceedings of the Combustion Institute 35 (3) (2015) 3185 3192.

[259] N. Noiray, D. Durox, T. Schuller, S. Candel, Passive control of combustion instabilities involving premixed flames anchored on perforated plates, Proc. Combust. Inst. 31 (2007) 1283 1290.

[260] M.Abom, H. Boden, Error analysis of two-microphone measurements in ducts with flow, Journal of the Acoustical Society of America 83 (6) (1988) 2429 2438.